The University of Sheffield

NOVEL SENSORLESS CONTROL OF PERMANENT MAGNET BRUSHLESS MACHINES FOR HIGH SPEED APPLICATION

Lei Yang

A thesis submitted for the degree of Doctor of Philosophy

Department of Electronic and Electrical Engineering

University of Sheffield

Mappin Street, Sheffield, S1 3JD, UK

22 July 2020

ABSTRACT

This thesis is focused on sensorless brushless DC (BLDC) and brushless AC (BLAC) drives, particularly for high-speed application.

For BLDC drives, zero-crossing detection (ZCD) of back EMF is the most popular solution for sensorless control. In order to further improve its performance and robustness in the high-speed range, a comprehensive investigation is carried out. Firstly, the oversampling technique is employed to detect the zero-crossing points (ZCPs) of back EMF, which can considerably reduce the sampling delay when the sampling ratio is insufficient. Secondly, two non-ideal factors that will deviate the ZCPs, i.e. asymmetric machine parameters and the resistance tolerance of back EMF measurement circuit, are studied. The corresponding commutation correction algorithms are developed to eliminate the commutation errors caused by these non-ideal factors. Thirdly, the ZCP may be undetectable due to a long freewheeling angle, which is a critical burden of the ZCD based sensorless method operating towards high-speed. Consequently, a PWM pattern resulting in a minimum freewheeling angle is identified and a theoretical technique is developed to predict the maximum torque and speed region for sensorless control.

In the high-speed range, the PWM switching ratio is usually insufficient. It is found that conventional commutation patterns, i.e. regular-sampled commutation (RSC) and natural-sampled commutation (NSC), may lead to commutation delay, unstable sensorless control and abundant sideband harmonics. To suppress these adverse influences, a novel commutation pattern, i.e. carrier-synchronized commutation (CSC), is proposed, which can considerably improve the control performance when the switching ratio is insufficient.

For high-speed BLAC drives, the main challenge is the design of a decoupling current controller and a rotor position observer. To tackle this challenge, a generic discrete-time BLAC model considering the fractional period sampling delay is developed. Based on this model, a new decoupling current controller and a new rotor position observer are designed directly in discrete-time domain, which can guarantee good control performance in the low sampling ratio condition.

ACKNOWLEDGEMENTS

I would like to thank my supervisor, Prof. Z. Q. Zhu, for his professional technical guidance, invaluable support and encouragement during my whole PhD study. I have learned not only the knowledge but also the way of thinking from him.

I also would like to express my thanks to the PhD students and staff in the Electrical Machines and Drives Group, including Dr. Yanxin Li and Dr. Yu Wang, for their help and support in the starting point of my PhD study, Mr. Bo Shuang for his assistance in the test rig construction, Dr. Rui Zhou and Dr. Kai Zhang for their discussion, Dr. Zhan-Yuan Wu for his help in my experiments and other colleagues for their help in many ways.

Thanks for the financial support from the China Scholarship Council (CSC) and the Midea Group.

Finally, I am very grateful to my wife Dr. Yan Fu for her love. She always encourages me and understands me when I got confused and lost in my life. I would also like to thank my parents for their support and endless care.

CONTENTS

ABSTRACT II
ACKNOWLEDGEMENTS III
CONTENTS IV
LIST OF SYMBOLS VIII
LIST OF ABBREVIATIONS X

CHAPTER 1 1
General Introduction 1
1.1 Introduction....1
1.2 Brushless DC and AC Motor Drives....2
1.2.1 Basic Principles....2
1.2.2 Brushless DC and AC Operation....3
1.3 Review of Sensorless Methods for Brushless Motor Drives....8
1.3.1 Sensorless Brushless DC Operation in High-speed Range....9
1.3.2 Sensorless Brushless DC Operation in Low-speed Range....13
1.3.3 Sensorless Brushless AC Operation in High-speed Range....14
1.3.4 Sensorless Brushless AC Operation in Low-speed Range....18
1.4 Issues with High-speed Brushless DC and AC Drives....21
1.4.1 Issues in High-speed BLDC Operation....21
1.4.2 Issues in High-speed BLAC Operation....28
1.5 Outline and Contributions of the Thesis....30

CHAPTER 2 33
Virtual Third Harmonic Back-EMF Based Sensorless BLDC Drives Considering Machine Parameter Asymmetries 33
2.1 Introduction....33
2.2 ZCP Detection of Virtual Third Harmonic Back EMF....35
2.2.1 Virtual Third Harmonic Back EMF....35
2.2.2 Zero-crossing Detection Based on Over-sampling Method....38
2.3 Phase Compensation for Asymmetric Parameters....41
2.3.1 Commutation Errors Caused by Asymmetric Parameters....41
2.3.2 Phase Compensation of Commutation Errors....44
2.4 Experimental Validation....48
2.5 Summary....55

CHAPTER 3 57
Adaptive Threshold Correction Strategy for BLDC Drives Considering Zero Crossing Point Deviation 57
3.1 Introduction....57

3.2 Horizontal Deviation Caused by Machine Parameter Asymmetry 59
3.2.1 BLDC Machine Model 59
3.2.2 Horizontal Deviation of EMF Envelopes 61
3.2.3 Influence of Machine Parameter Asymmetry on ZCP Detection 65
3.3 Vertical Deviation Caused by Resistance Tolerance of RVD 67
3.3.1 Resistance Tolerance of Measurement Circuit 67
3.3.2 Voltage Shift and ZCP Angle Errors 68
3.4 Proposed Adaptive Threshold Correction Algorithm for Envelope Deviation 69
3.4.1 Vertical Correction 70
3.4.2 Horizontal Correction 73
3.5 Experimental Validation 75
3.6 Summary 83

CHAPTER 4 84

Safe Operating Area of Zero-Crossing Detection Based Sensorless High-Speed BLDC Motor Drives 84

4.1 Introduction 84
4.2 PWM Switching Patterns and Freewheeling Angle 86
4.3 Analysis of Commutation Freewheeling Processes 90
4.3.1. Commutation Mode 1 91
4.3.1. Commutation Mode 2 95
4.4 Freewheeling Angles and Sensorless SOA 98
4.4.1 Comparison of Current Descent Rates 98
4.4.2 Prediction of Sensorless SOA 102
4.5 Simulation and Experiment Results 103
4.6 Summary 107
4.7 Appendix: Review on Other Factors of Freewheeling Angle 108
4.7.1 Resistance and Inductance 108
4.7.2 DC-link Voltage 111
4.7.3 PWM Duty-Ratio 112
4.7.4 Summary of Appendix 113

CHAPTER 5 114

PWM Switching Delay Correction Method for High-Speed BLDC Drives 114

5.1 Introduction 114
5.2 Commutation Delay Caused by Conventional PWM Generation 117
5.2.1 Six-step Control and Digital PWM Generation 117
5.2.2 Graphic Representation of Inverter Output 118
5.3 Accumulative Errors in Sensorless BLDC Drives 120
5.3.1 Principle of Zero Crossing Detection 121
5.3.2 Instability Caused by Accumulative Errors 123

5.4 Principle of Carrier-Synchronized Commutation 124
5.4.1 Synchronization Scheme 124
5.4.2 Spectral Characteristic Analysis 126
5.4.3 Keeping Linearity between Reference and Output 129
5.5 Simulation and Experimental Results 131
5.5.1 Simulation Results 131
5.5.2 Experimental Results 132
5.6 Summary 138

CHAPTER 6 139

Spectral Analysis and Sideband Harmonic Cancellation of Six-Step BLDC Operation with Low Switching Ratio 139

6.1 Introduction 139
6.2 Mechanism of Six-Step Commutation With PWM Generation 142
6.2.1 Regular-Sampled Commutation (RSC) 143
6.2.2 Natural-Sampled Commutation (NSC) 144
6.2.3 Carrier-Synchronized Commutation (CSC) 145
6.3 Spectral Characteristics of NSC and RSC Patterns 146
6.3.1 Extended Geometric Wall Model and Double Fourier Series 147
6.3.2 Spectral Analysis of NSC Pattern 149
6.3.3 Spectral Analysis of RSC Pattern 151
6.3.4 Harmonic Distribution 153
6.4 Spectral Characteristics of CSC Pattern 156
6.5 Torque Ripples Caused by Harmonic Currents 158
6.5.1 Sideband Harmonic Currents of RSC and NSC Patterns 158
6.5.2 Torque Ripple Analysis of RSC and NSC Patterns 159
6.5.3 Torque Ripple Analysis of CSC Pattern 160
6.6 Simulation and Experimental Validations 161
6.7 Summary 167

CHAPTER 7 168

Discrete-time Current Controller and EMF Observer based on Generic Delay Model for High-speed BLAC Drive 168

7.1 Introduction 168
7.2 Generic Delay Model in Discrete-time Domain 171
7.2.1 Review of Current Sampling in Regular-sampled PWM 171
7.2.2 Continuous-time Model 173
7.2.3 Discrete-time Model Considering Voltage Latch 173
7.2.4 Discrete-time Model Considering Sampling Delay 175
7.2.5 Particular Cases: Single and Half Period Sampling Delay 177
7.3 Discrete-time Current Controller with Enhanced Decoupling Capability 179
7.3.1 Review of Existing Decoupling Controllers 179

7.3.2 Enhanced Decoupling Controller Based on Proposed Model 182
7.3.3 Evaluation of Tracking and Decoupling Capabilities 182
7.3.4 Simulation Results 187
7.4 Discrete-time State Observer for Rotor Position Estimation 192
7.4.1 EMF Observer based on Proposed Model 192
7.4.2 Influence of Improper Delay Modelling on Rotor Position Estimation 193
7.4.3 Particular Case: Single Period Sampling Delay 196
7.4.4 Simulation Results 197
7.5 Summary 201

CHAPTER 8 202

General Conclusions and Discussions 202

8.1 Sensorless High-speed Brushless DC Control 202
8.2 Sensorless High-speed Brushless AC Control 205
8.3 Future Work 206

REFERENCES 208

APPENDIX 1 223

Specification and Parameters of Test Rig and PM Brushless Motors 223

A1.1 Hardware Design of Test Rig 223
A1.2 High-speed PM Brushless Motors 228

APPENDIX 2 230

Specification and Parameters of Simulation Models 230

APPENDIX 3 231

Publications During PhD Study 231

LIST OF SYMBOLS

Symbol	Explanation of Symbol	Unit
e_A, e_B, e_C	3-phase back EMFs	V
$\boldsymbol{e}_{dq}$	Back EMF complex vector in *d-q* synchronous frame	V
$\boldsymbol{e}_{\alpha\beta}$	Back EMF complex vector in *α-β* stationary frame	V
f_c	PWM switching (carrier) frequency	Hz
f_e	Fundamental frequency	Hz
f_s	Sampling frequency	Hz
i_A, i_B, i_C	3-phase currents	A
i_d, i_q	*d*- and *q*-axis currents	A
$\boldsymbol{i}_{dq}$	Current complex vector in *d-q* synchronous frame	A
i_α, i_β	*α*- and *β*-axis currents	A
$\boldsymbol{i}_{\alpha\beta}$	Current complex vector in *α-β* stationary frame	A
L_A, L_B, L_C	3-phase inductances	H
M	PWM duty ratio	
N	Sector carrier ratio $N = f_c / 6f_e$	
p_n	Pole pairs	
R_A, R_B, R_C	3-phase resistances	Ω
R_1, R_2	Low and high side resistances of RVD	Ω
T_d	Sampling delay	s
T_s	Sampling period	s
$\boldsymbol{u}_{dq}$	Voltage complex vector in *d-q* synchronous frame	V
$\boldsymbol{u}_{\alpha\beta}$	Voltage complex vector in *α-β* stationary frame	V
v_{AG}, v_{BG}, v_{CG}	Terminal voltages	V
v_{AS}, v_{BS}, v_{CS}	Virtual phase voltages	V
v_d, v_q	*d*- and *q*-axis voltages	V
v_{NG}	Voltage of machine neutral point “N” in respect to ground	V
v_{SG}	Voltage of resistor-network point “S” in respect to ground	V

v_{SM}	Voltage of resistor-network point "S" in respect to DC-link central point "M"	V
v_{α}, v_{β}	α- and β-axis voltages	V
Δv_{H}, Δv_{V}	Voltage errors of horizontal and vertical deviations	V
V_{RL}	Voltage drop on resistance and inductance	V
V_{AD}	Maximum sampling voltage	V
V_{dc}	DC-link voltage	V
η_{m1}^{on}, η_{m1}^{off}	Current descent rates during chop-on and chop-off in mode 1	
η_{m2}^{on}, η_{m2}^{off}	Current descent rates during chop-on and chop-off in mode 2	
θ_e	Electrical rotor position	rad
$\theta_{\mathrm{CTN\text{-}IDL}}$	Ideal commutation position	rad
$\theta_{\mathrm{CTN\text{-}ACT}}$	Actual commutation position	rad
$\theta_{\mathrm{CTN\text{-}TRG}}$	Triggered commutation position	rad
$\theta_{\mathrm{ZCP\text{-}IDL}}$	Ideal ZCP position	rad
θ_{ZCP}	Detected ZCP position	rad
θ_{FRW}	Position where freewheeling completes	rad
$\Delta\theta_{\mathrm{A}}$, $\Delta\theta_{\mathrm{B}}$, $\Delta\theta_{\mathrm{C}}$	Position errors of zero-crossing points	rad
$\Delta\theta_{\mathrm{CTN}}$	Commutation error	rad
φ_{m1}, φ_{m2}	Freewheeling angles in modes 1 and 2	rad
$\varphi_{m1}^{\mathrm{sup}}$	Upper bound of freewheeling angle in mode 1	rad
ψ_f	Flux linkage of PM	wb
ω_{c}	PWM switching (Carrier) frequency	rad/s
ω_e	Electrical rotor speed	rad/s
ω_{pu}	Per-unit value of rotor speed $\omega_{\mathrm{pu}} = \omega_e / \omega_{\mathrm{base}}$	
ω_{base}	Base rotor speed $\omega_{\mathrm{base}} = V_{\mathrm{dc}} / \sqrt{3}\psi_f$	rad/s

LIST OF ABBREVIATIONS

AC	Alternating current
AD	Analog to digital
ADC	Analog to digital converter
BLAC	Brushless AC
BLDC	Brushless DC
CSC	Carrier-synchronized commutation
CSI	Current source inverter
DC	Direct current
DSP	Digital signal processor
EKF	Extended Kalman filter
EMF	Electromotive force
FOC	Field oriented control
FPGA	Field programmable gate array
LDF	Lower-diode freewheeling
LPF	Low-pass filter
NSC	Natural-sampled commutation
PCB	Printed circuit boards
PI	Proportional integral
PLL	Phase lock loop
PM	Permanent magnet
PWM	Pulse width modulation
RSC	Regular-sampled commutation
RVD	Resistive voltage divider
SMO	Sliding mode observer
SOA	Safe operating area
UDF	Upper-diode freewheeling
VSI	Voltage source inverters
WTHD	Weighed total harmonic distortion

ZCD	Zero-crossing detection
ZCP	Zero-crossing point

CHAPTER 1

General Introduction

1.1 Introduction

Equation Chapter 1 Section 1Permanent magnet (PM) brushless motor drives have been widely adopted in industrial and domestic applications for their superior efficiency and power density. In addition, the development of modern power-electronics and microelectronics are facilitating the drive applications trending towards high-speed. A common advantage of high-speed motor drive is the reduction of system weight and size. On one hand, due to increased speed, the size and weight of high-speed motors are lower than those of normal speed motors for a given power level. On the other hand, for some applications, such as turbo chargers and vacuum cleaners, it enables direct drive, which means the elimination of intermediate gearing. Thus, high-speed PM brushless motor drives have received much research attention these years.

Generally, the rotor position signal is necessary in the PM brushless motor control. However, rotor position sensors, such as Hall-effect sensors, optical encoders and resolvers, will increase the system cost and reduce the reliability. Especially, low installation precision of these mechanical sensors will limit the maximum speed. Therefore, for high-speed PM brushless motor drives, it is preferred to estimate the rotor position from sensorless techniques. On the other hand, as the motor speed increases, the PWM switching ratio and sampling ratio will become insufficient, which generates various problems to the high-speed motor control. Those are the motivations of the investigation in this thesis.

The main focus of this chapter is to briefly introduce PM brushless DC (BLDC) and brushless AC (BLAC) operation, as well as the review of various sensorless control techniques. Besides, some issues with high-speed PM brushless motor drives and corresponding solutions proposed in this thesis are introduced. The outline and the contributions of the thesis are also listed at the end of this chapter.

1.2 Brushless DC and AC Motor Drives

1.2.1 Basic Principles

Generally, PM brushless motors can be classified as being trapezoidal and sinusoidal back EMF motors as shown in Fig. 1.1. The control strategies can be classified as BLDC and BLAC operation, whose phase currents are ideally square-wave and sinusoidal, respectively. To achieve the torque maximization and torque ripple minimization, it is preferred to operate the trapezoidal back EMF motor in BLDC mode, and the sinusoidal back EMF motor in BLAC mode. However, in practice, the back EMF may be significantly different from the ideal waveforms. Besides, the selection of BLDC or BLAC modes also depends on the specific application. Various factors should be taken into consideration, e.g. the implementation complexity, the system cost and the performance demand, etc. Hence, irrespective of the back EMF waveforms, the PM brushless machines may be operated in either BLDC or BLAC mode.

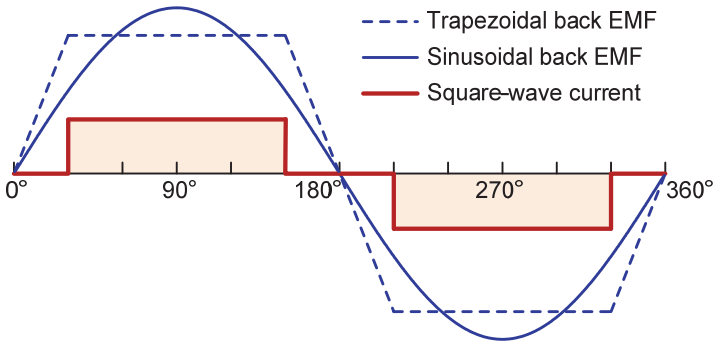

(a) Square-wave current in BLDC operation.

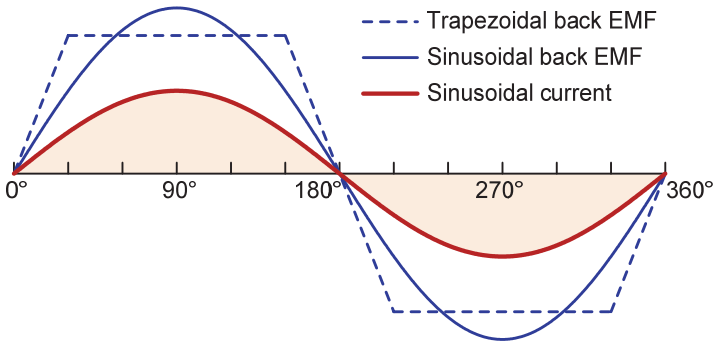

(b) Sinusoidal current in BLAC operation.

Fig. 1.1. Back EMF and phase current waveforms of BLDC and BLAC drives.

1.2.2 Brushless DC and AC Operation

1) BLDC Operation Based on Six-step Control

In the BLDC operation, the three-phase current should be aligned with the back EMF so that the angle between the stator flux and the rotor flux is kept within the range from 60° to 120° to produce the maximum torque. Generally, two types of six-step control can be employed in BLDC operation, i.e. two-phase 120° conduction and three-phase 180° conduction, which are shown in Fig. 1.2 (a) and (b), respectively [ZHU07][CHA15].

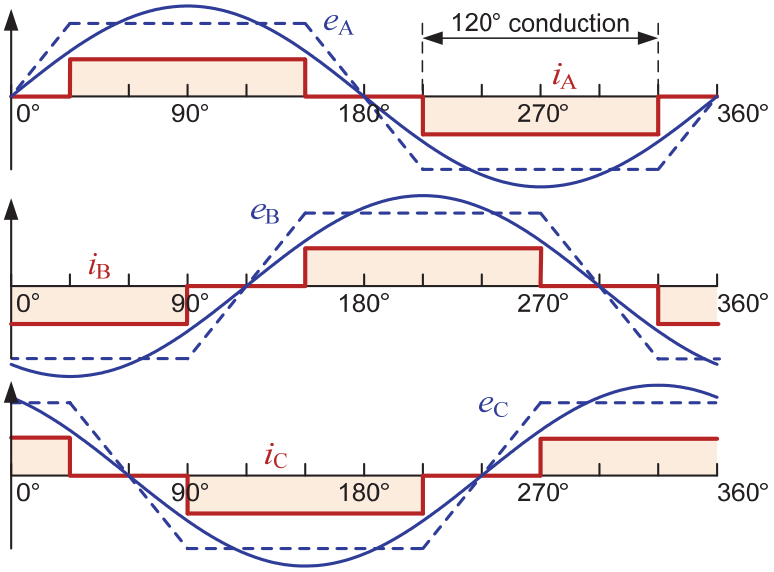

(a) Two-phase 120° conduction six-step control.

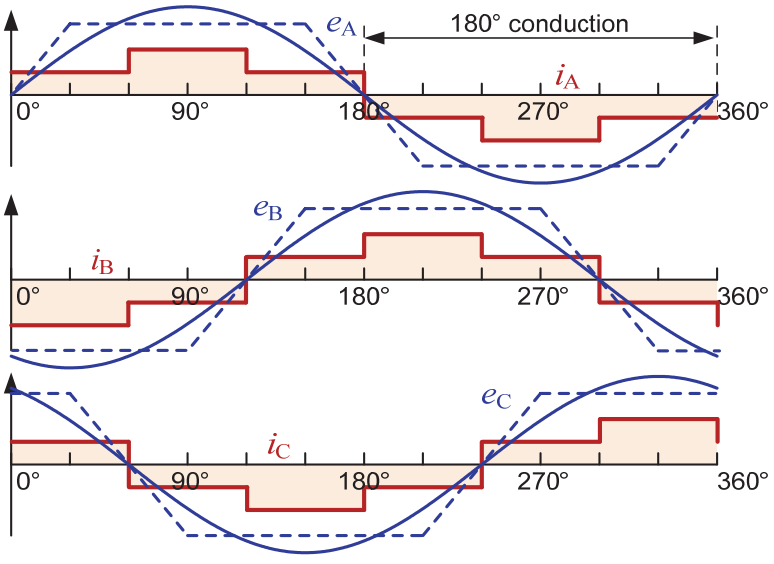

(b) Three-phase 180° conduction six-step control.

Fig. 1.2. Illustration of 120° and 180° conduction six-step control strategies.

In the two-phase 120° conduction six-step control, a fundamental cycle is divided into six sectors as shown in Fig. 1.2 (a). In each sector, two of the three phases are conducted and the third phase is floating. For each phase, it conducts for 120° and then rests for 60°. In this 60° floating interval, the back EMF can be measured, which provides a way to detect the rotor position. On the other hand, in the three-phase 180° conduction scheme as shown in Fig. 1.2 (b), at any instant, all the three phases are conducted. Thus, the back EMF cannot be directly measured, meaning that the sensorless method applied for the 120° conduction scheme cannot be applied to the 180° conduction scheme.

It was reported in [ZHU07] that the 120° conduction scheme takes the advantage of higher torque capability below the base speed; the 180° conduction scheme has better constant power performance above the base speed. In practice, the 120° conduction scheme is more preferable and relatively widely applied, due to two features: 1) the sensorless control of 120° conduction is easier to realize as discussed earlier. 2) the torque ripple of 120° conduction is smaller. This thesis is focused on high-speed sensorless control, and thus, the 120° conduction scheme is selected for the BLDC operation.

Fig. 1.3 shows block diagrams for the 120° conduction six-step control, where ω_e is the motor speed and i_{dc} is the DC-link current. The superscript "*" denote the reference value. As shown in Table 1.1, six sectors are defined according to the rotor position, which determine the conduction modes of the three phases. The conduction sequence across the six sectors are stored in the commutation logic block in Fig. 1.3.

Table 1.1 Definition of Sectors and Conduction Modes

Sector	Rotor position	Positive phase	Negative phase	Floating phase
I	30°-90°	A	B	C
II	90°-150°	A	C	B
III	150°-210°	B	C	A
IV	210°-270°	B	A	C
V	270°-330°	C	A	B
VI	330°-30°	C	B	A

Basically, the standard control system of 120° conduction six-step contains two control loops, i.e. the outer loop for speed control and the inner loop for current control, which are connected in cascade. The measured and estimated mechanical and electrical variables are fed back in each closed loop. The output of the speed controller is the reference input of the current controller i_{dc}^{*}. By adjusting the PWM duty ratio (output voltage), the feedback current i_{dc} can track the reference input i_{dc}^{*} and the feedback speed ω_e can track the reference input ω_e^{*}. That is the mechanism of the typical 120° conduction six-step control. Since the time constant of electrical variables (resistance and inductance) is far lower than the one of mechanical variables, the inner loop is much faster than the outer loop. In this way, there are no interferences between the current and speed controllers, and thus, they can be designed and tuned independently.

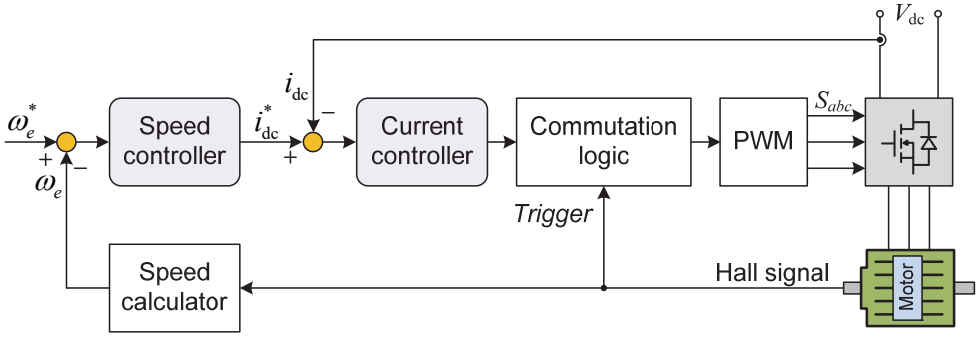

(a) Sensored scheme.

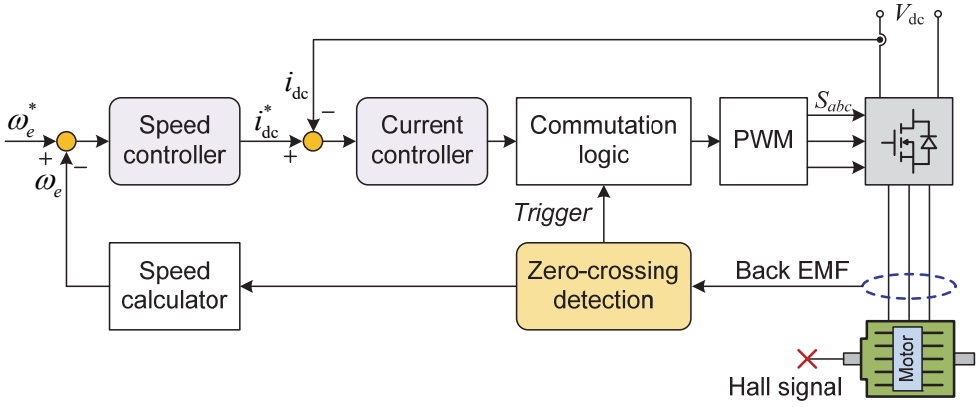

(b) Sensorless scheme.

Fig. 1.3. Block diagram of BLDC operation based on six-step control.

For the current control loop, since only two phases are conducted, the stator current is directly reflected on the DC-link. Then, the DC-link current signal is usually utilized in the current control loop. For the speed control loop, the motor speed and rotor position (commutation instants) information can be either derived from sensored or

sensorless scheme. For the former as shown in Fig. 1.3 (a), the commutation is triggered by the Hall-effect sensors. The motor speed can be calculated from the time-duration between two subsequent transitions of Hall-effect sensors. For the latter as shown in Fig. 1.3 (b), the commutation instant can be identified from the measured back EMF. The details for sensorless method will be discussed in the next section.

2) BLAC Operation Based on Field-oriented Control

Field-oriented control (FOC), also known as vector control, is widely applied for inverter fed induction and synchronous motor drives. Fig. 1.4 illustrates the basic diagram of FOC. Here, i_a and i_c are the currents in stationary *a-b-c* frame, i_α and i_β are the currents in stationary α-β frame, i_d and i_q are the currents in synchronous *d-q* frame, v_α and v_β are the voltages in stationary α-β frame, v_d and v_q are the voltages in synchronous *d-q* frame, ω_e and θ_e are the rotor speed and position. The superscript "*" denote the reference value and the superscript "^" denote the estimated value.

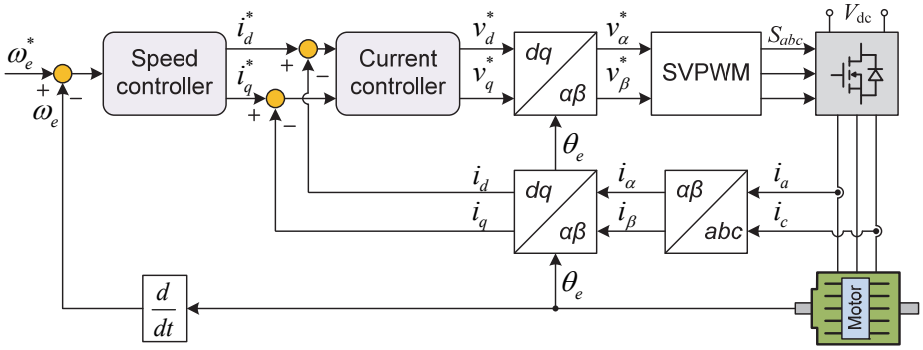

(a) Sensored scheme.

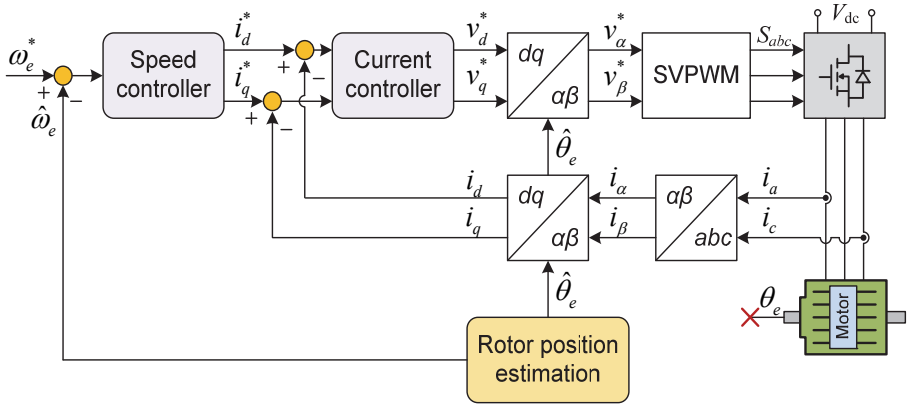

(b) Sensorless scheme.

Fig. 1.4. Block diagram of BLAC operation based on field-oriented control.

The advantage of FOC over six-step control is that it is possible to separate the control for torque and flux from each other. The three-phase currents in the stationary *a-b-c* frame are transformed to the synchronous *d-q* frame i_d and i_q, which correspond to flux and electric torque generation, respectively. To this end, the continuous rotor position signal is necessary, which can be obtained either from sensored or sensorless technique. For the former as shown in Fig. 1.4 (a), it usually needs high resolution sensors such as resolver and optical encoder. For the latter as shown in Fig. 1.4 (b), some sensorless methods such as the model based method and the saliency based method can be used, which will be discussed in the next section.

3) Comparison between BLDC and BLAC Operation

A comparison of the BLDC and BLAC drives is listed in Table 1.2. Good features are denoted by shaded background. Overall, the advantage of BLDC operation lies in easy-to-implement (low control and sensorless complexity) and low cost (cheap position sensors and just one current sensor); the BLAC operation features high comfort (low current ripples, torque ripples and acoustic noise).

Table 1.2. Comparison between BLDC and BLAC drives

	BLDC	BLAC
Control strategy	Six-step	Field-oriented control
Position sensors	Low resolution (Hall-effect sensors)	High resolution (Encoder/resolver)
Sensorless complexity	Low	High
Current sensors	1 (DC-link current)	≥2 (Three-phase currents)
Current harmonics	High	Low
Torque ripples	High	Low
Acoustic noise	High	Low
Control complexity	Low	High

1.3 Review of Sensorless Methods for Brushless Motor Drives

For both BLDC and BLAC drives, as introduced earlier, the rotor position signals are necessary, which can be obtained either from sensored or sensorless scheme. It is commonly known that all the sensors have inevitable drawbacks. The Hall-effect sensors applied for BLDC operation are quite difficult to achieve high installation accuracy, especially in small size motors. Besides, the Hall-effect sensors are sensitive to the environment, including high temperature surrounding and electromagnetic interference. The optical encoder and resolver applied for BLAC operation have to be equipped on the motor shaft, which will enlarge the rotor axial length, leading to rotor vibrations for high speed applications [EDE02]. Hence, various sensorless schemes have attracted much attention in last decades. Fig. 1.5 summaries these sensorless methods. In particular, this thesis focuses on sensorless methods for high-speed BLDC and BLAC operation.

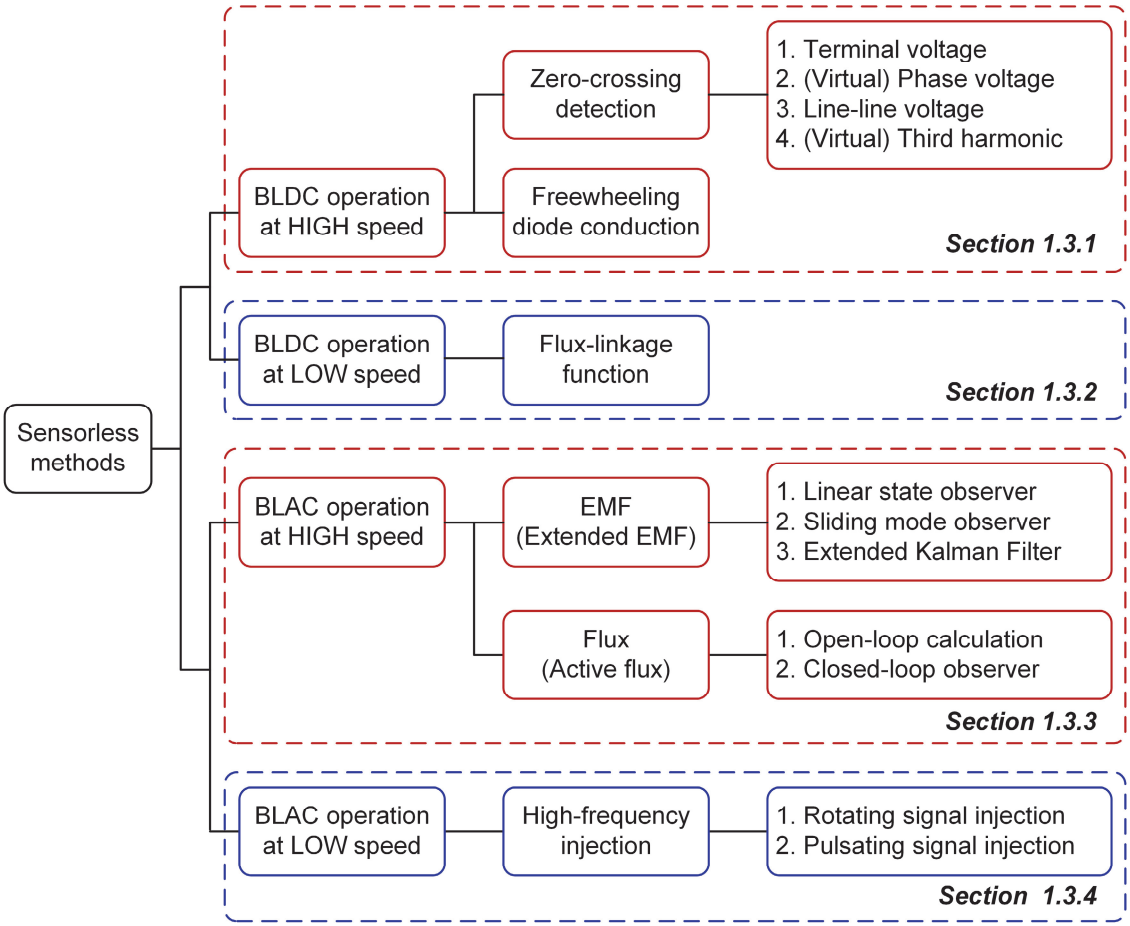

Fig. 1.5. Classification of sensorless methods for BLDC and BLAC operation and corresponding sections reviewed in this chapter.

1.3.1 Sensorless Brushless DC Operation in High-speed Range

1) Zero-crossing Detection of Back EMF

For sensorless BLDC drives, the back EMF based methods are the primary schemes. Through measuring the back EMF voltage, which contains position information, the commutation points can be found. It is clear in Fig. 1.6 that the zero-crossing points (ZCPs) of back EMF locate in the middle between two consecutive commutation points. The zero-crossing detection (ZCD) method is to search the ZCPs of the back EMF and then identify the commutation points.

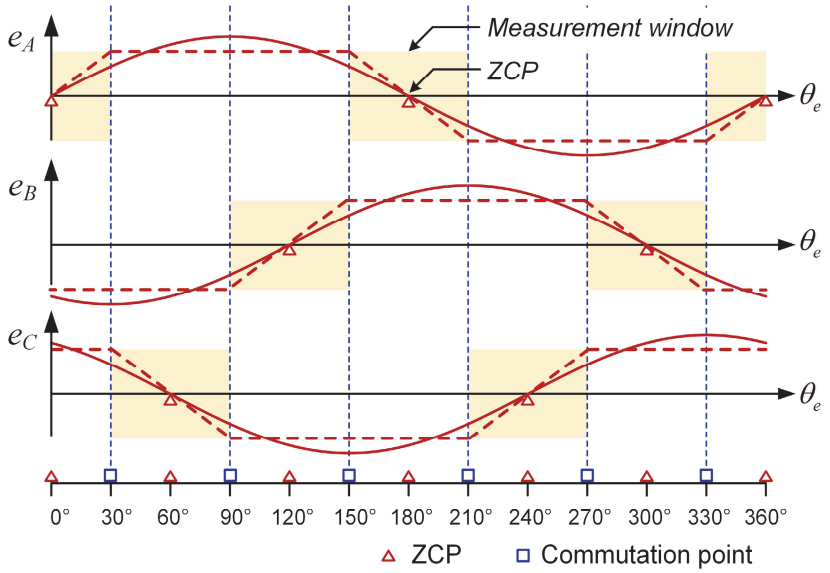

Fig. 1.6. Illustration of back EMFs and zero-crossing points.

Fig. 1.7 shows the diagram of the inverter and the BLDC motor. The BLDC model can be expressed as

$$\begin{cases} v_{\mathrm{AN}} = Ri_{\mathrm{A}} + (L-M)\frac{d}{dt}i_{\mathrm{A}} + e_{\mathrm{A}} \\ v_{\mathrm{BN}} = Ri_{\mathrm{B}} + (L-M)\frac{d}{dt}i_{\mathrm{B}} + e_{\mathrm{B}} \\ v_{\mathrm{CN}} = Ri_{\mathrm{C}} + (L-M)\frac{d}{dt}i_{\mathrm{C}} + e_{\mathrm{C}} \end{cases} \tag{1.1}$$

where v_{XN}, i_{X} and e_{X} are the phase voltage, current and back EMF, R, L and M are the phase resistance, the self-inductance and the mutual inductance. Here, the subscript "X" denotes phase A, B, or C.

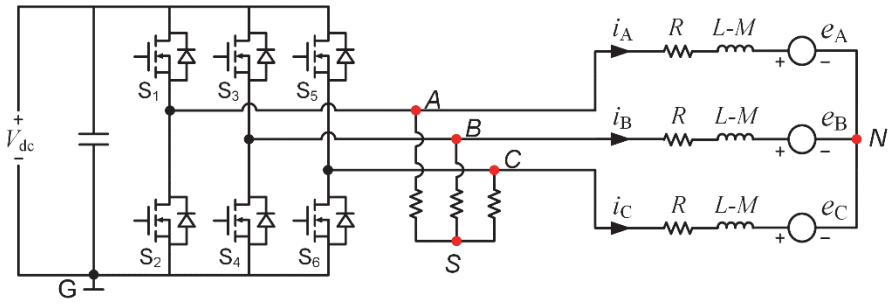

Fig. 1.7. Diagram of inverter and motor.

The basic principle of back EMF measurement is as follows. In the 120° conduction six-step control, two of the three phases are conducted and the third one is floating. For instance, when phases A and B are conducted, the current of phase C is zero $i_C = 0$, which generates a measurement window. During this interval, the back EMF of the floating phase C can be directly measured with $v_{CN} = e_C$. Specifically, the back EMF measurement can be implemented in various ways, which can be classified into four groups.

A. Terminal voltage [HAI16][LAI11][LAI08b][TSO15]

The most common and easy-to-implement ZCD method is based on the terminal voltage measurement, i.e. the voltages of A, B and C in respect to the ground. Usually the terminal voltage can be acquired using simple resistive voltage dividers (RVDs). The resistance tolerance of RVDs will affect the commutation accuracy, which will be discussed in Chapter 3.

B. Phase voltage and virtual phase voltage

When the motor neutral wire *N* is available, the phase voltage can be used for ZCD [CHE17a][ZHO17a][LIU17]. For the motor without a neutral wire, the virtual neutral point *S* can be constructed with the star-resistors [JIA05][TSO12]. It should be noted that additional operational amplifiers (OA) are required to obtain the (virtual) phase voltage since the voltage of *N* or *S* is floating in respect to the ground.

C. Line-line voltage [CHU14][WAN15][LIU16g]

The back EMF can be measured from the line-line voltage. The same as the above (virtual) phase voltage measurement, the line-line voltage measurement also requires additional OAs. The feature of this measurement method is that the ZCPs of the line-line voltage correspond to the commutation points, which means the 30° (elec.) angle delay is not required.

D. Third-harmonic and virtual third-harmonic

For the trapezoidal back EMF motors, the back EMF harmonics (mainly the third harmonic) can be measured from the voltage of motor neutral wire *N* in respect to the ground [MOR96][SHE04]. For the motor without the neutral wire, the voltage of virtual neutral point *S* in respect to the ground can be used for back EMF measurement, i.e. virtual third-harmonic [CUI15a][SON18a] [SON18b]. Besides, the virtual third harmonic can be used not only for trapezoidal back EMF motors, but also for the sinusoidal ones. Compared to above back EMF measurement methods, the (virtual) third-harmonic method just need to measure a single voltage, which saves the interface resource of the digital controller. However, the drawback is that the signal magnitude is relatively small compared to other methods.

Various back EMF measurement methods are summarised and compared in Table 1.2. Good features are denoted by shaded background. Note that the 30° delay is neither advantage nor disadvantage. The line-line voltage measurement does not need the additional 30° shift, which is easier to implement. However, it also increases the difficulty to realize the phase advance control. Whether the OA is required or not is a critical factor considering the system cost and complexity. On the other hand, the neutral wire will limit the applicability. Considering all the listed factors, two back EMF measurement methods will be investigated in this thesis, i.e. virtual third-harmonic in Chapter 2 and terminal voltage in Chapter 3.

Table 1.2. Comparison of EMF measurement methods.

	OA (Y/N)	Neutral wire (Y/N)	30° delay (Y/N)	Magnitude	EMF (Sin/Trz)	No. of signals
Terminal voltage	N	N	Y	Large	Both	3
Phase voltage	Y	Y	Y	Large	Both	3
Virtual phase voltage	Y	N	Y	Large	Both	3
Line-Line voltage	Y	N	N	Large	Both	3
Third-harmonic	N	Y	Y	Small	Trz	1
Virtual third-harmonic	N	N	Y	Small	Both	1

2) Freewheeling Diode Conduction

This method estimates the rotor position through detecting the freewheeling diode conduction of the floating phase [OGA91]. Around the ZCPs of the back EMF in the floating phase, a tiny current will flow through the freewheeling diode in a very short interval. Using this mechanism, the ZCPs can be detected indirectly from the freewheeling diode conduction with the circuits in Fig. 1.8. The main drawback of this method is that at least six voltage comparators are required to detect the freewheeling diode conduction, which are costly and thereby limit its practical application.

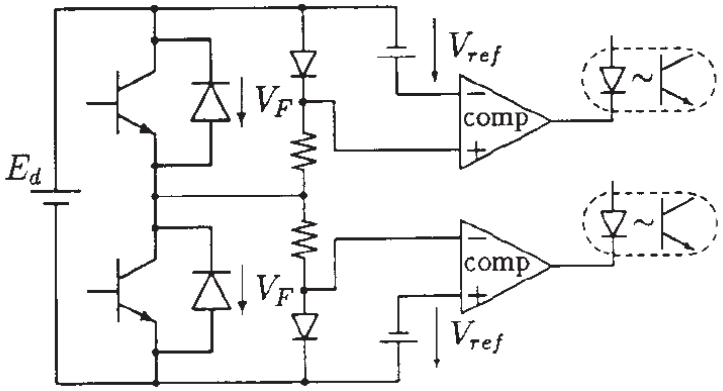

Fig. 1.8. Detecting circuit for conduction of freewheeling diodes [OGA91].

1.3.2 Sensorless Brushless DC Operation in Low-speed Range

Since the magnitude of back EMF is very small in low-speed range, the sensorless methods based on ZCD are hard to implement. To estimate the commutation point in low-speed range, the flux-linkage function based sensorless method and its improved versions have been presented in [KIM04][CHE19w][CHE17a][SUN18]. The basic flux-linkage function can be expressed by three functions as

$$\begin{cases} G(\theta)_x = \dfrac{H(\theta)_{ca}}{H(\theta)_{bc}} = \dfrac{v_{\mathrm{CA}} + R(i_{\mathrm{C}} - i_{\mathrm{A}}) + L(\frac{d}{dt} i_{\mathrm{C}} - \frac{d}{dt} i_{\mathrm{A}})}{v_{\mathrm{BC}} - R(i_{\mathrm{B}} - i_{\mathrm{C}}) - L(\frac{d}{dt} i_{\mathrm{B}} - \frac{d}{dt} i_{\mathrm{C}})} \\ G(\theta)_y = \dfrac{H(\theta)_{bc}}{H(\theta)_{ab}} = \dfrac{v_{\mathrm{BC}} + R(i_{\mathrm{B}} - i_{\mathrm{C}}) + L(\frac{d}{dt} i_{\mathrm{B}} - \frac{d}{dt} i_{\mathrm{C}})}{v_{\mathrm{AB}} - R(i_{\mathrm{A}} - i_{\mathrm{B}}) - L(\frac{d}{dt} i_{\mathrm{A}} - \frac{d}{dt} i_{\mathrm{B}})} \\ G(\theta)_z = \dfrac{H(\theta)_{ab}}{H(\theta)_{ca}} = \dfrac{v_{\mathrm{AB}} + R(i_{\mathrm{A}} - i_{\mathrm{B}}) + L(\frac{d}{dt} i_{\mathrm{A}} - \frac{d}{dt} i_{\mathrm{B}})}{v_{\mathrm{CA}} - R(i_{\mathrm{C}} - i_{\mathrm{A}}) - L(\frac{d}{dt} i_{\mathrm{C}} - \frac{d}{dt} i_{\mathrm{A}})} \end{cases} \tag{1.2}$$

where $G(\theta)$ and $H(\theta)$ are the established flux-linkage functions. The subscripts x, y and z of $G(\theta)$ correspond to different commutation instants as shown in Fig. 1.9, which illustrates the waveforms of the functions together with the phase current and commutation signal. The commutation instant is when the $G(\theta)$ function changes from positive infinity to negative infinity. It is reported in these literature, the $G(\theta)$ function is speed independent, and thereby can estimate the commutation in low-speed range.

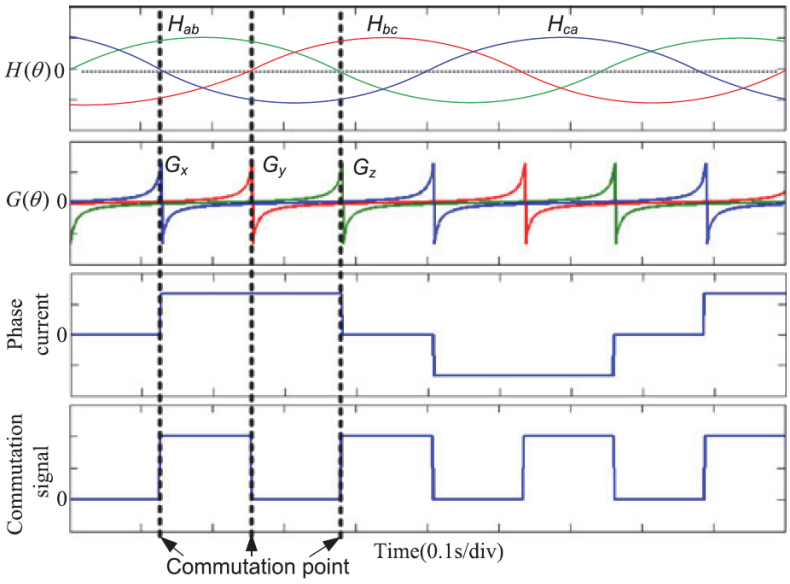

Fig. 1.9. Function $H(\theta)$, $G(\theta)$, phase current, and rotor position signal [CHE17a].

Some other speed independent flux-linkage functions have been proposed on the basis of (1.2), including simplified computation [CHE18], improved commutation accuracy [CHE17] and no need for analog filters [SUN18].

1.3.3 Sensorless Brushless AC Operation in High-speed Range

Sensorless BLAC drive methods can be roughly classified into two categories, i.e. the model-based sensorless method and the saliency-based sensorless method. The model-based sensorless method estimates the rotor position using the back EMF or flux, which presents good performance in medium- and high-speed range but fails in the zero- and low-speed region. On the contrary, the saliency-based sensorless method estimates the rotor position through injecting high frequency voltage or current, which can operate in low-speed region including standstill.

1) EMF and Extended EMF

The back EMF contains the rotor position information and can be used for sensorless control. The back EMF estimation can be implemented either in synchronous *d-q* frame [ZHA17b][YAN17b] or stationary *α-β* frame [WAN13a] [KIM11]. In the synchronous *d-q* frame, the model of non-salient motors can be expressed as

$$\begin{bmatrix} v_d \\ v_q \end{bmatrix} = \begin{bmatrix} R+L\frac{d}{dt} & -\omega_e L \\ \omega_e L & R+L\frac{d}{dt} \end{bmatrix} \begin{bmatrix} i_d \\ i_q \end{bmatrix} + \begin{bmatrix} 0 \\ \omega_e \psi_f \end{bmatrix} \tag{1.3}$$

where v_d, v_q, i_d and i_q are the voltages and currents in *d-q* frame, R and L are the stator resistance and inductance, ω_e is the rotor angular speed and ψ_f is the flux linkage of PM. Transforming (1.3) into the stationary *α-β* frame, the model can be expressed as

$$\begin{bmatrix} v_\alpha \\ v_\beta \end{bmatrix} = \begin{bmatrix} R+L\frac{d}{dt} & 0 \\ 0 & R+L\frac{d}{dt} \end{bmatrix} \begin{bmatrix} i_\alpha \\ i_\beta \end{bmatrix} + \omega_e \psi_f \begin{bmatrix} -\sin\theta_e \\ \cos\theta_e \end{bmatrix} \tag{1.4}$$

where v_α, v_β, i_α and i_β are voltages and currents in the α-β frame, θ_e is the rotor position.

For salient machines, the mathematical model is relatively complicated. Since the *d*- and *q*-axis inductances are different, i.e. $L_d \neq L_q$, the position information is contained not only in the EMF, but also in the impedance matrix, which increases the difficulty of EMF estimation. To simplify the model of salient machines, the extended EMF model was introduced in [CHE03] as

$$\begin{bmatrix} v_d \\ v_q \end{bmatrix} = \begin{bmatrix} R + L_d \frac{d}{dt} & -\omega_e L_q \\ \omega_e L_q & R + L_d \frac{d}{dt} \end{bmatrix} \begin{bmatrix} i_d \\ i_q \end{bmatrix} + \begin{bmatrix} 0 \\ E_{ex} \end{bmatrix} \tag{1.5}$$

where E_{ex} is the extended EMF $E_{ex} = \omega_e \psi_f + (L_d - L_q)(\omega_e i_d - \frac{d}{dt} i_q)$. By transforming (1.5) into the stationary α-β frame, it yields

$$\begin{bmatrix} v_\alpha \\ v_\beta \end{bmatrix} = \begin{bmatrix} R + L \frac{d}{dt} & \omega_e (L_d - L_q) \\ -\omega_e (L_d - L_q) & R + L \frac{d}{dt} \end{bmatrix} \begin{bmatrix} i_\alpha \\ i_\beta \end{bmatrix} + E_{ex} \begin{bmatrix} -\sin\theta_e \\ \cos\theta_e \end{bmatrix} \tag{1.6}$$

It is shown in (1.6) that by introducing the extended EMF, the impedance matrix of salient machine model can be written symmetrically like a non-salient machine.

Based on above models from (1.3) to (1.6), various EMF based sensorless methods have been proposed. In the early stage, some literature tried to calculate the EMF directly from the measured voltages and currents. However, any uncertainties such as machine parameter deviation and disturbance will cause errors to the rotor position estimation. For this reason, such open-loop EMF calculation methods have been rarely used nowadays. Alternatively, closed-loop observer techniques can be used for EMF estimation, which is introduced as follows.

A. Linear state observer

As shown in Fig. 1.10, the state observer method constructs a system whose structure and parameters are the same as the plant [ZHA17b][YAN17b][KSH12]. Here, $v_{\alpha,\beta}$, $i_{\alpha,\beta}$ and $e_{\alpha,\beta}$ denote the voltage vectors, current vectors and EMF vectors in stationary α-β axe, $\hat{\omega}_e$ and $\hat{\theta}_e$ denote the estimated rotor speed and

position. The hat superscript "^" denotes the estimation signals. The control command applied to the plant is simultaneously fed into the observer. Through forcing the estimation error to zero, the estimated states will converge to the actual ones. For linear state observer, the convergence is achieved by multiplying the estimation error with a gain G and then feeding back to the observer. Usually, the current and back EMF are regarded as the states. The current is measurable but the back EMF is not. When the current converges, the back EMF can be estimated, which can be used for rotor position estimation. The main drawback of this approach is that the accuracy of the system model has a great influence on the accuracy of the position estimation.

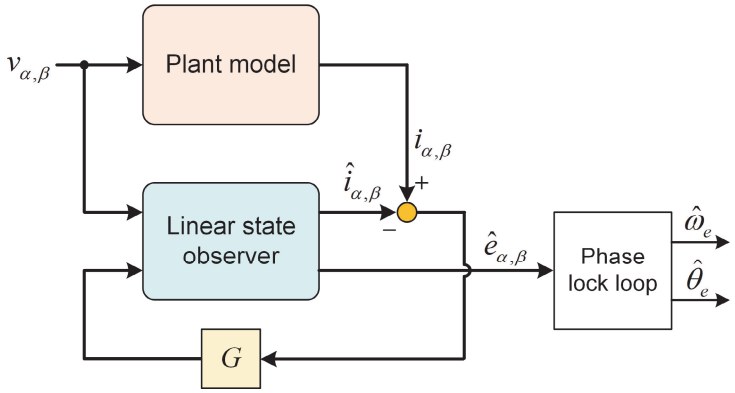

Fig. 1.10. Structure of linear state observer.

B. Sliding mode observer

The sliding mode observer (SMO) is originated from the variable structure control. The SMO is a typical nonlinear observer, which utilizes nonlinear and even discontinuous gains to force the estimation error to zero as shown in Fig. 1.11. This method is widely used for sensorless control due to the advantage of high robustness against the system uncertainties. The SMO suffers from the chattering problem due to the usage of discontinuous gains, e.g. the sign function. To reduce the chattering, some improvements have been made, including replacing the sign function with the sigmoid function [WAN13a][KIM11][QIA13] or super-twisting function [LIA17]. In particular, for high-speed applications, some discrete-time SMO methods have been proposed, which are suitable for the low sampling ratio condition [BER14][DIN20].

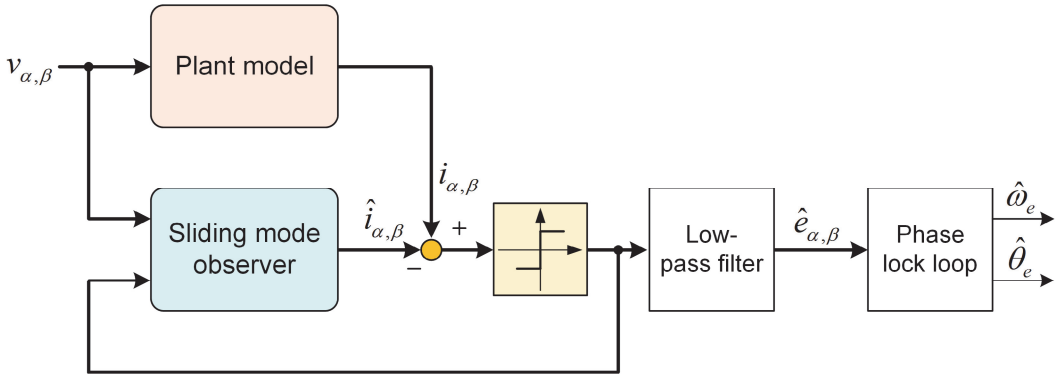

Fig. 1.11. Structure of sliding mode observer.

C. *Extended Kalman filter*

The Kalman filter and its nonlinear version known as extended Kalman filter (EKF) can be utilized for the EMF estimation [SHI12][BOL03]. The EKF takes the state noise and measurement noise into consideration in the system model, which provides a way to obtain the optimal state estimation. The main drawback of EKF is the heavy computation burden, because it needs matrix operations. Besides, the computation burden increases significantly with the matrix order. To solve this problem, some literature proposed the reduced order EKF to simplify the computation processes [QUA14][YAN20].

2) *Flux and Active Flux*

For PM machines, since the direction of the rotor flux is aligned with the PM pole, the rotor position can be obtained from the rotor flux, which is the integration of back EMF. The non-salient PM machine can be modelled as

$$\begin{bmatrix} v_\alpha \\ v_\beta \end{bmatrix} = \begin{bmatrix} R + L\frac{d}{dt} & 0 \\ 0 & R + L\frac{d}{dt} \end{bmatrix} \begin{bmatrix} i_\alpha \\ i_\beta \end{bmatrix} + \frac{d}{dt} \begin{bmatrix} \psi_f \cos\theta_e \\ \psi_f \sin\theta_e \end{bmatrix} \tag{1.7}$$

where the last term is the rotor flux. For salient machines, the active flux model developed in [BOL08][BOL09] can be used as

$$\begin{bmatrix} v_\alpha \\ v_\beta \end{bmatrix} = \begin{bmatrix} R + L_q\frac{d}{dt} & 0 \\ 0 & R + L_q\frac{d}{dt} \end{bmatrix} \begin{bmatrix} i_\alpha \\ i_\beta \end{bmatrix} + \frac{d}{dt} \begin{bmatrix} \psi_{act} \cos\theta_e \\ \psi_{act} \sin\theta_e \end{bmatrix} \tag{1.8}$$

where $\psi_{act} = \psi_f + (L_d - L_q) i_d$ is the active flux. The concept of active flux is similar to the extended EMF. It is illustrated in (1.8) that this model is symmetrical as a

nonsalient machine, which simplifies the rotor position estimation process. Basically, the flux can be obtained from open-loop calculation or closed observer techniques.

A. Open-loop calculation

The rotor flux can be directly calculated for nonsalient machines as

$$\begin{bmatrix} \psi_f \cos\theta_e \\ \psi_f \sin\theta_e \end{bmatrix} = \int \begin{bmatrix} v_\alpha - Ri_\alpha \\ v_\beta - Ri_\beta \end{bmatrix} dt - L \begin{bmatrix} i_\alpha \\ i_\beta \end{bmatrix} \tag{1.9}$$

and for salient machines as

$$\begin{bmatrix} \psi_{act} \cos\theta_e \\ \psi_{act} \sin\theta_e \end{bmatrix} = \int \begin{bmatrix} v_\alpha - Ri_\alpha \\ v_\beta - Ri_\beta \end{bmatrix} dt - L_q \begin{bmatrix} i_\alpha \\ i_\beta \end{bmatrix} \tag{1.10}$$

Since the integration is required for the calculation, it may suffer from the dc offset issue caused by parameter mismatches, nonzero initial flux values and current detection errors. To solve this problem, some special structures can be used to replace the pure integrator [XUW19][JIA19].

B. Closed-loop observer

The rotor flux can be estimated with closed-loop observer techniques, which is similar to the EMF estimation. Full-order state observers [PON12][ZHA19] and reduced-order state observers [HIN12][TUO12] for flux estimation have been developed. Since the speed information is required in the observer, those approaches usually needs speed adaptation algorithm. Besides, some types of nonlinear observers that do not rely on speed information have been proposed [ORT11][KHL12][CHO19]. Compared to the back EMF observers, the flux observers have better estimation performance at low speed, since the rotor flux does not change with the motor speed, but remains constant.

1.3.4 Sensorless Brushless AC Operation in Low-speed Range

In the low-speed range, the rotor position can be estimated by tracking the rotor saliency with the high frequency signal injection method. This method can be roughly

categorized into rotating signal injection and pulsating signal injection, which are illustrated in Fig. 1.12 (a) and (b), respectively. Since the injection frequency ω_h is far higher than the fundamental frequency ω_e, the voltage drop on the stator resistance and the terms associated with ω_e can be neglected [WAN20]. Then, the high-frequency model for BLAC motor can be expressed in the synchronous *d*-*q* frame as

$$\begin{bmatrix} v_{dh} \\ v_{qh} \end{bmatrix} = \begin{bmatrix} L_d & 0 \\ 0 & L_q \end{bmatrix} \frac{d}{dt} \begin{bmatrix} i_{dh} \\ i_{qh} \end{bmatrix} \tag{1.11}$$

and in the stationary *α*-*β* frame as

$$\begin{bmatrix} v_{\alpha h} \\ v_{\beta h} \end{bmatrix} = \begin{bmatrix} L_1 + L_2 \cos 2\theta_e & L_2 \sin 2\theta_e \\ L_2 \sin 2\theta_e & L_1 - L_2 \cos 2\theta_e \end{bmatrix} \frac{d}{dt} \begin{bmatrix} i_{\alpha h} \\ i_{\beta h} \end{bmatrix} \tag{1.12}$$

Here, the subscript "h" indicates the high frequency component and $L_1 = \dfrac{L_d + L_q}{2}$, $L_2 = \dfrac{L_d - L_q}{2}$.

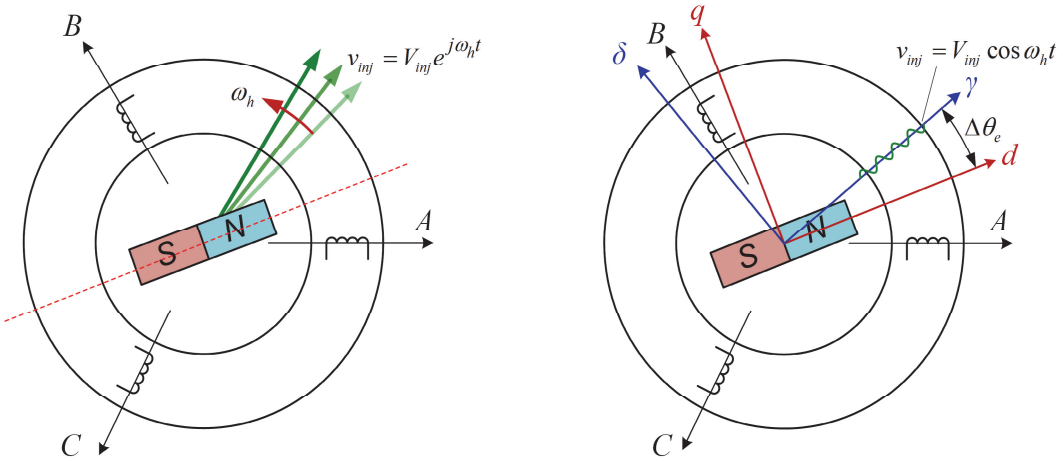

(a) Rotating signal injection (b) Pulsating signal injection.

Fig. 1.12. Illustration of high frequency signal injection scheme.

1) Rotating Signal Injection

Fig. 1.11 (a) illustrates the rotating signal injection scheme. A rotating high-frequency voltage vector $v_{inj} = V_{inj} e^{j\omega_h t}$ is injected in the stationary frame, where V_{inj} and ω_h are the injection magnitude and frequency. Since the salient rotor is anisotropic, the high-frequency current response is modulated by the rotor position. The rotor

position can be extracted with negative-sequence current method [KIM16][GAB13] or zero-sequence voltage method [XUP16a][ALM17].

Compared to the pulsating signal injection, this rotating signal injection scheme does not require initial rotor position. However, it is subject to the inverter nonlinearity effect [RAC08][GON11]. Besides, to ensure that the high frequency voltage and the induced current are sinusoidal, the injection frequency should be set far less than the switching frequency.

2) Pulsating Signal Injection

Fig. 1.11 (b) illustrates the pulsating signal injection scheme. This method is implemented in the estimated synchronous γ-δ frame, which has a position error $\Delta\theta_e$ to the actual synchronous *d-q* frame. The high-frequency voltage is usually injected in the γ-axis (estimated *d*-axis) for the reason of less effect on the torque production. Then, due to the rotor saliency, the position error $\Delta\theta_e$ is reflected on the current response of δ-axis (estimated *q*-axis). By extracting the $\Delta\theta_e$ and forcing it to zero, the γ-δ frame will converge to the *d-q* frame and the rotor position is identified.

This pulsating signal injection is less sensitive to the inverter nonlinearity effect [RAC08][GON11]. Generally, two types of signals can be applied for injection, i.e. sinusoidal wave [JAN03][HAJ03] and square-wave [YOO11][KIM12]. The injection frequency of pulsating sinusoidal injection is similar to the one of rotating injection, while for the pulsating square-wave injection, the injection frequency can be increased significantly. Higher injection frequency facilitates the high frequency signal extraction and position estimation.

1.4 Issues with High-speed Brushless DC and AC Drives

This thesis focuses on the issues with high-speed BLDC and BLAC drives. Fig. 1.13 illustrates the research structure and the issues discussed in each chapter. Since the BLDC operation is more suitable for high-speed applications compared to BLAC, more attention is paid on the former. Details of each issue are introduced as follows.

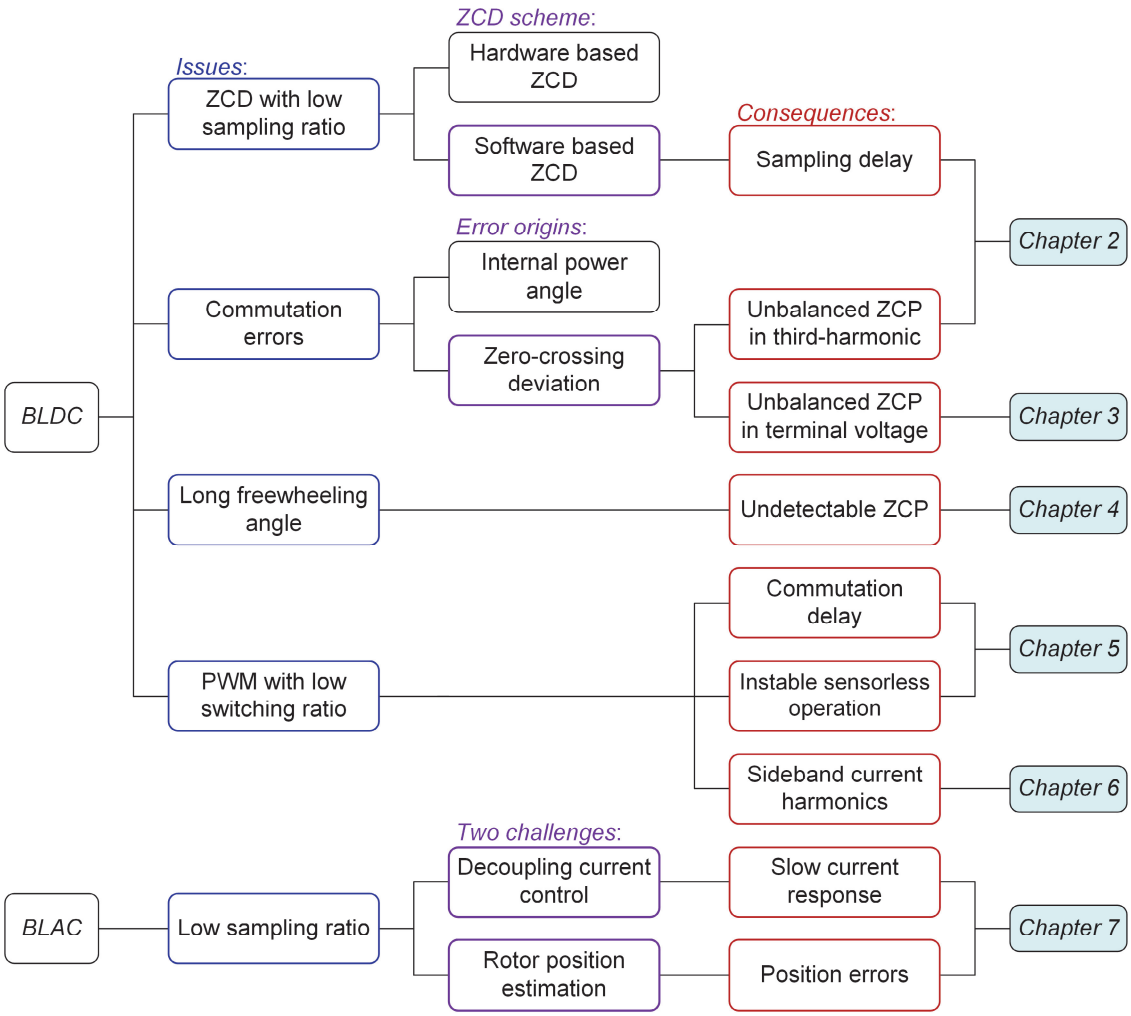

Fig. 1.13. Issues discussed in each chapters.

1.4.1 Issues in High-speed BLDC Operation

Although the BLDC operation has been widely used for modern industry and home appliances, some problems are still not solved perfectly, especially for sensorless high-speed BLDC drives. Four issues with BLDC operation are discussed in the thesis.

1) Zero-crossing Detection with Low Sampling Ratio

Chapter 1.3.1 introduces the methods for back EMF measurement. After the back EMF signals are acquired from the inverter and motor sides, the ZCPs of back EMF can be detected. Basically, as shown in Fig. 1.14, there are two methods to detect the ZCPs, i.e. hardware based method and software based method.

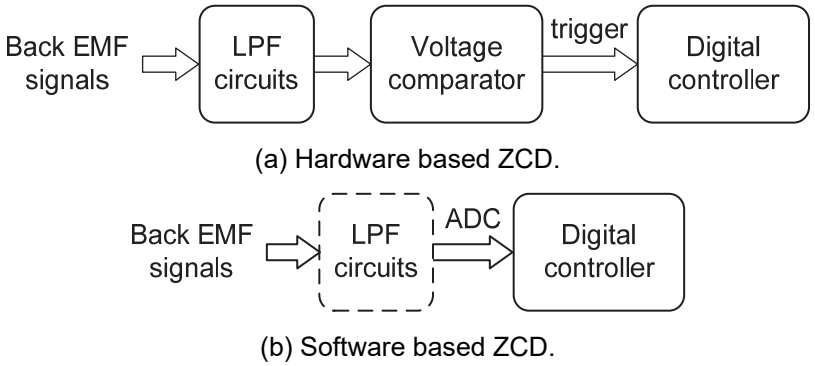

Fig. 1.14. Block diagrams of two ZCD methods.

A. Hardware based ZCD [LIU16g][CHE07ch]

In this method, the signum signal (higher or lower than zero) of back EMF can be obtained by voltage comparator circuits. Then, the signum signal will be sent to the digital controller to trigger the peripheral interrupt for commutation. When the output signal changes the sign (from positive to negative or from negative to positive), the zero-crossing is detected. Considering that the measured voltage signals contain high frequency noises, which perhaps cause spurious triggering, some analog low-pass filter (LPF) circuits have to be employed. These LPF circuits will inevitably lead to commutation delay that increases with the motor speed. Although some improved LPF design methods and compensation methods for commutation errors have been investigated in existing literature [ZHO17][LIH17], the system complexity and flexibility will be influenced.

B. Software based ZCD [DAR15][LAI11][SHA06][HAI16]

Another ZCD method is based on software, i.e. back EMF envelope extraction. The voltage signal is sampled with the analog-to-digital converter (ADC), and then, the ZCD can be implemented with algorithm. Compared to the hardware method, the software method features high flexibility and low system cost. To

suppress the PWM noise, the ADC can operate in synchronization with the PWM generation, which can considerably increase the signal-to-noise ratio. The back EMF envelope can be extracted with high-cutoff frequency LPFs or without LPFs. In this way, the adverse influences of the LPF can be reduced or even avoided.

The main drawback of the software method is that the ZCD precision is limited by the sampling frequency. Conventional back EMF envelope extraction identifies the ZCP only once in each PWM period. In the high-speed range, there will be insufficient samplings in each fundamental cycle, which will cause non-negligible commutation errors. To guarantee the commutation accuracy in high-speed range, a ZCD method based on over-sampling is proposed in Chapter 2.

2) Commutation Errors Caused by Non-ideal Factors

In practice, there exist various non-ideal factors that will lead to commutation errors. These non-ideal factors can be roughly classified into two categories, i.e. internal power angle related factors and ZCP deviation related factors. Plenty of literature can be found for the first category and many solutions can be employed. However, it is found the second category is not fully investigated, which is motivation of this thesis.

The commutation errors will increase the current magnitude, leading to more copper loss. Besides, fluctuated commutation errors will produce current ripples, which will further cause torque ripples, vibration, audible noise and even drive failure. Thus, it is desirable to reduce such commutation errors.

A. Internal power angle

The first category is related to the internal power angle between the current vector and the back EMF vector as shown in Fig. 1.15. In some documents, this issue was also called phase advance control [LEE18a]. It is reported in [GUC18] that there exists an optimal phase current whose fundamental phase is aligned with the back EMF. However, due to the phase inductance, the practical phase current always lags behind the optimal one, which can be reflected in the internal power angle.

Many commutation correction methods have been proposed to determine the optimal commutation instant. In [LEE18a], a phase advance control method based on Fourier-series was proposed, in which the back EMF harmonics were taken into consideration. In [TAN19], an analytical study on the phase advance angle was carried out. However, in these two solutions, the machine parameters are required to derive the phase advance angle. Some self-tuning methods for phase advance control were proposed. In [LIU16][SON18a], the optimal commutation instant is determined by balancing the back EMF envelope in the former-half sector and latter-half sector. In [LEE16] [LEE17], it proposed a feedback compensation method by balancing the current integrals of two successive sectors. Note that this issue exists for both sensor and sensorless operations.

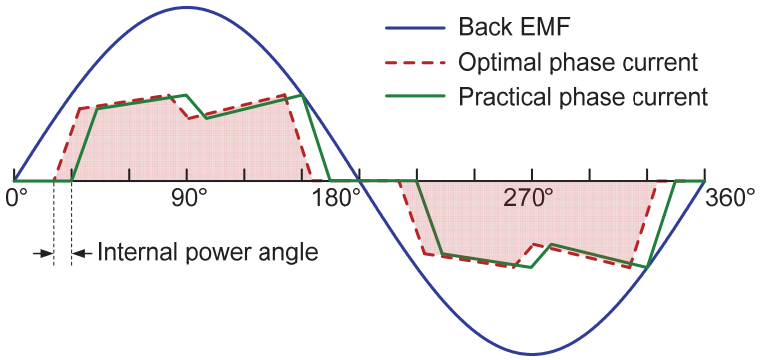

Fig. 1.15. Illustration of internal power angle.

B. ZCP deviation

Another category of non-ideal factors is related to the ZCP deviation, which happens in the sensorless operation. Ideally, the ZCP locates in the middle of each 60° sector, and the commutation instant locates 30° behind the ZCP. When the ZCP position deviates due to various reasons, it will lead to commutation errors. The most common reason of ZCP deviation is the phase delay caused by LPF circuits as shown in Fig. 1.16 (a). In [ZHO17][LIH17], the method to select suitable LPF cut-off frequency and the phase delay compensation were introduced. Some other non-ideal factors can also lead to ZCP deviation but are not fully investigated. [PAR19] described an issue of unbalanced ZCPs that could be caused by DC-link voltage drop as shown Fig. 1.16 (b). The unbalanced ZCP is much more complicated than the purely lagged ZCP in Fig. 1.16 (a). This unbalanced

ZCPs will lead to current ripple and torque ripple. In fact, two more reasons will also lead to unbalanced ZCPs, i.e. resistance tolerance of back EMF measurement circuits and the machine parameter asymmetry. The influence of resistance tolerance on ZCP deviation is similar to the issue in Fig. 1.16 (b), and will be discussed in Chapter 3. Fig. 1.16 (c) illustrates the influence of machine parameter asymmetry on ZCP deviation, which will be discussed in Chapters 2 and 3.

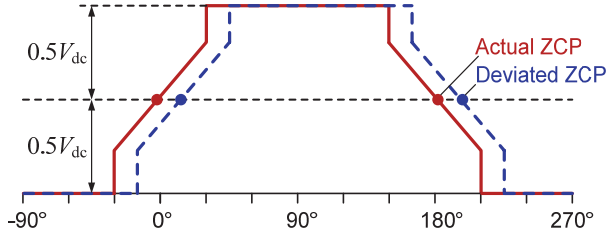

(a) ZCP deviation caused by LPF circuits.

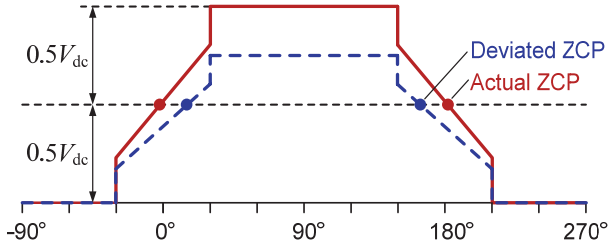

(b) ZCP deviation caused by DC-link voltage drop or resistance tolerance.

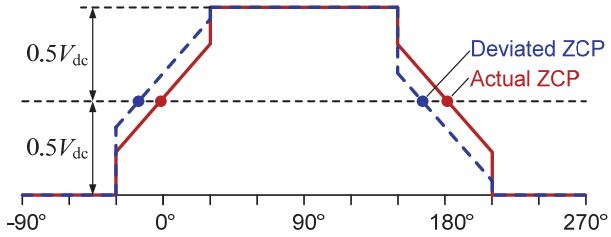

(c) ZCP deviation caused by asymmetric machine parameters.

Fig. 1.16. Illustration of ZCP deviation in terminal voltage measurement.
Note that the freewheeling notch is not reflected in this schematic.

3) Long Freewheeling Angle

The ZCD based sensorless method suffers from long freewheeling angle issue. As shown in Fig. 1.17, when two of the three phases are conducted, the back EMF of the floating phase can be measured and used to identify the commutation instant. However, in practice, the phase current cannot descent to zero immediately after the commutation, but flowing through the freewheeling diode. This clamps the floating phase to the DC-link and increase the difficulty to detect the ZCPs. When the

freewheeling angle is larger than 30°, the ZCP will disappear and be undetectable [ZHU01]. This long freewheeling angle is one of the main issues that prevents the sensorless BLDC drive running towards high-speed.

The freewheeling angle is complicated to analyse since it is related to many factors, including electromagnetic and mechanical parameters [ZHU01], electrical time constant [HAN08], DC-link voltage [XUY16][CHE17][LIX16][JIA18], motor speed and current [LIW16][LIH17], PWM duty ratio [SHI17][PAR20][ACH20]. However, existing documents only analysed part of these factors and none of them have taken all of the factors into consideration. In Chapter 4, a complete analytical study on the freewheeling angle will be carried out.

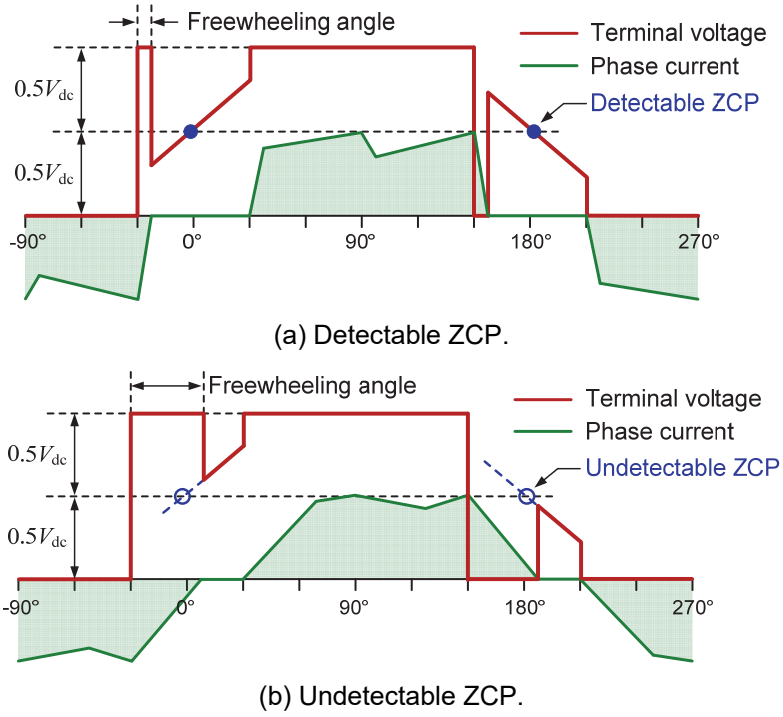

(a) Detectable ZCP.

(b) Undetectable ZCP.

Fig. 1.17. Schematics of terminal voltage and phase current.

4) PWM Generation with Low Switching Ratio

The PWM generation with insufficient switching ratio is a critical issue for high-speed BLDC operation. As shown in Fig. 1.18 (a), for the low-speed BLDC operation, there are sufficient PWM waves in each fundamental period. As the motor speed increases, fewer PWM waves can be generated in each fundamental period as shown in Fig. 1.18 (b). This will impose adverse impacts on the BLDC operation, which can be summarized as follows.

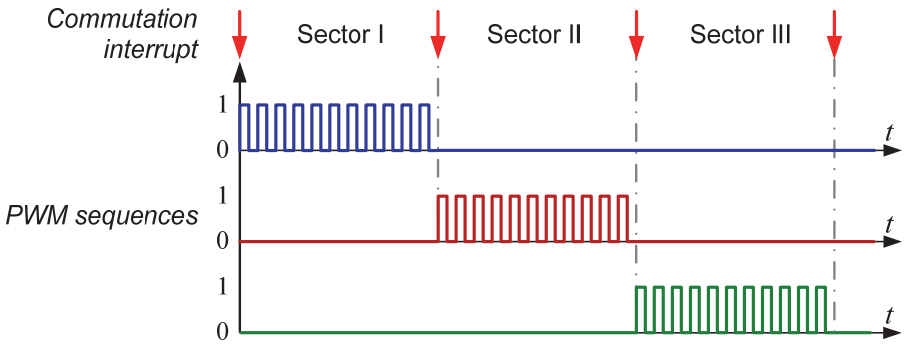

(a) PWM in low-speed BLDC operation.

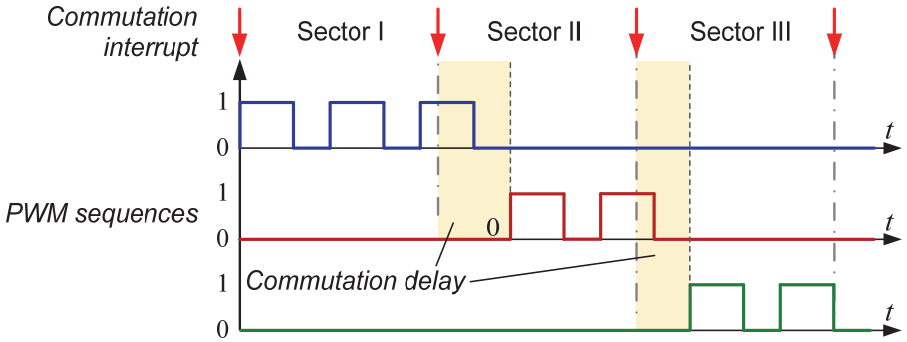

(b) PWM in high-speed BLDC operation.

Fig. 1.18. Schematic of PWM for normal speed and high-speed BLDC operations.

A. Commutation delay

In the conventional regular-sampled PWM technique, the PWM output updates only once in each carrier period. As shown in Fig. 1.17 (b), when the commutation interrupt arrives, the inverter will not update the switching status until the next carrier period arrives. It indicates that even if accurate commutation instants are identified, the inverter may still perform the commutation with phase delay, which will deteriorate the control performance. In Chapter 5, this issue will be discussed and a solution is proposed.

B. Unstable sensorless operation

As introduced in last section, when the freewheeling angle is larger than 30°, the ZCP is not detectable and the sensorless operation will fail. Unfortunately, the commutation delay will make the situation worse. It will be shown in Chapter 5 that in the condition of low switching ratio, the commutation delay will produce accumulative position errors. For this reason, the sensorless drive perhaps fails

when the freewheeling angle is less than 30°. This issue will restrict the maximum sensorless operation speed and load.

C. Sideband current harmonics

It will induce abundant sideband current harmonics when the switching ratio is insufficient. Such undesired sideband current harmonics will lead to torque ripples [LIA13], additional copper and iron losses [XUE17], vibration and acoustic noise [WUS19]. A spectral analysis on the sideband harmonics will be carried out in Chapter 6.

As introduced above, the insufficient switching ratio imposes many adverse impacts on the high-speed BLDC operation. As the speed increases, such adverse impacts will become more severe and deteriorate the control performance. To suppress these adverse influences, a novel modulation method, i.e. carrier-synchronised commutation (CSC), will be proposed in Chapters 5 and 6.

1.4.2 Issues in High-speed BLAC Operation

Although the BLAC operation is relatively complicated compared to the BLDC operation, the BLAC operation has some significant advantages, including lower torque ripples, lower acoustic noise and higher efficiency. Most importantly, the sensorless BLAC method is not restricted by the long freewheeling angle. Thus, it is meaningful to develop high-speed BLAC control strategies. In the high-speed range, there will be limited current samplings in each fundamental period. As a result, in the low sampling ratio condition, it faces two great challenges, i.e. decoupling current control and rotor position estimation.

A. Decoupling current control

Generally, the current control is implemented in the synchronous *d-q* frame. It is commonly known that the cross-coupling exists between synchronous *d-q* axes, which will cause slow current tracking response and undesired interaction between *d-q* components. The cross-coupling increases with the motor speed. Especially

when the speed increases further, the sampling ratio becomes insufficient, and then it will lead to a stronger cross-coupling due to the enlarged digital control delay [BAE03][ZHO17s]. Thus, it is quite a challenge to develop decoupling current control in the condition of limited sampling ratio.

B. Rotor position estimation

As introduced earlier, various rotor position observers have been proposed for sensorless control. Most of the observers are designed in continuous-time domain and then discretized with Euler or Tustin approximation. In fact, the machine dynamic response is quite different when the sampling (switching) ratio is not sufficient [YAN17b][ZHA17b]. Under this effect, the continuous-time observers might not be useful for high-speed sensorless drives. To ensure the stability and control performance, it is desirable to design a rotor position observer directly in the discrete-time domain.

To overcome these two challenges, the discrete-time BLAC model will be proposed in Chapter 7. Based on this model, the corresponding decoupling current controller and rotor positon observer can be designed directly in the discrete-time domain, which can guarantee good stability and control performance.

1.5 Outline and Contributions of the Thesis

The main research focus of this thesis is the sensorless control of high-speed BLDC and BLAC drives. Since the former has more advantages in high-speed range, this thesis pays more attention on the sensorless BLDC drives (from Chapter 2 to Chapter 6), while Chapter 7 is for sensorless BLAC drives. As shown in Fig. 1.19, the thesis is organized in the following chapters:

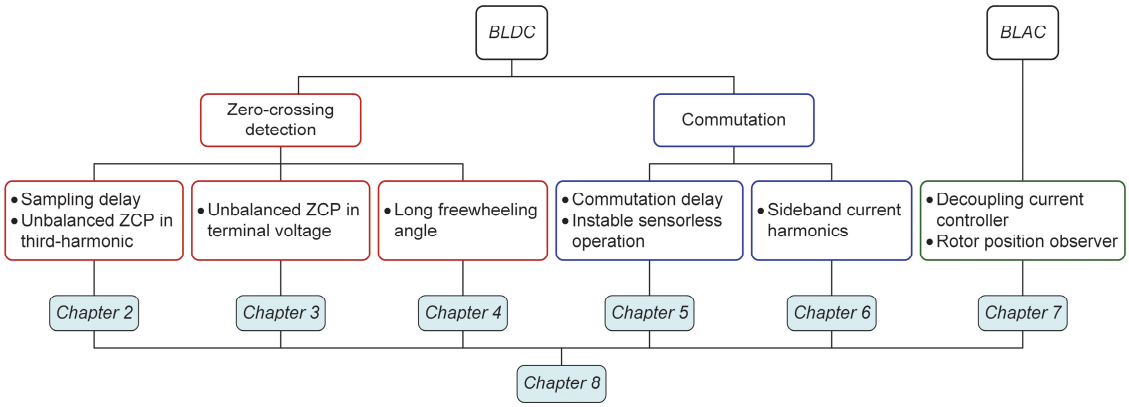

Fig. 1.19. Research structure of this thesis.

Chapter 2: This chapter presents the virtual third-harmonic based sensorless method. It focuses on two issues, 1) ZCD with oversampling to reduce the sampling delay; 2) commutation delay compensation for the errors caused by asymmetric machine parameters.

Chapter 3: It discusses the influence of two nonideal factors on commutation errors of BLDC drives, i.e. 1) asymmetric machine parameters and 2) the resistance tolerance of back EMF measurement circuits. In order to suppress the commutation errors, an adaptive threshold correction strategy, including horizontal and vertical corrections is proposed for eliminating the influence of these two nonideal factors, respectively.

Chapter 4: It investigates the issue of long freewheeling angle. In extreme cases when the freewheeling angle exceeds 30º, the ZCPs of back EMF will be undetectable, resulting in the failure of sensorless drives. An analytical study is carried out on the freewheeling angle and a PWM pattern resulting in minimum freewheeling angle is

identified. A theoretical way to predict the maximum torque and speed area for sensorless control is presented.

Chapter 5: This chapter investigates the influence of PWM switching delay on the commutation of high-speed BLDC drives. It is found that the switching delay will lead to unneglectable commutation errors when the switching ratio is insufficient. Besides, the commutation errors will be accumulated and finally result in instability of ZCD based sensorless methods. The mechanism of the instability is identified and a novel PWM commutation pattern (carrier synchronized commutation, CSC) that is suitable for high-speed application is proposed.

Chapter 6: This chapter is an in-depth investigation of Chapter 5. An analytical study of spectral characteristics of three commutation patterns is carried out, including two conventional PWM commutation patterns, i.e. regular-sampled commutation (RSC) and natural-sampled commutation (NSC) together with the novel CSC pattern proposed in Chapter 5. To reveal the spectral characteristics of conventional RSC and CSC patterns, an extended geometric wall model is introduced, which can be used for the Fourier decomposition of complex vectors. It is found that two conventional commutation patterns will lead to sideband current harmonics when the switching ratio is insufficient, while the proposed CSC pattern can virtually eliminate these sideband current harmonics.

Chapter 7: This chapter investigates the discrete-time current controller and EMF observer for sensorless high-speed BLAC drives considering low sampling ratio. A generic discrete-time BLAC model considering fractional period sampling delay is established. Based on this model, new current controller and rotor position observer are directly designed in discrete-time domain. The new current controller can achieve enhanced current tracking and decoupling capabilities; the new EMF observer can avoid the position estimation error caused by improper delay modelling.

Chapter 8: It summarizes this research work and gives some discussions about future work.

The major contributions of this thesis are:

1) Improved ZCD based sensorless method for high-speed BLDC drives is established. The improvements include oversampling method for lower sampling delay, commutation correction methods for asymmetric machine parameters and resistance tolerance of back EMF measurement circuits.

2) The freewheeling angle of BLDC drives is studied. The PWM pattern resulting in minimum freewheeling angle is identified. A theoretical way to predict the maximum torque and speed area for sensorless control is presented.

3) A comprehensive investigation on the PWM commutation for BLDC drives with insufficient switching ratio is presented. The unstable sensorless operation caused by the commutation delay in conventional commutation patterns is analysed. An extended geometric wall model is introduced to reveal the sideband current harmonics of conventional commutation patterns. A novel commutation pattern that can avoid these adverse effects is proposed.

4) A generic discrete-time BLAC model considering fractional period sampling delay is established. Based on this model, new current controller and rotor position observer can be designed directly in discrete-time domain, which can guarantee good control performance in the low sampling ratio condition.

The publications of the research are listed in Appendix 2.

CHAPTER 2

Virtual Third Harmonic Back-EMF Based Sensorless BLDC Drives Considering Machine Parameter Asymmetries

2.1 Introduction

For a six-step control scheme, six discrete rotor positions are required in each fundamental period, which could be obtained from position sensors, e.g. Hall-effect sensors. However, position sensors increase the volume and complexity, and reduce the reliability. Besides, these position sensors are difficult to assemble precisely, particularly for high-speed motors which has smaller motor size for the same power [SCE16], [PAR17]. Accordingly, various sensorless drive techniques have been investigated because they have the superiority of low cost and high reliability.

Among all the sensorless drive methods, the back EMF zero-crossing point (ZCP) detection based method is the most popular one. The back EMF can be acquired from the terminal voltage [SHA06] [TSO15], the line-to-line voltage [CHE07] [CHU14] and the third harmonic [LIU14] [SHE04] [CUI15] [SON18a] [SON18b]. The third harmonic back EMF can be measured from the motor neutral wire. Unlike the method of terminal voltage or line-to-line voltage that needs to measure three voltage signals, the third harmonic method needs just one voltage signal, which can help to save the interface resources of micro-controllers. Besides, it is reported in [LIU14] that the third harmonic method is able to achieve wider speed range and thus very suitable for high-speed applications. However, sometimes the motor neutral wire is not provided, which means the third harmonic signal is not measureable in this case. Alternatively, a virtual neutral wire can be constructed with artificial Y-connected resistors. In this way, the virtual third harmonic obtained from the Y-connected resistors can be used for sensorless control [CUI15] [SON18a] [SON18b]. In addition, different from the conventional third harmonic method that requires trapezoidal back EMF, the virtual third harmonic can be used for both trapezoidal and sinusoidal back EMF type motors.

This offers a decent sensorless solution for high-speed motors with sinusoidal back EMF.

Unfortunately, the virtual third harmonic suffers from high frequency noise caused by PWM, which increases the difficulty of ZCP detection. To remove the high frequency noise, low pass filters (LPFs) are used in most existing literature [CUI15] [SON18a] [SON18b]. The usage of LPFs will cause serious phase lag to the commutation and consequently deteriorate the control performance. Therefore, these documents are focused on the design of filters and the phase delay compensation. Furthermore, it is found that the envelope construction method offers a potential alternative solution [HAI16] [DAR15] [LAI11]. With the help of the analog-digital converter (ADC), the back EMF signal can be reconstructed and then the ZCP can be detected in algorithm. The LPFs are not necessary and thereby the resulting phase lag can be avoided. However, most of these approaches are based on terminal voltage. The scheme of envelope construction of the virtual third harmonic was rarely investigated up to now.

In addition to LPF phase lag, some other factors can also cause commutation errors. Firstly, the DC-link voltage offset will cause ZCP deviation and then distribute the ZCPs unbalanced. To solve this problem, a phase compensation algorithm using direct calculation was proposed in [PAR19]. Besides, [ZHO19] proposed a method based on terminal voltage symmetry to avoid the problem of DC-link voltage offset. Apart from this factor, the machine parameter asymmetry can also lead to unbalanced ZCP distribution. When the parameter asymmetry happens, the ZCP intervals will be repeatedly lengthened and shortened, leading to commutation position errors. In [YAN19a], the influence of parameter asymmetries on virtual third harmonic was briefly analysed. In this chapter, an in-depth research of position errors caused by parameter asymmetries is presented and the corresponding phase compensation strategy is proposed.

This chapter contains two aspects. In the first place, the virtual third harmonic based sensorless drive is introduced. The algorithmic envelope construction technique

is employed to detect the ZCP of virtual third harmonic. In this way, the phase lag caused by hardware LPFs and voltage comparators in conventional ZCP detection methods can be avoided. In addition, to guarantee the accuracy of ZCP detection and to fully utilize the available sampling duration, the number of sampling points per PWM period is dynamically adjusted according to the PWM duty ratio. Furthermore, the influence of asymmetric parameters on ZCP detection is analysed in-depth. The corresponding phase compensation method is proposed. All the theoretical analyses are validated by experiments at a high-speed BLDC drive platform.

The study in this chapter has been published in

L. Yang, Z. Q. Zhu, H. Bin, Z. Zhang, and L. Gong, "Virtual third harmonic back-EMF based sensorless drive for high speed BLDC motors considering machine parameter asymmetries," *IEEE Trans. Ind. Appl.*

2.2 ZCP Detection of Virtual Third Harmonic Back EMF

2.2.1 Virtual Third Harmonic Back EMF

Fig. 2.1 shows the topology diagram of high-speed BLDC motor drive, in which a Y-connected resistor network is utilized for position sensorless control. The nodes *M*, *S* and *N* denote the middle point of DC-link, the neutral point of resistor network and the neutral point of motor, respectively. The mathematical model of a high-speed BLDC motor can be expressed as

$$\begin{cases} v_{\mathrm{AG}} = i_{\mathrm{A}}\left(R_{\mathrm{A}} + pL_{\mathrm{A}}\right) + e_{\mathrm{A}} + v_{\mathrm{NG}} \\ v_{\mathrm{BG}} = i_{\mathrm{B}}\left(R_{\mathrm{B}} + pL_{\mathrm{B}}\right) + e_{\mathrm{B}} + v_{\mathrm{NG}} \\ v_{\mathrm{CG}} = i_{\mathrm{C}}\left(R_{\mathrm{C}} + pL_{\mathrm{C}}\right) + e_{\mathrm{C}} + v_{\mathrm{NG}} \end{cases} \tag{2.1}$$

where v_{XG} is the terminal voltage, i_{X} is the current, e_{X} is the phase back EMF, v_{NG} is the motor neutral voltage with respect to ground, p is the differential operator, R_{X} and L_{X} are the winding resistance and inductance, respectively. The subscript "X" denotes phase A, B or C. Here, for general situation, it is assumed that the winding resistances and inductances in three phases are asymmetric.

It should be noted that high-speed BLDC motors have sinusoidal phase back EMFs as a result of 2-pole diametrically magnetized magnet [GUC18]. However, it is preferred to apply six-step BLDC control to this motor for the reason of easy-to-implement. From the Y-connected resistor network, the following equations can be easily obtained.

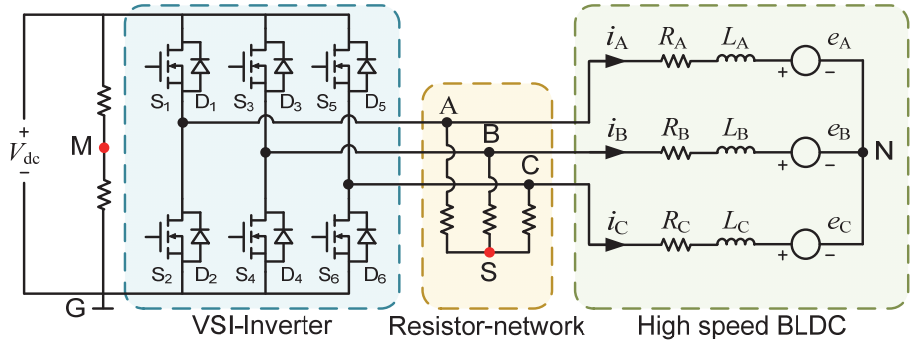

Fig. 2.1. Diagram of high-speed BLDC motor drive with Y-connected resistors.

$$\begin{cases} v_{AS} + v_{SG} = v_{AG} \\ v_{BS} + v_{SG} = v_{BG} \\ v_{CS} + v_{SG} = v_{CG} \end{cases} \tag{2.2}$$

$$v_{AS} + v_{BS} + v_{CS} = 0 \tag{2.3}$$

Then, v_{SM} can be calculated as

$$\begin{aligned} v_{SM} &= \frac{1}{3}\left(v_{AG} + v_{BG} + v_{CG}\right) - \frac{1}{2}V_{dc} \\ &= \frac{1}{3}\left(i_A Z_A + i_B Z_B + i_C Z_C\right) + \frac{1}{3}\left(e_A + e_B + e_C\right) - \frac{1}{2}V_{dc} + v_{NG} \end{aligned} \tag{2.4}$$

where $Z_X = \left(R_X + pL_X\right)$ is the phase impedance. The equation (2.4) describes the voltage signal v_{SM} in general situation. For the six-step commutation method, an electric drive cycle can be divided into six sectors as shown in Fig. 2.2. In each sector, two phases are conducting and the third one is floating. The phases connected to the positive and negative DC-link rails are defined as phases H and L, respectively. The third phase that is floating can be defined as phase O. Then, the voltage v_{NG} can be calculated as

$$v_{NG} = \frac{1}{2}\left(v_{HG} + v_{LG}\right) - \frac{1}{2}\left(i_H Z_H + i_L Z_L\right) - \frac{1}{2}\left(e_H + e_L\right) \tag{2.5}$$

In each sector, the current flows from phase H to phase L. Hence, the current in three phases can be calculated as

$$\begin{aligned} i_{\mathrm{H}} &= \frac{\left(v_{\mathrm{HG}} - v_{\mathrm{LG}}\right) - \left(e_{\mathrm{H}} - e_{\mathrm{L}}\right)}{Z_{\mathrm{H}} + Z_{\mathrm{L}}} \\ i_{\mathrm{L}} &= -i_{\mathrm{H}} \\ i_{\mathrm{O}} &= 0 \end{aligned} \tag{2.6}$$

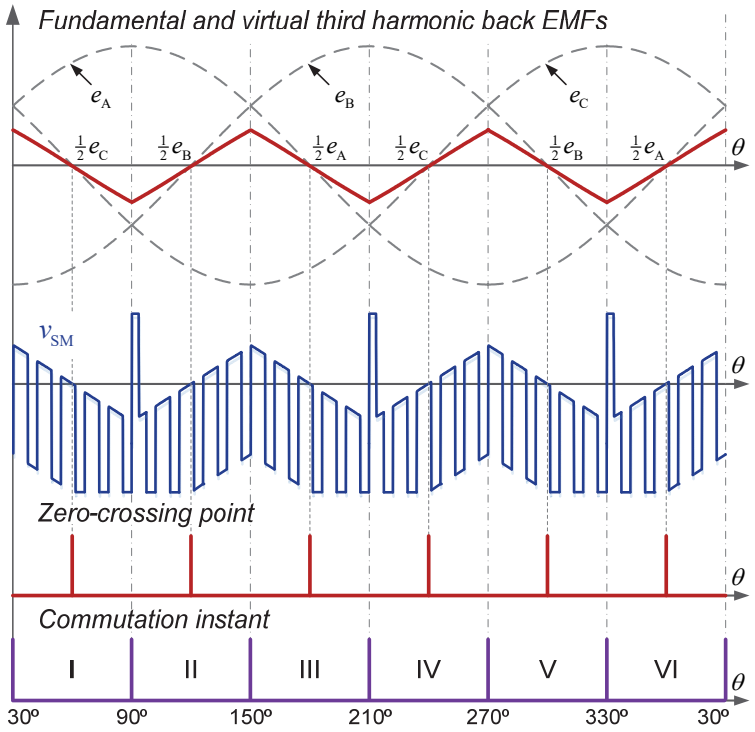

Fig. 2.2. ZCPs of virtual third harmonic and commutation positions.

Taking the H_PWM-L_ON scheme for instance, the high side power devices are controlled by PWM chopping signals and low side power devices keep on or off in each sector. Thus, the terminal voltages v_{HG} and v_{LG} can be described as

$$\begin{aligned} v_{\mathrm{HG}} &= \Lambda \cdot V_{\mathrm{dc}} = \begin{cases} V_{\mathrm{dc}} & \text{PWM-on} \\ 0 & \text{PWM-off} \end{cases} \\ v_{\mathrm{LG}} &= 0 \end{aligned} \tag{2.7}$$

where Λ is the PWM switching function as

$$\Lambda = \begin{cases} 1 & \text{PWM-on} \\ 0 & \text{PWM-off} \end{cases} \tag{2.8}$$

By substituting (2.5) and (2.6) into (2.4), the voltage v_{SM} can be obtained as

$$v_{\mathrm{SM}} = \underbrace{\frac{1}{6}\left(2e_{\mathrm{O}} - e_{\mathrm{H}} - e_{\mathrm{L}}\right)}_{\text{Back EMF}} + \underbrace{\frac{1}{2}\left(\Lambda - 1\right)V_{\mathrm{dc}}}_{\text{PWM fulactuation}} \underbrace{- \frac{1}{6}\frac{Z_{\mathrm{H}} - Z_{\mathrm{L}}}{Z_{\mathrm{H}} + Z_{\mathrm{L}}}\left(\Lambda \cdot V_{\mathrm{dc}} - \left(e_{\mathrm{H}} - e_{\mathrm{L}}\right)\right)}_{\text{Asymmetric parameters}} \tag{2.9}$$

It can be seen from (2.9) that v_{SM} consists of three parts, i.e. the back EMF, the voltage fluctuation caused by PWM and the voltage drift introduced by asymmetric parameters. Actually, the latter two parts are undesired components and should be removed. Only the first part $\left(2e_{\mathrm{O}} - e_{\mathrm{H}} - e_{\mathrm{L}}\right)/6$ contains the rotor position information. For typical sinusoidal and trapezoidal back EMF models, it yields

$$\begin{cases} e_{\mathrm{H}} + e_{\mathrm{L}} = -e_{\mathrm{O}} & \text{sinusoidal EMF} \\ e_{\mathrm{H}} + e_{\mathrm{L}} = 0 & \text{trapezoidal EMF} \end{cases} \tag{2.10}$$

Then, $\left(2e_{\mathrm{O}} - e_{\mathrm{H}} - e_{\mathrm{L}}\right)/6$ in (2.9) can be simplified as

$$\frac{1}{6}\left(2e_{\mathrm{O}} - e_{\mathrm{H}} - e_{\mathrm{L}}\right) = \begin{cases} \frac{1}{2}e_{\mathrm{O}} & \text{sinusoidal EMF} \\ \frac{1}{3}e_{\mathrm{O}} & \text{trapezoidal EMF} \end{cases}. \tag{2.11}$$

Thus, for both sinusoidal and trapezoidal back EMF type motors, the voltage v_{SM} contains the floating phase back EMF signal, which can be used for sensorless control.

2.2.2 Zero-crossing Detection Based on Over-sampling Method

To detect the ZCP under the circumstance of high frequency PWM fluctuation, LPFs and voltage comparators are used in most previous literature regarding the virtual third harmonic method. The voltage signal is firstly processed by LPFs to remove the high frequency fluctuation, and then the voltage comparators are used to detect the ZCP of virtual third harmonic. The LPFs are usually designed with very low cut-off frequency, leading to serious phase lag to the commutation. Alternatively, the envelope construction method that is usually employed in terminal voltage method [HAI16] [DAR15] [LAI11] offers another potential solution.

As shown in Fig. 2.2, although the voltage signal v_{SM} is influenced by high frequency PWM fluctuation, the back EMF can be reflected on its upper envelope. The commutation instant can be estimated from the ZCP of this envelope signal. This can

be realized by sampling the voltage v_{SM} during PWM-on period. By substituting $\Lambda = 1$ into (2.9), the upper envelope $\hat{v}_{\mathrm{SM}}$ can be expressed as

$$\hat{v}_{\mathrm{SM}} = v_{\mathrm{SM}}\big|_{\Lambda=1} = \frac{1}{2}e_{\mathrm{O}} - \Delta v_{\mathrm{HL}} \tag{2.12}$$

where Δv_{HL} is the voltage error caused by asymmetric parameters. Here, the hat "^" denotes the upper envelope. After obtaining the upper envelope $\hat{v}_{\mathrm{SM}}$, the ZCP can be detected with

$$\begin{cases} \hat{v}_{\mathrm{SM}}[n-1] \le 0 \\ \hat{v}_{\mathrm{SM}}[n] \ge 0 \end{cases} \quad \text{or} \quad \begin{cases} \hat{v}_{\mathrm{SM}}[n-1] \ge 0 \\ \hat{v}_{\mathrm{SM}}[n] \le 0 \end{cases} \tag{2.13}$$

where $\hat{v}_{\mathrm{SM}}[n-1]$ and $\hat{v}_{\mathrm{SM}}[n]$ denote the previous and the present samplings, respectively. Obviously, it is illustrated by (2.12) that the envelope contains the voltage error, which is caused by asymmetric parameters can be expressed as

$$\Delta v_{\mathrm{HL}} = \frac{1}{6}\frac{Z_{\mathrm{H}} - Z_{\mathrm{L}}}{Z_{\mathrm{H}} + Z_{\mathrm{L}}}\left(\Lambda \cdot V_{\mathrm{dc}} - \left(e_{\mathrm{H}} - e_{\mathrm{L}}\right)\right) \tag{2.14}$$

Considering the excitation voltage term contains PWM switching function Λ. The PWM period is much less than the winding electromagnetic time constant *L*/*R*. In this situation, within the very short period when the circuit switches from PWM-off ($\Lambda = 0$) to PWM-on ($\Lambda = 1$), the asymmetric impedance term can be simplified as

$$\frac{Z_{\mathrm{H}} - Z_{\mathrm{L}}}{Z_{\mathrm{H}} + Z_{\mathrm{L}}} \approx \frac{L_{\mathrm{H}} - L_{\mathrm{L}}}{L_{\mathrm{H}} + L_{\mathrm{L}}} \tag{2.15}$$

which means the asymmetric impedances mainly depend on the asymmetric inductances. Then, assuming the phase back EMF amplitude is $\psi_f \omega_e$, where ψ_f is the flux linkage and ω_e is the electrical speed, the line-line back EMF $e_{\mathrm{H}} - e_{\mathrm{L}}$ around the ZCP can be expressed as

$$e_{\mathrm{H}} - e_{\mathrm{L}} = \begin{cases} \sqrt{3}\psi_f \omega_e & \text{sinusoidal EMF} \\ 2\psi_f \omega_e & \text{trapezoidal EMF} \end{cases} \tag{2.16}$$

Finally, let $V_{\mathrm{RL}} = V_{\mathrm{dc}} - \left(e_{\mathrm{H}} - e_{\mathrm{L}}\right)$ denote the voltage drop on winding resistance and inductance, (2.14) can be expressed as

$$\Delta v_{\mathrm{HL}} = \frac{1}{6} \cdot \frac{L_{\mathrm{H}} - L_{\mathrm{L}}}{L_{\mathrm{H}} + L_{\mathrm{L}}} \cdot V_{\mathrm{RL}} \tag{2.17}$$

Then, after obtaining the envelope $\hat{v}_{\mathrm{SM}}$, the ZCP can be detected in algorithm without the influence of PWM fluctuation. Actually, according to (2.12), $\hat{v}_{\mathrm{SM}}$ is proportional to the floating phase back EMF, if the asymmetric parameter term Δv_{HL} is neglected. The influence of Δv_{HL} will be addressed in the next section.

Fig. 2.3 shows the diagram of ZCP detection of virtual third harmonic. Since ADC works in a discrete way, the sampling delay is inevitable in ZCP detection, especially in high-speed region. It is reasonable to increase the sampling rate to minimize the sampling delay. However, the available sampling duration is limited by the PWM-on period. Thus, to fully utilize the available sampling duration, the number of sampling points per PWM wave N_{s} is dynamically adjusted according to the PWM duty ratio. As shown in Fig. 2.3, assuming the PWM-on duration is T_{on} and the minimum sampling interval is T_{s}, the number of sampling points N_{s} can be expressed as

$$N_s = \mathrm{floor}\left(\frac{T_{on}}{T_s} \right) \tag{2.18}$$

where $\mathrm{floor}\,(x)$ denotes the greatest integer less than or equal to x. As the motor speed increases, it has higher demand for the ZCP detection precision. Fortunately, the duty ratio also becomes larger with the motor speed. Thus, it provides longer PWM-on duration T_{on} to enable more sampling points. In this way, the number of sampling points N_{s} is dynamically adjusted according to the PWM duty ratio. The precision of ZCP detection can be guaranteed within wide speed range.

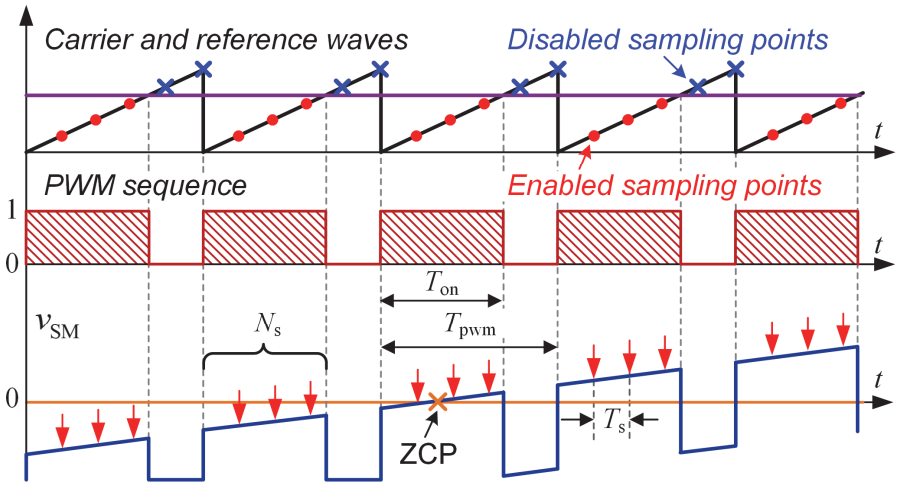

Fig. 2.3. Schematic diagram of dynamic over-sampling technique on the virtual third harmonic back EMF.

2.3 Phase Compensation for Asymmetric Parameters

2.3.1 Commutation Errors Caused by Asymmetric Parameters

Machine parameter asymmetry is a common problem, especially in high-speed motors that usually have relatively low number of turns per phase and thus low resistance and inductance. This problem could be caused by cabling, inverter, modular manufacturing, rotor eccentricity, or winding fault [XUP16] [REI10]. Under the ideal circumstance with symmetrical parameters, the ZCPs can be detected with regular interval. However, when the parameter asymmetry happens due to aforementioned reasons, ZCPs will deviate from correct positions and distribute unevenly. The ZCP interval will be repeatedly lengthened and shortened, causing commutation position errors. In order to illustrate this phenomenon, sectors III and VI are taken for instance. In these two sectors, phases B and C are conducting and phase A is floating. In addition, the conducting directions are opposite in the two sectors, which can be described as follows.

In sector III, the current flows from phase B to phase C. Phases B and C are connected to positive and negative DC rails, respectively. As shown in Fig. 2.4 (a), the asymmetric parameters cause a voltage error Δv_{HL} to the envelope, which can be expressed as

$$\Delta v_{\mathrm{HL}} = \Delta v_{\mathrm{BC}} = \frac{1}{6} \cdot \frac{L_{\mathrm{B}} - L_{\mathrm{C}}}{L_{\mathrm{B}} + L_{\mathrm{C}}} \cdot V_{\mathrm{RL}} . \tag{2.19}$$

Oppositely, in sector VI, current flows from phase C to phase B. Phase B connects to the negative DC rail and phase C connects to the positive one. As shown in Fig. 2.4 (b), in this situation, the voltage error can be expressed as

$$\Delta v_{\mathrm{HL}} = \Delta v_{\mathrm{CB}} = \frac{1}{6} \cdot \frac{L_{\mathrm{C}} - L_{\mathrm{B}}}{L_{\mathrm{C}} + L_{\mathrm{B}}} \cdot V_{\mathrm{RL}} . \tag{2.20}$$

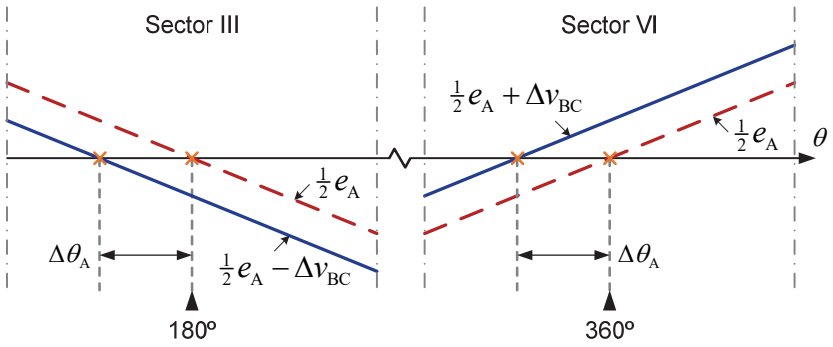

(a) Sector III. (b) Sector VI.

Fig. 2.4. Illustration of virtual third harmonic envelopes and ZCP position errors.

It can be concluded that $\Delta v_{\mathrm{BC}} = -\Delta v_{\mathrm{CB}}$. As shown in Fig. 2.4, the voltage envelope moves oppositely in sectors III and VI. Similarly, this conclusion can be deduced in all six sectors as

$$\begin{cases} \Delta v_{\mathrm{AB}} + \Delta v_{\mathrm{BA}} = 0 \\ \Delta v_{\mathrm{BC}} + \Delta v_{\mathrm{CB}} = 0 \\ \Delta v_{\mathrm{AC}} + \Delta v_{\mathrm{CA}} = 0 \end{cases} . \tag{2.21}$$

The voltage errors caused by asymmetric parameters will deviate the ZCP of back EMF. As shown in Fig. 2.4, the back EMF envelope around ZCP can be regarded as a straight line with slope K_{ω}. Then, it yields the ZCP position error is proportional to the voltage error as

$$\left[\Delta\theta_{\mathrm{C}} \ \Delta\theta_{\mathrm{A}} \ \Delta\theta_{\mathrm{B}}\right] = K_{\omega} \left[\Delta v_{\mathrm{AB}} \ \Delta v_{\mathrm{BC}} \ \Delta v_{\mathrm{CA}}\right] \tag{2.22}$$

where

$$K_\omega = \begin{cases} \dfrac{2}{\psi_f \omega_e} & \text{sinusoidal EMF} \\ \dfrac{\pi}{2\psi_f \omega_e} & \text{trapezoidal EMF} \end{cases} \tag{2.23}$$

The ZCP position errors and the virtual third harmonic envelope are listed in Table 2.1. For the direction of errors, lag is defined as positive and lead is defined as negative. Fig. 2.5 shows the analysis result of ZCP position errors with respect to the parameters listed in Appendix B. As it is shown, the ZCP position error increases with the unbalanced inductances. In addition, the error has a non-linear relationship with the motor speed.

Table 2.1 ZCP Position Errors Caused by Asymmetric Parameters

Sector	Mode	Envelope	Position Errors
I	A+B-	$\frac{1}{2}e_C - \Delta v_{AB}$	$\Delta\theta_C$
II	A+C-	$\frac{1}{2}e_B + \Delta v_{CA}$	$\Delta\theta_B$
III	B+C-	$\frac{1}{2}e_A - \Delta v_{BC}$	$\Delta\theta_A$
IV	B+A-	$\frac{1}{2}e_C + \Delta v_{AB}$	$\Delta\theta_C$
V	C+A-	$\frac{1}{2}e_B - \Delta v_{CA}$	$\Delta\theta_B$
VI	C+B-	$\frac{1}{2}e_A + \Delta v_{BC}$	$\Delta\theta_A$

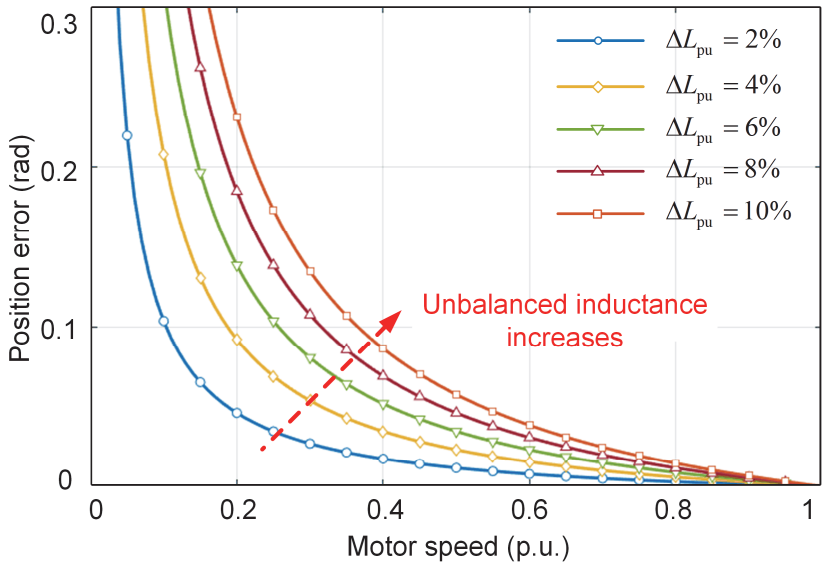

Fig. 2.5. Analysis result of ZCP position errors caused by asymmetric machine parameters, where $\Delta L_{pu} = (L_X - L_Y)/(L_X + L_Y)$ (parameters of motor-I in Appendix is simulated).

For conventional BLDC sensorless methods, the deviation of ZCP will influence the commutation accuracy. In the ideal case without ZCP position errors, every ZCP

interval should equal to 60º and the next commutation instant is 30º after the ZCP. Thus, in conventional methods, the commutation instant is usually calculated with the present ZCP interval as

$$\varphi[n] = \frac{\pi}{6} = \frac{1}{2}\hat{\theta}[n] \tag{2.24}$$

where $\hat{\theta}[n]$ is the n^{th} measured ZCP interval and $\varphi[n]$ is the n^{th} delay angle from the ZCP to next commutation instant. However, if the error exists, ZCPs will be detected at inaccurate positions. In addition, the ZCP interval will be repeatedly lengthened and shortened, which means the determination of 30º delay angle in (2.24) is also incorrect. That is how the asymmetric parameters undermine the conventional BLDC sensorless method.

2.3.2 Phase Compensation of Commutation Errors

In order to suppress the influence of asymmetric parameters on the sensorless drive, a phase compensation is proposed in this part. Fig. 2.6 shows the overall sensorless control diagram. Firstly, it constructs the signal $\hat{v}_{\text{SM}}$ by the over-sampling approach discussed previously. Then, the time interval between two adjacent ZCPs is measured by the high resolution CPU timer, since the ZCP time interval is dependent on the motor speed. The CPU timer starts at the previous ZCP and stops at the present ZCP. In this way the present ZCP time interval is measured and stored as $t_\theta[n]$ (the previous ZCP time interval is stored as $t_\theta[n-1]$). Finally, the position errors can be calculated and compensated with (2.33), which will be discussed later.

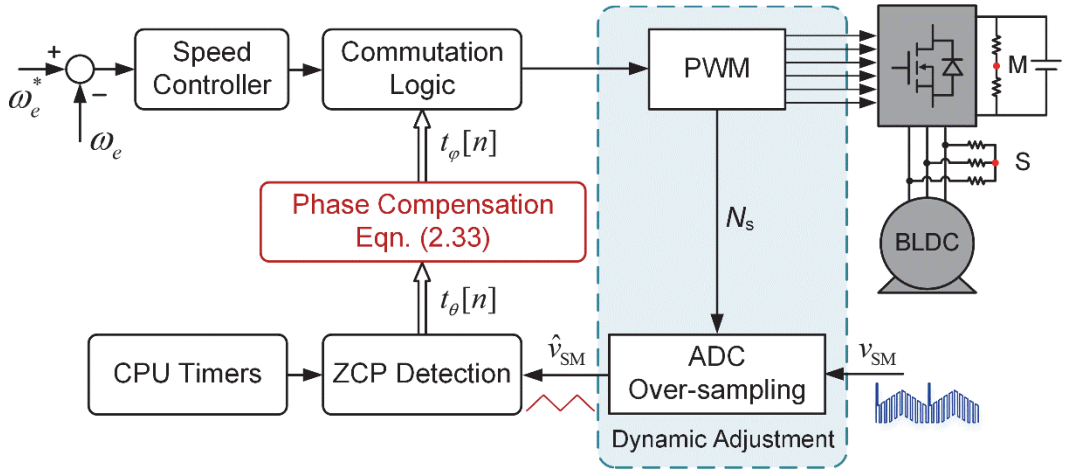

Fig. 2.6. Schematic diagram of sensorless control system with commutation phase compensation.

Fig. 2.7 illustrates the relation between the theoretical ideal and the measured ZCPs. The theoretical ideal ZCPs always locate in the middle of each 60° sector; and measured ZCPs could deviate due to asymmetric impedances. Then, the ZCP position errors can be modelled as

$$\begin{aligned}
\hat{\theta}_{12} &= \theta_{12} + \Delta\theta_{\mathrm{B}} - \Delta\theta_{\mathrm{C}} \\
\hat{\theta}_{23} &= \theta_{23} + \Delta\theta_{\mathrm{A}} - \Delta\theta_{\mathrm{B}} \\
\hat{\theta}_{34} &= \theta_{34} + \Delta\theta_{\mathrm{C}} - \Delta\theta_{\mathrm{A}} \\
\hat{\theta}_{45} &= \theta_{45} + \Delta\theta_{\mathrm{B}} - \Delta\theta_{\mathrm{C}} \\
\hat{\theta}_{56} &= \theta_{56} + \Delta\theta_{\mathrm{A}} - \Delta\theta_{\mathrm{B}} \\
\hat{\theta}_{61} &= \theta_{61} + \Delta\theta_{\mathrm{C}} - \Delta\theta_{\mathrm{A}}
\end{aligned} \tag{2.25}$$

where θ_{xy} represents the ZCP interval from sector x to sector y, the hat "^" represents measured results. The term in the bracket indicates they have the same value, e.g. $\hat{\theta}_{12} = \hat{\theta}_{45}$. It yields that $\theta_{12}...\theta_{61} = \pi/3$. Besides, the sum of three voltage errors can be calculated as

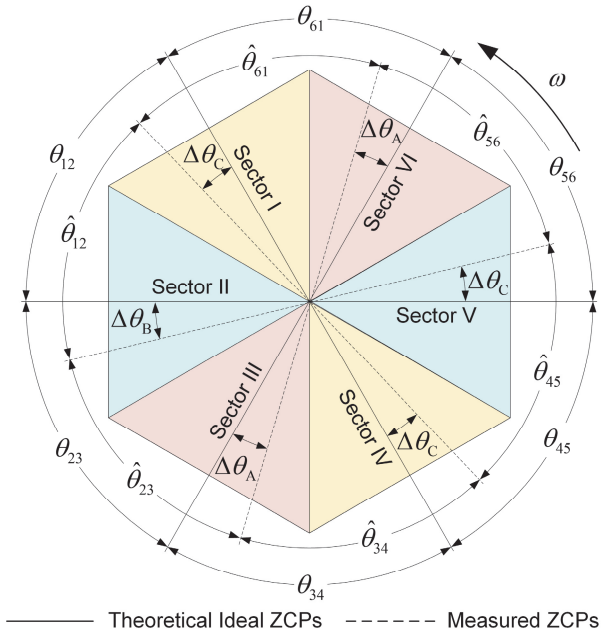

Fig. 2.7. Relationship between theoretical ideal and measured ZCPs.

$$\begin{aligned}
&\Delta v_{\mathrm{AB}} + \Delta v_{\mathrm{BC}} + \Delta v_{\mathrm{CA}} \\
&= \frac{1}{6} V_{\mathrm{RL}} \left(\frac{L_{\mathrm{A}} - L_{\mathrm{B}}}{L_{\mathrm{A}} + L_{\mathrm{B}}} + \frac{L_{\mathrm{B}} - L_{\mathrm{C}}}{L_{\mathrm{B}} + L_{\mathrm{C}}} + \frac{L_{\mathrm{C}} - L_{\mathrm{A}}}{L_{\mathrm{C}} + L_{\mathrm{A}}} \right) \\
&= -\frac{1}{6} V_{\mathrm{RL}} \cdot \frac{L_{\mathrm{A}} - L_{\mathrm{B}}}{L_{\mathrm{A}} + L_{\mathrm{B}}} \cdot \frac{L_{\mathrm{B}} - L_{\mathrm{C}}}{L_{\mathrm{B}} + L_{\mathrm{C}}} \cdot \frac{L_{\mathrm{C}} - L_{\mathrm{A}}}{L_{\mathrm{C}} + L_{\mathrm{A}}}
\end{aligned} \tag{2.26}$$

Since every inductance term in (2.26) is very small, their product is approximately equal to zero as

$$\Delta v_{\mathrm{AB}} + \Delta v_{\mathrm{BC}} + \Delta v_{\mathrm{CA}} \approx 0 \tag{2.27}$$

Then, due to the linear relationship in (2.22), the sum of three ZCP position errors also equals to zero as

$$\Delta\theta_{\mathrm{A}} + \Delta\theta_{\mathrm{B}} + \Delta\theta_{\mathrm{C}} \approx 0\,. \tag{2.28}$$

Finally, by solving (2.25) and (2.28), the ZCP position errors can be calculated as

$$\begin{bmatrix} \Delta\theta_{\mathrm{A}} \\ \Delta\theta_{\mathrm{B}} \\ \Delta\theta_{\mathrm{C}} \end{bmatrix} = \frac{1}{3} \begin{bmatrix} 1 & 2 & 0 \\ 2 & 0 & 1 \\ 0 & 1 & 2 \end{bmatrix} \begin{bmatrix} \hat{\theta}_{12}\left(\hat{\theta}_{45}\right) \\ \hat{\theta}_{23}\left(\hat{\theta}_{56}\right) \\ \hat{\theta}_{34}\left(\hat{\theta}_{61}\right) \end{bmatrix} - \frac{\pi}{3} \begin{bmatrix} 1 \\ 1 \\ 1 \end{bmatrix} \tag{2.29}$$

Although the ZCPs deviate from theoretical ideal positions due to asymmetric parameters, according to (2.28), the sum of three consecutive ZCP intervals identically equal to π as

$$\hat{\theta}[n]+\hat{\theta}[n-1]+\hat{\theta}[n-2]=\pi \tag{2.30}$$

Fig. 2.8 shows the calculation of (2.29), in which it can be derived that the coefficients (2 and 1) in the square matrix of (2.29) always correspond to the present and the previous ZCP intervals, respectively. Thus, (2.29) can be simplified as

$$\begin{aligned}\Delta\theta[n]&=\frac{1}{3}\left(2\hat{\theta}[n]+\hat{\theta}[n-1]\right)-\frac{1}{3}\left(\hat{\theta}[n]+\hat{\theta}[n-1]+\hat{\theta}[n-2]\right)\\&=\frac{1}{3}\left(\hat{\theta}[n]-\hat{\theta}[n-2]\right)\end{aligned}. \tag{2.31}$$

where $\Delta\theta[n]$ is the n^{th} calculated ZCP position error as shown in Fig. 2.9. Then, considering the ZCP position errors, the delay angle in (2.24) can be modified as

$$\begin{aligned}\varphi[n]&=\frac{\pi}{6}-\Delta\theta[n]\\&=\frac{1}{6}\left(\hat{\theta}[n]+\hat{\theta}[n-1]+\hat{\theta}[n-2]\right)-\frac{1}{3}\left(\hat{\theta}[n]-\hat{\theta}(n-2)\right)\\&=\frac{1}{6}\left(-\hat{\theta}[n]+\hat{\theta}(n-1)+3\hat{\theta}(n-2)\right)\end{aligned} \tag{2.32}$$

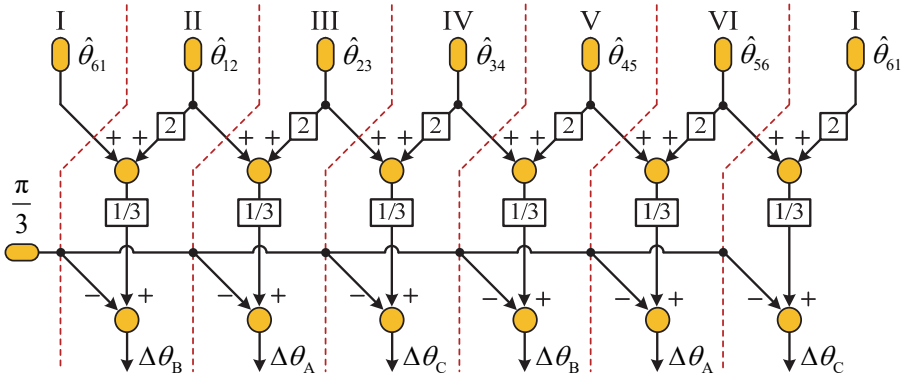

Fig. 2.8. Schematic diagram of ZCP error calculation.

In practice, CPU timers are usually employed to measure the ZCP interval and execute the commutation. Finally, (2.32) can be implemented as

$$t_{\varphi}[n]=\frac{1}{6}\left(-t_{\theta}[n]+t_{\theta}[n-1]+3t_{\theta}[n-2]\right) \tag{2.33}$$

where $t_\varphi[n]$ is the n^{th} ZCP time interval measured by CPU timers and $t_\varphi[n]$ is the n^{th} time delay for commutation instant. In this way, with the three last ZCP time intervals obtained from CPU timers, the ZCP errors caused by the parameter asymmetry can be compensated.

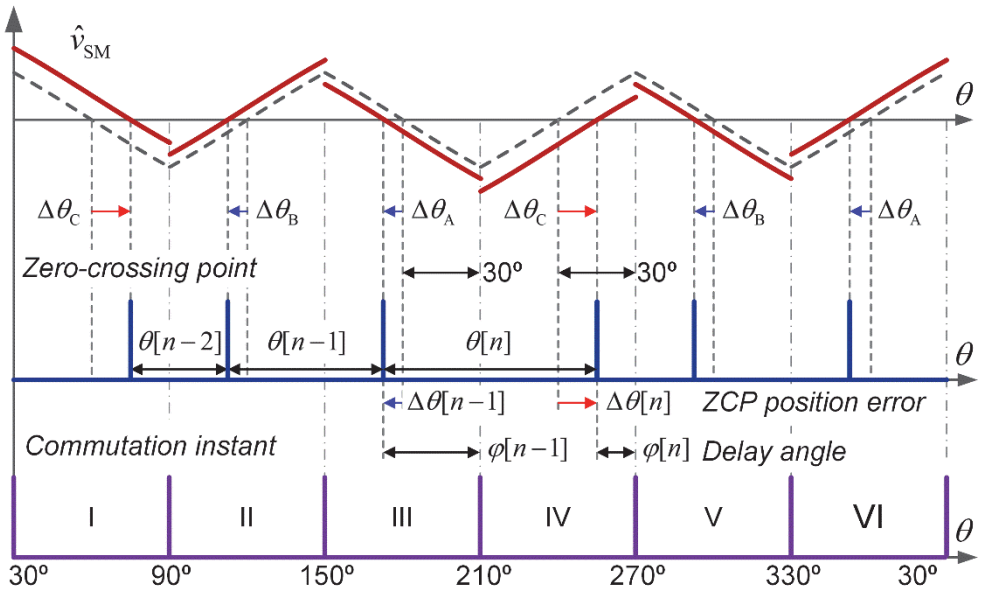

Fig. 2.9. Sequence diagram of ZCP interval $\hat{\theta}[n]$, ZCP error $\Delta\theta[n]$ and commutation delay angle $\varphi[n]$.

2.4 Experimental Validation

The proposed compensation algorithm is verified at the high-speed motor experimental platform as shown in Appendix 1. The high-speed BLDC Motor-I is used here. The DC-link voltage is 15V. The PWM switching frequency is 40 kHz and the minimum ZCP sampling interval is 5 μs. To simulate the asymmetric condition, from Fig. 2.11 to Fig. 2.14, an extra 5-μH inductor is connected in series to the phase A, which is equivalent to $\Delta L_{pu} = 10.2\%$

Fig. 2.10 shows the dynamic adjustment of sampling points, in which the voltage signal v_{SM} and its sampling result $\hat{v}_{SM}$ are given. As the theoretical analysis, the voltage v_{SM} is influenced by the high frequency PWM fluctuation. The virtual third harmonic signal can be reflected on its upper envelope. By arranging the sampling points on the PWM-on time, this back EMF envelope can be constructed as $\hat{v}_{SM}$.

Besides, in the right zoomed subplot, some details including the sampling instants are presented. The PWM period is 25 μs and the minimum sampling interval is 5 μs. The number of sampling points N_s is adjusted according to the PWM duty ratio as listed in Table II. As the motor speed increases, the PWM duty ratio becomes higher. There will be longer PWM-on duration to arrange more sampling points. Therefore, within a wide range of PWM duty ratio, the proposed dynamic over-sampling method is effective to construct the envelope signal $\hat{v}_{SM}$.

Table 2.2 Dynamic Adjustment of Sampling Points

Duty ratio	0~0.4	0.4~0.6	0.6~0.8	0.8~1.0	1.0
T_{on} (μs)	0~10	10~15	15~20	20~25	25
N_s	1	2	3	4	5

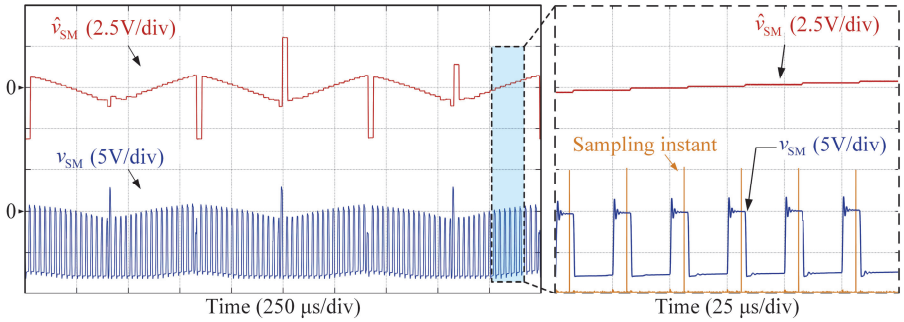

(a) Ns=1.

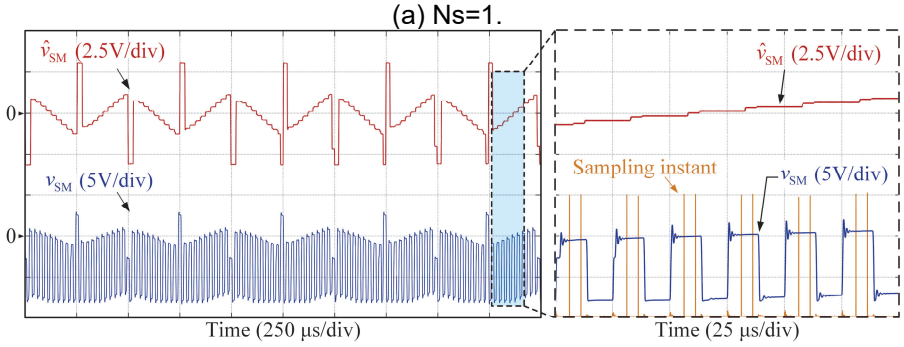

(b) Ns=2.

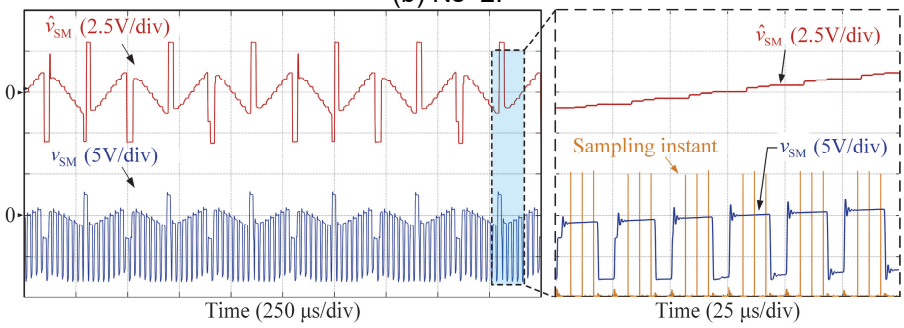

(c) Ns=3.

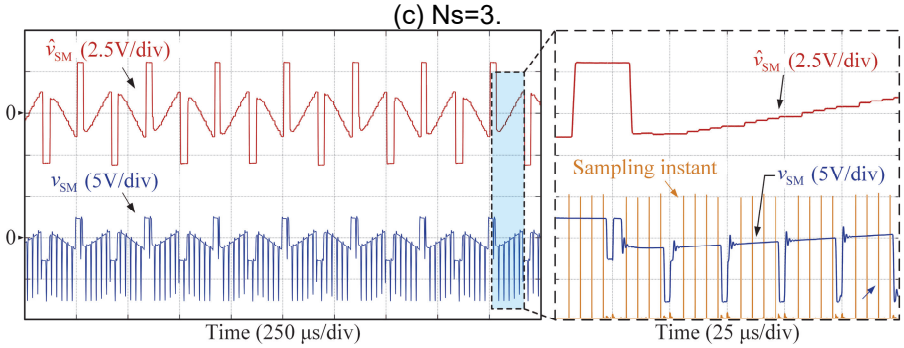

(d) Ns=4.

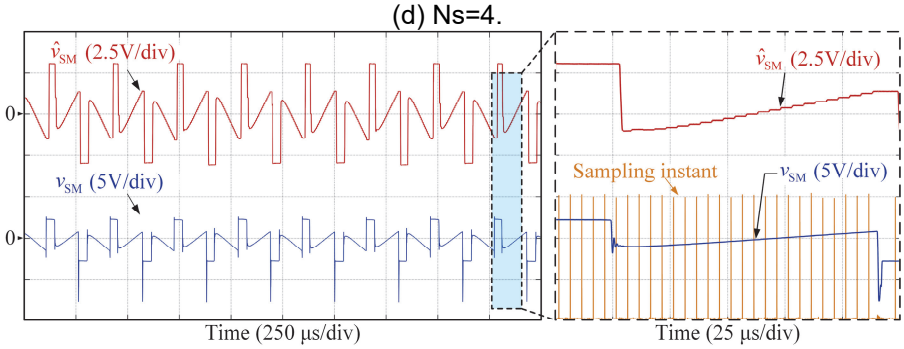

(e) Ns=5.

Fig. 2.10. Voltage signal v_{SM} and sampling result $\hat{v}_{SM}$.

Fig. 2.11, Fig. 2.12 and Fig. 2.13 compare the results before and after employing the proposed compensation scheme of 20 000 r/min, 40 000 r/min and 60 000 r/min, respectively. To simulate the asymmetric condition $\Delta L_{pu} = 10.2\%$, an extra 5-μH inductor is connected in series to the phase A, which is equivalent to. From top to bottom, the voltage v_{SM} with its sampling result $\hat{v}_{SM}$, the commutation interval (measured by the CPU timer), the commutation interrupt signal and the phase currents and presented. As shown in Fig. 2.11 (a), when the motor operates at 20 000 r/min without compensation, the ZCP interval repeatedly lengthened and shortened. The commutation interval fluctuates drastically within 45º to 80º, leading to significant phase current oscillations. It can be seen, the sensorless control performance is deteriorated by the asymmetric inductances. When the proposed compensation is enabled in Fig. 2.11 (b), the ZCP interval can remain at 60º stably. The peak-peak amplitude of phase currents is reduced from 6.05A to 4.37A.

The comparative results before and after compensation at 40 000 r/min and 60 000 r/min are shown in Fig. 2.12 and Fig. 2.13. Likewise, before the compensation, the commutation interval cannot remain at 60º, which makes the phase currents fluctuate drastically. After the compensation, the commutation interval can remain at 60º accurately. The amplitudes of phase currents are reduced from 13.85A to 12.95A at 40 000 r/min and from 24.40A to 23.46A at 60 000 r/min. Therefore, the proposed method is effective to compensate the commutation errors caused by asymmetric machine parameters.

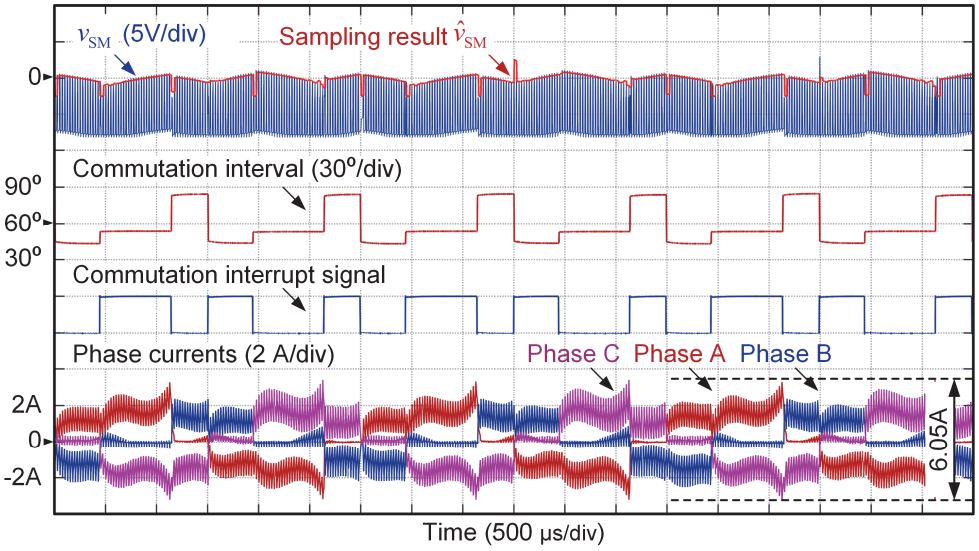

(a) Before compensation.

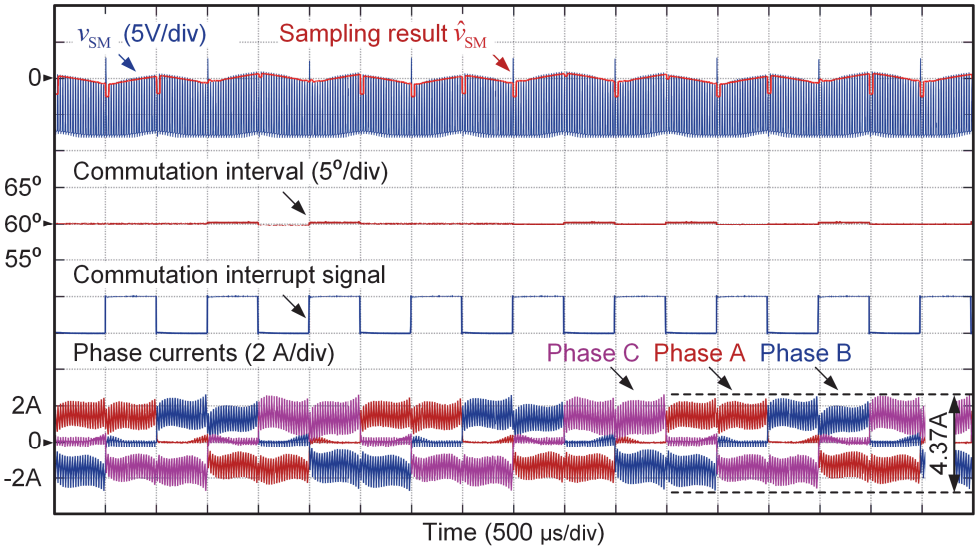

(b) After compensation.

Fig.2.11. Comparative results of steady state at 20 000 r/min.

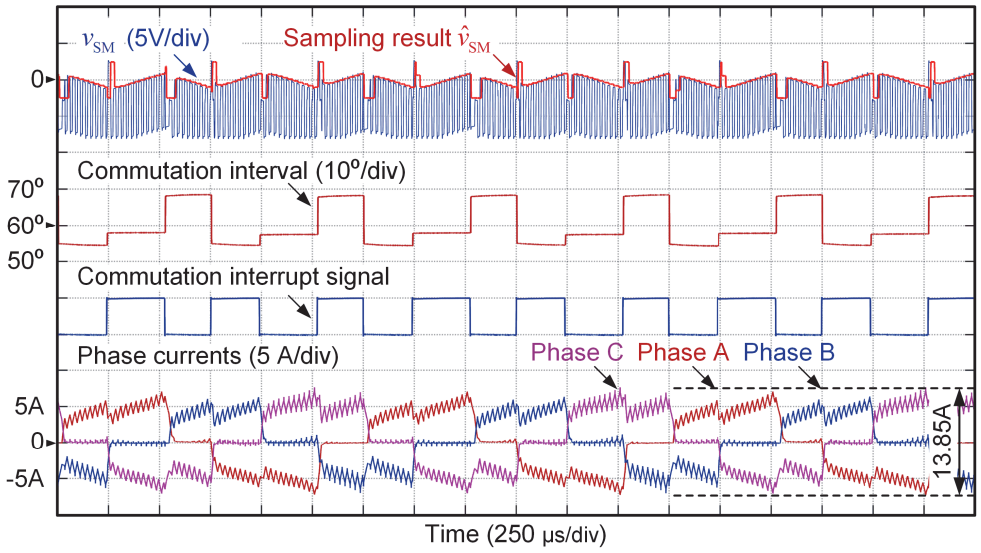

(a) Before compensation.

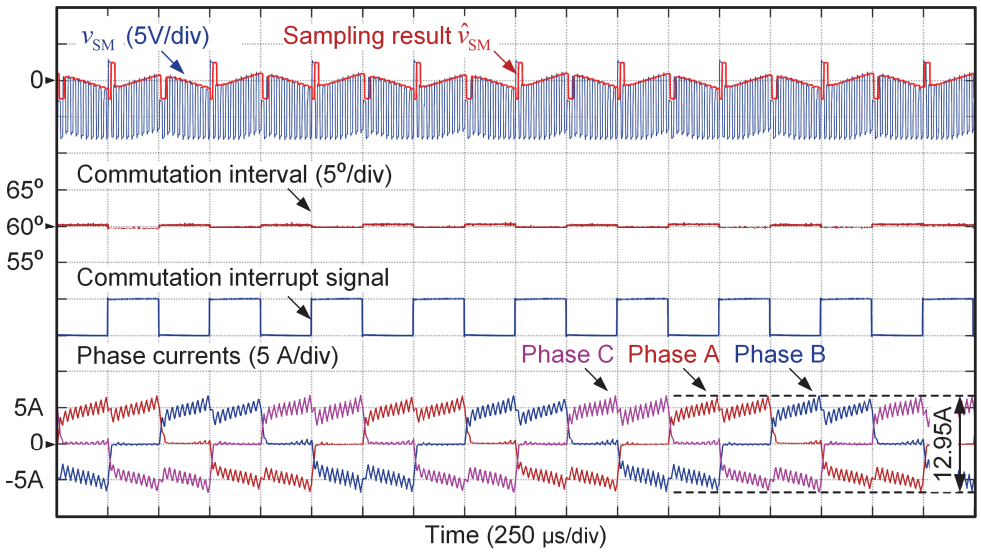

(b) After compensation.

Fig.2.12. Comparative results of steady state at 40 000 r/min.

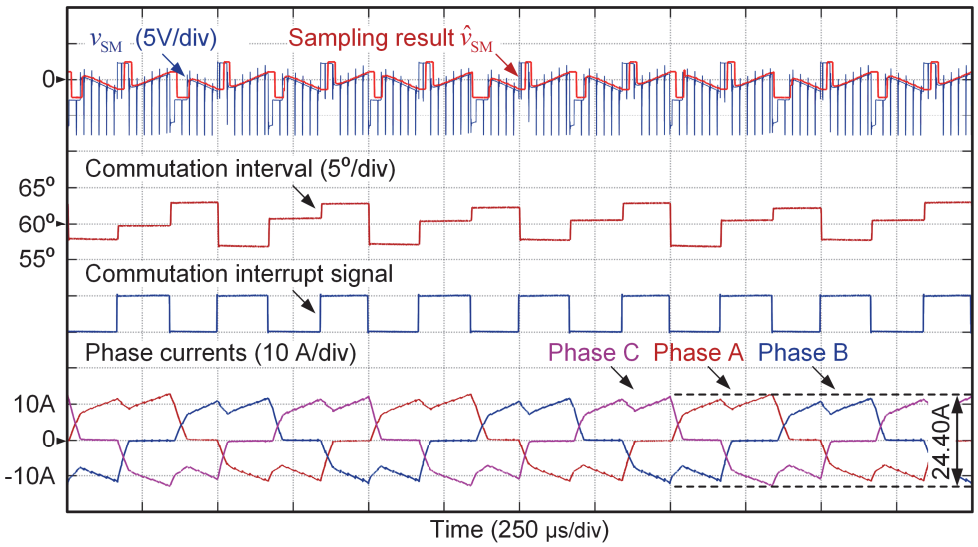

(a) Before compensation.

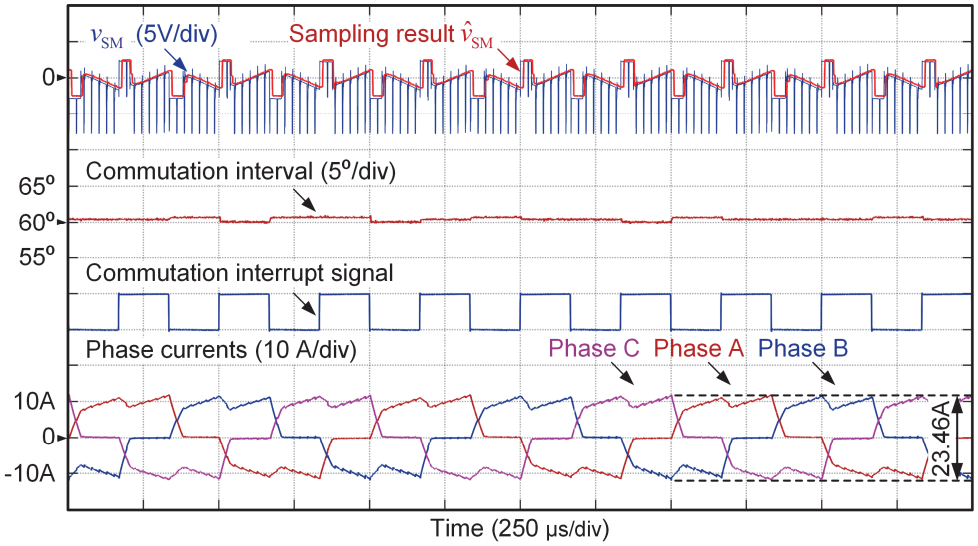

(b) After compensation.

Fig.2.13. Comparative results of steady state at 60 000 r/min.

Fig. 2.14 shows the comparative results at transient state with the extra 5-μH inductor. The motor accelerates from 20 000 r/min to 60 000 r/min, and then decelerates back to 20 000 r/min. As shown in Fig. 2.14 (a), before the compensation algorithm is employed, the commutation interval experiences considerable oscillations during acceleration and deceleration processes. Besides, some spikes can be observed on the estimated speed signal, reflecting its poor dynamic performance. On the other hand, when the phase compensation is utilized in Fig. 2.14 (b), the fluctuation range of commutation interval can maintain at 60° closely, although it amplifies slightly during transient processes. Accordingly, the proposed phase compensation method can improve both the steady and dynamic performances.

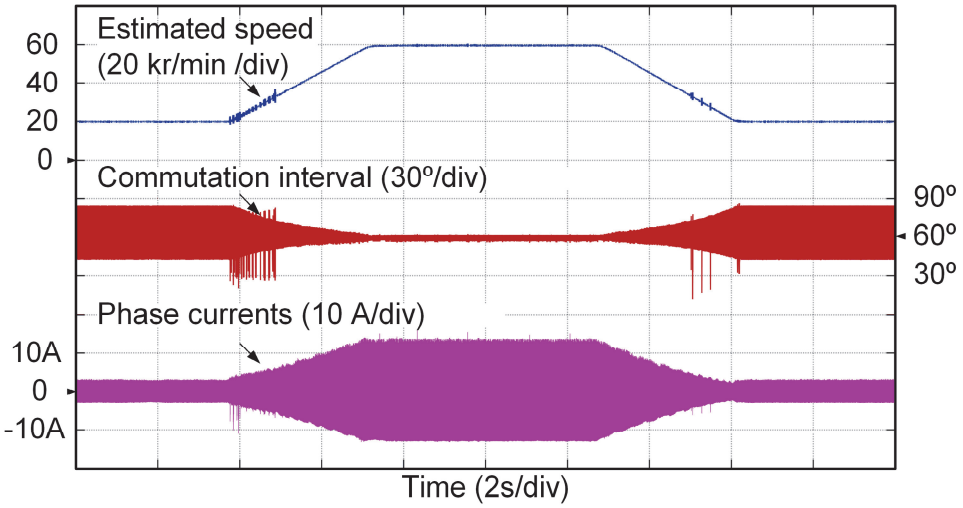

(a) Before compensation.

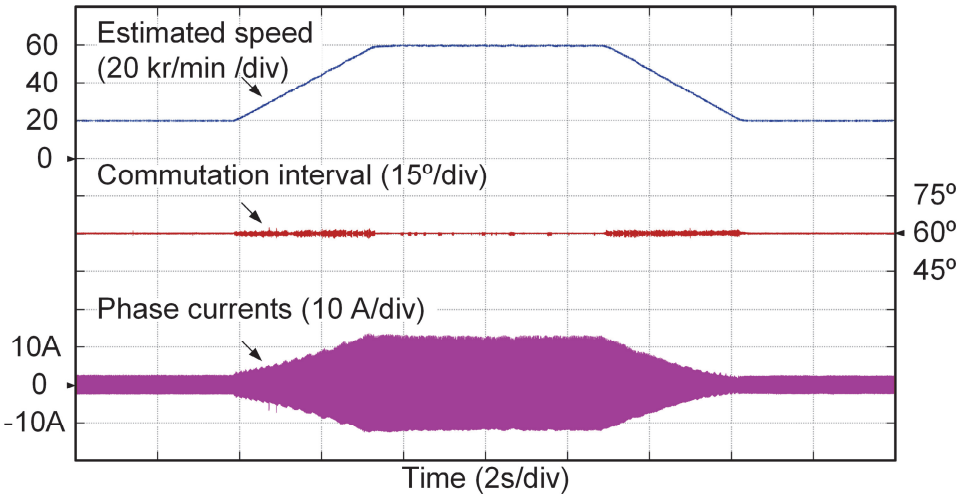

(b) After compensation.

Fig. 2.14. Comparative results at acceleration and deceleration processes.

2.5 Summary

This chapter has investigated the virtual third harmonic back EMF based BLDC sensorless drives. In the first place, the ZCP detection method of virtual third back EMF is introduced. The LPFs used in conventional methods are not utilized and thus the resulting phase lag is avoided. Besides, the dynamic over-sampling technique is employed for ZCP detection to reduce the sampling delay in high-speed region. Furthermore, the influence of asymmetric motor parameters is analysed in depth. With asymmetric parameters, the ZCPs of virtual third harmonic back EMF deviate from their ideal positions and the commutation is executed inaccurately. Based on the above

analysis, a novel phase compensation method is proposed to suppress the commutation errors. Experimental results demonstrate the effectiveness of the proposed method.

CHAPTER 3

Adaptive Threshold Correction Strategy for BLDC Drives Considering Zero Crossing Point Deviation

3.1 Introduction

Sensorless BLDC schemes can be classified into back EMF zero-crossing point (ZCP) detection [LIU16] [SON18] [CHE07] [DAR15] [LAI08] [LAI11] [SHA06], back EMF integration [HAI16], [SHE06] and flux linkage functions [CHE17] [CHE19] [SUN18]. The latter two methods rely on high sampling frequency ratio, which are not suited in high-speed region. Besides, the ZCP detection of back EMF is easy to implement and requires minimal knowledge of machine parameters. Hence, for high-speed applications, the ZCP detection method is the most popular solution.

In order to improve the commutation accuracy, some non-ideal factors have been investigated, which could be classified into two categories. The first category is related to the internal power angle between the current vector and the back EMF vector. It is reported that this internal power angle is influenced by winding inductance [GUC18], [LEE18a] and non-ideal back EMF [FAN14], [LEE17]. These literatures have shown that by setting appropriate commutation point, the internal power angle can be minimized and the control performance can be improved. The second category refers to the factors that can cause ZCP position errors. The most common reason is the phase delay caused by low-pass filters (LPFs) in the signal process of zero-crossing detection. In [ZHO17] and [LIH17], the method to select suitable LPF cut-off frequency and the phase delay compensation were introduced. Besides, [PAR19] described an issue of unbalanced ZCPs that could be caused by DC-link voltage drop and offset. The unbalanced ZCP detection will lead to current ripple and torque ripple. However, the research of second category is not sufficient at present. Two other potential factors that will lead to ZCP deviation are rarely investigated, i.e. asymmetric machine parameters and the resistance tolerance of back EMF measurement circuit.

The effect of machine parameter asymmetry on sensorless field oriented control (FOC) was widely investigated [REI10], [XUP16]; While for the six-step control, this effect is rarely investigated except in [AHF10]. However, this method can be only used for saliency BLDC motors, and bipolar PWM is required. In practice, many factors will cause machine parameter asymmetry, including cabling, inverter, rough mechanical manufacturing, rotor eccentricity, or winding fault [REI10][XUP16]. Especially for the high-speed BLDC motor with low resistance and inductance, the parameters are very sensitive. Even the asymmetric PCB layout may lead to parameter asymmetry. This effect will have a negative influence on ZCP detection and deteriorate the control performance.

Besides, the resistance tolerance of back EMF measurement circuit is another ZCP deviation cause, which was ignored in most previous literatures. Basically, there are two methods to detect the ZCP. One is based on the voltage comparator [LIU16] [SON18] [CHE07]. In this method, the polar signal of back EMF can be obtained by the voltage comparator. Then, it will trigger the peripheral interrupt of the digital processor for commutation. The other ZCP detection method is PWM synchronization sampling by the analog-to-digital converter (ADC) [DAR15] [LAI08] [LAI11] [SHA06]. The back EMF signal on the floating phase is sampled once or more during each PWM period. Then the ZCP detection is implemented in algorithm. No matter which scheme is selected, the resistive voltage divider (RVD) is usually employed as the back EMF transducer for its simplicity and low cost. When considering the resistance tolerance, the resistance ratio will deviate from its nominal value due to temperature rise and aging effect. Especially for those applications in which the motor and drive boards are integrated within a compact space, the temperature will change dramatically during operation. The resistance ratio shift will cause ZCP deviation and further decrease the commutation accuracy, which will be demonstrated in the chapter.

In brief, the asymmetric machine parameters and the resistance tolerance of back EMF measurement circuit will lead to ZCP deviation and further deteriorate the drive performance. Moreover, the parameters of the machine and the measurement circuit are not constant. For every single motor and drive, the parameters may initially be different

and may also change during operation. Therefore, a commutation correction method that is parameter independent is expected. In this chapter, an adaptive threshold correction scheme for ZCP deviation is proposed. Firstly, the theoretical analyses of asymmetric machine parameters and the resistance tolerance are illustrated. It demonstrates that these two non-ideal factors decrease the commutation accuracy and deteriorate the control performance. Then, in order to suppress the commutation errors, an adaptive threshold correction strategy, including horizontal and vertical corrections, is proposed for eliminating the influence of these two non-ideal factors, respectively. Finally, the theoretical analysis and the proposed correction method are verified by experiments on a high-speed brushless DC drive platform.

The study in this chapter has been published in

L. Yang, Z. Q. Zhu, B. Shuang and H. Bin, "Adaptive threshold correction strategy for sensorless high-speed brushless DC drives considering zero-crossing-point deviation," *IEEE Trans. Ind. Electron.*, vol. 67, no. 7, pp. 5246-5257, Jul. 2020.

3.2 Horizontal Deviation Caused by Machine Parameter Asymmetry

3.2.1 BLDC Machine Model

The drive topology of high-speed motor is shown in Fig. 3.1 (a). The BLDC motor can be modelled as

$$\begin{cases} v_{\mathrm{AG}} - v_{\mathrm{NG}} = R_{\mathrm{A}} i_{\mathrm{A}} + L_{\mathrm{A}} \frac{d}{dt} i_{\mathrm{A}} + e_{\mathrm{A}} \\ v_{\mathrm{BG}} - v_{\mathrm{NG}} = R_{\mathrm{B}} i_{\mathrm{B}} + L_{\mathrm{B}} \frac{d}{dt} i_{\mathrm{B}} + e_{\mathrm{B}} \\ v_{\mathrm{CG}} - v_{\mathrm{NG}} = R_{\mathrm{C}} i_{\mathrm{C}} + L_{C} \frac{d}{dt} i_{\mathrm{C}} + e_{\mathrm{C}} \end{cases} \tag{3.1}$$

where v_{XG} is the terminal voltage, v_{NG} is the machine neutral voltage, i_{X} is the phase current, e_{X} is the phase back EMF, R_{X} is the stator resistance. L_{X} is the stator inductance combining self-inductance L_{X}' and mutual inductance M, i.e. $L_{\mathrm{X}} = L_{\mathrm{X}}' - M$. The subscript "X" denotes phase A, B, or C. Here the resistances and self-inductances in three phases are assumed unbalanced. According to previous documents [GUC18],

high-speed BLDC motors have sinusoidal phase back EMFs as a result of 2-pole diametrically magnetized magnet. Thus, the back EMFs can be expressed as

$$\begin{bmatrix} e_{\mathrm{A}} \\ e_{\mathrm{B}} \\ e_{\mathrm{C}} \end{bmatrix} = \psi_f \omega_e \begin{bmatrix} \sin(\theta_e) \\ \sin(\theta_e - \frac{2}{3}\pi) \\ \sin(\theta_e + \frac{2}{3}\pi) \end{bmatrix} \tag{3.2}$$

where ψ_f , ω_e and θ_e are the flux linkage, electrical speed and rotor position, respectively.

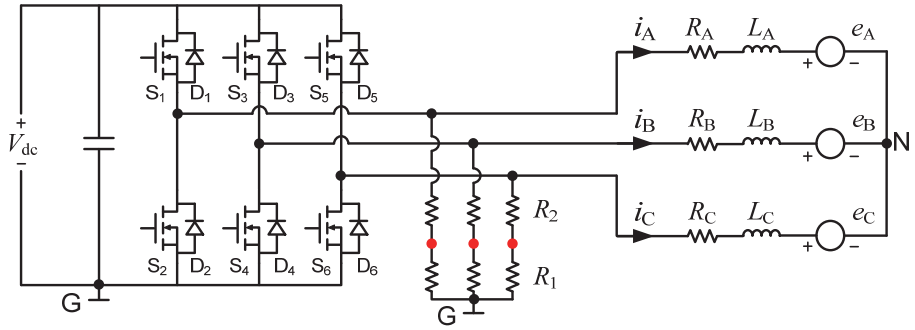

(a) Overall drive circuit

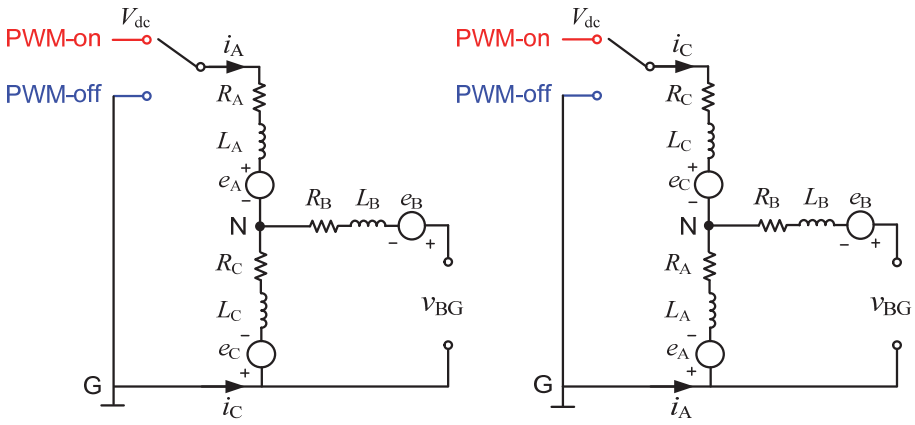

(b) Equivalent circuit in sector II. (c) Equivalent circuit in sector V.

Fig. 3.1. Drive topology of high-speed BLDC motor.

For the six-step commutation scheme, an electrical cycle is divided into six sectors as shown. In each 60º sector, only two of the three phases are energized. The floating phase contains the back EMF information, which can be used for commutation detection. In position sensorless BLDC motor drives, the commutation signal can be obtained by lagging 30º after the ZCP of back EMF.

3.2.2 Horizontal Deviation of EMF Envelopes

In this part, the influence of machine parameter asymmetry on ZCP detection will be analysed. Two opposite sectors, II and V as shown in Fig. 3.1 (b), (c) and Fig. 3.2 are illustrated first and other sectors can be derived.

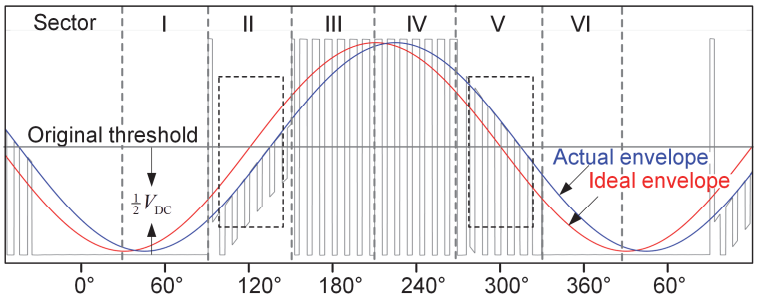

(a) Terminal voltage, ideal & actual envelopes.

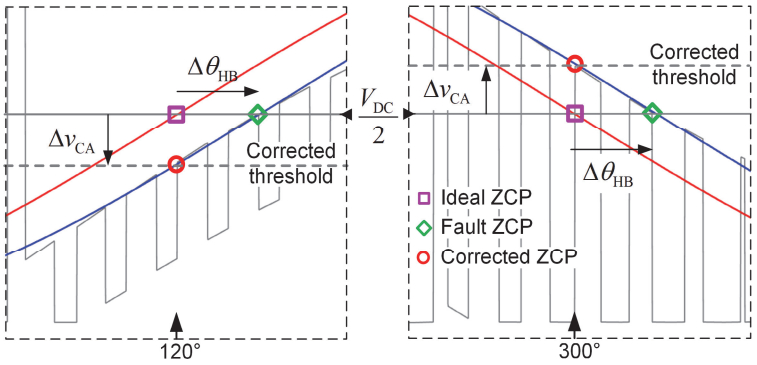

(b) Zoomed window for Sector II. (c) Zoomed window for Sector V.

Fig. 3.2. Schematic diagram of terminal voltage in Phase B considering machine parameter asymmetry.

The BLDC model (3.1) can be transformed into Laplace domain as

$$\begin{cases} V_{AG}(s)-V_{NG}(s)=\left(R_A+sL_A\right)\cdot I_A(s)+E_A(s) \\ V_{BG}(s)-V_{NG}(s)=\left(R_B+sL_B\right)\cdot I_B(s)+E_B(s) \\ V_{CG}(s)-V_{NG}(s)=\left(R_C+sL_C\right)\cdot I_C(s)+E_C(s) \end{cases} \tag{3.3}$$

where s denotes the Laplace operator. In sectors II and V, phases A and C are conducting and phase B is floating, it yields $I_A(s)+I_C(s)=0$ and $I_B(s)=0$. The terminal voltage $V_{BG}(s)$ can be calculated as

$$\begin{aligned} V_{BG}(s) &= V_{NG}(s)+E_B(s) \\ &= \frac{1}{2}\left(V_{AG}(s)+V_{CG}(s)\right)+\frac{3}{2}E_B(s)-\frac{1}{2}\Delta V_H(s) \end{aligned} \tag{3.4}$$

$$\Delta V_{\mathrm{H}}(s)=\left[V_{\mathrm{AG}}(s)-V_{\mathrm{CG}}(s)-\left(E_{\mathrm{A}}(s)-E_{\mathrm{C}}(s)\right)\right]\frac{\Delta R_{\mathrm{AC}}+s\Delta L_{\mathrm{AC}}}{\Sigma R_{\mathrm{AC}}+s\Sigma L_{\mathrm{AC}}} \tag{3.5}$$

where $\Delta V_{\mathrm{H}}(s)$ is related to asymmetric parameters, and $\Delta R_{\mathrm{AC}}=R_{\mathrm{A}}-R_{\mathrm{C}}$, $\Delta L_{\mathrm{AC}}=L_{\mathrm{A}}-L_{\mathrm{C}}$, $\Sigma R_{\mathrm{AC}}=R_{\mathrm{A}}+R_{\mathrm{C}}$, and $\Sigma L_{\mathrm{AC}}=L_{\mathrm{A}}+L_{\mathrm{C}}$. Then, transform $V_{\mathrm{BG}}(s)$ back to time domain, it yields

$$\begin{aligned} v_{\mathrm{BG}}(t) &= \mathcal{L}^{-1}\left[V_{\mathrm{BG}}(s)\right] \\ &= \frac{1}{2}\left(v_{\mathrm{AG}}(t)+v_{\mathrm{CG}}(t)\right)+\frac{3}{2}e_{\mathrm{B}}(t)-\frac{1}{2}\mathcal{L}^{-1}\left[\Delta V_{\mathrm{H}}(s)\right] \end{aligned} \tag{3.6}$$

The additional term $-\frac{1}{2}\mathcal{L}^{-1}\left[\Delta V_{\mathrm{H}}(s)\right]$ is the voltage shift caused by asymmetric parameters. The terminal voltage $v_{\mathrm{BG}}(t)$ will be calculated in sectors II and V, respectively.

A. Terminal Voltage in Sector II

During sector II as shown in Fig. 3.1 (b), phases A and C are energized and phase B is floating. This floating phase B containing the back EMF signal information can be used for commutation detection. Power device S_1 is controlled by chopper signal and S_6 keeps conducting in this sector. The circuit switches between PWM-on and PWM-off states as follows.

PWM-ON: phases A and C are connected to positive and negative DC-link rails through S_1 and S_6, respectively.

PWM-OFF: due to the freewheeling effect, both two phases are connected to the negative DC-link rail with D_2 and S_6.

The back EMF envelope can be extracted by sampling at either PWM-on or PWM-off state [LAI08] [LAI11] [SHA06]. As the motor speed and PWM duty ratio increase, the PWM-on duration increases and the PWM-off duration decreases. To guarantee the detection of ZCP at high-speed region, this proposed method is based on back EMF sampling at PWM-on time. The back EMF is sampled during the PWM-on time, then $v_{\mathrm{AG}}=V_{\mathrm{DC}}$, $v_{\mathrm{CG}}=0$. Then, in order to calculate $\mathcal{L}^{-1}\left[V_{\mathrm{BG}}(s)\right]$, it should obtain every term in (3.5). Around the ZCP instant of sector II, $\theta_e=\omega_e t+2\pi/3$, it yields

$$e_{\mathrm{A}}(t)-e_{\mathrm{C}}(t)=\sqrt{3}\psi_f\omega_e\cos\left(\omega_e t\right) \tag{3.7}$$

Its Laplace transformation is

$$E_{\mathrm{A}}(s)-E_{\mathrm{C}}(s)=\frac{\sqrt{3}\psi_f\omega_e s}{s^2+\omega_e{}^2} \tag{3.8}$$

In PWM-on period of sector II, $v_{\mathrm{AG}}(t)$ is a step of V_{dc} and $v_{\mathrm{CG}}(t)$ is zero, thus $V_{\mathrm{AG}}(s)=\frac{1}{s}V_{\mathrm{dc}}$ and $V_{\mathrm{CG}}(s)=0$. Substitute all these terms into (3.5), then $\Delta V_{\mathrm{H}}(s)$ in sector II can be expressed as

$$\Delta V_{\mathrm{H2}}(s)=\left[\frac{1}{s}V_{\mathrm{dc}}-\frac{\sqrt{3}\psi_f\omega_e s}{s^2+\omega_e{}^2}\right]\frac{\Delta R_{\mathrm{AC}}+s\Delta L_{\mathrm{AC}}}{\Sigma R_{\mathrm{AC}}+s\Sigma L_{\mathrm{AC}}} \tag{3.9}$$

Although the inverse Laplace term $\mathcal{L}^{-1}\left[\Delta V_{\mathrm{H}}(\mathrm{s})\right]$ is difficult to calculate, its initial value can be easily estimated as

$$\begin{aligned}\mathcal{L}^{-1}\left[\Delta V_{\mathrm{H2}}(s)\right]&\approx\lim_{t\to 0}\Delta v_{\mathrm{H2}}(t)=\lim_{s\to\infty}s\cdot\Delta V_{\mathrm{H2}}(s)\\&=\lim_{s\to\infty}s\cdot\left[\frac{1}{s}V_{\mathrm{dc}}-\frac{\sqrt{3}\psi_f\omega_e s}{s^2+\omega_e{}^2}\right]\frac{\Delta R_{\mathrm{AC}}+s\Delta L_{\mathrm{AC}}}{\Sigma R_{\mathrm{AC}}+s\Sigma L_{\mathrm{AC}}}\\&=\left(V_{\mathrm{dc}}-\sqrt{3}\psi_f\omega_e\right)\frac{L_{\mathrm{A}}-L_{\mathrm{C}}}{L_{\mathrm{A}}+L_{\mathrm{C}}}\end{aligned} \tag{3.10}$$

The voltage shift $\Delta v_{\mathrm{H2}}(t)$ in sector II will stay around the initial value in short duration within a PWM period, since this short duration is much less than the fundamental period of motor drive $2\pi/\omega_e$ and the RL time constant L/R.

Then, by substituting (3.10) into (3.6), the terminal voltage envelope of floating phase $v_{\mathrm{BG}}(t)$ in sector II can be expressed as

$$v_{\mathrm{BG}}(t)=\frac{1}{2}V_{\mathrm{dc}}+\frac{3}{2}e_{\mathrm{B}}(t)+\Delta v_{\mathrm{AC}} \tag{3.11}$$

where the voltage shift Δv_{AC} is

$$\Delta v_{\mathrm{AC}}=-\frac{1}{2}\left(V_{\mathrm{dc}}-\sqrt{3}\psi_f\omega_e\right)\frac{L_{\mathrm{A}}-L_{\mathrm{C}}}{L_{\mathrm{A}}+L_{\mathrm{C}}} \tag{3.12}$$

As shown in Fig. 3.2 (b), with symmetrical parameters, the DC offset of terminal voltage envelope is $\frac{1}{2}V_{\mathrm{dc}}$. However, when the machine parameter asymmetry is taken into account, the additional term Δv_{AC} moves the terminal voltage envelope as shown in Fig. 3.2 (b). If $\frac{1}{2}V_{\mathrm{dc}}$ is still selected as the zero crossing threshold, an angle error will be definitely caused.

B. Terminal Voltage in Sector V

Opposite to sector II, as shown in Fig. 3.1 (c), S_5 is controlled by chopper signal and S_2 keeps conducting in sector V. The circuit switches between PWM-on and PWM-off states as follows.

PWM-ON: phases A and C are connected to negative and positive DC-link rails through S_2 and S_5, respectively.

PWM-OFF: due to the freewheeling effect, both two phases are connected to the negative DC-link rail with S_2 and D_6.

During PWM-on period, $v_{\mathrm{AG}}=0$, $v_{\mathrm{CG}}=V_{\mathrm{dc}}$. Around the ZCP instant of sector V, it yields $\theta_e=\omega_e t+5\pi/3$. Besides, $v_{\mathrm{AG}}(t)$ is zero and $v_{\mathrm{CG}}(t)$ is a step of V_{dc}, thus $V_{\mathrm{AG}}(s)=0$ and $V_{\mathrm{CG}}(s)=\frac{1}{s}V_{\mathrm{dc}}$. Then, it yields

$$\Delta V_{\mathrm{H5}}(s)=\left[-\frac{1}{s}V_{\mathrm{dc}}+\frac{\sqrt{3}\psi_f\omega_e s}{s^2+{\omega_e}^2}\right]\frac{\Delta R_{\mathrm{AC}}+s\Delta L_{\mathrm{AC}}}{\Sigma R_{\mathrm{AC}}+s\Sigma L_{\mathrm{AC}}} \tag{3.13}$$

Its initial value can be calculated as

$$\begin{aligned}\mathcal{L}^{-1}\left[\Delta V_{\mathrm{H5}}(s)\right]&\approx\lim_{t\to 0}\Delta v_{\mathrm{H5}}(t)=\lim_{s\to\infty}s\cdot\Delta V_{\mathrm{H5}}(\mathrm{s})\\&=\left(-V_{\mathrm{DC}}+\sqrt{3}\psi_f\omega_e\right)\frac{L_{\mathrm{A}}-L_{\mathrm{C}}}{L_{\mathrm{A}}+L_{\mathrm{C}}}\\&=\left(V_{\mathrm{DC}}-\sqrt{3}\psi_f\omega_e\right)\frac{L_{\mathrm{C}}-L_{\mathrm{A}}}{L_{\mathrm{C}}+L_{\mathrm{A}}}\end{aligned} \tag{3.14}$$

Then, the terminal voltage envelope of floating phase $v_{\mathrm{BG}}(t)$ in sector V can be expressed as

$$v_{\mathrm{BG}}(t)=\frac{1}{2}V_{\mathrm{dc}}+\frac{3}{2}e_{\mathrm{B}}(t)+\Delta v_{\mathrm{CA}} \tag{3.15}$$

where the voltage shift Δv_{CA} is

$$\Delta v_{\mathrm{CA}}=-\frac{1}{2}\left(V_{\mathrm{dc}}-\sqrt{3}\psi_f\omega_e\right)\frac{L_{\mathrm{C}}-L_{\mathrm{A}}}{L_{\mathrm{C}}+L_{\mathrm{A}}} \tag{3.16}$$

It is shown in Fig. 3.2 (c), the terminal voltage envelope moves by Δv_{CA}. From (3.11) and (3.15), it can be found the voltage errors Δv_{AC} and Δv_{CA} exist in the terminal voltage of the floating phase during sectors II and V, respectively. Besides, it yields $\Delta v_{\mathrm{AC}}+\Delta v_{\mathrm{CA}}=0$, since the motor speed will not change dramatically in steady state operation.

3.2.3 Influence of Machine Parameter Asymmetry on ZCP Detection

The terminal voltage envelopes in sectors II and V have been analysed. The results of other sectors can also be obtained in the similar way. Table 3.1 summaries voltage shifts, position errors and the back EMF direction of floating phase, i.e. rising or falling. The symbols "+", "-" and "~" denote the positive driven, negative driven and floating phases. We define the voltage shift caused by parameter asymmetry as

$$\Delta v_{\mathrm{XY}}=-\frac{1}{2}\left(V_{\mathrm{DC}}-\sqrt{3}\psi_f\omega_e\right)\cdot\frac{L_{\mathrm{X}}-L_{\mathrm{Y}}}{L_{\mathrm{X}}+L_{\mathrm{Y}}}. \tag{3.17}$$

Table 3.1 Terminal Voltage Envelope Shifts and ZCP Position Errors

Sector	Mode	EMF (F/R)	Δv_{H}	Δv_{V}	$\Delta\theta$
I	A+B-C~	F	Δv_{AB}	Δv_{VC}	$\Delta\theta_{\mathrm{HC}}+\Delta\theta_{\mathrm{VC}}$
II	A+B~C-	R	$-\Delta v_{\mathrm{CA}}$	Δv_{VB}	$\Delta\theta_{\mathrm{HB}}-\Delta\theta_{\mathrm{VB}}$
III	A~B+C-	F	Δv_{BC}	Δv_{VA}	$\Delta\theta_{\mathrm{HA}}+\Delta\theta_{\mathrm{VA}}$
IV	A-B+C~	R	$-\Delta v_{\mathrm{AB}}$	Δv_{VC}	$\Delta\theta_{\mathrm{HC}}-\Delta\theta_{\mathrm{VC}}$
V	A-B~C+	F	Δv_{CA}	Δv_{VB}	$\Delta\theta_{\mathrm{HB}}+\Delta\theta_{\mathrm{VB}}$
VI	A~B-C+	R	$-\Delta v_{\mathrm{BC}}$	Δv_{VA}	$\Delta\theta_{\mathrm{HA}}-\Delta\theta_{\mathrm{VA}}$

From the above analysis, asymmetric machine parameters result in the movement of the terminal voltage envelope in the floating phase. As shown in Fig. 3.2, the envelope moves down by Δv_{CA} in sector II and moves up by Δv_{CA} in sector V. In the vertical direction, the envelope moves oppositely in sectors II and V. From another point of view, both the vertical movements in sectors II and V can be unified into a horizontal movement of $\Delta\theta_{\mathrm{HB}}$. Hence, influenced by the machine parameter asymmetry, the terminal voltage envelopes move horizontally, leading to ZCP deviations.

The envelope around each ZCP can be regarded as a straight line with a slope of $\frac{3}{2}\psi_f\omega_e$. The voltage shifts have linear relationship with ZCP angle errors as

$$\left[\Delta v_{\mathrm{AB}}\ \Delta v_{\mathrm{BC}}\ \Delta v_{\mathrm{CA}}\right]=\frac{3}{2}\psi_f\omega_e\cdot\left[\Delta\theta_{\mathrm{HC}}\ \Delta\theta_{\mathrm{HA}}\ \Delta\theta_{\mathrm{HB}}\right] \tag{3.18}$$

As shown in Table 3.1, it should be noted that Δv_{AB}, Δv_{BC} and Δv_{CA} denote the voltage errors for sectors I, III and V, and are opposite to the voltage errors in sectors II, IV and VI. Besides, as shown in (3.17), the sign of the voltage error depends on the relation of L_{X} and L_{Y}. According to (3.18), it will further determine the sign of the angle error (lag error is defined positive and lead error is defined negative). The sum of three voltage shifts can be calculated as

$$\begin{aligned}
&\Delta v_{\mathrm{AB}}+\Delta v_{\mathrm{BC}}+\Delta v_{\mathrm{CA}}\\
&=-\frac{1}{2}\left(V_{\mathrm{dc}}-\sqrt{3}\psi_f\omega_e\right)\left(\frac{L_{\mathrm{A}}-L_{\mathrm{B}}}{L_{\mathrm{A}}+L_{\mathrm{B}}}+\frac{L_{\mathrm{B}}-L_{\mathrm{C}}}{L_{\mathrm{B}}+L_{\mathrm{C}}}+\frac{L_{\mathrm{C}}-L_{\mathrm{A}}}{L_{\mathrm{C}}+L_{\mathrm{A}}}\right)\\
&=\frac{1}{2}\left(V_{\mathrm{dc}}-\sqrt{3}\psi_f\omega_e\right)\cdot\underbrace{\frac{L_{\mathrm{A}}-L_{\mathrm{B}}}{L_{\mathrm{A}}+L_{\mathrm{B}}}}_{\Delta L_{\mathrm{AB}}}\cdot\underbrace{\frac{L_{\mathrm{B}}-L_{\mathrm{C}}}{L_{\mathrm{B}}+L_{\mathrm{C}}}}_{\Delta L_{\mathrm{BC}}}\cdot\underbrace{\frac{L_{\mathrm{C}}-L_{\mathrm{A}}}{L_{\mathrm{C}}+L_{\mathrm{A}}}}_{\Delta L_{\mathrm{CA}}}
\end{aligned} \tag{3.19}$$

It should be noted that three inductance related terms, ΔL_{AB}, ΔL_{BC} and ΔL_{CA} are all very small. Then, their product is actually close to zero. Thus, (3.19) can be written as

$$\Delta v_{\mathrm{AB}}+\Delta v_{\mathrm{BC}}+\Delta v_{\mathrm{CA}}\approx 0\,. \tag{3.20}$$

Additionally, due to the linear relation of (3.18), the sum of three ZCP angle errors is also approximately zero.

$$\Delta\theta_{\mathrm{HA}} + \Delta\theta_{\mathrm{HB}} + \Delta\theta_{\mathrm{HC}} \approx 0 \tag{3.21}$$

The commutation instant is obtained by lagging 30^{o} after every ZCP. Without an accurate ZCP, the commutation instant will not be identified. Therefore, machine parameter asymmetry has a negative impact on position sensorless BLDC drives.

3.3 Vertical Deviation Caused by Resistance Tolerance of RVD

3.3.1 Resistance Tolerance of Measurement Circuit

The resistance tolerance of measurement circuit is another ZCP deviation cause. The maximum terminal voltage reaches DC-link level. However, the on-chip AD converter can only sample low voltage signal, e.g. 0-3V. Thus, the RVD is usually employed as the transducer for terminal voltage sampling. The resistance precision will definitely effect the commutation accuracy. In this section, the commutation error caused by resistance tolerance is analysed.

As shown in Fig. 3.1, the AD converter samples the terminal voltage signal on the low side resistor of RVD. The scale factor of the resistance can be designed as

$$\frac{R_1}{R_1 + R_2} = \frac{V_{\mathrm{AD}}}{V_{\mathrm{dc}}} \tag{3.22}$$

where V_{AD} denotes the maximum sampling voltage, R_1 and R_2 are the low and high side resistance of RVD, respectively. In practice, the actual resistance has a slight difference from the nominal value. Hence, the equivalent gain K_{R} is

$$K_{\mathrm{R}} = \frac{R_1'}{R_1' + R_2'} \cdot \frac{R_1 + R_2}{R_1} \tag{3.23}$$

where superscript " ' " denotes the value taking resistance tolerance into account. Then, the acquired phase B terminal voltage can be expressed as

$$v_{\mathrm{BG}}' = v_{\mathrm{BG}} \cdot K_{\mathrm{R}} = \frac{1}{2} K_{\mathrm{R}} V_{\mathrm{dc}} + \frac{3}{2} K_{\mathrm{R}} e_{\mathrm{B}} \,. \tag{3.24}$$

3.3.2 Voltage Shift and ZCP Angle Errors

As shown here, the original DC offset $\frac{1}{2}V_{\mathrm{dc}}$ is shifted to $\frac{1}{2}K_{\mathrm{R}}V_{\mathrm{dc}}$ due to the resistance tolerance of RVD. The voltage shift can be expressed as

$$\Delta v_{\mathrm{VB}} = \frac{1}{2}\left(K_{\mathrm{R}} - 1\right)V_{\mathrm{dc}}. \tag{3.25}$$

Similar to the analysis method in (3.18), the ZCP angle errors and voltage shifts shown in Table 3.1 have linear relation as

$$\left[\Delta v_{\mathrm{VA}}\ \Delta v_{\mathrm{VB}}\ \Delta v_{\mathrm{VC}}\right] = \frac{3}{2}\psi_f \omega_e \left[\Delta\theta_{\mathrm{VA}}\ \Delta\theta_{\mathrm{VB}}\ \Delta\theta_{\mathrm{VC}}\right] \tag{3.26}$$

Therefore, as the resistance value deviates from nominal one, the voltage error increases. Let us consider an extreme situation, R_1' and R_2' have upper and lower limit values, i.e. $R_1' = \left(1+\sigma\right)R_1$ and $R_2' = \left(1-\sigma\right)R_2$, where σ is the tolerance ratio. Finally, the ZCP angle error can be calculated as

$$\Delta\theta_{\mathrm{VB}} = \frac{1}{\sqrt{3}\omega_{\mathrm{pu}}} \cdot \left(\frac{1+\sigma}{\left(1+\sigma\right)+\left(1-\sigma\right)\left(\frac{V_{\mathrm{dc}}}{V_{\mathrm{AD}}}-1\right)} \cdot \frac{V_{\mathrm{dc}}}{V_{\mathrm{AD}}} - 1 \right) \tag{3.27}$$

where $\omega_{\mathrm{pu}} = \omega_e / \omega_{\mathrm{base}}$ denotes the per-unit value of speed, the base-speed ω_{base} can be defined as $\sqrt{3}\psi_f \omega_{\mathrm{base}} = V_{\mathrm{dc}}$.

Obviously, the voltage acquisition accuracy is limited by the resistance tolerance. The resistance will change with the temperature. Especially for those applications in which the motor and the drive boards are integrated within a compact space, the temperature will change significantly during operation. Besides, as the resistor gets old the resistance will change. For high voltage application, due to voltage limit, more than two resistors are cascaded to reduce the voltage drop on each resistor. This situation is even more complicated. If the parameter design in the software algorithm is just based on the nominal resistance, it will definitely lead to commutation errors.

Fig. 3.3 shows analysis results of the ZCP angle error. Some popular resistance tolerances from 0.1% to 10% are analysed. As we can see, the ZCP angle error

increases as the resistance precision decreases. High precision resistors minimize the tolerance, the temperature shift and aging, which means high commutation accuracy. But the cost will be high, which is the last thing the consumers want, especially in household appliance market.

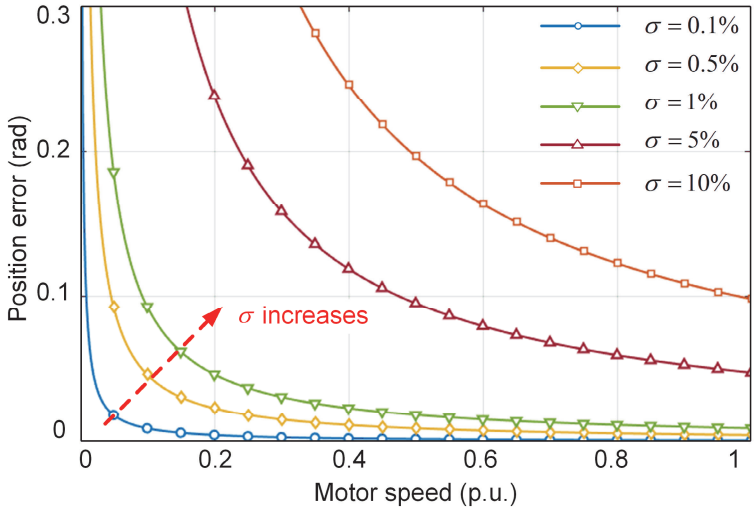

Fig. 3.3. Analysis result of ZCP angle error caused by vertical shift of terminal voltage, V_{AD}=3V, V_{dc}=15V.

3.4 Proposed Adaptive Threshold Correction Algorithm for Envelope Deviation

In this section, an adaptive threshold correction scheme is proposed. Fig. 3.4 illustrates the implementation of the overall scheme. The terminal voltage signals are sampled with RVD by the on-chip ADC. Then an adaptive threshold correction loop is utilized. In this algorithm, six independent zero-crossing thresholds are used for ZCP detection. These six thresholds are adjusted during operation in real time. Two CPU timers are utilized. Timer A is for time interval measurement of ZCPs. Six latest measurement results of ZCP time intervals, denoted as t_{12}…t_{61}, are stored in a buffer. Timer B is used to trigger commutation 30º after each ZCP.

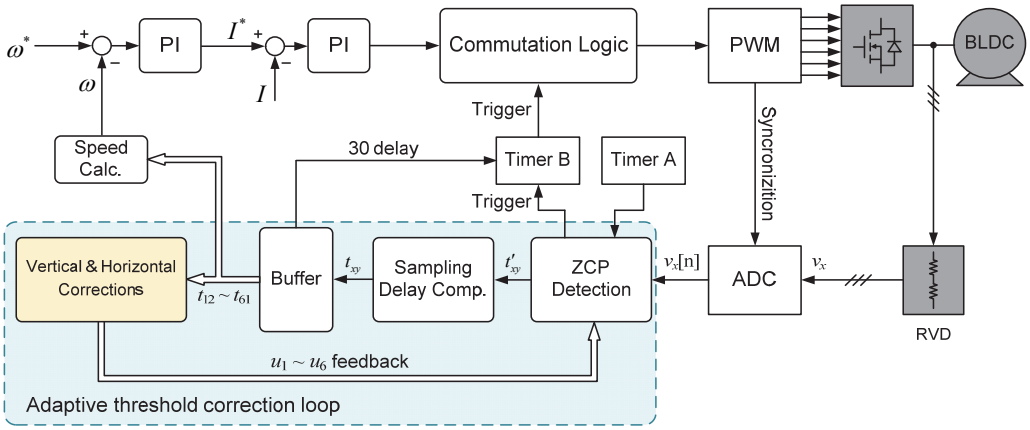

Fig. 3.4. Schematic diagram of sensorless control system with adaptive threshold correction strategy

3.4.1 Vertical Correction

Fig. 3.5 shows the vertical shift of back EMF envelope caused by resistance tolerance of measurement circuit. Fig. 3.6 shows the zoomed area of the triangles in Fig. 3.5. The dashed and solid lines demote the back EMF envelopes before and after shift, respectively. It is assumed that $K_{\mathrm{R}} > 1$ and the back EMF envelope moves upward. Ideally, the phase B ZCPs should locate at the intersection of the phase B envelope e_{B} and the half DC-link voltage $\frac{1}{2}V_{\mathrm{dc}}$, i.e. 120º in sector II and 300º in sector V. However, when the resistance ratio changes, the envelope moves upward by Δv_{VB} to $\hat{e}_{\mathrm{B}}$, and a fault ZCP will be detected with the original threshold $\frac{1}{2}V_{\mathrm{dc}}$.

As shown in Fig. 3.6, the principle of the vertical correction is to superpose a common mode bias u_{VB} to $\frac{1}{2}V_{\mathrm{dc}}$, i.e. $\frac{1}{2}V_{\mathrm{dc}} + u_{\mathrm{VB}}$. This new threshold is adopted for both sectors II and V. The angle error $\varepsilon_{\mathrm{VB}}$ can be extracted in the real time. By controlling $\varepsilon_{\mathrm{VB}}$ to zero, the common mode bias u_{VB} will converge to Δv_{VB}. Then, even if the vertical shift exists, the ZCP will be corrected back to the ideal position, i.e. 120º and 300º.

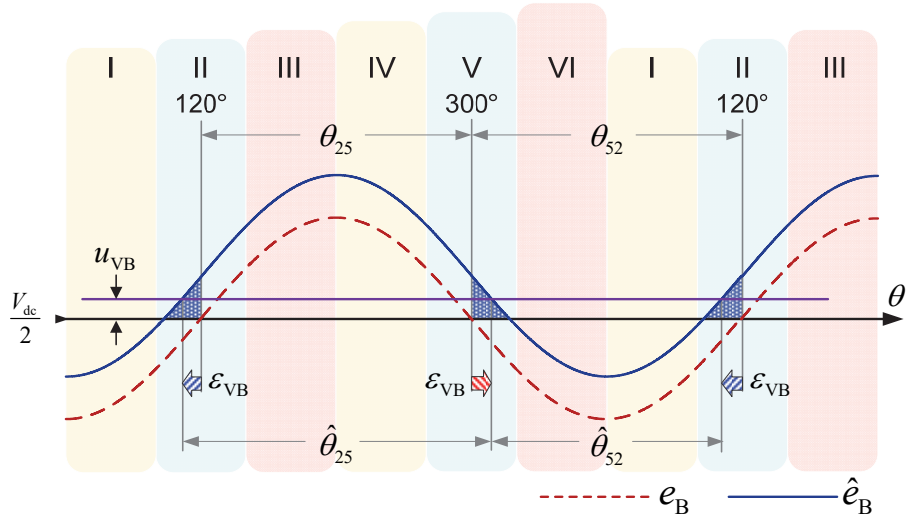

Fig. 3.5. Schematic diagram of vertical deviation of back EMF envelopes caused by resistance tolerance of measurement circuit.

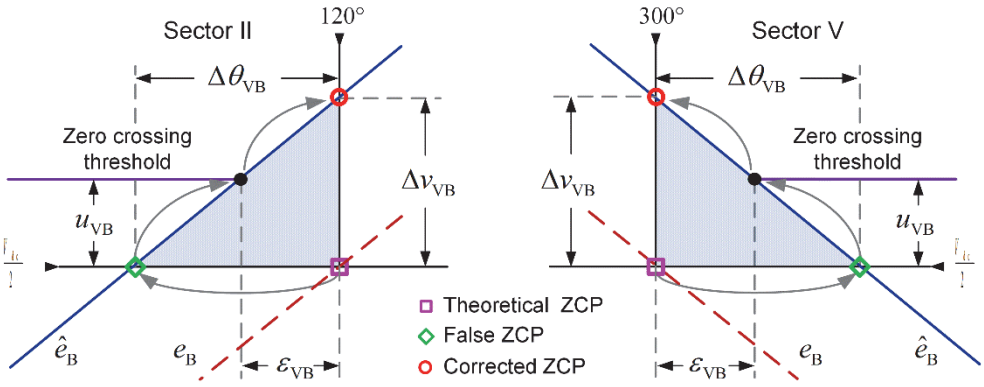

Fig. 3.6. Vertical correction process of zero crossing threshold.

As shown in Fig. 3.5, the phase-ZCP-interval $\hat{\theta}_{25}$ (II to V) and $\hat{\theta}_{52}$ (V to II) can be expressed as

$$\begin{cases} \hat{\theta}_{25} = \theta_{25} + 2\varepsilon_{VB} \\ \hat{\theta}_{52} = \theta_{52} - 2\varepsilon_{VB} \end{cases} \tag{3.28}$$

where the superscript "^" denotes measurement values. It is obvious that $\theta_{25} = \theta_{52} = \pi$ in (3.28), then the angle errors can be deduced as

$$\varepsilon_{VB} = \frac{1}{4}\left(\hat{\theta}_{25} - \hat{\theta}_{52}\right). \tag{3.29}$$

In practice, $\hat{\theta}_{25}$ and $\hat{\theta}_{52}$ can be calculated by the CPU timer

$$\begin{cases} \hat{\theta}_{25} = \dfrac{t_{25}}{t_{\text{period}}} \cdot 2\pi = \dfrac{t_{23} + t_{34} + t_{45}}{t_{\text{period}}} \cdot 2\pi \\ \hat{\theta}_{52} = \dfrac{t_{52}}{t_{\text{period}}} \cdot 2\pi = \dfrac{t_{56} + t_{61} + t_{12}}{t_{\text{period}}} \cdot 2\pi \end{cases} \tag{3.30}$$

where t_{period} is the fundamental period and be expressed as

$$t_{\text{period}} = t_{12} + t_{23} + \ldots + t_{61}. \tag{3.31}$$

Here, the correction process of phase B is taken for instance. The correction for other two phases can also be achieved by the same way, which is shown in Fig. 3.7.

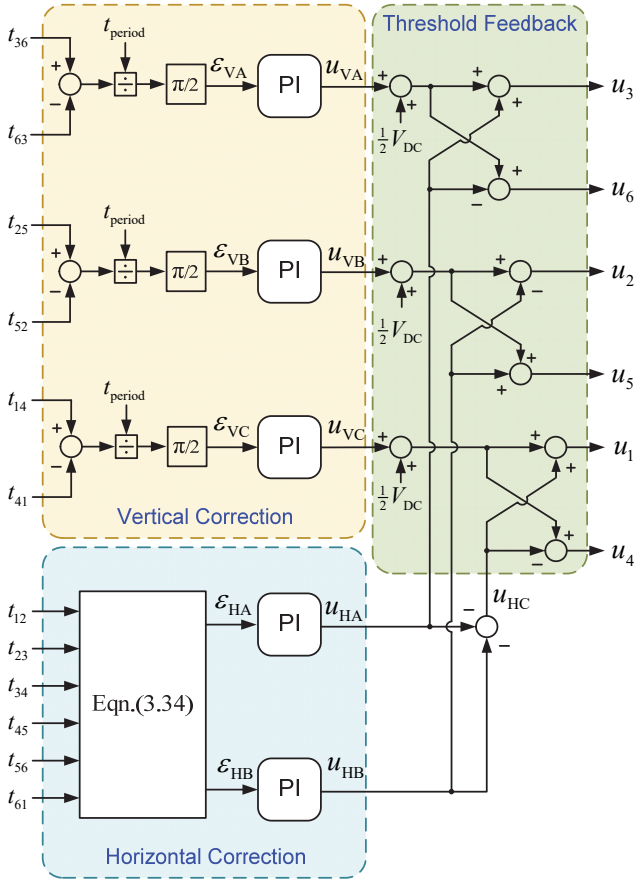

Fig. 3.7. Schematic diagram of adaptive threshold correction including vertical and horizontal corrections.

The main principle is to search for a threshold, with which the upper- and lower-half-cycle have the same time duration. With higher gains, the correction controller can achieve higher convergence speed. Since the ZCP position errors are dependent on the motor speed, it is recommended to tune the correction controller with higher bandwidth than the speed loop controller. In this way, it can guarantee small commutation errors

during the dynamic speed change situation. It should be noted that precise resistance values are not required to be determined in advance during this process. Therefore, no matter how the resistance ratio of RVD changes, the suitable zero crossing threshold can be searched.

3.4.2 Horizontal Correction

Fig. 3.8 shows the horizontal shift of back EMF envelope caused by machine parameter asymmetry. Fig. 3.9 shows the zoomed area of the triangles of phase B in Fig. 3.8. Influenced by asymmetric parameters, the envelope moves downward in sector II and moves upward in sector V, which can be unified into a right movement of $\Delta\theta_{\mathrm{HB}}$. Thus, fault ZCPs will be detected with the original threshold $\frac{1}{2}V_{\mathrm{DC}}$.

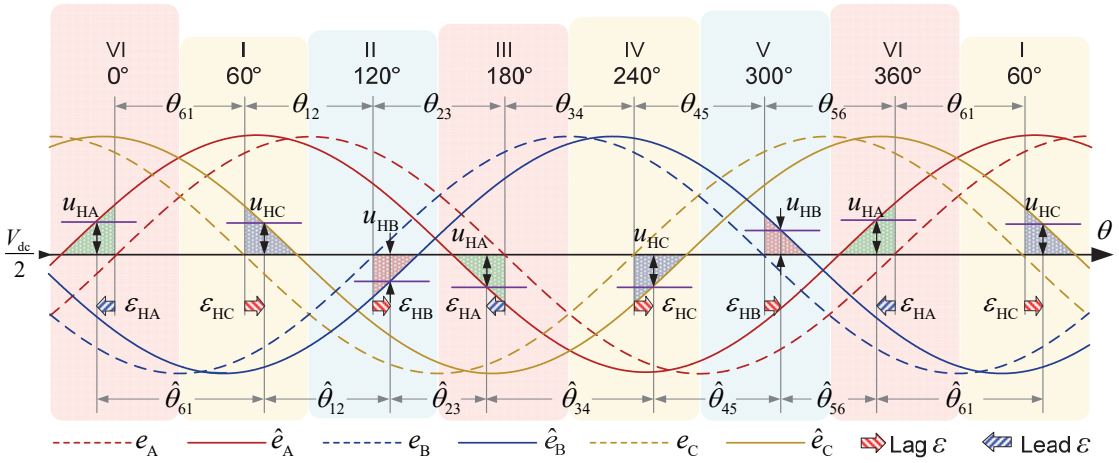

Fig. 3.8. Schematic diagram of horizontal deviation of back EMF envelopes caused by machine parameter asymmetry.

As shown in Fig. 3.9, the horizontal correction process is similar to the vertical correction. The difference is that differential-mode biases are used, which means $\frac{1}{2}V_{\mathrm{dc}}-u_{\mathrm{HB}}$ is used for sector II and $\frac{1}{2}V_{\mathrm{dc}}+u_{\mathrm{HB}}$ is used for sector V as new thresholds. Then, by controlling $\varepsilon_{\mathrm{HB}}$ to zero, the differential- mode bias u_{HB} will converge to Δv_{CA} and the ZCP will be corrected. When considering horizontal correction for all three phases, it should be noted that only two of the three terms u_{HA} and u_{HB} are required and the third one u_{HC} can be calculated directly from $u_{\mathrm{HA}}+u_{\mathrm{HB}}+u_{\mathrm{HC}}=0$ as a result of (3.20).

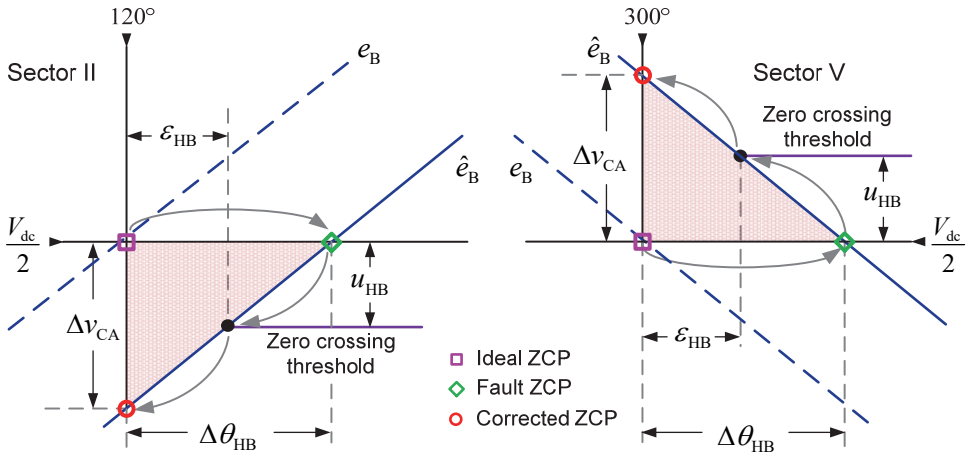

Fig. 3.9. Horizontal correction process of zero crossing threshold.

According to (3.21), the sum of three ZCP angle errors is approximately zero. Hence, there are two advanced phases and one lagged phase or one advanced phase and two lagged phases. In Fig. 3.8, phase A is assumed advanced and other two phases are assumed lagged. The sector-ZCP-intervals $\hat{\theta}_{12} \ldots \hat{\theta}_{61}$ can be modelled as

$$\begin{cases} \hat{\theta}_{12}\left(\hat{\theta}_{45}\right) = \theta_{12}\left(\theta_{45}\right) + \varepsilon_{HB} - \varepsilon_{HC} \\ \hat{\theta}_{23}\left(\hat{\theta}_{56}\right) = \theta_{23}\left(\theta_{56}\right) + \varepsilon_{HA} - \varepsilon_{HB} \\ \hat{\theta}_{34}\left(\hat{\theta}_{61}\right) = \theta_{34}\left(\theta_{61}\right) + \varepsilon_{HC} - \varepsilon_{HA} \end{cases}. \tag{3.32}$$

The term in the bracket indicates they have the same value, for instance $\hat{\theta}_{12} = \hat{\theta}_{45}$. Due to the linear relation, the following equation can be obtained

$$\varepsilon_{HA} + \varepsilon_{HB} + \varepsilon_{HC} = 0 \tag{3.33}$$

Also we have $\theta_{12}=\theta_{23}=\ldots=\theta_{61}=\pi/3$. Now, (3.33) and any two of three equations in (3.32) can be used to solve the equations to obtain the ZCP angle errors, it yields

$$\begin{bmatrix} \varepsilon_{HA} \\ \varepsilon_{HB} \end{bmatrix} = \frac{1}{3}\begin{bmatrix} 1 & 2 & 0 \\ 2 & 0 & 1 \end{bmatrix}\begin{bmatrix} \hat{\theta}_{12}\left(\hat{\theta}_{45}\right) \\ \hat{\theta}_{23}\left(\hat{\theta}_{56}\right) \\ \hat{\theta}_{34}\left(\hat{\theta}_{61}\right) \end{bmatrix} - \frac{\pi}{3}\begin{bmatrix} 1 \\ 1 \end{bmatrix}. \tag{3.34}$$

In practice, all the angle terms can be calculated by time interval signals obtained from the CPU timer as

$$\begin{bmatrix} \varepsilon_{\mathrm{HA}} \\ \varepsilon_{\mathrm{HB}} \end{bmatrix} = \frac{1}{3} \cdot \frac{2\pi}{t_{\mathrm{period}}} \cdot \begin{bmatrix} 1 & 2 & 0 \\ 2 & 0 & 1 \end{bmatrix} \begin{bmatrix} t_{12}\left(t_{45}\right) \\ t_{23}\left(t_{56}\right) \\ t_{34}\left(t_{61}\right) \end{bmatrix} - \frac{\pi}{3} \begin{bmatrix} 1 \\ 1 \end{bmatrix}. \tag{3.35}$$

Here, (3.35) gives the method to extract the angle errors $\varepsilon_{\mathrm{HA}}$ and $\varepsilon_{\mathrm{HB}}$. By controlling these angle errors to zero, differential-mode biases u_{HA}, u_{HB} and u_{HC} will converge to Δv_{BC}, Δv_{AB} and Δv_{CA}, respectively. Then the horizontal deviation caused by asymmetric parameters can be eliminated.

Finally, as shown in Fig. 3.7, three common-mode biases u_{VA}, u_{VB} and u_{VC} can be obtained in the vertical correction; three differential-mode biases u_{HA}, u_{HB} and u_{HC} can be obtained in the horizontal correction. Based on Table 3.1, six zero crossing thresholds can be calculated as

$$\begin{cases} u_3 = \frac{1}{2} V_{\mathrm{dc}} + u_{\mathrm{VA}} + u_{\mathrm{HA}} \\ u_6 = \frac{1}{2} V_{\mathrm{dc}} + u_{\mathrm{VA}} - u_{\mathrm{HA}} \end{cases}, \tag{3.36}$$

$$\begin{cases} u_2 = \frac{1}{2} V_{\mathrm{dc}} + u_{\mathrm{VB}} - u_{\mathrm{HB}} \\ u_5 = \frac{1}{2} V_{\mathrm{dc}} + u_{\mathrm{VB}} + u_{\mathrm{HB}} \end{cases}, \tag{3.37}$$

$$\begin{cases} u_1 = \frac{1}{2} V_{\mathrm{dc}} + u_{\mathrm{VC}} + u_{\mathrm{HC}} \\ u_4 = \frac{1}{2} V_{\mathrm{dc}} + u_{\mathrm{VC}} - u_{\mathrm{HC}} \end{cases}. \tag{3.38}$$

It should be noted that during the whole process, any parameters of the machine or the measurement circuit of back EMF are not required. Besides, the proposed adaptive correction strategy does not rely on a specified back EMF. No matter trapezoidal or sinusoidal back EMFs, the ZCP positions are the same and the mechanism is similar. Accordingly, this scheme has a good adaptive capacity and can overcome the parameter change.

3.5 Experimental Validation

The proposed adaptive threshold correction strategy is verified with the high-speed Motor-II in Appendix 1. The resistance and inductance values are asymmetric as shown in Fig. 3.2. The PWM switching frequency and sampling frequency are both 40 kHz and the DC-link voltage is 15V. In addition, to simulate the resistance tolerance of

RVD, three different resistance ratios are used in three phases as shown in Table 3.3. The equivalent gains K_R are 110%, 100% and 90% in phases A, B and C, respectively. It should be noted that no capacitors are utilized in the back EMF measurement circuits to avoid the phase delay of LPFs.

Table 3.2 Parameters of Motor-II

Parameter	Phase A	Phase B	Phase C
Phase resistance	R_A=38.1mΩ	R_B=37.5mΩ	R_C=43.5mΩ
Phase self-inductance	L_A=27.5μH	L_B=27.2μH	L_C=28.6μH
Mutual inductance		4μH	

Table 3.3 Resistances of RVD in Three Phases

Phase	R1	R2	Resistance ratio	K_R
A	3.24 kΩ	11.5 kΩ	0.22	110%
B	3 kΩ	12 kΩ	0.2	100%
C	2.8 kΩ	12.7 kΩ	0.18	90%

Fig. 3.10 shows the comparison results with and without the proposed adaptive threshold correction scheme at 20000 r/min. From top to bottom, the estimated sector number, sector-ZCP-interval, estimated commutation instants and three phase currents are given, respectively. The period is 3 ms and thus the motor commutes twice in each millisecond. It is convenient to judge the commutation accuracy through observing the estimated commutation instant signal in the grids. Without correction as shown in Fig. 3.10 (a), the sector-ZCP-interval ($\hat{\theta}_{12} \ldots \hat{\theta}_{61}$) varies from 50º to 75º. Due to the machine parameter asymmetry and the resistance tolerance of RVD, the sector-ZCP-interval cannot remain at 60º, but fluctuates within a wide range. Also, it is obvious that the commutation instants occur with inconsistent intervals. In this case the current fluctuates drastically, the peak-peak value reaches 7.44A.

When vertical correction is enabled in Fig. 3.10 (b), the sector-ZCP-interval ($\hat{\theta}_{12} \ldots \hat{\theta}_{61}$) becomes closer to 60º, range from 55º to 65º. The commutation is still executed with inconsistent intervals, as the commutation instant signal is not aligned with the grids. The fluctuation can be observed in three phase currents, with the peak-peak value 6.52A. The vertical shift effect caused by the tolerance of RVD has been eliminated, so the remaining inconsistence is mainly caused by machine parameter asymmetry.

When both vertical and horizontal corrections are enabled in Fig. 3.10 (c), the sector-ZCP-interval ($\hat{\theta}_{12} \ldots \hat{\theta}_{61}$) converges to 60º. The motor commutes with consistent intervals and the commutation instant signal is aligned with the grids. The phase currents maintain almost identical in each sector. The current peak-peak value is 6.02A, reduced by 19% compared to Fig. 3.10 (a). Accordingly, both the vertical and horizontal envelope shift effects are eliminated with the proposed correction method.

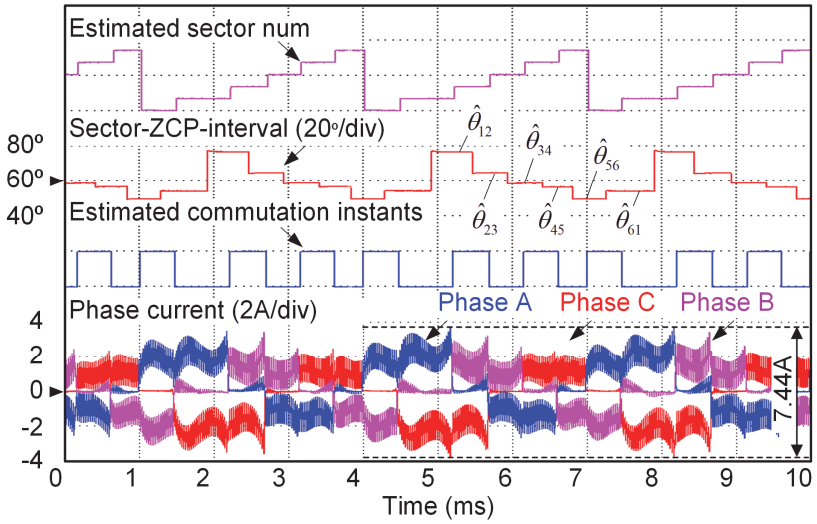

(a) without correction

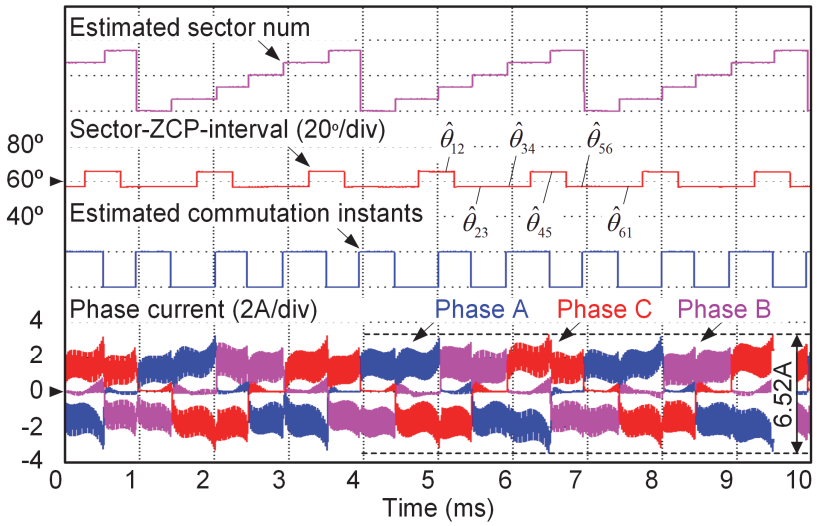

(b) with only vertical correction

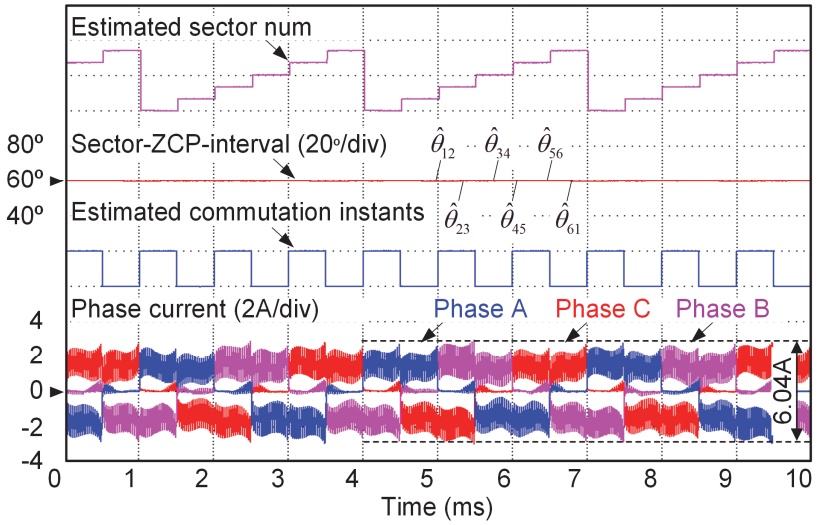

(c) with both vertical and horizontal corrections.

Fig. 3.10. Comparison results with and without the proposed adaptive threshold correction scheme at 20000 r/min (333Hz).

Fig. 3.11 shows the comparison results with and without the proposed adaptive threshold correction strategy at 54000 r/min (900Hz). The PWM duty reaches 100% and thus it is the maximum speed. Without correction as shown in Fig. 3.11 (a), the sector-ZCP-interval cannot stay at 60º. The currents fluctuate with peak-peak value 26.2A. With only vertical correction enabled in Fig. 3.11 (b), the sector-ZCP-interval becomes closer to 60º, but still cannot remain at 60º. When both vertical and horizontal corrections are enabled in Fig. 3.11 (c), the sector-ZCP-interval converges to 60º. Three phase currents maintain almost identical and the phase current peak-peak value is reduced to 22.2A. Therefore, the proposed adaptive threshold correction scheme is effective at rated speed.

Fig. 3.12 shows the convergence process of the zero crossing thresholds at 18000 r/min. From top to bottom, the sector-ZCP-interval ($\hat{\theta}_{12} \ldots \hat{\theta}_{61}$), phase-ZCP-interval ($\hat{\theta}_{63} \ldots \hat{\theta}_{41}$) and the zero crossing thresholds for each corresponding phase are presented. The vertical correction is enabled at 2 s. Then the phase-ZCP-interval gradually converges to 180º. As can be seen here, although the three phase-ZCP-intervals are all corrected to 180º, the sector-ZCP-interval still deviates from 60º. The vertical shift caused by RVD tolerance is eliminated. The remaining deviation is caused by the machine parameter asymmetry. For phases A and C, the zero crossing thresholds converges to 0.55 pu and 0.45 pu, respectively, which are in accord with their corresponding resistance ratio of RVD. At 6 s, the horizontal correction is enabled. Then the sector-ZCP-interval converges to 60º by adjusting the six zero crossing thresholds. Finally, with the vertical and horizontal corrections enabled, each phase-ZCP-interval converges to 180º and sector-ZCP-interval converges to 60º. The results verify that the proposed strategy has a strong adaptive capacity for parameter change, reflecting its engineering application value.

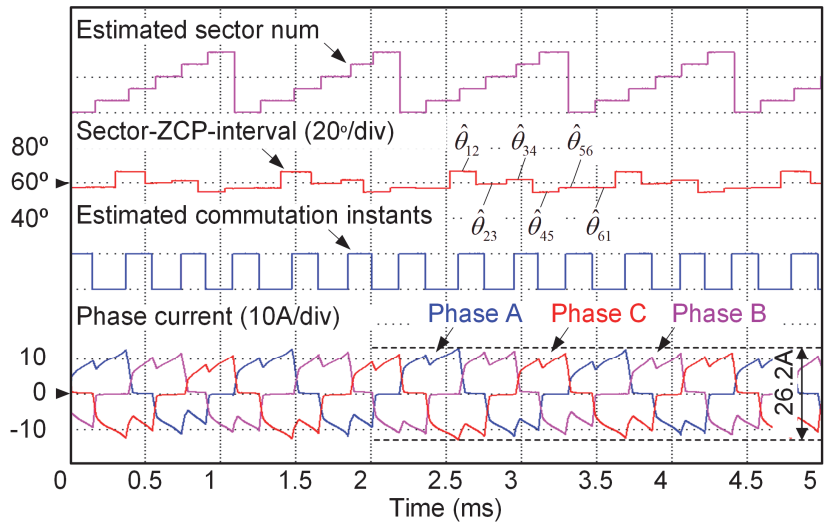

(a) without correction

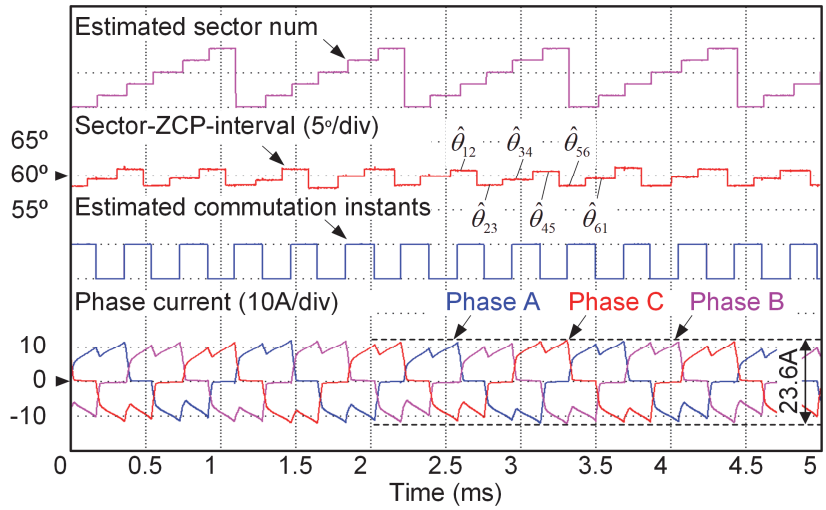

(b) with only vertical correction

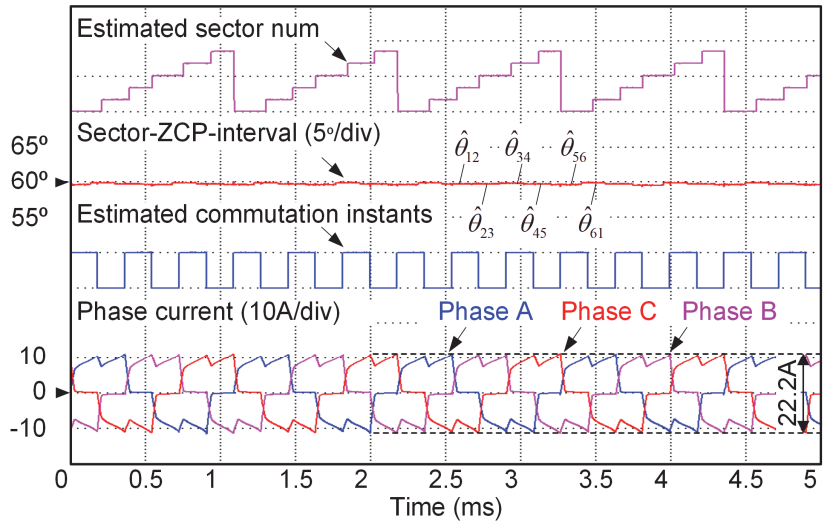

(c) with both vertical and horizontal corrections.

Fig. 3.11. Comparison results with and without the proposed adaptive threshold correction scheme at 54000 r/min (900Hz).

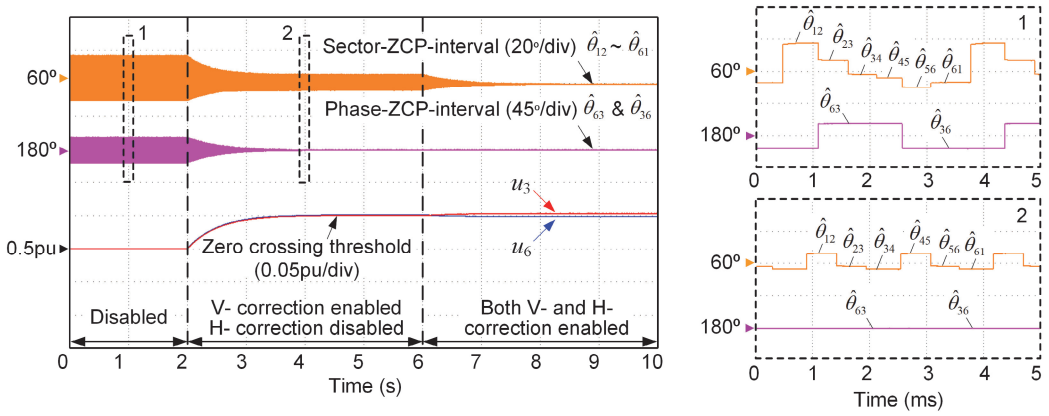

(a) Convergence process of phase A.

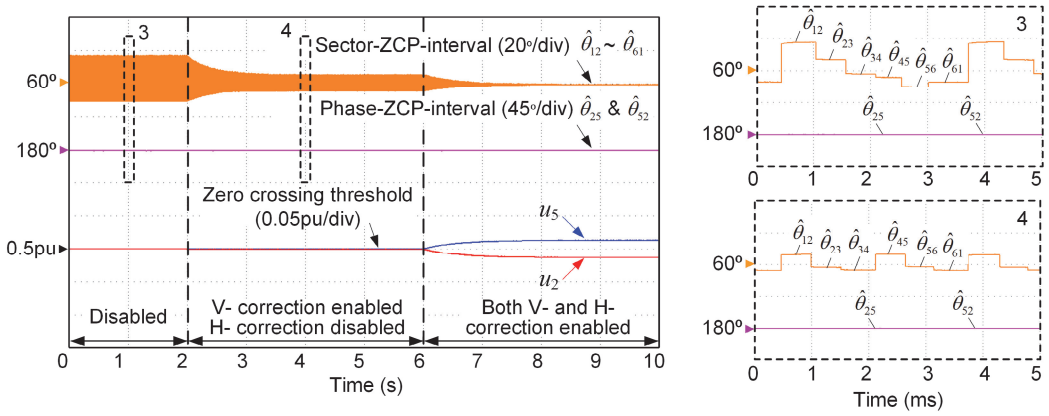

(b) Convergence process of phase B

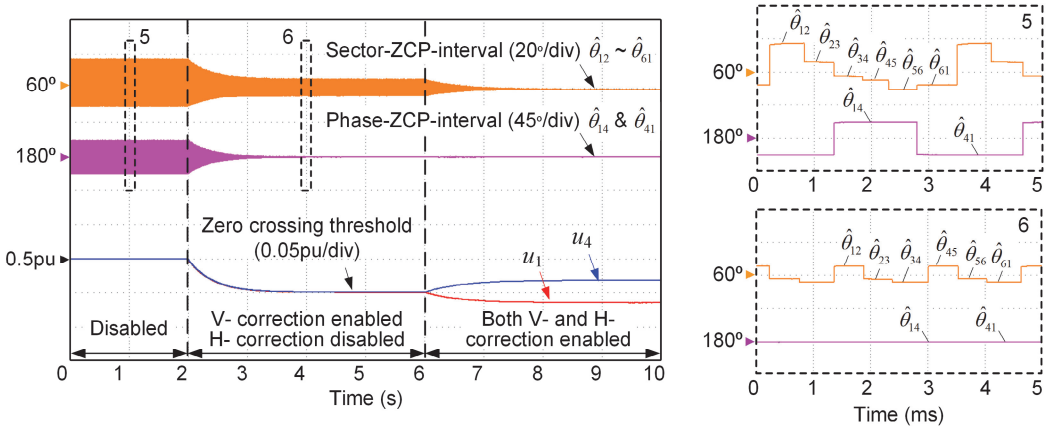

(c) Convergence process of phase C.

Fig. 3.12. Convergence process of zero crossing thresholds.

Fig. 3.13 shows the sensorless operation at acceleration and deceleration processes. The motor accelerates from 18000 r/min to 54000 r/min within only 3 s, and then decelerates back to 18000 r/min with the same slope. When no correction is utilized in Fig. 3.13 (a), the sector-ZCP-interval fluctuates from 50º to 75º at 18000 r/min. In the zoomed window, it is obvious that the speed begins to oscillate and the phase currents fluctuate drastically. It eventually triggers over-current protection and fails during

acceleration. With only vertical correction enabled in Fig. 3.13 (b), the sector-ZCP-interval fluctuation range is 53º-66º at 18000 r/min, then shrinks to 57º-62º at 54000 r/min. Finally, when both vertical and horizontal corrections are enabled in Fig. 3.13 (c), the fluctuation range maintains in 59º-61º during the whole operation. It can be seen that with the proposed adaptive threshold correction technique, the sector-ZCP-interval can be accurately kept at 60º in a wide speed range.

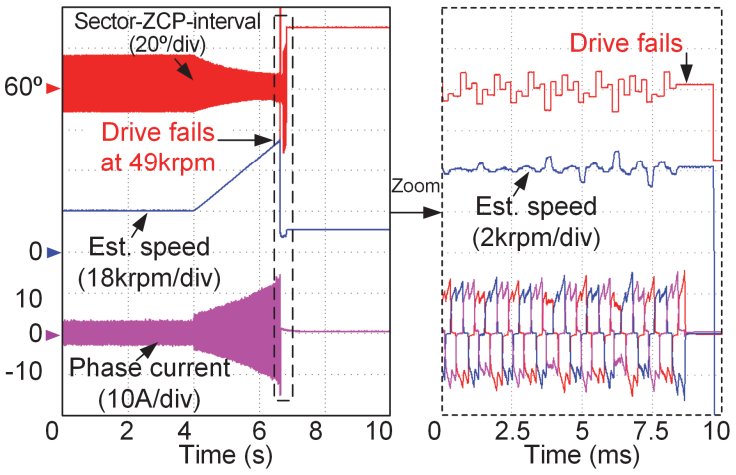

(a) without correction

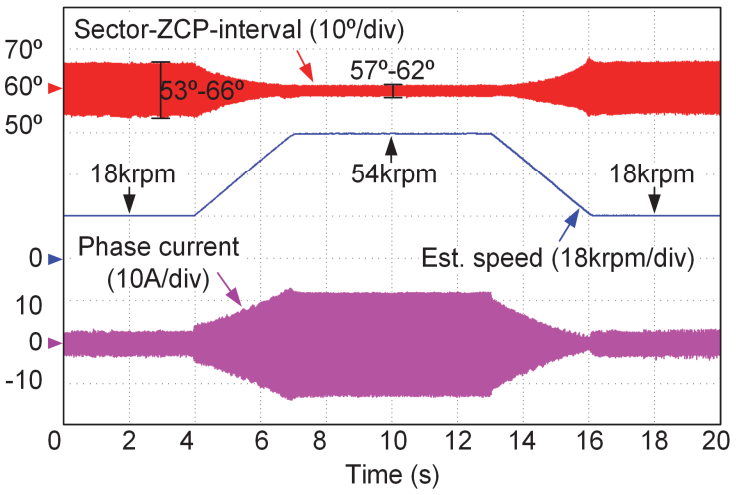

(b) with only vertical correction.

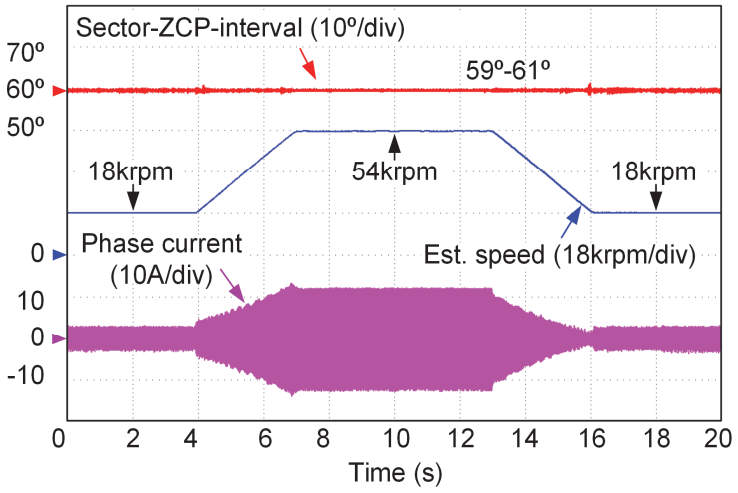

(c) with both vertical and horizontal corrections

Fig. 3.13. Experimental comparison of sector ZCP angle interval at acceleration and deceleration processes

3.6 Summary

This chapter has investigated the influence of asymmetric machine parameters and the resistance tolerance of back EMF measurement circuit on ZCP detection based sensorless control of high-speed BLDC motor. First, these two non-ideal factors are analysed theoretically. It shows that when machine parameters are asymmetric, the back EMF envelope will deviate horizontally, whilst, inaccurate back EMF sampling caused by the resistance tolerance of measurement circuit will cause vertical deviation of envelopes. These two non-ideal factors will lead to commutation errors and deteriorate the control performance. Based on the theoretical analysis, an adaptive threshold correction strategy has been proposed to suppress the commutation errors. Besides, this strategy does not rely on the parameters of the machine or measurement circuits, which makes it suitable for batch production. Experimental results demonstrate that the proposed method can eliminate the commutation errors caused by the two non-ideal factors, and improve the performance of the sensorless high-speed BLDC drive.

The method in Chapter 3 is a closed-loop correction for terminal voltage; and the one in Chapter 2 is an open-loop correction for virtual third harmonic. This closed-loop correction has better compatibility and can also be applied to the virtual third harmonic.

CHAPTER 4

Safe Operating Area of Zero-Crossing Detection Based Sensorless High-Speed BLDC Motor Drives

4.1 Introduction

Among various sensorless BLDC drive methods, the most popular one is based on the detection of zero-crossing point (ZCP) of back EMF. In each 60º sector, two of the three phases are conducted and the third one is floating, whose back EMF is exposed and can be measured. This technique can be implemented on terminal voltage [TSO15] [SHA06], line-line voltage [CHE07] [CHU14] and third harmonic voltage [SON18] [CUI15]. However, influenced by winding inductances and limited DC-link voltage, the current of the outgoing phase cannot vanish to zero immediately after commutation, but flow through the freewheeling diode. The floating phase will be clamped to the DC-link temporarily and thereby it will prevent the detection of the ZCPs of the back EMF. Long freewheeling duration increases the difficulty of zero-crossing detection. In the extreme situation of high-speed and high load operation, the freewheeling angle perhaps exceeds 30 electrical degrees (°). In this circumstance, the ZCP will be overridden and the sensorless drive will fail. It is generally supposed that the freewheeling angle increases with the motor speed and load torque [ZHO19] [SHE04]. Thus, for zero-crossing detection based sensorless drives, the safe operating area (SOA) can be defined as the available torque and speed areas in which the freewheeling angle is within 30º.

The freewheeling angle is complicated to analyse since it is related to many factors. This issue was firstly documented in [ZHU01], which investigated the influences of motor electromagnetic and mechanical parameters on the freewheeling angle. It demonstrated proper stator flux density and stator core axial length-to-diameter can minimize the freewheeling angle. The literature [HAN08] investigated the influence of phase resistance and inductance on the freewheeling angle, and pointed out that lower

electrical time constant can facilitate the freewheeling process. In [XUY16], the influence of DC-link voltage on freewheeling angle was studied. It proposed a double DC-link inverter topology to increase the DC-link voltage and accelerate the freewheeling process. Similarly, in [CHE17c][LIX16][JIA18], DC-DC converters were inserted between the DC-link side and the inverter. In this way, the input voltage can be adjustable and current freewheeling processes can be facilitated. In [LIW16][LIH17], the freewheeling duration for unmodulated six-step control was studied. It described the influence of motor speed and initial current on freewheeling duration. In [SHI17] [PAR20][ACH20], the relation between the current freewheeling slope and the PWM duty ratio was analysed. Through selecting suitable PWM duty ratio, the freewheeling duration can be adjusted. To summarize, the factors including electromagnetic and mechanical parameters [ZHU01], electrical time constant [HAN08], DC-link voltage [XUY16][CHE17c][LIX16][JIA18], motor speed and current [LIW16][LIH17], PWM duty ratio [SHI17][PAR20][ACH20], have been modelled well. However, it is found that the PWM switching patterns also have significant influences on the freewheeling angle issue, but are neglected in most previous literature. In this chapter, the analysis of PWM switching patterns on freewheeling angle is carried out.

Up to now, various PWM switching patterns have been proposed for BLDC drives. According to the combination sequence of PWM and constant ON signals, they can be defined as H-PWM-L-ON, H-ON-L-PWM, PWM-ON and ON-PWM [LIU19a] [LEE19][LAI08a][LAI08b] (Definition of these patterns will be illustrated in Section 4.2). These documents have investigated these four patterns in terms of some characteristics, including torque ripple [LIU19a][LEE19], reversal DC-link current and circulating current [LAI08a], and sensorless implementation [LAI08b]. However, the freewheeling angle is rarely studied, which is the motivation of this chapter. Actually, the freewheeling angle is a critical issue in high-speed BLDC drives. As above mentioned, it directly determines the SOA of zero-crossing detection based sensorless methods. Especially for those high-speed drives for portable home appliances, low voltage batteries are usually employed as the power. In this situation of low DC-link voltage, the phenomenon of long freewheeling angle becomes a serious and common problem, which restricts the sensorless SOA. In this chapter, it is found that the PWM

patterns have a big influence on the freewheeling angle. Thus, through analytical methods, the mechanism that how different PWM techniques affect the freewheeling angle is investigated.

In summary, in terms of the SOA issue, two concerns are worth exploring: 1) in the stage of drive design, when the freewheeling angle becomes the main choke point of the drive operating towards higher torque and speed, how to minimize the freewheeling angle and broaden the SOA; 2) in the stage of motor design, for given motor parameters (flux density, phase resistance and inductance), how to predict the sensorless SOA. Those are the motivations of this chapter. In [YAN19b], the SOA issue was described briefly. As an extension, this chapter discusses this issue in depth. In section 4.2, the influence of freewheeling angle on zero-crossing detection is described. In section 4.3, the freewheeling paths of various PWM switching patterns are analysed. According to the freewheeling paths, the commutation events can be classified into two modes, which have different current descent rates. In section 4.4, a comparative study is carried out on the freewheeling angles among these switching patterns. Besides, a simple method to predict the SOA is described. Simulation and experiment results are shown in section 4.5. Finally, section 4.6 summaries this chapter. A comprehensive review on the factors of freewheeling angle is given in appendix 4.7.

The study in this chapter has been published in

L. Yang, Z. Q. Zhu, H. Bin, Z. Zhang, and L. Gong, "Safe operation area of zero-crossing detection based sensorless high speed BLDC motor drives," *IEEE Trans. Ind. Appl.*

4.2 PWM Switching Patterns and Freewheeling Angle

Fig. 4.1 shows the BLDC motor drive based on a three-phase voltage source inverter. The BLDC motor can be modelled as

$$\begin{bmatrix} v_{\mathrm{AN}} \\ v_{\mathrm{BN}} \\ v_{\mathrm{CN}} \end{bmatrix} = \begin{bmatrix} i_{\mathrm{A}}R + pi_{\mathrm{A}}L + e_{\mathrm{A}} \\ i_{\mathrm{B}}R + pi_{\mathrm{B}}L + e_{\mathrm{B}} \\ i_{\mathrm{C}}R + pi_{\mathrm{C}}L + e_{\mathrm{C}} \end{bmatrix}. \tag{4.1}$$

where R, L, e_X, i_X, v_{XN} and p denote the resistance, inductance, back EMF, phase currents, phase voltages and differential operator, respectively. Here, the subscript "X" denotes the phases A, B and C.

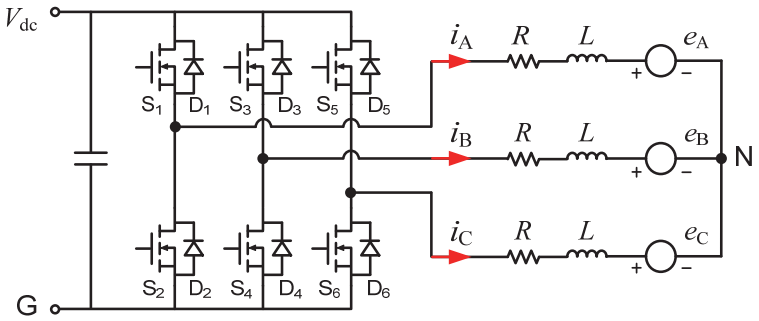

Fig. 4.1. Schematic diagram of BLDC motor drives.

In a typical six-step control scheme, a drive cycle is divided into six sectors as listed in Table I. In each 60º sector, two of the three phases are conducting. Usually, one of the conducting phase is controlled by PWM signal; and the other phase keeps constant on. Then, as shown in Fig. 4.2, four PWM switching patterns can be used in a BLDC drive. According to the combination sequence of PWM and constant ON signals, they are defined as H-PWM-L-ON, H-ON-L-PWM, PWM-ON and ON-PWM. Details are shown as follows.

(1) For the H-PWM-L-ON pattern in Fig. 4.2 (a), the gate signal for the upper switch S1 is controlled by PWM signal in sectors I and II; the gate signal for the lower switch S2 keeps constant on in sectors IV and V.

(2) On the contrary, for the H-ON-L-PWM pattern in Fig. 4.2 (b), the PWM signal and constant-on signal are reversed, i.e. the gate signal for the upper switch S1 keeps on in sectors I and II; the gate signal for the lower switch S2 is controlled by PWM signal in sectors IV and V.

(3) For the PWM-ON pattern in Fig. 4.2 (c), the former 60° is controlled by PWM signal and then the latter 60° keeps constant on.

(4) In contrary, for the ON-PWM pattern in Fig. 4.2 (d), the former 60° keeps constant on and then the latter 60° is controlled by PWM signal.

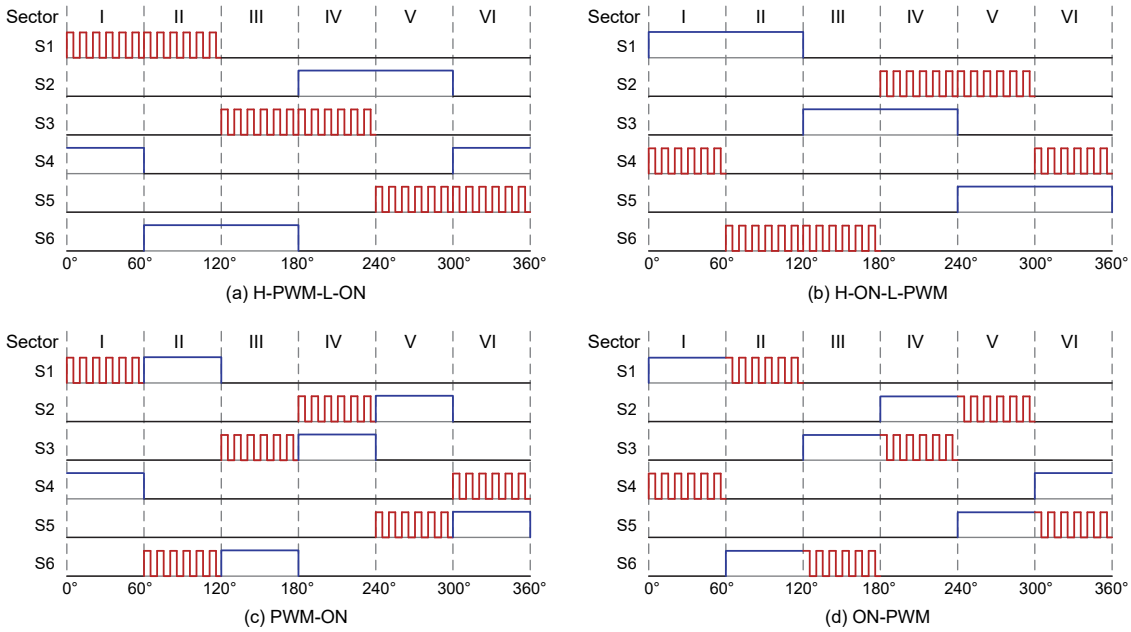

Fig. 4.2. Schematic of PWM switching patterns.

As shown in Table 4.1, in each sector, there is always a phase that is floating. The BLDC sensorless method estimates the commutation instant by detecting the ZCP of back EMF of the floating phase. However, as shown in Fig. 4.3, when the commutation performs, the freewheeling current of the outgoing phase cannot vanish to zero immediately due to the winding inductance. Instead, it flows through freewheeling diode, which clamps the floating phase to the DC-link. At this time, the back EMF signal is not measureable until the freewheeling current vanishes to zero. Obviously, as shown in Fig. 4.3 (b), when the freewheeling angle exceeds 30º, the ZCP of back EMF is undetectable and the sensorless drive will fail. In practice, considering sampling delay, as long as the freewheeling angle reaches around 25°, it will be difficult to extract the ZCP accurately.

Table 4.1 Six-Step Commutation Sequence

Sector	Conducting phases	Floating phase	Freewheeling diode
I	A+B-	C	lower
II	A+C-	B	upper
III	B+C-	A	lower
IV	B+A-	C	upper
V	C+A-	B	lower
VI	C+B-	A	upper

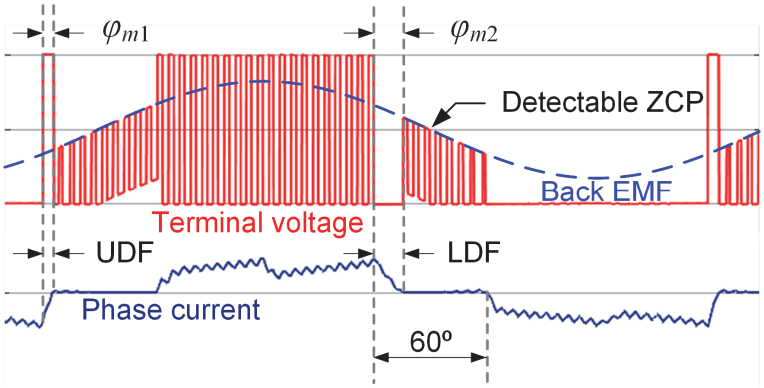

(a) Short commutation freewheeling duration, ZCP is detectable.

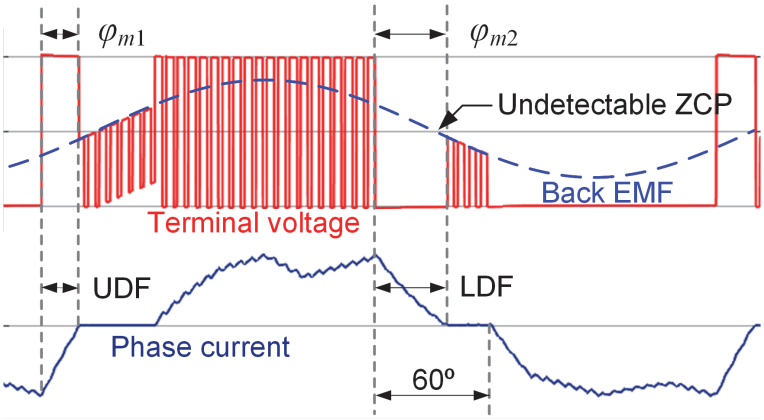

(b) Long commutation freewheeling duration (φ_{m2} > 30º), ZCP is undetectable.

Fig. 4.3. Waveforms of typical terminal voltages and phase currents, where φ_{m1}, φ_{m2} are the freewheeling angles in modes 1 and 2, respectively.

Usually, the freewheeling angle increases with the motor speed and current (load torque). Thus, the freewheeling angle is related to the maximum speed and torque that the sensorless technique can achieve. The advanced commutation technique adjusts the position relation between commutation instants and back EMFs, which can move the ZCPs of back EMF outside the freewheeling angle and make the ZCPs detectable. However, this can just mitigate the problem to some extent since the freewheeling angle is not reduced. It is found that the PWM switching patterns have a significant influence on the freewheeling angle. For a given speed and load torque, shorter freewheeling angle will definitely facilitate the zero-crossing detection. It can also deduce that if the freewheeling angle of a certain PWM pattern is less, it can achieve higher speed and higher load torque. Therefore, an analytical study is carried out to compare the freewheeling angle of these four switching patterns.

4.3 Analysis of Commutation Freewheeling Processes

According to the floating phase is clamped to positive or negative DC-link, the freewheeling processes in sectors II, IV and VI are defined as upper-diode freewheeling (UDF); ones in sectors I, III and V are defined as lower-diode freewheeling (LDF). Besides, in the two conducting phases, either can be selected to perform PWM and the other one keeps on during the whole sector. Thus, according to the selection of the PWM performing phase, the commutation processes can be classified into two modes, which can be defined as follows.

Mode 1: The switch in the parallel side of the freewheeling diode is controlled by PWM signal; and the one in the opposite side keeps conducting (see Figs. 4.4 and 4.5). For instance, when D_1 is freewheeling in Fig. 4.4, the switch S_5 that is in the parallel side of D_1 is controlled by PWM signal; and the switch S_4 in the opposite side keeps conducting.

Mode 2: The switch in the opposite side of the freewheeling diode is controlled by PWM signal; and the one in the parallel side keeps conducting (see Figs. 4.6 and 4.7). For instance, when D_1 is freewheeling in Fig. 4.6, the switch S_4 that is in the parallel side of D_1 is controlled by PWM signal; and the switch S_5 in the opposite side keeps conducting.

In the four basic PWM switching patterns, i.e. H-PWM-L-ON, H-ON-L-PWM, PWM-ON and ON-PWM, the commutation modes across six sectors are summarized in Table II. Note that H-PWM-L-ON and H-ON-L-PWM patterns contain both modes 1 and 2; PWM-ON only contains mode 2 and ON-PWM only contains mode 1. Modes 1 and 2 will determine the freewheeling paths of the outgoing phase current, which will further influence the current descent rate and the freewheeling angle. Based on this, the freewheeling processes of four basic PWM switching patterns can be analysed.

4.3.1. Commutation Mode 1

1) UDF in Mode 1

Fig. 4.4 shows the freewheeling paths in UDF of mode 1. Taking sector VI for instance, the upper-diode D_1 is freewheeling, the upper-switch S_5 is controlled by PWM signal and the lower-switch S_4 keeps conducting. Figs. 4.4 (b) and (c) show the equivalent circuits of chop-on and chop-off periods, respectively.

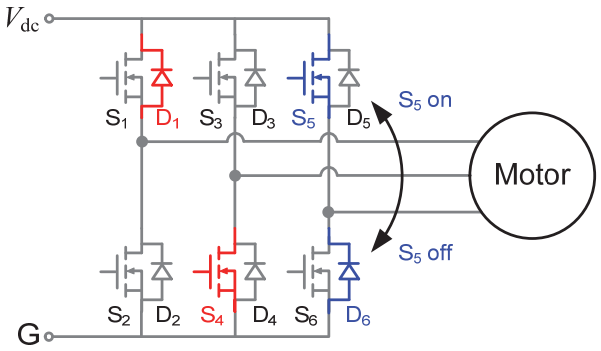

(a) Freewheeling paths.

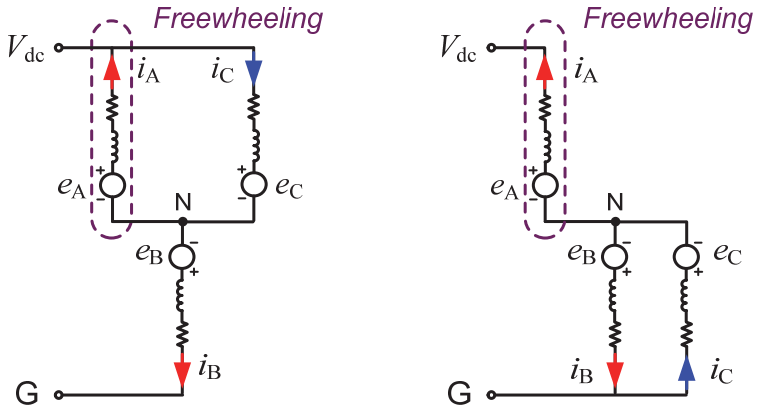

(b) Equivalent circuits in PWM chop-on period. (c) Equivalent circuits in PWM chop-off period.

Fig. 4.4. Freewheeling paths of UDF process in mode 1, sector VI.

- *Chop-on Period*

As shown in Fig. 4.4 (b), during chop-on period, phases A and C are both connected to the positive DC-link and phase B is connected to the negative one. Then, the voltage can be calculated as

$$\begin{bmatrix} V_{dc} - v_{NG} \\ -v_{NG} \\ V_{dc} - v_{NG} \end{bmatrix} = \begin{bmatrix} i_A R + p i_A L + e_A \\ i_B R + p i_B L + e_B \\ i_C R + p i_C L + e_C \end{bmatrix} \tag{4.2}$$

For sinusoidal back EMF type motors, the sum of three phase back EMF equals zero, i.e. $e_A + e_B + e_C = 0$; while for trapezoidal ones, the sum of back EMF in upper and lower side phases equals zero, i.e. $e_B + e_C = 0$ in sector VI. Then, the neutral voltage v_{NG} can be calculated as

$$v_{NG} = \begin{cases} \frac{2}{3}V_{dc} & \text{sinusoidal EMF} \\ \frac{2}{3}V_{dc} - \frac{1}{3}e_A & \text{trapezoidal EMF} \end{cases} \tag{4.3}$$

The current response can be calculated by substituting (4.3) into (4.2). During the chop-on period, the differential equation of the freewheeling current i_A can be expressed as

$$i_A(t)R + pi_A(t)L = \frac{1}{3}V_{dc} + e_{UDF}(t) \tag{4.4}$$

where

$$e_{UDF}(t) = \begin{cases} -\omega_e \psi_f \sin(\frac{11}{6}\pi + \omega_e t) & \text{sinusoidal EMF} \\ \frac{2}{3}\omega_e \psi_f & \text{trapezoidal EMF} \end{cases}. \tag{4.5}$$

- *Chop-off Period*

As shown in Fig. 4.4 (c), when S_5 switches off, the current in phase C will flow through D_6 and it will clamp phase C to the negative DC-link. Thus, the three-phase voltages can be expressed as

$$\begin{bmatrix} V_{dc} - v_{NG} \\ -v_{NG} \\ -v_{NG} \end{bmatrix} = \begin{bmatrix} i_A R + pi_A L + e_A \\ i_B R + pi_B L + e_B \\ i_C R + pi_C L + e_C \end{bmatrix}. \tag{4.6}$$

With the same calculation method above, it derives the freewheeling current response as

$$i_A(t)R + pi_A(t)L = \frac{2}{3}V_{dc} + e_{UDF}(t). \tag{4.7}$$

2) LDF in Mode 1

Similarly, as shown in Fig. 4.5, consider the LDF event in sector III. The lower-diode D_2 is freewheeling, the lower-switch S_6 is controlled by PWM signal and the upper-switch S_3 keeps conducting. The freewheeling current in chop-on and chop-off periods are analysed as follows.

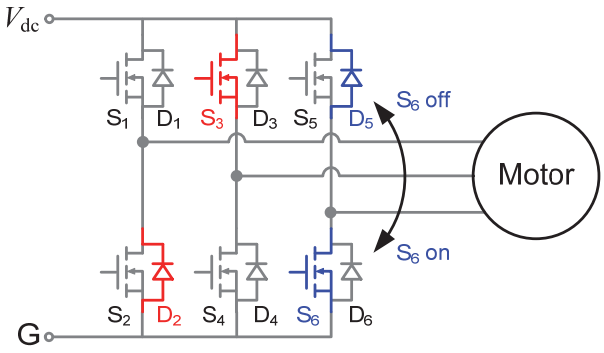

(a) Freewheeling paths.

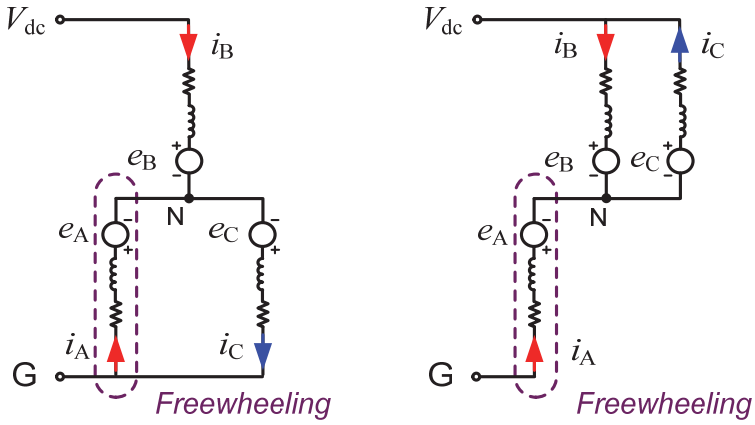

(b) Equivalent circuits in PWM chop-on period. (c) Equivalent circuits in PWM chop-off period.

Fig. 4.5. Freewheeling paths of LDF process in mode 1, sector III

- *Chop-on Period*

In Fig. 4.5 (b), during the chop-on period, phases A and C are connected to negative DC-link with D_2 and S_6, and phase B is connected to positive DC-link with S_3. The voltage can be expressed as

$$\begin{bmatrix} -v_{NG} \\ V_{dc} - v_{NG} \\ -v_{NG} \end{bmatrix} = \begin{bmatrix} i_A R + p i_A L + e_A \\ i_B R + p i_B L + e_B \\ i_C R + p i_C L + e_C \end{bmatrix}. \tag{4.8}$$

By solving (4.8), the freewheeling current can be described as

$$i_{\mathrm{A}}(t)R + pi_{\mathrm{A}}(t)L = -\frac{1}{3}V_{\mathrm{dc}} + e_{\mathrm{LDF}}(t) \tag{4.9}$$

where

$$e_{\mathrm{LDF}}(t) = \begin{cases} -\omega_e \psi_f \sin(\frac{5}{6}\pi + \omega_e t) & \text{sinusoidal EMF} \\ -\frac{2}{3}\omega_e \psi_f & \text{trapezoidal EMF} \end{cases}. \tag{4.10}$$

- *Chop-off Period*

In Fig. 4.5 (c), during chop-off period, D_5 will conduct after S_6 turns off, clamping phase C to positive DC-link. Thus, the voltage can be expressed as

$$\begin{bmatrix} -v_{\mathrm{NG}} \\ V_{\mathrm{dc}} - v_{\mathrm{NG}} \\ V_{\mathrm{dc}} - v_{\mathrm{NG}} \end{bmatrix} = \begin{bmatrix} i_{\mathrm{A}}R + pi_{\mathrm{A}}L + e_{\mathrm{A}} \\ i_{\mathrm{B}}R + pi_{\mathrm{B}}L + e_{\mathrm{B}} \\ i_{\mathrm{C}}R + pi_{\mathrm{C}}L + e_{\mathrm{C}} \end{bmatrix} \tag{4.11}$$

Then, the freewheeling current can be described as

$$i_{\mathrm{A}}(t)R + pi_{\mathrm{A}}(t)L = -\frac{2}{3}V_{\mathrm{dc}} + e_{\mathrm{LDF}}(t). \tag{4.12}$$

The current descent rate depends on the voltage excitations. Take chop-on period for instance, the voltage excitations of UDF in (4.4) and LDF in (4.9) have the same absolute value, which can be expressed as

$$\eta_{m1}^{on} = \left|\frac{1}{3}V_{\mathrm{dc}} + e_{\mathrm{UDF}}(t)\right| = \left|-\frac{1}{3}V_{\mathrm{dc}} + e_{\mathrm{LDF}}\right| \tag{4.13}$$

Besides, for the chop-off period, the absolute values of voltage excitations in (4.7) and (4.12) equal to

$$\eta_{m1}^{off} = \left|\frac{2}{3}V_{\mathrm{dc}} + e_{\mathrm{UDF}}(t)\right| = \left|-\frac{2}{3}V_{\mathrm{dc}} + e_{\mathrm{LDF}}(t)\right| \tag{4.14}$$

Thus, it concludes that for commutation mode 1, the current descent rate just depends on the chop-on and chop-off periods, irrespective of UDF and LDF processes. In addition, in mode 1, the current descent rate of the chop-on period η_{m1}^{on} is lower than that of the chop-off period η_{m1}^{off} since

$$\eta_{m1}^{on} = \left|\frac{1}{3}V_{dc} + e_{UDF}(t)\right| < \left|\frac{2}{3}V_{dc} + e_{UDF}(t)\right| = \eta_{m1}^{off}. \quad (4.15)$$

In another word, the chop-off period will accelerate the freewheeling process in mode 1. In practice, since the freewheeling duration usually covers several PWM periods, the freewheeling is the combination of chop-on and chop-off sequences.

4.3.1. Commutation Mode 2

1) UDF in Mode 2

Fig. 4.6 shows the freewheeling paths in UDF of mode 2. In sector VI, the upper-diode D_1 is freewheeling. The main difference from mode 1 is that the lower-switch S_4 is controlled by PWM signal and upper-switch S_5 keeps conducting.

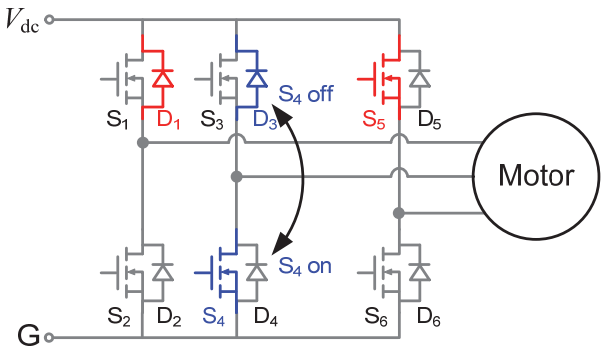

(a) Freewheeling paths.

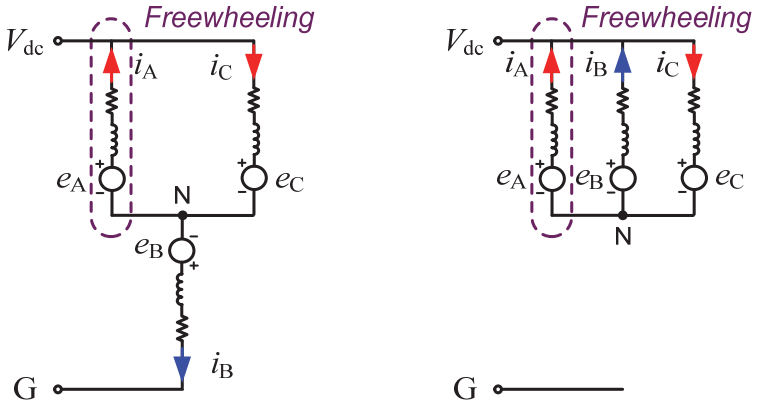

(b) Equivalent circuits in PWM chop-on period. (c) Equivalent circuits in PWM chop-off period.

Fig. 4.6. Freewheeling paths of UDF process in mode 2, sector VI.

- *Chop-on Period*

Actually, as shown in Fig. 4.4 (b) and Fig. 4.6 (b), the equivalent circuit in chop-on period of mode 2 is the same as that in mode 1. Thus, the freewheeling current response can also be expressed as (4.4).

- *Chop-off Period*

As shown in Fig. 4.6 (c), during chop-off period of commutation mode 2, D_3 will conduct after S_4 turns off, clamping all three phases to the positive DC-link. In this situation, the three-phase voltages can be described as

$$\begin{bmatrix} V_{\mathrm{dc}} - v_{\mathrm{NG}} \\ V_{\mathrm{dc}} - v_{\mathrm{NG}} \\ V_{\mathrm{dc}} - v_{\mathrm{NG}} \end{bmatrix} = \begin{bmatrix} i_{\mathrm{A}}R + pi_{\mathrm{A}}L + e_{\mathrm{A}} \\ i_{\mathrm{B}}R + pi_{\mathrm{B}}L + e_{\mathrm{B}} \\ i_{\mathrm{C}}R + pi_{\mathrm{C}}L + e_{\mathrm{C}} \end{bmatrix}. \tag{4.16}$$

Because all three phases are connected to the same point, the current response only depends on the back EMF as shown in

$$i_{\mathrm{A}}(t)R + pi_{\mathrm{A}}(t)L = e_{\mathrm{UDF}}(t) \tag{4.17}$$

2) LDF in Mode 2

Fig. 4.7 shows the freewheeling paths in LDF of mode 2. The lower-diode D_2 is in freewheeling. The main difference from mode 1 is that the upper-switch S_3 is controlled by PWM signal and the lower-switch S_6 keeps conducting.

- *Chop-on Period*

Actually, as shown in Fig. 4.5 (b) and Fig. 4.7 (b), the equivalent circuits in chop-on period of mode 2 are the same as that in mode 1. Thus, the freewheeling current response can also be expressed as (4.9).

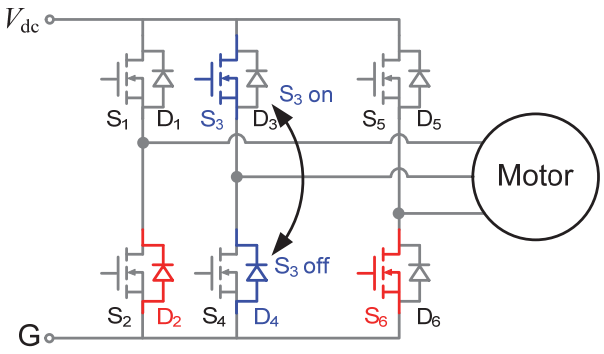

(a) Freewheeling paths

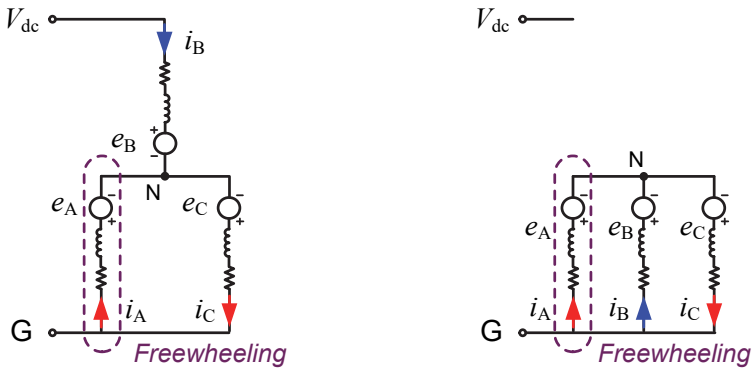

(b) Equivalent circuits in PWM chop-on period. (c) Equivalent circuits in PWM chop-off period.

Fig. 4.7. Freewheeling paths of LDF process in mode 2, sector III.

- *Chop-off Period*

As shown in Fig. 4.7 (c), D_4 will conduct after S_3 turns off. Then, all three phases are connected to the negative DC-link. In this situation, the voltage can be expressed as

$$\begin{bmatrix} -v_{NG} \\ -v_{NG} \\ -v_{NG} \end{bmatrix} = \begin{bmatrix} i_A R + p i_A L + e_A \\ i_B R + p i_B L + e_B \\ i_C R + p i_C L + e_C \end{bmatrix} \tag{4.18}$$

The current response can be calculated as

$$i_A(t)R + p i_A(t)L = e_{LDF}(t). \tag{4.19}$$

Likewise, the voltage excitations of the chop-on periods in UDF and LDF processes are the same, it yields

$$\eta_{m1}^{on} = \eta_{m2}^{on} = \left| \frac{1}{3} V_{dc} + e_{UDF}(t) \right| = \left| -\frac{1}{3} V_{dc} + e_{LDF} \right| \tag{4.20}$$

For the chop-off period, the voltage excitations in (4.17) and (4.19) equal to

$$\eta_{m2}^{off} = \left|e_{\mathrm{UDF}}(t)\right| = \left|e_{\mathrm{LDF}}\right|. \tag{4.21}$$

In addition, the conclusion of mode 2 is opposite to mode 1, i.e. the current descent rate of the chop-on period η_{m2}^{on} is higher than that of the chop-off period η_{m2}^{off} since

$$\eta_{m2}^{on} = \left|\frac{1}{3}V_{\mathrm{dc}} + e_{\mathrm{UDF}}(t)\right| > \left|e_{\mathrm{UDF}}(t)\right| = \eta_{m2}^{off}. \tag{4.22}$$

Thus, the chop-off period slows down the freewheeling process compared with chop-on period.

4.4 Freewheeling Angles and Sensorless SOA

4.4.1 Comparison of Current Descent Rates

Above analyses illustrate the freewheeling paths and the behaviours of the freewheeling current in the two commutation modes. The relation of the current descent rates can be concluded as

$$\eta_{m1}^{off} > \eta_{m1}^{on} = \eta_{m2}^{on} > \eta_{m2}^{off}. \tag{4.23}$$

Note that the overall current descent rates of mode 1 (η_{m1}^{on} and η_{m1}^{off}) are higher than or equals to those of mode 2 (η_{m2}^{on} and η_{m2}^{off}). Accordingly, for the same initial current value, the freewheeling process in mode 1 is always faster than that in mode 2. This is because the freewheeling currents flow through different paths in these two modes, and mode 1 can accelerate the freewheeling processes. When the freewheeling angle exceeds 30º, the ZCP is undetectable and sensorless drive will fail. In this sense, the switching pattern that only contains mode 1, i.e. ON-PWM pattern, can minimize the freewheeling angle and achieve broader sensorless SOA.

Fig. 4.8 (a) compares the phase currents in four PWM switching patterns in simulation. The speed is 60000 r/min and the current is about 20 A. A sinusoidal back EMF type motor is simulated here, and the main parameters are shown in Table III in Appendix A. The zoomed current waveforms for LDF and UDF processes are shown in Fig. 4.8 (b), in which the difference of current descent rates is illustrated. For the LDF

process in the left side dashed block, the freewheeling angle φ_{m2} (H-PWM-L-ON and PWM-ON) almost reaches up to 30º, which means the ZCP is nearly undetectable. In contrast, the freewheeling angles φ_{m1} (H-ON-L-PWM and ON-PWM) is much smaller. On the other hand, for the UDF process in the right side dashed block, the freewheeling angles φ_{m1} (H-PWM-L-ON and ON-PWM) are less than φ_{m2} (H-ON-L-PWM and PWM-ON). Note that among the four patterns, the ON-PWM always has less freewheeling angle irrespective of UDF or LDF process. Thus, the simulation results confirm that the ON-PWM pattern has broader SOA compared with other three patterns.

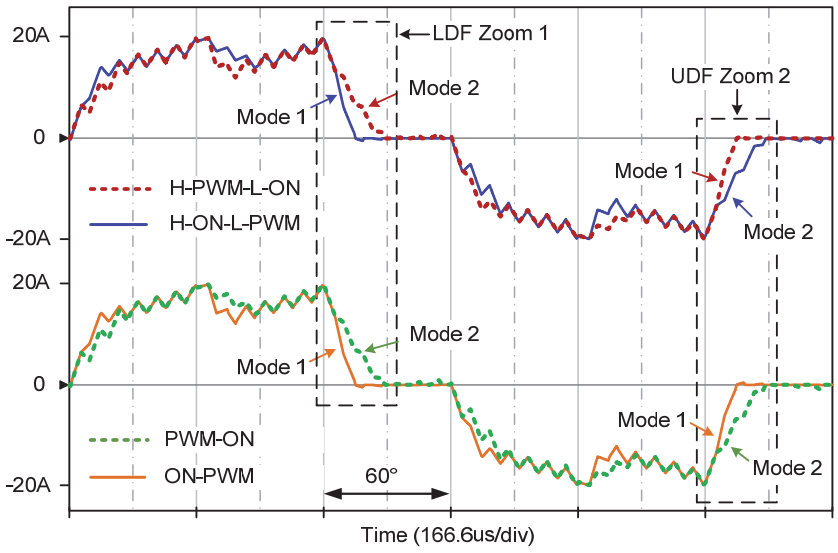

(a) Phase currents in a fundamental period.

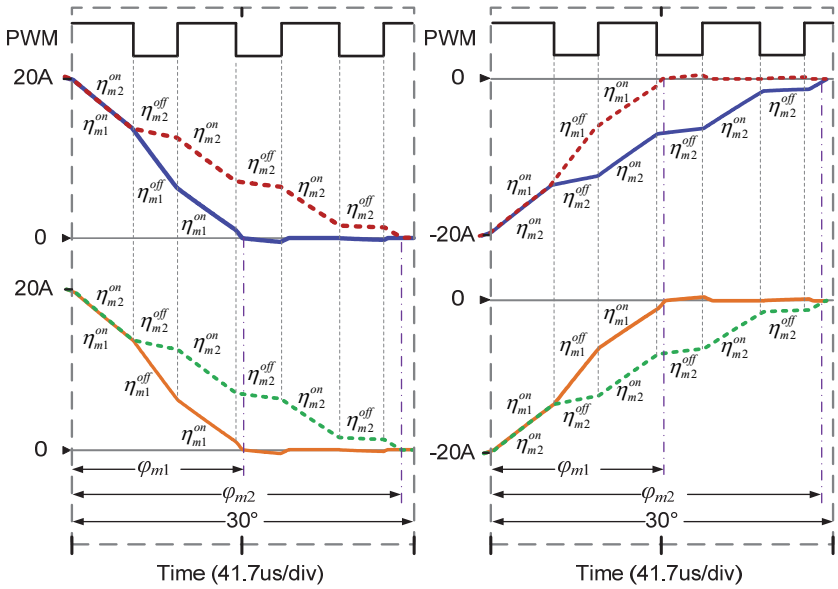

(b) Zoomed current waveforms for LDF and UDF processes.

Fig. 4.8. Comparison of phase currents in four PWM switching patterns at 60000 r/min.

Figs. 4.9 and Fig. 4.10 show the simulation results of the freewheeling duration (angle) for various speed and current. In the simulation, the motor accelerates gradually from 10 000 r/min to the maximum speed with the current 10A, 20A and 30A, respectively. The terminal voltage waveforms are recorded and a program is used to analyze the freewheeling duration and angle.

Fig. 4.9 shows the analysis results of freewheeling duration and angle in the two modes. Parameters of Motor-I in Appendix are used. The speed range is from 10 000 r/min to 120 000 r/min and the current range is from 10 A to 30 A. For a given speed and initial current, the freewheeling duration is not fixed but varies in a certain range. This is because the commutation may occur at any instants in a PWM carrier wave, and various initial PWM states are taken into consideration. In addition, it can be observed that the variation range for mode 2 is stair-like; and the variation range for mode 1 is smoother. In fact, the “stair” of the variation range is related to the switching period (25μs). The variation range for mode 2 is relatively long and covers several switching periods. In contrast, the variation range for mode 1 is relatively short and is thereby smoother. It is obvious that for any given speeds and initial currents, the freewheeling duration in mode 1 is shorter than that in mode 2. Besides, the freewheeling duration of mode 1 changes slightly with speed and mainly depends on the initial current. For mode 2, the freewheeling duration increases with initial current, and decreases with the speed. This is because the duty ratio increases with the speed. Then, the chop-off period, which slows down the freewheeling process of mode 2, reduces its proportion as duty ratio increases. When the duty ratio reaches 100%, modes 1 and 2 converge to the same freewheeling duration. Fig. 4.9 (b) shows the results in freewheeling angle. It is clear that for both modes, the freewheeling angle increases with speed and current. However, mode 1 has relatively small freewheeling angle and thereby can achieve broader sensorless SOA.

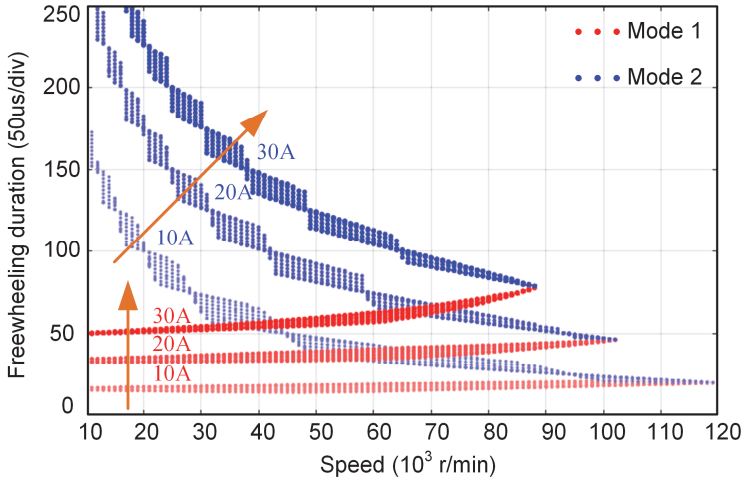

(a) Freewheeling duration.

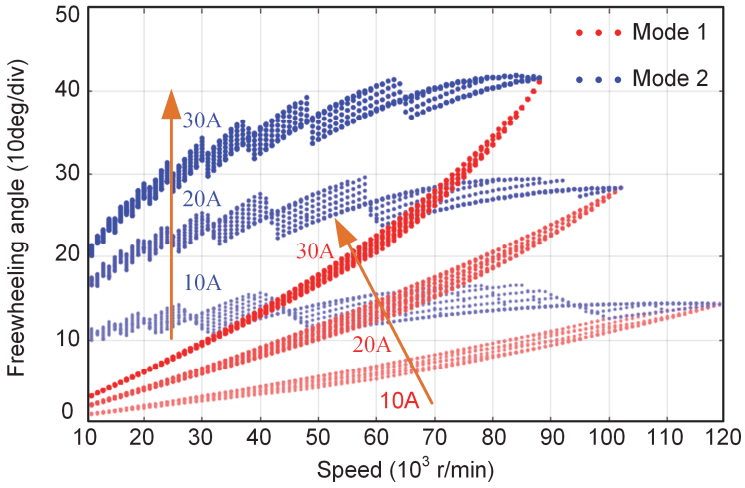

(b) Freewheeling angle.

Fig. 4.9. Freewheeling duration and angle for two modes with various speeds and initial currents.

Fig. 4.10 shows the contour maps of the freewheeling angle in terms of various initial currents and speeds in two modes. Parameters of Motor-I in Appendix are used. When the freewheeling angle exceeds 30º, the ZCP will be undetectable. In practice, considering the discrete sampling of the back EMF signal, it is close to the sensorless safety boundary as long as the freewheeling angle reaches 25°. Thus, the ON-PWM switching pattern, which only contains commutation mode 1, can achieve broader sensorless SOA in theory. In the stage of drive design stage, the freewheeling angle often becomes the choke point of the drive operating towards higher torque and speed. In this situation, the ON-PWM switching pattern provides an effective and easy-to-realize way to reduce the freewheeling angle and broaden the SOA.

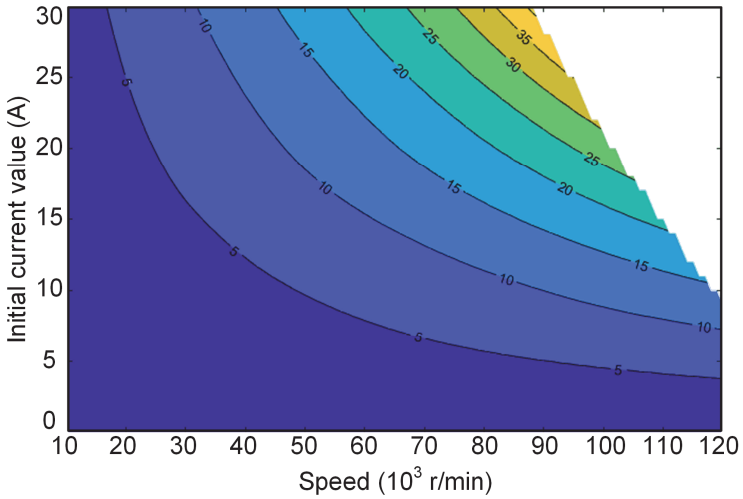

(a) Mode 1.

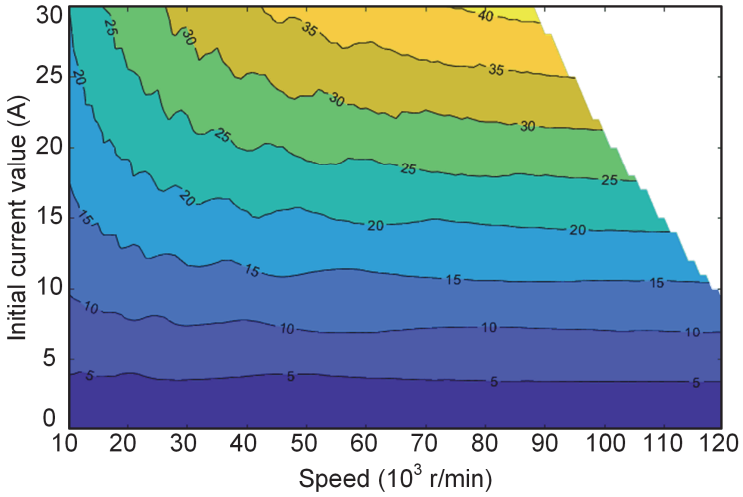

(b) Mode 2.

Fig. 4.10. Contour maps of the freewheeling angle in terms of various initial currents and speeds.

4.4.2 Prediction of Sensorless SOA

It has been proved the ON-PWM pattern can accelerate the freewheeling process and achieve broader sensorless SOA. In addition, in the stage of motor design, a method that can predict the SOA of ON-PWM pattern is required. This will help verify whether the predesigned torque and speed area can be achieved with the given parameters (flux density, resistance and inductance). Conventionally, this is usually accomplished by large amount of simulation verifications, which is quite laborious. In this part, a simple numerical iterative method is illustrated.

For the ON-PWM switching pattern, since the current descent rates in chop-on period η_{m1}^{on} and chop-off period η_{m1}^{off} are different, the freewheeling angle φ_{m1} will be dependent on the PWM duty ratio. Hence, accurate freewheeling angle of ON-PWM pattern is difficult to obtain. Instead, it is easy to determine the upper bound of the freewheeling angle, i.e. the maximum freewheeling angle $\varphi_{m1}^{\sup}$. Since the current descent rate in chop-on period is lower than that of chop-off period, i.e. $\eta_{m1}^{on} < \eta_{m1}^{off}$, the maximum freewheeling angle happens when the current descents with the rate η_{m1}^{on} all the way. Thus, according to (4.9), the maximum freewheeling angle $\varphi_{m1}^{\sup}$ can be obtained by solving the nonlinear differential equation

$$i[n+1] = i[n] + \frac{\Delta t}{L}\left(-\frac{1}{3}V_{\mathrm{dc}} + e[n] - i[n]R \right) \tag{4.24}$$

$$e[n] = \begin{cases} -\omega_e \psi_f \sin(\frac{5}{6}\pi + \omega_e t[n]) & \text{sinusoidal EMF} \\ -\frac{2}{3}\omega_e \psi_f & \text{trapezoidal EMF} \end{cases} \tag{4.25}$$

where Δt is the time step, the initial current value $i[0]$ can be determined by the load torque. The maximum freewheeling duration (angle) is the span that the current in (4.24) descents from initial value $i[0]$ to zero. The calculation is much easier, since it does not need the PWM duty ratio information. Note that $\varphi_{m1}^{\sup}$ indicates the upper bound of the freewheeling angle in ON-PWM pattern. In practice, the freewheeling angle φ_{m1} is definitely less than the upper bound $\varphi_{m1}^{\sup}$. Usually, the freewheeling angle increases with the motor speed and current. The sensorless SOA refers to the speed and current area in which the maximum freewheeling angle is less than 30° i.e. $\varphi_{m1}^{\sup} \le 30^\circ$. By sweeping the initial current value and motor speed, the SOA can be identified.

4.5 Simulation and Experiment Results

Fig. 4.11 shows the simulation results of electrical torque waveforms using four PWM switching patterns. The speed is 60000 r/min and the load torque is 20e-3 Nm. It can be observed that for all the switching patterns, torque ripples will be introduced whose frequency is six times of the fundamental frequency. Every time when the inverter proceeds commutation, it will lead to a torque ripple. This is a common issue

of the six-step BLDC operation. In terms of the torque ripple level, PWM-ON pattern in Fig. 4.11 (c) has the minimized torque ripple magnitude. The torque ripples of other three patterns (including the recommended ON-PWM pattern) are slightly larger, but are also acceptable. This phenomenon was also noticed in [22], [23].

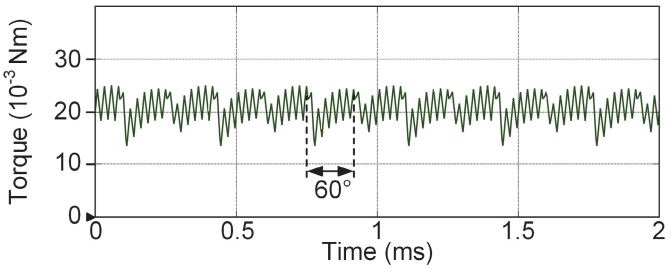

(a) H-PWM-L-ON.

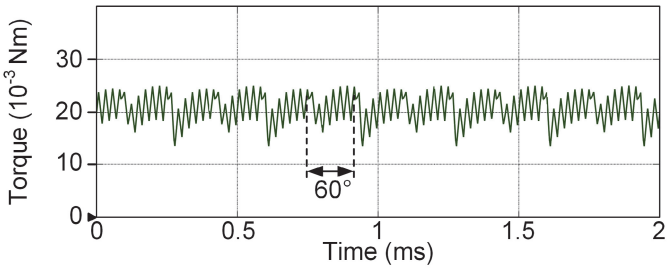

(b) H-ON-L-PWM.

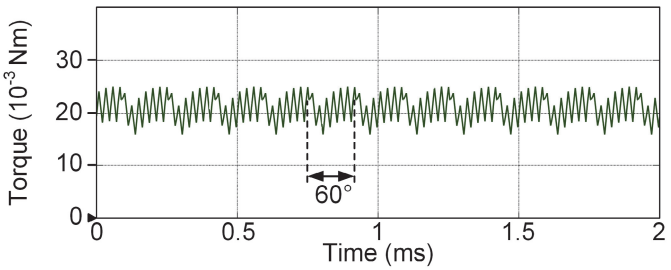

(c) PWM-ON.

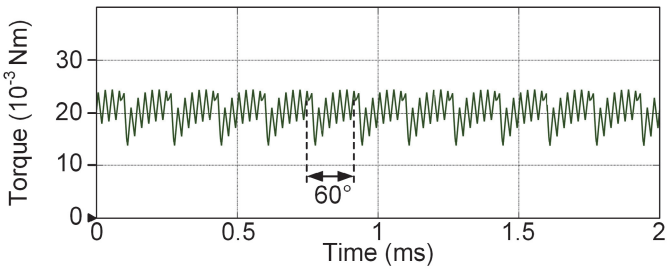

(d) ON-PWM.

Fig. 4.11. Simulation results of torque waveforms.

Considering that the motor drive is for high-speed applications, whose fundamental frequency is usually above 1000 Hz, the torque ripple frequency is high enough so that the influence can be neglected. Since a long freewheeling angle will restrict the safe

operating area, the freewheeling angle definitely plays a more important role than the torque ripple does for high-speed sensorless BLDC drives. Thus, torque ripple of the ON-PWM pattern can be acceptable when compared to the advantage it brings.

The theoretical analysis is verified with the high-speed Motor-I in Appendix 1. The PWM switching frequency and the sampling frequency are both 40 kHz, and the DC-link voltage is 25V.

Fig. 4.12 shows the sensorless operation at 60 000 r/min using four basic PWM switching patterns. The initial current at commutation instant is about 14A. It can be seen, the freewheeling duration for commutation mode 1 is less than 25μs (9º). For mode 2, however, the freewheeling duration reaches over 50μs (about 20º). Besides, as shown in the zoomed figures, the ZCP of commutation mode 2 is not clear. Although it is not overridden by the freewheeling duration, it has been difficult to identify the ZCP accurately. Therefore, for mode 2, it has been close to the sensorless safety boundary. For mode 1, the freewheeling duration is acceptable, and the ZCP can be recognized clearly. It should be pointed that, the ON-PWM only contains commutation mode 1, thus both the ZCPs can be clearly identified. It can achieve broader sensorless SOA.

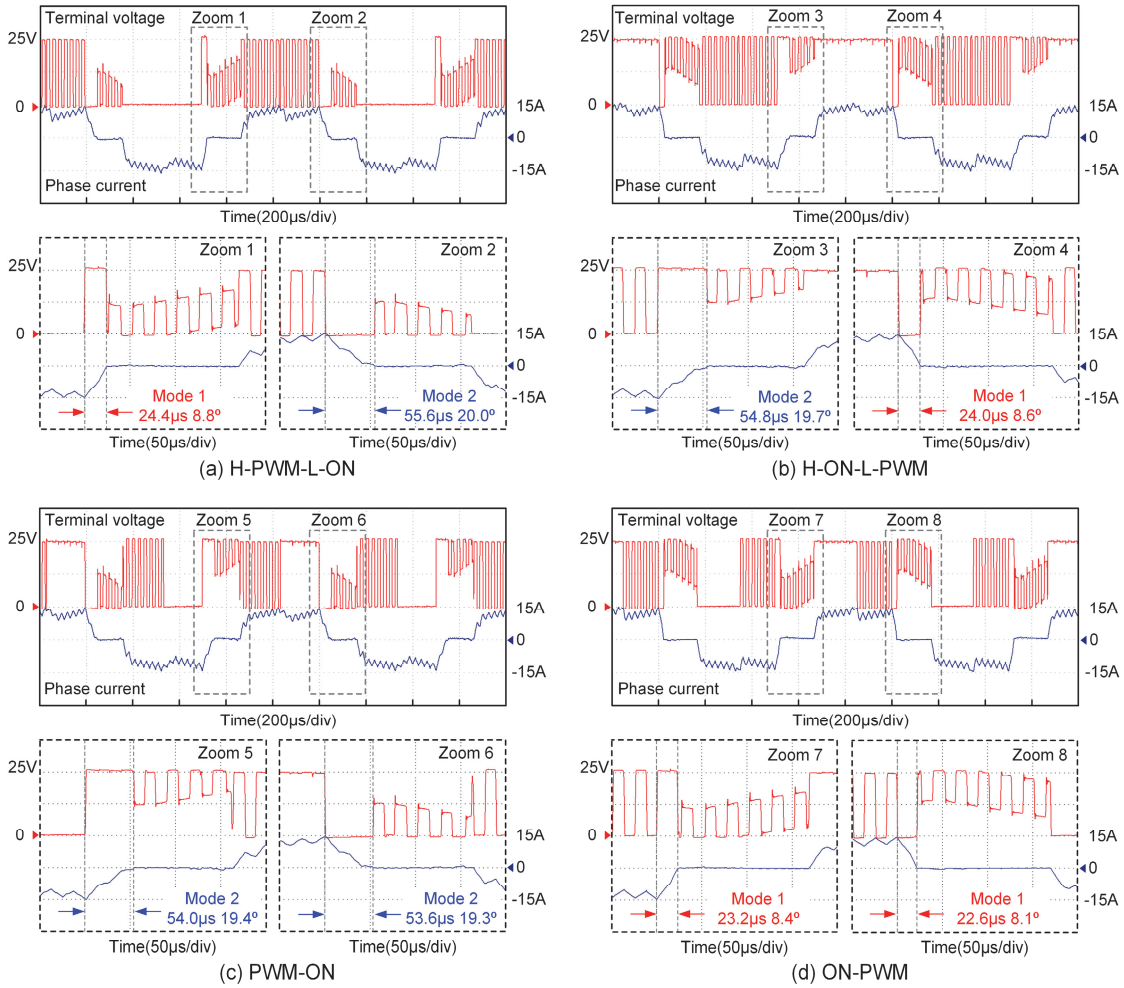

Fig. 4.12. Sensorless operation at 60 000 r/min using various PWM switching patterns.

Fig. 4.13 compares the measured freewheeling angles φ_{m1}, φ_{m2} and the predicted maximum freewheeling angle $\varphi_{m1}^{\text{sup}}$ in mode 1. The speed range is from 30 000r/min (500Hz) to 90 000 r/min (1500 Hz). The measured freewheeling angles φ_{m1}, φ_{m2} are obtained from ON-PWM and PWM-ON patterns, respectively. As above mentioned, the freewheeling angles are not fixed values for a given speed, but vary within a certain range due to random PWM initial states. Due to this reason, vertical bars are used to describe the measured range. In addition, since the load torque is produced by fan blades connected on the motor shaft, the current increases with the motor speed, which is shown by the grey curve. As it is shown, in both modes, the freewheeling angles rise with the motor speed. Besides, φ_{m1} is always smaller than φ_{m2}, which agrees with the theoretical analysis.

Note that the freewheeling angle of 30º is a critical point for sensorless drive. When the motor speed exceeds 72 000 r/min, the sensorless drive using PWM-ON pattern fails because φ_{m1} reaches 30º. In this case, the SOA is limited by the long freewheeling angle. In contrast, with the pattern ON-PWM, the sensorless SOA is extended to 90 000 r/min. In addition, the curve of predicted maximum freewheeling angle $\varphi_{m1}^{\text{sup}}$ has the similar trend with the measured φ_{m1}. Therefore, in the first place, it demonstrates the ON-PWM pattern can effectively minimize the freewheeling angle and broaden the sensorless SOA. In addition, the method in (4.24) can help predict the sensorless SOA of ON-PWM pattern, which provides a simple solution to verify the motor parameters in motor design stage.

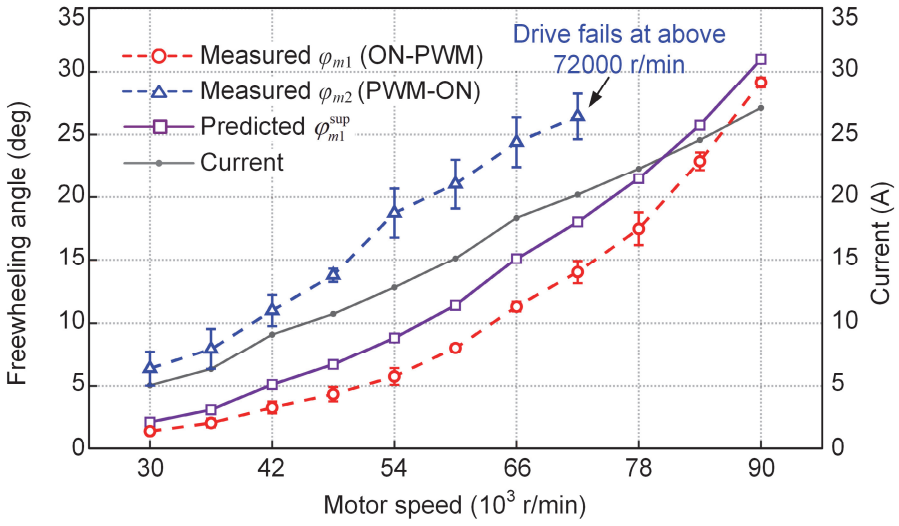

Fig. 4.13. Comparison of measured freewheeling angles φ_{m1}, φ_{m2}, predicted maximum freewheeling angle $\varphi_{m1}^{\text{sup}}$ in mode 1 and the initial current.

4.6 Summary

This chapter has investigated the freewheeling angle issue in sensorless high-speed BLDC drives. When the freewheeling angle is larger than 30 electrical degrees, the zero-crossing point will disappear and the sensorless drive will fail. It is found that the PWM switching patterns, which is neglected in most previous literature, have a significant influence in the freewheeling angle. Hence, through analytical methods, the mechanism that how different PWM techniques affect the freewheeling angle is investigated. Various patterns correspond to different freewheeling path and current

descent rates. It demonstrates that when the freewheeling angle is the main choke point of the drive operating towards higher torque and speed, the ON-PWM pattern can minimize the freewheeling angle and broaden the sensorless SOA. Besides, a simple numerical iterative method to predict the SOA for high-speed BLDC drives is presented. Finally, the analysis is verified through simulation and experiment results.

4.7 Appendix: Review on Other Factors of Freewheeling Angle

As analysed in this chapter, the freewheeling angle depends on many factors as listed as follows. The influence of the PWM switching pattern has been studied in this chapter. To make a comprehensive analysis of how other factors affect the freewheeling angle, a review is carried out in this part. Through solving nonlinear differential equations (4.24), the relation between the freewheeling angle and these factors can be studied. To control variables, in each subsection 4.7.1, 4.7.2 and 4.7.3, only one factor is changed and others are kept as constant. In this way, the influence of these factors can be investigated and the results are shown in Fig. 4.14 to Fig. 4.17.

1) Machine parameters (resistance R, inductance L) [HAN08].
2) Drive parameters (DC-link voltage V_{dc} [XUY16] [CHE17c] [LIX16] [JIA18], PWM duty ratio D [SHI17] [PAR20] [ACH20] and PWM switching pattern).
3) Operating conditions (speed ω and initial current I_0) [LIW16] [LIH17].

4.7.1 Resistance and Inductance

Figs. 4.14 (a) and (b) illustrate the freewheeling durations and angles for various resistances (ranging from 10mΩ to 40mΩ). Figs. 4.15 (a) and (b) illustrate the ones for various inductances (ranging from 10μH to 40μH). Other parameter are fixed and listed under the corresponding figure. It shows that the freewheeling durations (angle) rise as the resistances decrease and the inductances increase. This is because larger resistance-inductance time constant (L/R) will lead to larger freewheeling duration (angle). Besides, the inductance has relatively big influence on the freewheeling duration (angle) compared to the resistance. This is due to the fact that the freewheeling duration

is usually much less than the resistance-inductance time constant. Within this short duration, the inductance plays a dominant role in the current descent rate. As a result, the resistance has a very small influence on the freewheeling duration (angle).

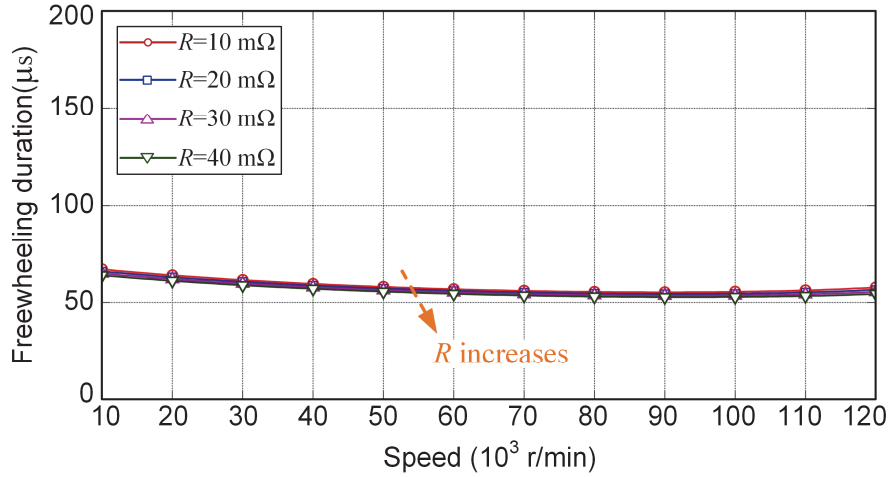

(a) Freewheeling durations.

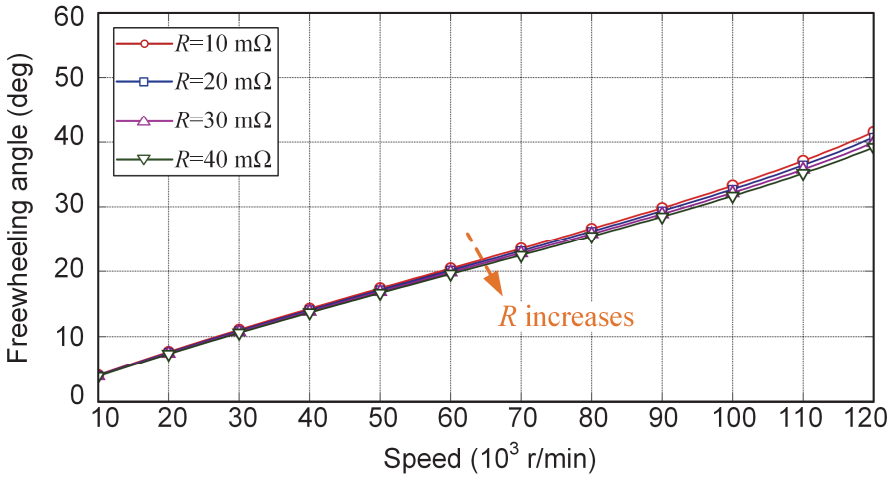

(b) Freewheeling angles.

Fig. 4.14. Freewheeling durations and angles for various resistances.

(L=20μH, ψ_f =1mWb, I_0=30A, V_{dc}=25V, D=1.0)

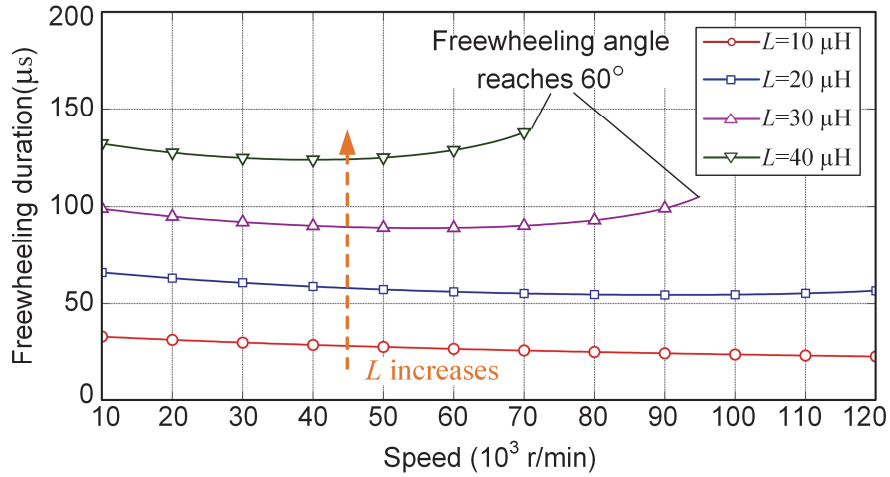

(a) Freewheeling durations.

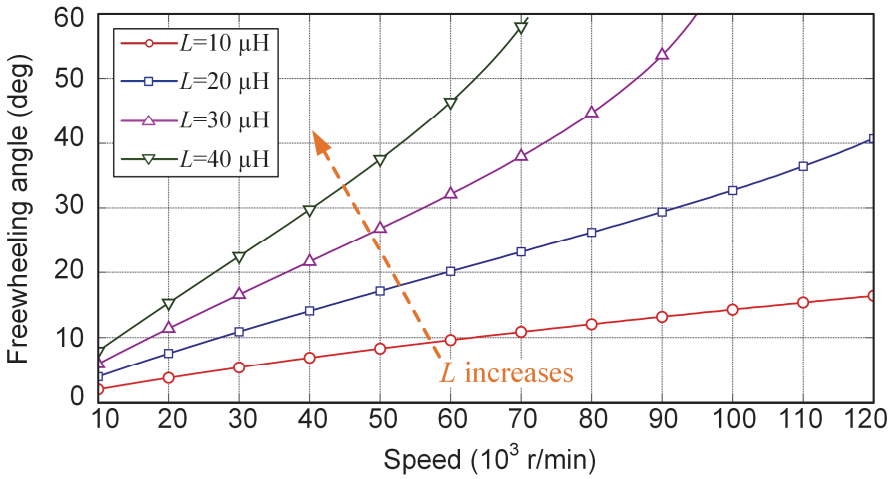

(b) Freewheeling angles.

Fig. 4.15. Freewheeling durations and angles for various inductances.

(R=20mΩ, ψ_f =1mWb, I_0=30A, V_{dc}=25V, D=1.0)

4.7.2 DC-link Voltage

Figs. 4.16 (a) and (b) show the freewheeling durations and angles for various DC-link voltages ranging from 15V to 30V. It illustrates the freewheeling duration (angle) decreases as the DC-link voltage rises. This is because higher DC-link voltage can achieve higher current descent rate, leading to less freewheeling duration (angle). Based on this mechanism, some literature tried to develop some specific converters [XUY16][CHE17c][LIX16][JIA18]. With these converters, the DC-link voltage can be increased temporarily within the freewheeling interval, and then, current freewheeling processes can be facilitated.

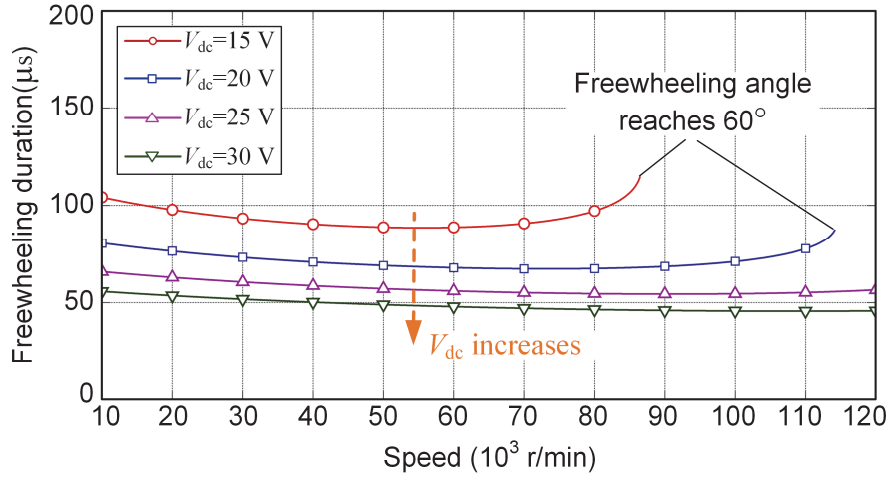

(a) Freewheeling durations.

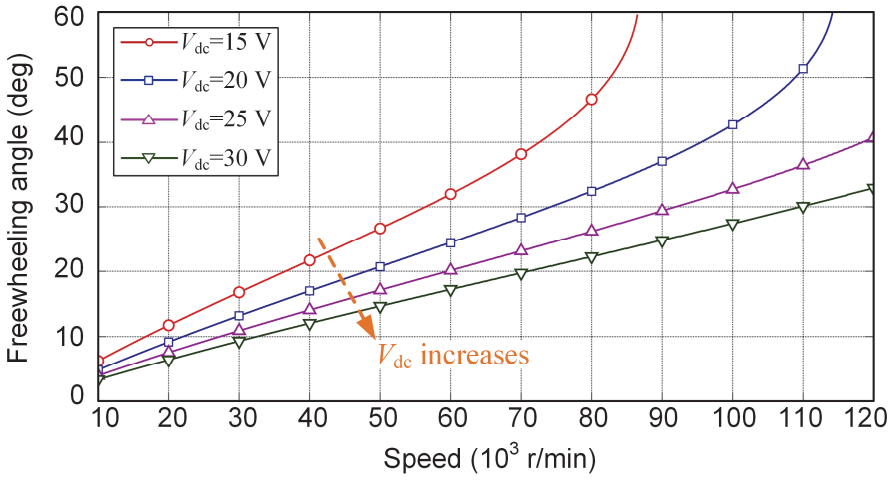

(b) Freewheeling angles.

Fig. 4.16. Freewheeling durations and angles for various DC-link voltages.

(R=20mΩ, L=20μH, ψ_f =1mWb, I_0=30A, D=1.0)

4.7.3 PWM Duty-Ratio

The most complicated factor is the PWM duty ratio. In [SHI17] [PAR20] [ACH20], the relation between the current freewheeling slope and the PWM duty ratio was analysed. However, the commutation modes also have influence on the freewheeling angle but were not considered. Figs. 4.17 (a) and (b) shows the freewheeling durations and angles for various PWM duty ratios, taking commutation modes 1 and 2 into consideration. It shows that for mode 1, the freewheeling angle increases with the duty ratio; for mode 2, the freewheeling angle decreases with the duty ratio. The reasons can be explained as follows. Firstly, the relation of the current descent rates can be concluded as

$$\eta_{m1}^{off} > \eta_{m1}^{on} = \eta_{m2}^{on} > \eta_{m2}^{off} \tag{4.26}$$

It shows that for mode 1, the current descent rate of the chop-off interval is higher than the one of chop-on interval. As a result, higher duty ratio will lead to less chop-off interval, lower current descent rate and finally larger freewheeling duration (angle). On the contrary, for mode 2, the current descent rate of the chop-off interval is lower than the one of chop-on interval. With the similar logic, as the duty ratio rises, the freewheeling duration (angle) will decrease. When the duty ratio reaches 1.0, the freewheeling angles of these two modes coincide with each other.

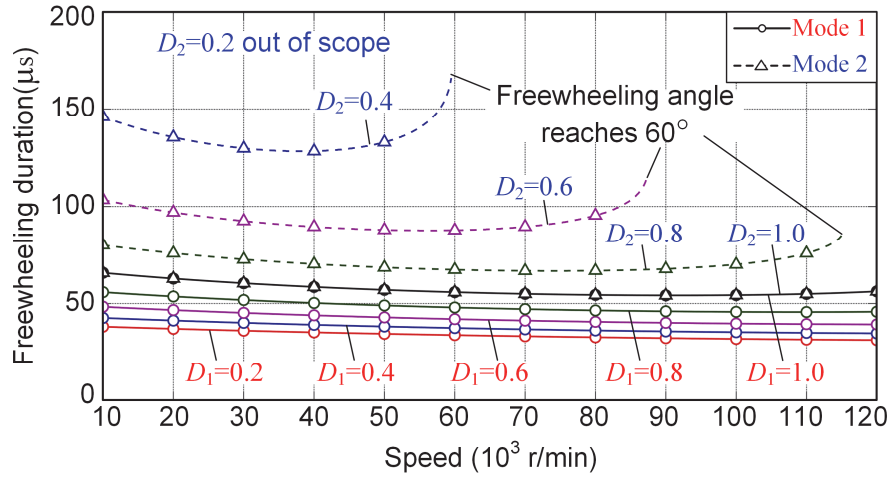

(a) Freewheeling durations.

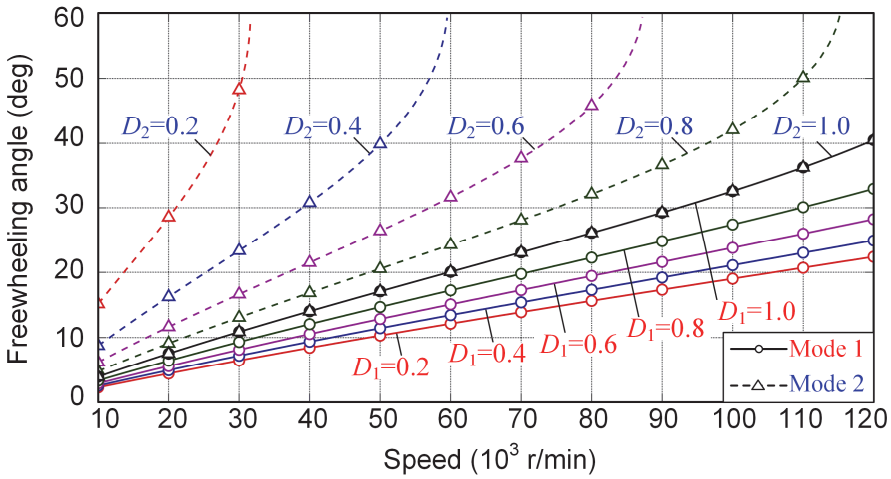

(b) Freewheeling angles.

Fig. 4.17. Freewheeling durations and angles for various PWM duty ratios, where D_1 and D_2 denote the duty ratios for modes 1 and 2, respectively.

(R=20mΩ, L=20μH, ψ_f =1mWb, I_0=30A, V_{dc}=25V)

4.7.4 Summary of Appendix

This subsection presents a supplement analysis of the effects of other factors on the freewheeling angle. Important results are summarized as follows. The freewheeling duration (angle) increases with the inductance and nearly does not change with the resistance. Higher DC voltage can achieve lower freewheeling duration (angle). For mode 1, the freewheeling angle increases with the duty ratio; for mode 2, the freewheeling angle decreases with the duty ratio.

CHAPTER 5

PWM Switching Delay Correction Method for High-Speed BLDC Drives

5.1 Introduction

Carrier modulation is the most common technique for the inverter of modern digital motor drives. The switching ratio f_c / f_e of the inverter is usually set high enough in order to ensure smooth current control and less current harmonics (f_c denotes the carrier (switching) frequency and f_e denotes the fundamental frequency). However, in some applications, inverters have to operate with insufficient f_c / f_e, which will impose negative influences on the control performance. For instance, in high-speed motor drives, the fundamental frequency f_e is relatively high and may reach several thousand hertz [LEE18b]. Besides, for high-power motor drives, the carrier frequency f_c is strictly limited within 1 kHz considering the switching losses [RAT13]. In these applications, f_c / f_e is limited and there could only be a few PWM waves in each fundamental period, leading to some adverse influences on control performance.

For high-speed brushless DC (BLDC) drives, the influences of insufficient f_c / f_e are primarily in two aspects: low-frequency current oscillations and the instability of sensorless operation. The commonly used regular-sampled PWM method only updates once in each carrier period. Besides, the modulating signal of six-step control is discontinuous square wave. Thus, when the inverter operates with the regular-sampled commutation (RSC), the power switches may turn on and off at inaccurate instants, leading to commutation errors [KEZ17] [PAR18] [LIU19b]. The commutation errors will introduce low-frequency oscillations in three-phase currents, which will produce significant additional losses and torque ripples [STU12] [JAR11]. Additionally, the PWM switching delay may lead to instability phenomenon in the sensorless operation. Among all sensorless BLDC schemes, the zero crossing detection (ZCD) based method is the most popular one, because it is easy to implement and requires minimal

knowledge of machine parameters [LIW16] [ZHO17] [PAR19]. However, the ZCD-based method suffers from long freewheeling angle problem. It is generally supposed that if the freewheeling angle is larger than 30 electric degrees, the zero-crossing point (ZCP) will be overridden and the sensorless drive will fail [SHE04] [YAN19b]. Unfortunately, the PWM switching delay will aggravate this problem. The commutation delay will produce accumulative errors. As a result, the ZCD-based sensorless drive will lose its stability even when the freewheeling angle is less than 30º.

Some efforts have been made to mitigate the PWM switching delay phenomenon. A control algorithm to detect voltage polarity and correct the commutation point was proposed in [KEZ17]. By balancing the upper and lower half waves in a period, the commutation point can be corrected to accurate position. In [PAR18], it presented that when f_c / f_e is a multiple of six, the low-frequency current oscillations can be minimized. Based on this idea, a variable time step controller was proposed to adjust the switch on and off points. However, the above methods cannot be applied with the chopper operation, i.e. only all on and all off states are used for the power switches. Therefore, for the BLDC drives with the requirement of voltage adjustment, these methods are not appropriate.

In order to avoid the influence of PWM switching delay on BLDC drives, some two-stage drive topologies have been proposed, including voltage source inverters (VSI) [CUI15] [SCH14] and current source inverters (CSI) [SIL14]. In the two-stage drive, a DC/DC converter is comprised with a three-phase inverter to regulate the input voltage or current. In this way, the inverter operates with unmodulated six-step mode and thus the commutation is no longer influenced by the PWM switching delay. However, additional passive components are required, e.g. external inductors in VSI and external capacitors in CSI, which will increase the system volume and cost. For the application of classic inverter for the BLDC drive, it is promising to solve this problem from modulation schemes. The unipolar PWM pattern was introduced by [BAS18] and [VAL17], in which the chopper is alternately performed by upper and lower switches. In this way, the equivalent carrier frequency is doubled and the PWM delay can be reduced to half. In [KIM06], a method to synchronize the commutation point with

PWM update point by changing the carrier frequency before commutation was proposed. However, it only gives low speed experimental results without enough theoretical analysis or implementation details. Consequently, from the existing literature, the way to eliminate the PWM delay for high-speed BLDC drives is not fully investigated.

To guarantee low loss and high stability for the high-speed BLDC drives, further improvements on delay-free PWM strategy is expected. A potential solution is to adopt the idea of synchronized PWM, which has been verified for field-oriented control in reducing low-frequency oscillations [SAH16] [CHE16] [YAN17a]. If the carrier is generated in synchronization with the commutation, the power switches can switch on and off at accurate instant. As a result, commutation delay can be eliminated and the voltage vectors can be space symmetrical.

In this chapter, a novel carrier-synchronized commutation (CSC) strategy is proposed to eliminate the commutation delay caused by digital PWM generation. Firstly, the mechanisms of commutation delay and low-frequency current oscillations are discussed in section 5.2. The characteristics of the inverter output with insufficient f_c / f_e are illustrated by a graphic representation. Then, the instability of sensorless operation caused by commutation delay is analysed in section 5.3. An iterative sequence is constructed to describe the ZCD procedures and the stability analysis is carried out. In section 5.4, the implementation of the proposed CSC scheme is introduced. Finally, simulation and experimental validations are presented in section 5.5, and section 5.6 is the summary of this chapter.

5.2 Commutation Delay Caused by Conventional PWM Generation

5.2.1 Six-step Control and Digital PWM Generation

Fig. 5.1 shows the drive topology of 3-phase high-speed BLDC motors. In the six-step BLDC control, a drive cycle is divided into six sectors. In each 60º sector, two of three phases are conducting. The inverter needs to change the conducting status every 60 electric degrees, which can be denoted as voltage vectors $\boldsymbol{V}_1 \ldots \boldsymbol{V}_6$ corresponding to respective sectors. The six power switches of the inverter are usually controlled by six PWM gate signals generated by the digital microprocessor.

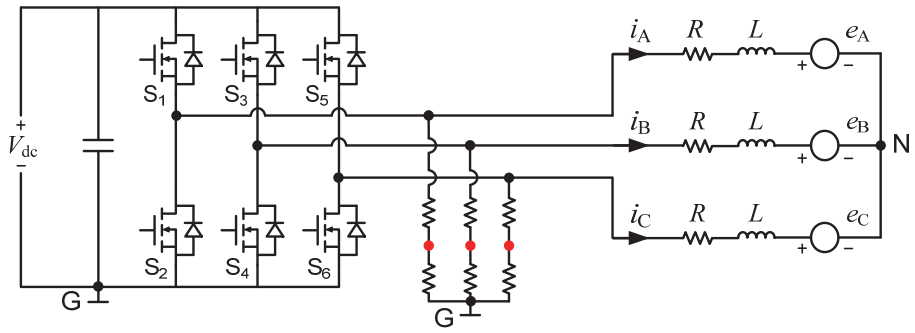

Fig. 5.1. Drive topology of high-speed BLDC motors.

For the commonly used regular-sampled PWM generation, the inherent update mechanism will lead to potential commutation delay of the inverter. This PWM generation operates with discrete way, which means the PWM output is only updated once at the beginning of a carrier period. When the commutation interrupt signal arrives as shown in Fig. 5.2, the PWM sequence cannot be updated until the next update instant. It means neither the previous PWM sequence ends nor the next one starts immediately, which introduces the commutation delay. Theoretically, the maximum commutation delay of RSC can reach a carrier period. This phenomenon is not serious and can be ignored when f_c / f_e is sufficient. However, for high-speed drives, there is only limited number of PWM pulses in each drive cycle. The commutation delay will be a serious issue.

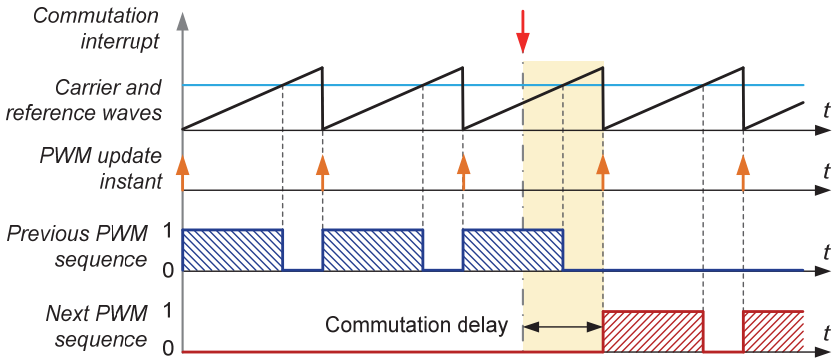

Fig. 5.2. Schematic diagram of conventional RSC scheme.

5.2.2 Graphic Representation of Inverter Output

To investigate the inverter output in the case of limited f_c / f_e, a sequence model is constructed in this part. In an ideal situation, the commutation should be performed every 60º as

$$\theta_{\text{CTN-IDL}}[k] = k \cdot 60° \tag{5.1}$$

where $\theta_{\text{CTN-IDL}}[k]$ denotes the k^{th} ideal commutation angle. When the motor operates at the fundamental frequency of f_e with carrier frequency of f_c, the sector carrier ratio N that is defined by the average number of PWM pulses in each sector can be expressed as

$$N = \frac{f_c}{6 f_e} = \frac{1}{6} F_{\text{ratio}} \tag{5.2}$$

and each carrier period is equivalent to 60/N electric degrees. Since the PWM can only update at the beginning of each carrier period, the actual commutation angle $\theta_{\text{CTN-ACT}}[k]$ can be modelled as

$$\theta_{\text{CTN-ACT}}[k] = \text{ceil}(kN) \cdot \frac{60°}{N} + \theta_0 \tag{5.3}$$

where θ_0 is the initial phase when $k = 0$. The function ceil(x) is used to map x to the least integer greater than or equal to x.

Fig. 5.3 shows the graphic representation of the inverter output. Imagine a dot is anti-clockwise moving along the colour arcs with a constant speed, representing the

motor is operating. Every small piece of arc represents a carrier period, equivalent to 60/N electric degrees. Various colours represent the voltage vectors $\boldsymbol{V}_1 \ldots \boldsymbol{V}_6$. The boundaries of different colours mean the commutation. Ideally, the voltage vectors $\boldsymbol{V}_1 \ldots \boldsymbol{V}_6$ should be confined within their corresponding sectors. However, when considering the retarding update behaviour of PWM, the actual commutation instant always lags behind the ideal instant.

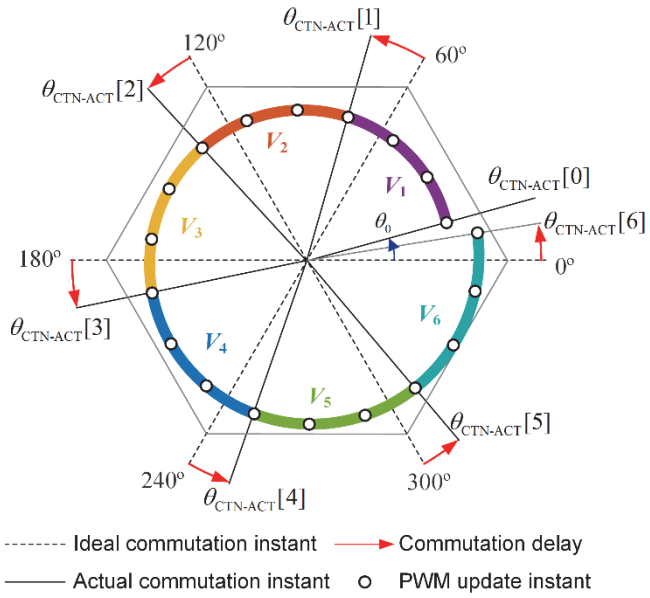

Fig. 5.3. Illustration of commutation delay caused by PWM.

Fig. 5.4 simulates the inverter output using Matlab software when f_c / f_e=17.9, 18 and 18.1. It is obvious that when the carrier ratio N is not an integer as shown in Figs. 5.4 (a) and (c), the commutation position will move gradually. The commutation error cyclically increases and decreases. This regular fluctuation will generate space asymmetric voltage excitation and will further cause low-frequency current oscillations. Particularly, even though N is an integer as in Fig. 5.4 (b), the commutation delay still exists due to θ_0. Thus, keeping f_c / f_e as a multiple of six can just remain the PWM delay unchanged, but cannot guarantee the commutation instant is exactly aligned with the PWM update instant.

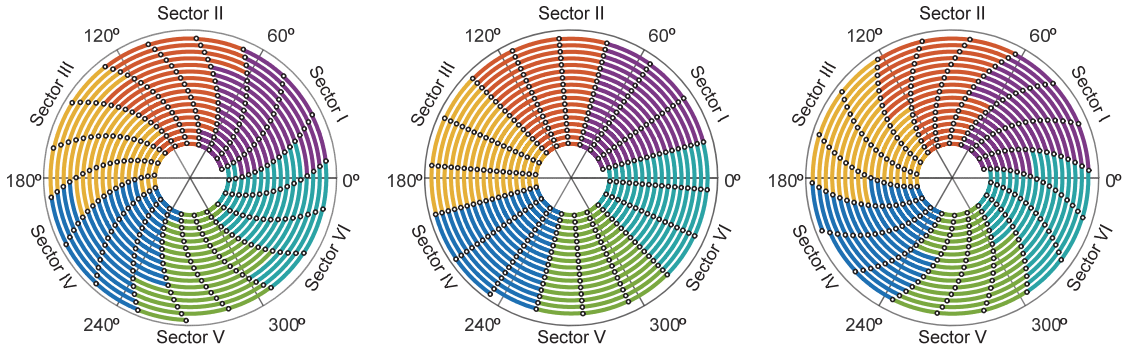

(a) $f_c / f_e = 17.9$, $\theta_0 = 15°$ (b) $f_c / f_e = 18$, $\theta_0 = 15°$ (c) $f_c / f_e = 18.1$, $\theta_0 = 15°$

Fig. 5.4. Graphic representation of inverter output.

The commutation delay has negative influences on motor drives, especially in high-speed applications. Firstly, the rotor of the high-speed motor will rotate a relatively large phase angle within a carrier period, leading to significant commutation delay. Secondly, high-speed BLDC motors usually have low winding inductances, which make them sensitive to commutation errors. Even a small commutation error will induce large current ripple and produce additional losses. Most importantly, the cyclically fluctuated commutation errors will induce low-frequency current oscillations.

Here, the low-frequency current oscillation issue of conventional RSC scheme is illustrated with simple graphic representations, i.e. Fig. 5.3 and Fig. 5.4. In the next chapter (chapter 6), this issue will be illustrated with the analytical spectral analysis.

5.3 Accumulative Errors in Sensorless BLDC Drives

The commutation delay will cause accumulative errors and further lead to instability issue for sensorless operation. Fig. 5.5 illustrates the principle of ZCD-based sensorless BLDC drive method. In the six-step drive method, only two of the three phases conduct and the third phase is floating. The back EMF of the floating phase is exposed and can be measured. By detecting the ZCPs of back EMF, the rotor position can be obtained and the commutation point can be identified. However, the ZCP could be postponed by the freewheeling angle and the commutation is retarded by the RSC mechanism. Influenced by these two non-ideal factors, the accumulative error will be produced and it could further cause the instability phenomenon. In this section, an

iterative sequence is constructed to describe the ZCD procedure and the stability analysis is carried out.

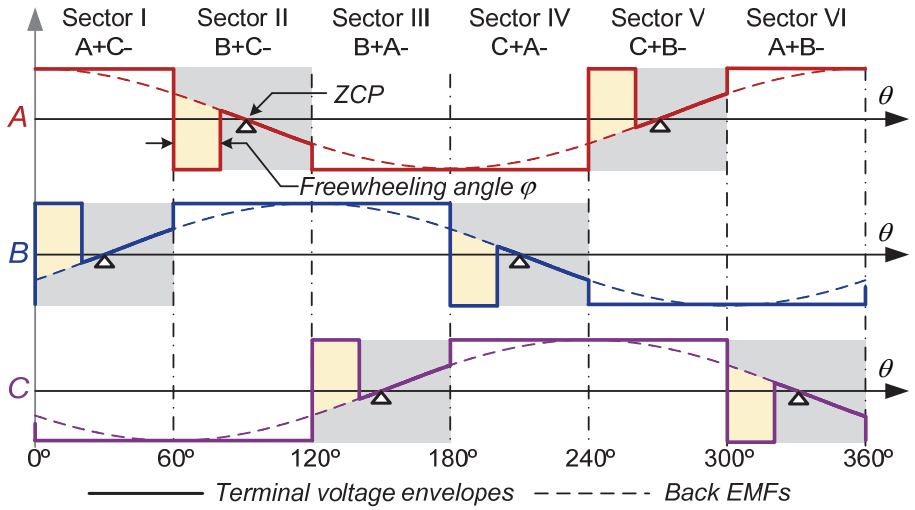

Fig. 5.5. Illustration of terminal voltage envelopes and ZCPs.

5.3.1 Principle of Zero Crossing Detection

Fig. 5.6 (a) shows combined three-phase terminal voltages. The commutation point is located 30º behind the ZCP. Thus, in ZCD-based sensorless method, the commutation point is usually identified by setting 30º delay after ZCP is detected. Assuming the $(k\text{-}1)^{\text{th}}$ ZCP is detected at the position $\theta_{\text{ZCP}}[k-1]$, then the k^{th} commutation is triggered at the position

$$\theta_{\text{CTN-TRG}}[k]=\theta_{\text{ZCP}}[k-1]+30^{\circ}. \tag{5.4}$$

Fig. 5.6 (b) shows the combined terminal voltages considering low f_c / f_e. Due to the retarding update effect of the RSC method, the actual commutation is executed at the position

$$\theta_{\text{CTN-ACT}}(k)=\text{ceil}\left(\theta_{\text{CTN-TRG}}(k)\cdot\frac{N}{60^{\circ}}\right)\cdot\frac{60^{\circ}}{N} \tag{5.5}$$

Then, it continues to detect next ZCP, sets the commutation point and repeats such a procedure. However, in practice, the inverter needs a freewheeling process every time after the commutation. As shown in Fig. 5.6 (b), within this freewheeling duration, the

voltage envelope is not detectable, and it could postpone the ZCP position. Thus, two conditions should be taken into consideration.

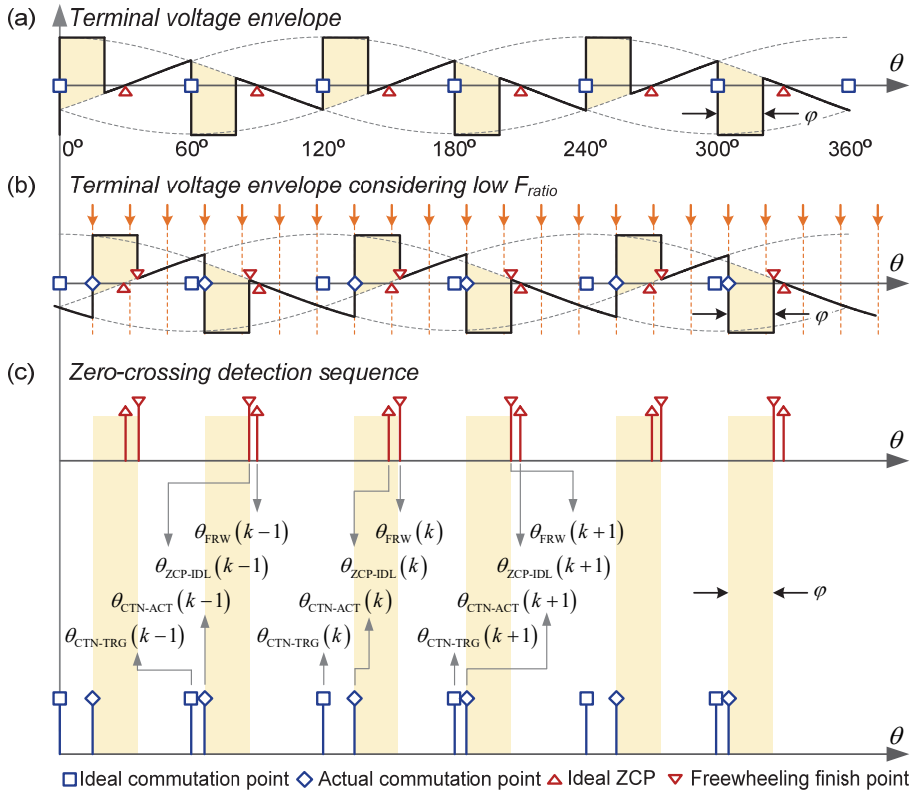

Fig. 5.6. Schematic diagram of terminal voltage envelopes and ZCD sequence. (a) Combined three-phase terminal voltage envelope. (b) Terminal voltage envelope considering low f_c / f_e. (c) ZCD sequence.

In the condition that the ZCP is not overridden by the freewheeling process, the ZCPs should locate at 30º, 90º, 150º…, which can be expressed as

$$\theta_{\text{ZCP-IDL}}[k] = k \cdot 60° + 30° \tag{5.6}$$

If the ZCP is overridden by the freewheeling process, the earliest time that the ZCP can be detected is when the freewheeling process is over, which can be expressed as

$$\theta_{\text{FRW}}[k] = \theta_{\text{CTN-ACT}}[k] + \varphi \tag{5.7}$$

where φ is the freewheeling angle. By combining these two conditions together, the ZCP can be detected at the angle

$$\theta_{\text{ZCP}}[k] = \begin{cases} \theta_{\text{ZCP-IDL}}[k] & \text{normal condition} \\ \theta_{\text{FRW}}[k] & \text{ZCP overriden} \end{cases} \\ = \max\left[\theta_{\text{ZCP-IDL}}[k],\ \theta_{\text{FRW}}[k]\right] \tag{5.8}$$

Then, by repeating the loop from (5.4) to (5.8), it yields an iterative sequence, and the initial value is $\theta_{\text{ZCP}}[k] = 30°$. This model describes the principle of ZCD, in which the freewheeling angle and the PWM update effect are taken into consideration. Thus, the accumulative errors can be analysed.

5.3.2 Instability Caused by Accumulative Errors

The accumulative error is defined as the difference between actual commutation position $\theta_{\text{CTN-ACT}}[k]$ in (5.5) and the ideal commutation position $\theta_{\text{CTN-IDL}}[k]$ in (5.1) as

$$\Delta\theta_{\text{CTN}}[k] = \theta_{\text{CTN-ACT}}[k] - \theta_{\text{CTN-IDL}}[k] \tag{5.9}$$

If the accumulative error sequence $\Delta\theta_{\text{CTN}}(k)$ is bounded, i.e. the sequence $\Delta\theta_{\text{CTN}}[k]$ has finite value as shown in Fig. 5.7 (c), it demonstrates the actual commutation position can keep a finite distance away from the ideal position, and then the sensorless drive is stable. Conversely, if the accumulative error $\Delta\theta_{\text{CTN}}[k]$ is unbounded, i.e. the sequence increases unrestrictedly as shown in Fig. 5.7 (b), it demonstrates the actual commutation position cannot follow the ideal position, and then the sensorless drive is unstable. Therefore, the stable domain of sensorless drive can be identified by checking whether the sequence $\Delta\theta_{\text{CTN}}[k]$ is bounded or not.

The boundedness of the sequence $\Delta\theta_{\text{CTN}}[k]$ depends on two parameters, the freewheeling angle φ and the sector carrier ratio N. By sweeping these two parameters, the stable domain can be identified. The analysis results are shown in Fig. 5.7 (a). The stable margin is zigzag-like and jumps can be observed when N is an integer. This implies potential instability phenomenon. An example is shown in Figs. 5.7 (b) and (c). As the motor speed increases, the number N decreases so the operating point moves left gradually. Assuming the freewheeling angle φ is 15º, when N crosses the integer three from right to left, the operating point will move from the stable domain into the unstable domain. Actually, according to the stable margin, as long as φ is larger than

10º, the sensorless drive cannot exceed the limit speed corresponding to N=3. Every time when N crosses an integer, the sensorless drive may lose stability if φ is larger than the corresponding stable margin. According to previous literature [SHE04] [YAN19b], the freewheeling angle φ increases with the motor speed and load. Accordingly, the PWM retarding update effect will restrict the maximum sensorless operation speed and load.

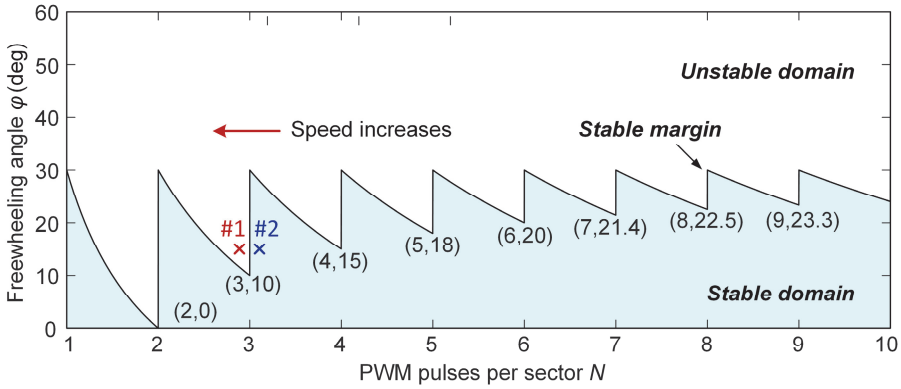

(a) Stable domain.

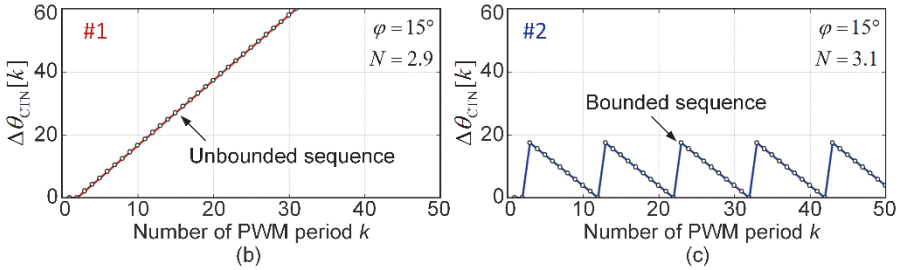

(b) Unbounded iteration, φ=15º, N=2.9. (c) Bounded iteration, φ=15º, N=3.1.

Fig. 5.7. Analysis results of stable domain of the ZCD sequence.

5.4 Principle of Carrier-Synchronized Commutation

5.4.1 Synchronization Scheme

The conventional RSC scheme will cause low-frequency current oscillations and even instability of sensorless operation. In order to solve this problem, a novel CSC strategy is proposed in this section. The initial idea is originated from the synchronized PWM technique used in field-oriented control [SAH16] [CHE16] [YAN17a]. For the synchronized PWM technique, f_c / f_e is maintained as a constant integer through

adjusting the carrier frequency (carrier period) in synchronization with the motor speed. Adopting this ideal in the modulation of BLDC control, as shown in Fig. 5.8 (a), the sector carrier ratio *N* should be maintained as a constant integer to ensure that the PWM sequences are evenly distributed in each sector. However, this method has two drawbacks. In the first place, it requires high resolution speed sensors in order to generate the carrier signal. For high-speed BLDC drives, the speed signal is usually estimated by sensorless algorithm. The accuracy is limited and thus the synchronized PWM technique is hard to implement. In the second place, it has been demonstrated in section 5.2 that synchronizing the carrier frequency will just ensure the commutation delay unchanged, but not eliminate it. Thus, for high-speed sensorless BLDC drive, a method that does not require high-resolution position signals and can eliminate the commutation delay is desired.

To meet the aforementioned requirements, the CSC strategy is proposed as shown in Fig. 5.8 (b). In this method, the carrier signal for each sector is generated independently. It just needs to manipulate the initial carrier phase in each sector, rather than changing the carrier frequency with motor speed. Here, every time when the commutation interrupt arrives, the initial carrier phase is reset to zero. The carrier frequency is fixed and allows fractional sector carrier ratio *N* to happen. When the commutation signal arrives, the previous PWM sequence will be turned off immediately regardless it is on or off at that instant. Then, a new PWM sequence will be generated immediately. In this way, the commutation instant is aligned with the PWM update instant and thereby the commutation is performed at the accurate instant. The delay can be eliminated and the instability caused by accumulative errors will be avoided. Besides, with the CSC strategy, both the conduction interval and the average voltage in each sector are constant, meaning the effective excitation is space symmetrical.

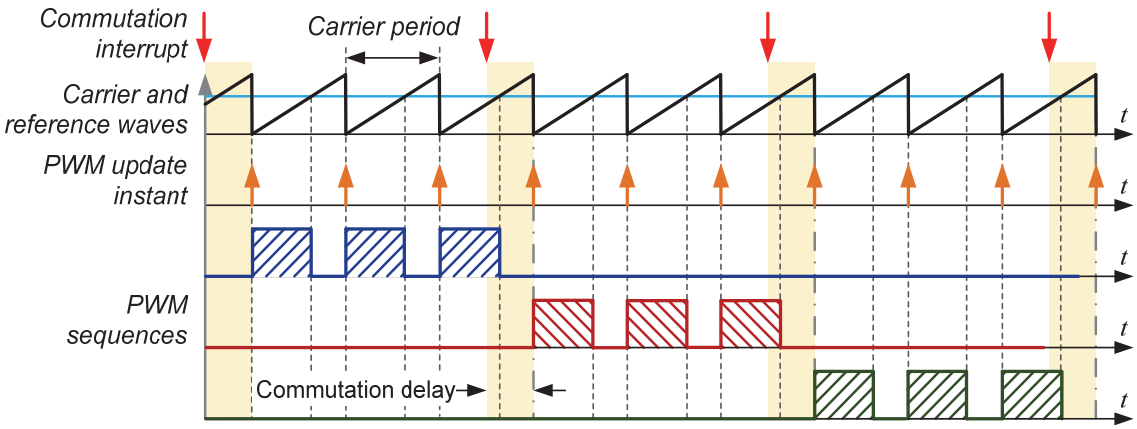

(a) Synchronized PWM [SAH16] [CHE16] [YAN17a].

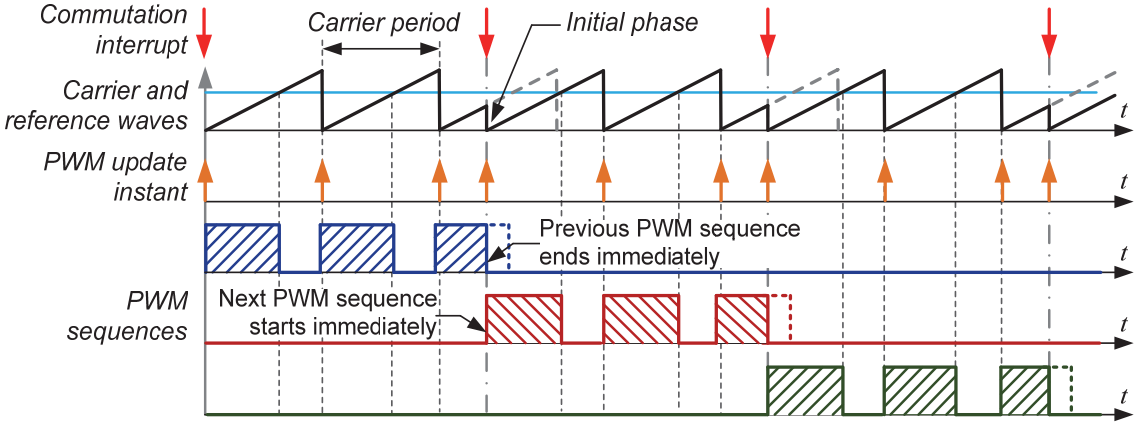

(b) CSC.

Fig. 5.8. Schematic diagrams of two synchronization schemes.

Since the CSC terminates the previous PWM period halfway at commutation instant, two potential concerns should be clarified: 1) whether it will cause additional harmonics; 2) the way to keep linearity between reference and output. These two concerns will be discussed as follows.

5.4.2 Spectral Characteristic Analysis

To investigate the spectral characteristic of CSC, the Fourier series is calculated in this part. Actually, in most time the motor operates with fractional sector carrier ratio N. In the first place, separate the number N by integer part N_Z and decimal part N_D as

$$N = N_Z + N_D \tag{5.10}$$

Fig. 5.9 shows the back EMF and the effective excitation using the CSC. When the commutation signal arrives, it terminates the previous PWM sequence. Depending on the state (on or off) of the previous PWM sequence at the commutation instant, two modes should be distinguished. In mode 1 as shown in Fig. 5.9 (a), the commutation happens when the previous PWM sequence is off and $M \le N_D$. In mode 2 as shown in Fig. 5.9 (b), the commutation happens when the previous PWM sequence is on and $M > N_D$. Then, the spectral analysis will be carried out in terms of these two modes.

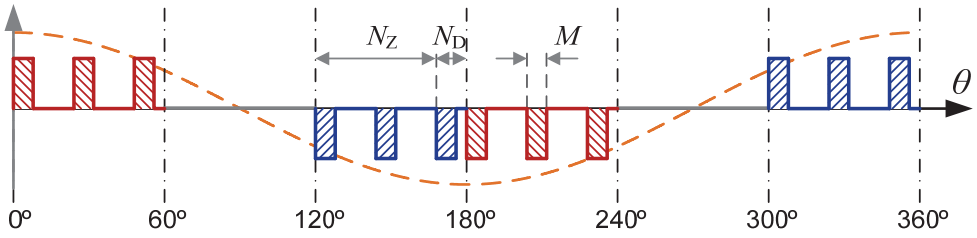

(a) Mode 1.

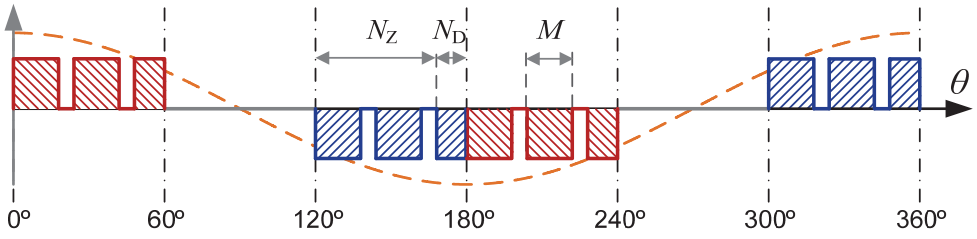

(b) Mode 2.

Fig. 5.9. Schematic diagram of back EMF and effective excitation using CSC.

1) Mode 1: $M \le N_D$

When the duty ratio M is less than or equal to N_D, as shown in Fig. 5.9 (a), there will be $N_Z + 1$ PWM pulses in each sector. Taking sector I for instance, the Fourier coefficient can be calculated as

$$C_{n(M1)} = \frac{1}{2\pi}\sum_{\lambda=0}^{N_Z}\int_{2\pi\frac{f_e}{f_c}\lambda}^{2\pi\frac{f_e}{f_c}(\lambda+M)} e^{-jn\theta}d\theta = \frac{1}{-j2\pi n}\frac{\left(E_n^{N_Z+1}-1\right)\left(E_n^{M}-1\right)}{E_n-1} \tag{5.11}$$

where

$$E_n = e^{-jn\frac{f_e}{f_c}2\pi} \tag{5.12}$$

Here, λ denotes the index of PWM pulse. Then, the effective excitation of phase A is the sum of the excitations in each sector. By using the time-shifting property, the Fourier coefficient can be calculated as

$$\begin{aligned} C_{n(\mathrm{A})} &= \frac{1}{2\pi}\sum_{\lambda=0}^{N_Z}\int_{2\pi\frac{f_e}{f_c}\lambda}^{2\pi\frac{f_e}{f_c}(\lambda+M)} e^{-jn\theta}d\theta - \frac{1}{2\pi}\sum_{\lambda=0}^{N_Z}\int_{2\pi\frac{f_e}{f_c}\lambda+\frac{2\pi}{3}}^{2\pi\frac{f_e}{f_c}(\lambda+M)+\frac{2\pi}{3}} e^{-jn\theta}d\theta \\ &\quad -\frac{1}{2\pi}\sum_{\lambda=0}^{N_Z}\int_{2\pi\frac{f_e}{f_c}\lambda+\pi}^{2\pi\frac{f_e}{f_c}(\lambda+M)+\pi} e^{-jn\theta}d\theta + \frac{1}{2\pi}\sum_{\lambda=0}^{N_Z}\int_{2\pi\frac{f_e}{f_c}\lambda+\frac{5\pi}{3}}^{2\pi\frac{f_e}{f_c}(\lambda+M)+\frac{5\pi}{3}} e^{-jn\theta}d\theta \\ &= C_{n(M1)} - C_{n(M1)}\cdot e^{-jn\frac{2\pi}{3}} - C_{n(M1)}\cdot e^{-jn\pi} + C_{n(M1)}\cdot e^{-jn\frac{5\pi}{3}} \\ &= \begin{cases} \left(3\pm j\sqrt{3}\right)C_{n(M1)} & n=6k\pm1 \\ 0 & elsewhere \end{cases} \end{aligned} \tag{5.13}$$

2) Mode 2: $M > N_D$

When the duty ratio M is greater than N_D, as shown in Fig. 5.9 (b), N_Z complete pulses and part of the last pulse are performed in each sector. In this case, its Fourier coefficient can be obtained by taking off the chop-off periods as

$$\begin{aligned} C_{n(M2)} &= \frac{1}{2\pi}\left(\int_0^{\frac{\pi}{3}} e^{-jny}dy - \sum_{\lambda=0}^{N_Z-1}\int_{2\pi\frac{f_e}{f_c}(\lambda+M)}^{2\pi\frac{f_e}{f_c}(\lambda+1)} e^{-jn\theta}d\theta\right) \\ &= \frac{1}{2\pi}\left(e^{-jn\frac{\pi}{3}} - 1 + \frac{1}{jn}\frac{\left(E_n^{N_Z}-1\right)\left(E_n-E_n^{M}\right)}{E_n-1}\right) \end{aligned} \tag{5.14}$$

With the same method as in (5.13), the effective excitation of phase A can be calculated as

$$\begin{aligned} C_{n(\mathrm{A})} &= C_{n(M2)} - C_{n(M2)}\cdot e^{-jn\frac{2\pi}{3}} - C_{n(M2)}\cdot e^{-jn\pi} + C_{n(M2)}\cdot e^{-jn\frac{5\pi}{3}} \\ &= \begin{cases} \left(3\pm j\sqrt{3}\right)C_{n(M2)} & n=6k\pm1 \\ 0 & elsewhere \end{cases} \end{aligned} \tag{5.15}$$

It concludes from (5.13) and (5.15) that only when $n=6k\pm1$ the Fourier coefficient has non-zero value. This means the CSC scheme will only induce $6k\pm1$ order harmonics regardless the carrier ratio N is an integer or a fraction. It should be noted that when N is a fraction, the last PWM period in each sector will be terminated

early; when N is an integer, all the PWM period in each sector is complete and thereby the CSC is equivalent to synchronized PWM techniques in [SAH16] [CHE16] [YAN17a] in this situation. Therefore, in terms of harmonic orders, the proposed method will not introduce additional harmonics orders compared to the synchronized PWM techniques.

In terms of the harmonic distortion, the theoretical analysis result using (5.13) and (5.15) is shown in Fig. 5.10, in which the harmonic spectrum with $M=0.5$ and the sector carrier ratio N ranging from 2 to 6 (including fractions) is analysed. It can be observed that for any harmonic orders, the magnitude varies continuously with the sector carrier ratio N. Besides, the weighed total harmonic distortion (WTHD) that can predict the distortion in the current and subsequent additional losses is calculated and shown in the last column of Fig. 5.10. Note that the WTHD also increases gradually with the speed without jumps. With the CSC scheme, the WTHD of a fraction N, e.g. $N=3.3$, is between those of its adjacent integers, e.g. $N=3$ and $N=4$. It demonstrates that the WTHD is not sensitive to integer or fraction N. Thus, the CSC scheme will not cause additional harmonic distortion compared to the synchronized PWM technique.

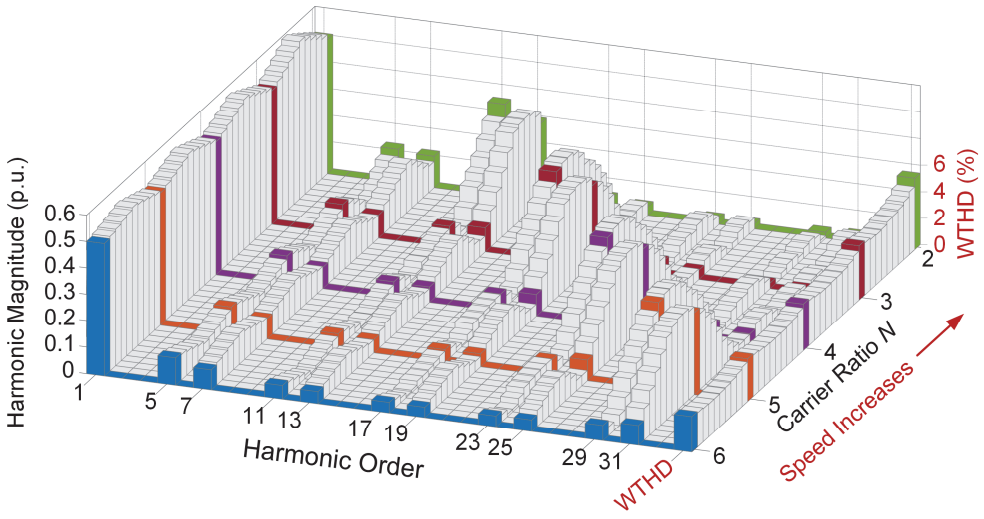

Fig. 5.10. Theoretical harmonic spectrum for effective excitation of CSC scheme, M=0.5.

5.4.3 Keeping Linearity between Reference and Output

Another concern that the CSC arouses is the nonlinear relation between the reference duty ratio M and the actual inverter output. Since it allows fractional pulses generated in each sector, the average excitation does not only depend on the reference duty ratio M, but also the sector carrier ratio N. In this part, the gain compensation for linearity is investigated by calculating the average excitation.

For the mode 1, assuming the reference duty ratio is M_1 and average excitation can be expressed as

$$M_{\text{ave}} = \frac{\left(N_{\text{Z}}+1\right)\cdot M_1 / f_{\text{c}}}{1/6f_e} = \frac{N_{\text{Z}}+1}{N}\cdot M_1 . \tag{5.16}$$

Likewise, for the mode 2, assuming the reference duty ratio is M_2, the average excitation can be calculated as

$$M_{\text{ave}} = 1-\frac{N_{\text{Z}}\cdot\left(1-M_2\right)/ f_{\text{c}}}{1/6f_e} = 1-\frac{N_{\text{Z}}}{N}\cdot\left(1-M_2\right). \tag{5.17}$$

By solving the equations (5.16) and (5.17), M_1 and M_2 can be calculated as

$$M = \begin{cases} M_1 = \dfrac{N}{N_{\text{Z}}+1}M_{\text{ave}} & \text{Mode 1 } M_1 \le N_{\text{D}} \\ M_2 = 1-\dfrac{N}{N_{\text{Z}}}\left(1-M_{\text{ave}}\right) & \text{Mode 2 } M_2 > N_{\text{D}} \end{cases}. \tag{5.18}$$

Fig. 5.11 shows the overall control system with the proposed CSC scheme. The ZCD-based sensorless method is employed to estimate the rotor position, speed and the sector carrier ratio N. After obtaining the average excitation M_{ave} from the output of the controller, the linearity compensation (5.18) is utilized to calculate the reference duty ratios M_1 and M_2 corresponding to modes 1 and 2, respectively. Then, it selects the mode by comparing M_1 (and M_2) with N_{D}. The calculated reference duty ratio will be utilized to generate the new PWM sequence. In this way, it ensures the linearity between the reference and the inverter output.

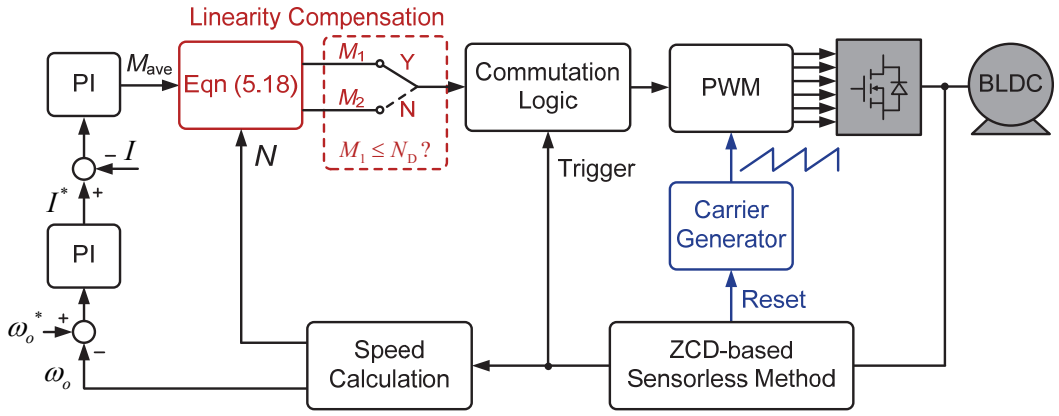

Fig. 5.11. Sensorless control system with CSC.

5.5 Simulation and Experimental Results

5.5.1 Simulation Results

Fig. 5.12 shows the Matlab simulation results of drive failure caused by accumulative errors of ZCD-based sensorless method. The carrier frequency of inverter is 20 kHz and the parameters of Motor-I in Appendix are used for simulation. In Fig. 5.12 (a), the relatively light load (20 mNm) is applied. In initial stage when the speed is lower than 1111 Hz ($N>3$), the amount of commutation delay is bounded and the drive can keep its stability, although low-frequency oscillations can be observed in the phase current. However, as the motor speed increases gradually, N tends to approach and cross the integer three. According to Fig. 5.7, once the speed exceeds 1111 Hz, then $N<3$ and the stable margin decreases to only 10º. Thus, the drive becomes unstable and the drive fails finally. Likewise, a relatively heavy load (30 mNm) is applied in Fig. 5.12 (b). The drive finally fails at the speed 833 Hz, corresponding to $N=4$ for the same reason. The simulation results demonstrate that with the conventional commutation method, the maximum sensorless operation speed and load are restricted.

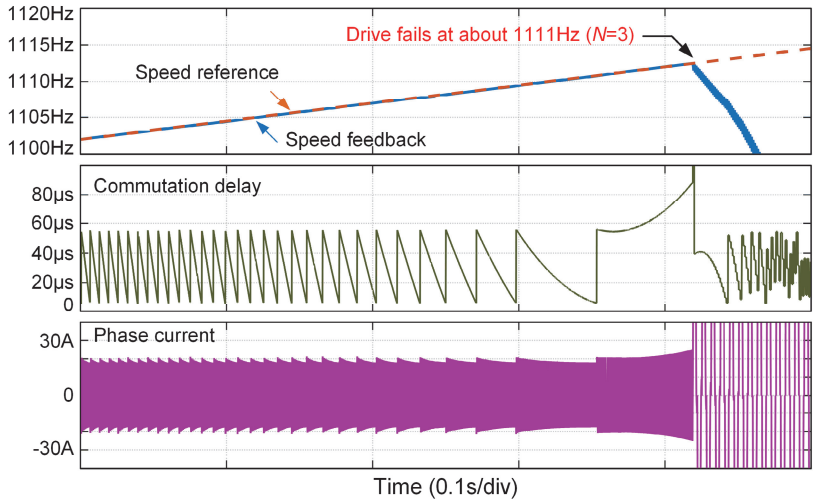

(a) Load torque is 20 mNm, drive fails at f_c=1111 Hz (N=3).

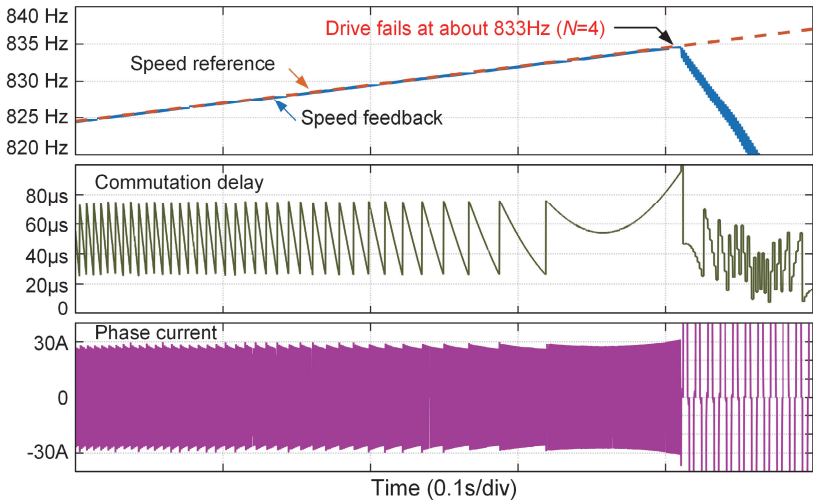

(b) Load torque is 30 mNm, drive fails at f_c=833 Hz (N=4).

Fig. 5.12. Simulation results of drive failure caused by accumulative errors in ZCD-based sensorless method, f_c=20 kHz.

5.5.2 Experimental Results

The proposed compensation algorithm is verified at the high-speed BLDC motor experimental platform shown in Appendix. The high-speed BLDC Motor-I in Appendix 1 is used in this chapter. The DC-link voltage is 25V.

Fig. 5.13 shows the experimental results of drive failure during acceleration. Two switching frequencies are adopted to verify the instability mechanism, f_c=16.67 kHz in Fig. 5.13 (a) and f_c=20 kHz in Fig. 5.13 (b). The drive always fails at the speed when N=3 due to accumulative errors. Both the experimental and simulation results agree

with the theoretical analysis. Therefore, it demonstrates that the maximum sensorless operation speed and load are restricted, if the conventional commutation method is utilized.

Fig. 5.14 shows the comparative experimental results of PWM gate signals between conventional and proposed methods. A general-purpose I/O port changes its high/low state to represent the commutation interrupt signal. With the carrier frequency of 20 kHz and fundamental frequency of 1 kHz, there are average 3.33 pulses in each sector. Therefore, as shown in Fig. 5.14 (a), since only integer number of PWM pulses can be generated in the conventional RSC scheme, there could be three or four pulses in a sector. Besides, the time grid is set as 166.7 μs, which is just equal to the sector period when f_e=1 kHz. Thus, it is obvious that there exists commutation delay for every gate signal. On the other hand, with the proposed CSC scheme utilized in Fig. 5.14 (b), every time when the commutation interrupt occurs, the previous gate signal ends and the next gate signal starts without any delay. Accordingly, from the point of view of PWM gate signals, the proposed CSC scheme is effective to eliminate the commutation delay caused by PWM.

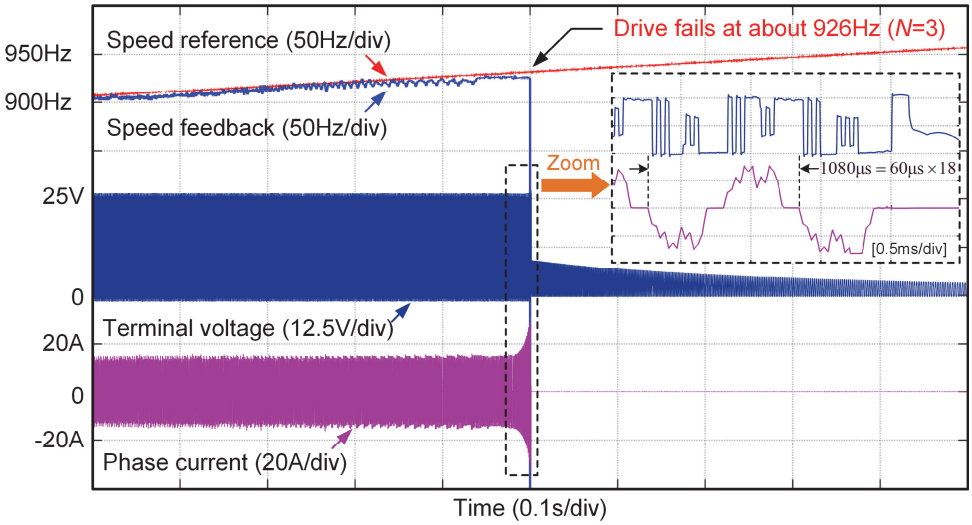

(a) f_c=16.67 kHz, drive fails at f_e=926 Hz (N=3).

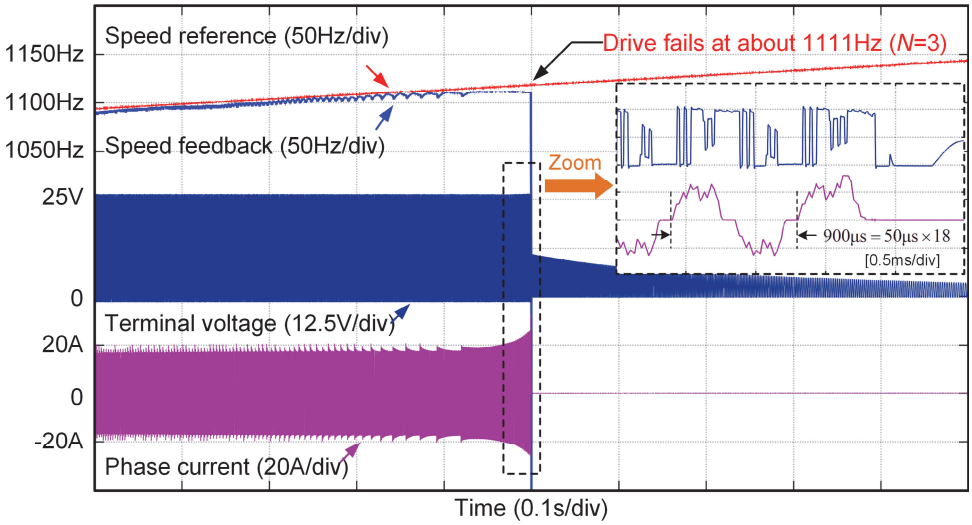

(b) f_c=20 kHz, drive fails at f_e=1111 Hz (N=3).

Fig. 5.13. Experimental results of drive failure caused by accumulative errors in ZCD-based sensorless method.

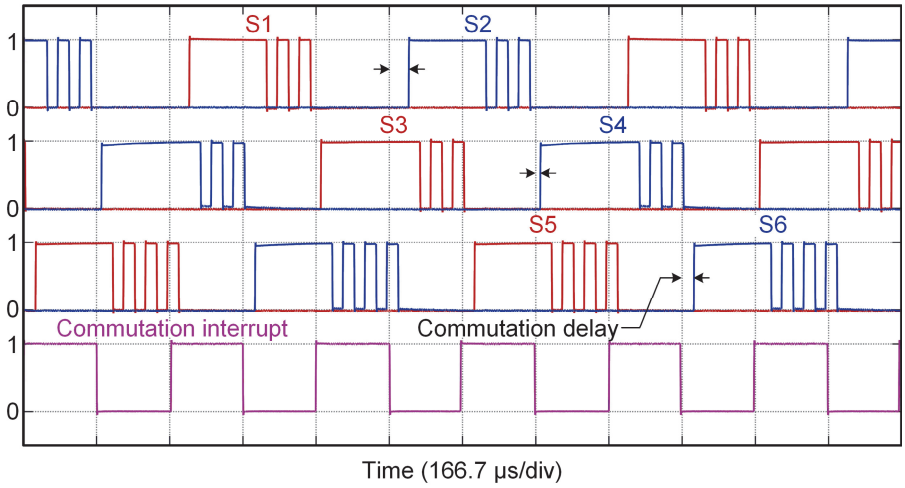

(a) Conventional RSC scheme.

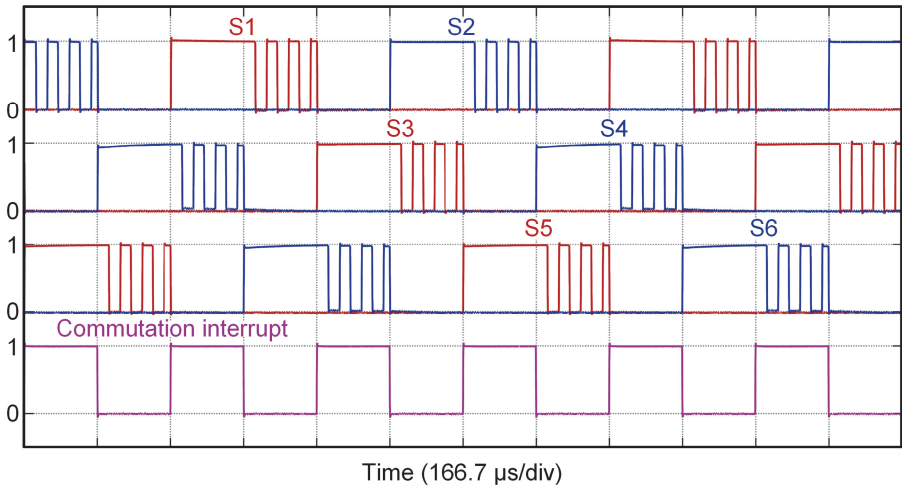

(b) Proposed CSC scheme.

Fig. 5.14. Experimental results of the commutation interrupt and six gate signals, f_c=1 kHz and f_c=20 kHz.

Fig. 5.15 shows comparative experimental results of sensorless operation at 60 000 r/min. From top to bottom, the terminal voltage, commutation interrupt signal, sector number and phase currents are given, respectively. Besides, the phase-A current is shown in long time scale. It is clear that the commutation interrupt occurs with consistent interval for both of the commutation methods. Under this premise, for conventional RSC method in Fig. 5.15 (a), the practical conduction duration in every sector is inconsistent, leading to drastic current fluctuations. When the proposed CSC is employed in Fig. 5.15 (b), the phase currents keep flat amplitude without fluctuations. Besides, the current amplitude is much smaller than that of conventional commutation method. The proposed CSC presents better steady-state performance than the conventional RSC does.

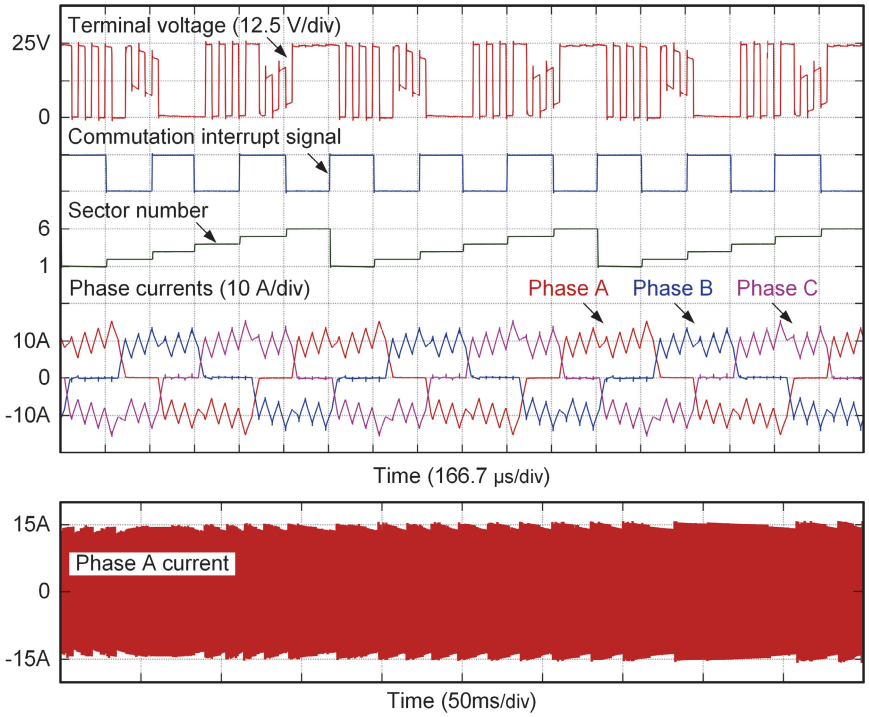

(a) Conventional RSC scheme.

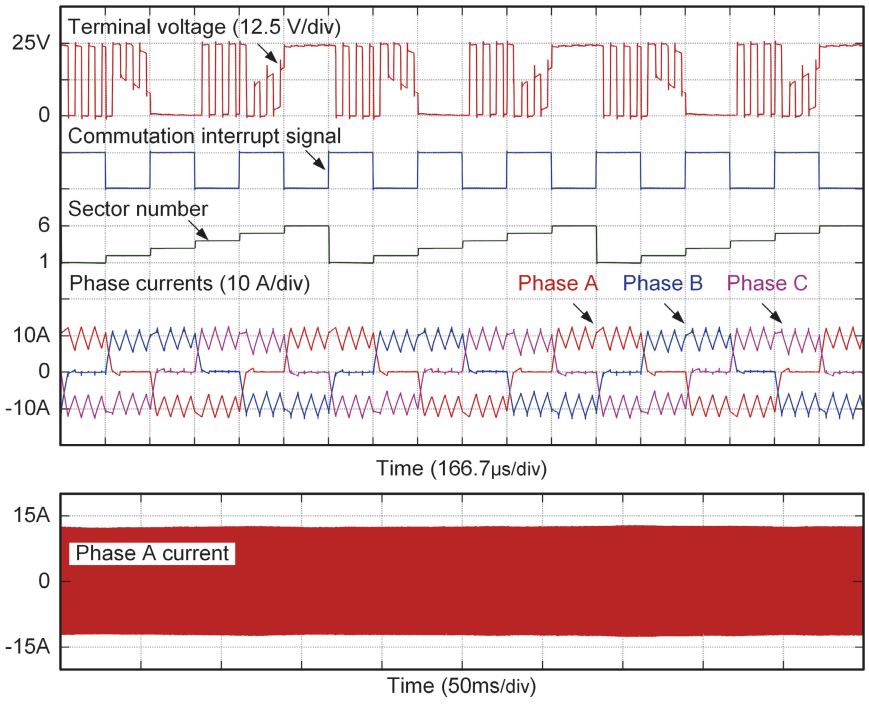

(b) Proposed CSC scheme.

Fig. 5.15. Performance comparison of sensorless operation at 60 000 r/min, f_e=1 kHz, f_c=20 kHz.

Fig. 5.16 compares the sensorless drive performance of machine acceleration from 500 Hz to 1.3 kHz. From top to bottom, the speed reference, the speed feedback and the phase current are shown, respectively. With the conventional commutation method in Fig. 5.16 (a), when the speed reaches 1111 Hz (N=3), the drive fails due to the

accumulative errors. When the proposed carrier synchronized commutation strategy is utilized in Fig. 5.16 (b), the drive can accelerate up to 1300 Hz. Besides, the phase current amplitude of proposed method is lower than that of conventional RSC in high-speed region (700 Hz and above). Therefore, it demonstrates the proposed CSC can remarkably reduce the phase current amplitude, and achieve higher speed and higher load, reflecting its engineering application value.

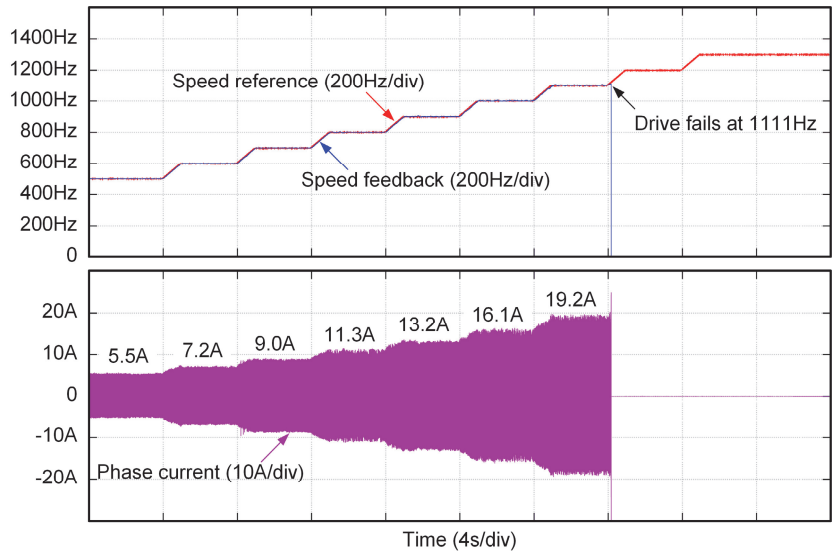

(a) Conventional RSC scheme.

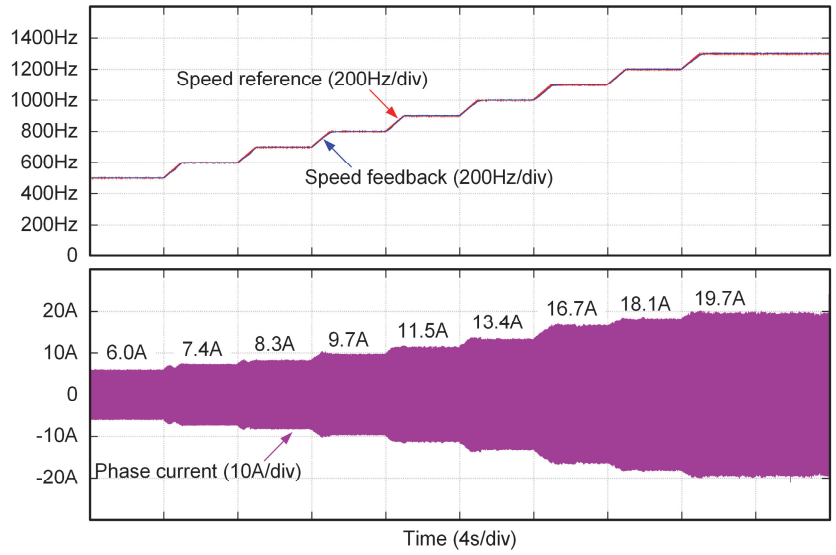

(b) Proposed CSC scheme.

Fig. 5.16. Comparison of sensorless drive performance for machine acceleration, f_c=20 kHz.

5.6 Summary

This chapter has investigated the influences of insufficient switching ratio and the commutation delay caused by PWM generation on high-speed BLDC drives. The retarding PWM update will cause low-frequency current oscillations and produce additional losses, especially when the switching ratio is not sufficient. Additionally, the conventional commutation method will cause accumulative errors in sensorless operation and will further lead to instability issue. Thus, to suppress these problems, a novel CSC strategy has been proposed. By enforcing the PWM update when the commutation interrupt occurs, the power switch can take action at the accurate instant. Experimental results demonstrate that the proposed method can eliminate the commutation delay caused by PWM generation. The instability phenomenon can be avoided and the current control performance can be remarkably improved.

CHAPTER 6

Spectral Analysis and Sideband Harmonic Cancellation of Six-Step BLDC Operation with Low Switching Ratio

6.1 Introduction

For high-speed drives, the inverter usually operates at the status of low switching ratio, which means insufficient PWM waves can be generated in each fundamental period. Consequently, abundant sideband harmonic current components will be produced, whose frequencies are widely distributed on the spectrum, not only around the carrier frequency, but also in low frequency range, even lower than the fundamental frequency [ODA13]. These undesired sideband harmonic components will lead to additional copper and iron losses [XUE17] [KOW15], vibration [WUS19] and acoustic noise [DEN19] [LIA18]. Besides, it is demonstrated in [JAR11] [STU12] that low frequency sideband harmonic components can cause serious malfunction and even breakdown.

Some efforts have been made to investigate the mechanism of the sideband harmonic generation [JAR11] [STU12] [LIA16] [SHI18]. A novel analysis approach based on flux trajectories was proposed by [JAR11], in which large amount of experimental tests were investigated to demonstrate the existence of subharmonics in high-speed motor drives. In [STU12], the influence of three different sampling methods on the subharmonics was compared, including regular-sampled, natural-sampled, and oversampled PWM techniques. However, no theoretical explanation has been presented for the generation of subharmonics. Some analytical models were introduced to describe the harmonic spectra of the voltage and current in [LIA16] [SHI18], but did not discuss the low frequency sideband harmonic and subharmonic problems. Besides, the above work mainly focused on continuous modulation approaches, e.g. sinusoidal PWM and space vector modulation. However, for the six-step BLDC operation, which is the most widely used method in high-speed applications, the modulating signal is

discontinuous square-wave. The sideband harmonics produced by PWM in BLDC drives are quite complicated and have hardly been investigated.

From another point of view, some potential techniques can mitigate the sideband harmonic issue. The most simple and direct solution is to increase the switching frequency of the inverter. When sufficient PWM waves are generated in each fundamental period, the sideband harmonic components can be reduced considerably. However, on the one hand, while the machine losses decrease due to higher switching frequencies, the converter losses increase due to the increased switching loss. Although the high-speed SiC [FUY18] and GaN [LEE18b] power devices can be used, the cost is hard to be accepted for low power and low cost applications. In addition, for those high power applications, the switching frequency is strictly limited within several hundred hertz considering the switching losses [SAH18]. Besides, another solution is to assign the functions of modulation and commutation to two independent converters. In [GUC18] and [ZWY08], a DC-DC converter is connected with inverter to regulate the input voltage or current. In this way, the inverter can operate at unmodulated square-wave mode and thus the sideband harmonic issue can be avoided. However, the additional DC-DC converter and passive components such as inductors and capacitors will inevitably increase the cost and system volume. In [LEE20], a sideband harmonic compensator was proposed to reduce the sideband harmonic currents. This method features no requirement of additional hardware. However, it is focused on continuous modulation and not appropriate for six-step BLDC operation. For the BLDC drives of classic inverters, the low-cost and practical solution would be based on improved PWM commutation techniques. Existing literature on PWM commutation techniques of BLDC drives are focused on torque ripple reduction [XIA14] [LIN11] and position sensorless facilitation [LAI11]. There is little work in published documents on PWM commutation patterns for sideband harmonic reduction of six-step BLDC control.

The main contribution of this chapter contains two aspects. In the first place, to describe the harmonic spectrum of six-step operation, an extended geometric wall model is proposed. The geometric wall model and double Fourier series are well-known analytical methods of determining the harmonic components of PWM

waveforms, which were proposed and developed by classical documents [HOL03] [BLA93]. However, this model is limited in real number field, which can only be used for the Fourier decomposition of one-dimensional scalar signals. In order to analyse two-dimensional space vector signal generated by three-phase inverter, this model is extended to complex number field in this chapter. It demonstrates the two conventional commutation patterns, i.e. regular-sampled commutation (RSC), natural-sampled commutation (NSC), will produce additional sideband harmonic currents, and will further lead to high-level torque ripples. The second contribution is that an improved commutation pattern, i.e. carrier-synchronized commutation (CSC), is proposed to diminish the undesired sideband harmonics.

The comparative investigation between RSC and CSC patterns in terms of the commutation delay issue have been carried out in chapter 5. In this chapter, the sideband harmonic issue will be investigated among three commutation patterns, i.e. RSC, NSC and CSC patterns.

The chapter is arranged as follows. Section 6.2 describes the six-step operation with three commutation patterns. In section 6.3, an analytical study on spectral analysis of RSC and NSC patterns is carried out. It theoretically elaborates how the high-level sideband harmonics are generated in the condition of low switching ratio. Then, section 6.4 discusses the spectral analysis of CSC pattern, which shows the sideband harmonics can be avoided in theory. In section 6.5, the issue of torque ripples is discussed. It describes how sideband harmonic currents produce low-frequency torque ripples. Simulation and experimental validation are presented in section 6.6, and section 6.7 summarize this chapter.

The study in this chapter has been published in

L. Yang, Z. Q. Zhu, Hong Bin, and Liming Gong, “Spectral analysis and sideband harmonic cancellation of six-step operation with low switching ratio for high-speed brushless DC drives,” *IEEE Trans. Ind. Electron.*

6.2 Mechanism of Six-Step Commutation With PWM Generation

Fig. 6.1 (a) shows a typical drive topology of BLDC motors. Here, V_{dc} is the DC-link voltage, i_A, i_B and i_C are the phase currents, e_A, e_B and e_C, are the back EMF, R and L are the phase resistance and inductance. For the six-step BLDC drive method, a drive cycle is divided into six sectors. In each 60º sector, two of the three phases are conducted, generating a voltage space vector. Taking sector I for instance, phases A and C are conducted through the switches S_1 and S_6, imposing a voltage space vectors on the motor, which can be represented by the switching state $\boldsymbol{V}_1$. Six basic switching states $\boldsymbol{V}_1 \ldots \boldsymbol{V}_6$ correspond to six sectors, respectively, as shown in Fig. 6.1 (b). When the rotor rotates from one sector to the next one, the inverter needs to commute its conducting status. Assuming that y denotes the rotor position, the switching states $\boldsymbol{v}(y)$ can be expressed as

$$\boldsymbol{v}(y)=\begin{cases} e^{j\frac{\pi}{6}}=\boldsymbol{V}_1 & y\in\left[0,\frac{1}{3}\pi\right), \quad e^{j\frac{7\pi}{6}}=\boldsymbol{V}_4 \quad y\in\left[\pi,\frac{4}{3}\pi\right) \\ e^{j\frac{\pi}{2}}=\boldsymbol{V}_2 & y\in\left[\frac{1}{3}\pi,\frac{2}{3}\pi\right), \quad e^{j\frac{3\pi}{2}}=\boldsymbol{V}_5 \quad y\in\left[\frac{4}{3}\pi,\frac{5}{3}\pi\right) \\ e^{j\frac{5\pi}{6}}=\boldsymbol{V}_3 & y\in\left[\frac{2}{3}\pi,\pi\right), \quad e^{j\frac{11\pi}{6}}=\boldsymbol{V}_6 \quad y\in\left[\frac{5}{3}\pi,2\pi\right) \end{cases} \tag{6.1}$$

In the digital drive system, this commutation behaviour of the inverter in Fig. 6.1 (a) is usually controlled by PWM signals of the microprocessor. When the commutation signal arrives, it should turn off the previous PWM sequence and turn on the next one. However, in high-speed region when the switching ratio is insufficient, there could be only a few PWM waves in each sector. Improper commutation patterns will result in time delay, sideband harmonics, torque ripples and significant additional losses. Here, two conventional BLDC commutation patterns, i.e. RSC and NSC patterns, together with the proposed CSC pattern, are introduced as follows.

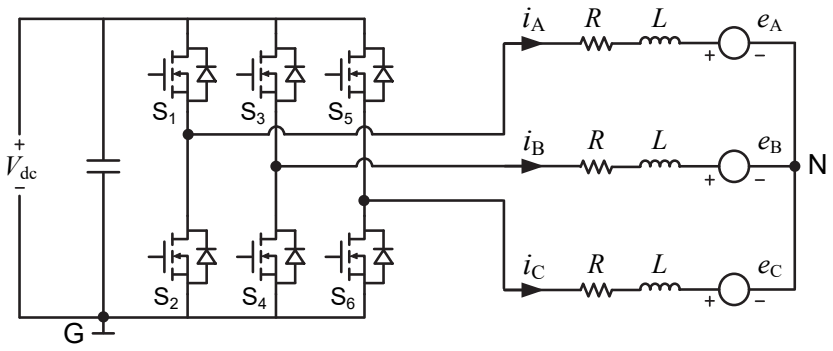

(a) Drive topology.

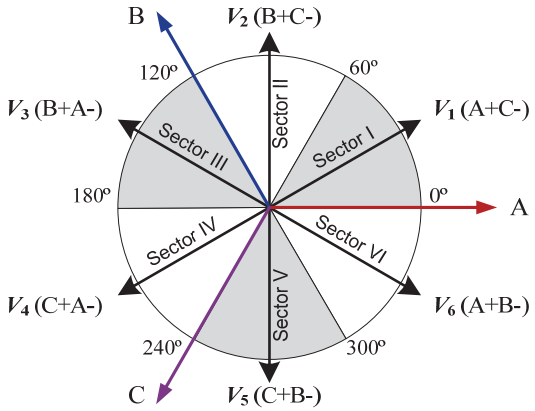

(b) Illustration of six sectors and switching states.

Fig. 6.1. High-speed BLDC drive with six-step operation.

6.2.1 Regular-Sampled Commutation (RSC)

Conventionally, for the discontinuous square-wave modulation, the default and most commonly used pattern is based on regular-sampled PWM method [CUI15] [PAR18]. As shown in Fig. 6.2, assuming that *M* demotes the duty ratio, the PWM sequences is regularly updated at the beginning of each carrier period. When the commutation interrupt arrives, the PWM sequence will not update until the present PWM wave is finished. Limited by this retarding updating mechanism, the actual commutation is not executed exactly at the interrupt instant. The commutation delay can reach a whole carrier period. In addition, since it only allows integer number of PWM waves generated in each sector, in practice, the conducting duration will be arranged unequally across the six sectors. For normal speed BLDC drives, these influences can be ignored, because the switching ratio is sufficient. As the speed increases, the number of PWM waves in a fundamental period becomes less. There could be only a few PWM waves in each sector in high-speed range. In such a situation,

the RSC will lead to serious sideband harmonic problems, which will be discussed in next section.

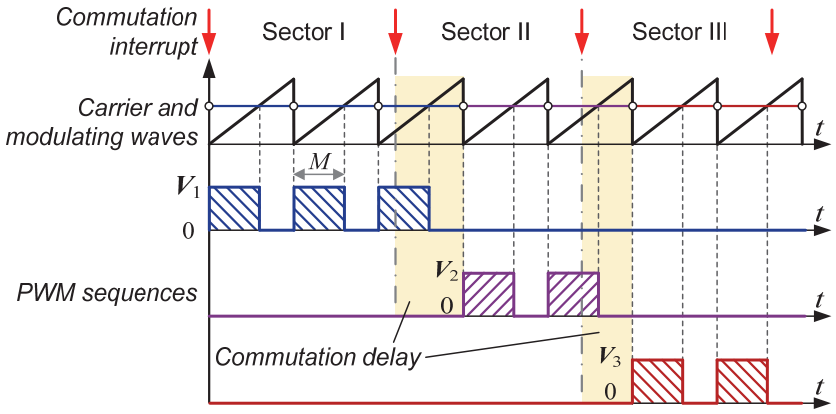

Fig. 6.2. Schematic of PWM generation scheme based on RSC pattern.

6.2.2 Natural-Sampled Commutation (NSC)

In the past, natural-sampled PWM was usually implemented with analog circuits. Nowadays, it can be realized by high-level digital controllers, e.g. field programmable gate array (FPGA) [LIN11]. In particular, for the six-step operation, since the modulating signal is square-wave, the natural-sampled PWM can be implemented by general-purpose microcontrollers with the voltage polarity detection algorithm [KEZ17].

Fig. 6.3 shows the six-step operation based on natural-sampled PWM method. In this method, the PWM sequences can be updated at any instant within a carrier period. When the commutation interrupt arrives, the previous PWM sequence terminates immediately, and the next PWM sequence is generated following up the previous one. In this way, the commutation signal is generated exactly at the interrupt instant. The remaining commutation delay is caused by some inevitable factors and is relatively small, e.g. dead time and device delay (turn on/off delay of the gate drivers and power switches) [KEZ17]. In addition, since this mechanism allows fraction number of PWM waves generated in each sector, it ensures every sector occupies the same duration. However, as shown in Fig. 6.3, the PWM sequences cannot be guaranteed symmetrical

in six sectors. The NSC pattern is also prone to generate sideband harmonic components (see next section).

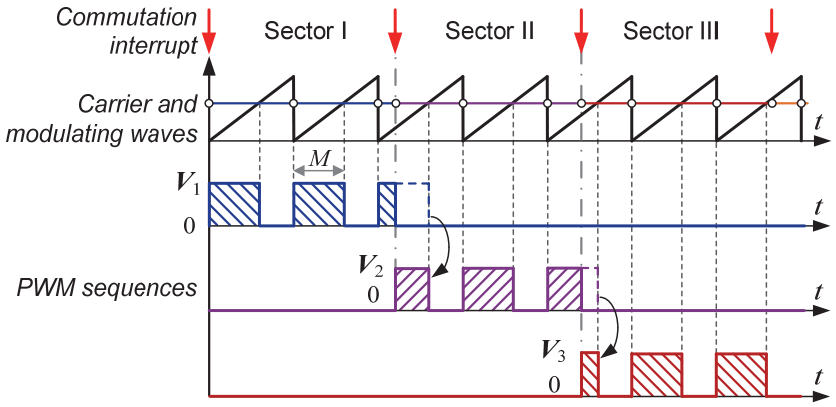

Fig. 6.3. Schematic of PWM generation scheme based on NSC pattern.

6.2.3 Carrier-Synchronized Commutation (CSC)

In continuous modulation schemes, the synchronized PWM strategy is usually employed to avoid the sideband harmonics [SAH18] [CHE16] [YAN17a]. In this method, the carrier frequency changes in synchronization with the motor speed to maintain integer times of fundamental frequency, which means the high resolution position or speed sensor is necessary. However, for high-speed BLDC drives, the speed signal is usually estimated by sensorless algorithm. The accuracy is limited and thus the synchronized PWM strategy is hard to implement. Alternatively, the proposed CSC pattern can be utilized, which does not require high-resolution position sensors and thereby is suitable for sensorless high-speed BLDC drives.

Fig. 6.4 illustrates the implementation of proposed CSC pattern. Instead of changing the carrier frequency with motor speed, the CSC pattern just needs to manipulate the initial carrier phase in each sector. In steady state, the period of every sector is the same. As long as the initial carrier phase of each sector is identical, the PWM sequences can be guaranteed symmetrical in space. Then, the sideband harmonics can be avoided. To realize this idea, every time when the commutation signal arrives, the initial carrier phase is synchronously reset to a zero. Then, the previous PWM sequences ends immediately and then the next PWM sequence starts to

generate. More details about the implementation of the CSC pattern have been described in chapter 5.

The commutation signal of the CSC pattern is generated exactly at the interrupt instant (remaining delays include dead time and device delay). Each sector occupies the same duration and the PWM sequences are symmetrical in space. Consequently, the sideband harmonic issue can be avoided (see section 6.4). Considering the commutation interrupt could happen when the present PWM status is either on or off, two cases are distinguished in Fig. 6.4.

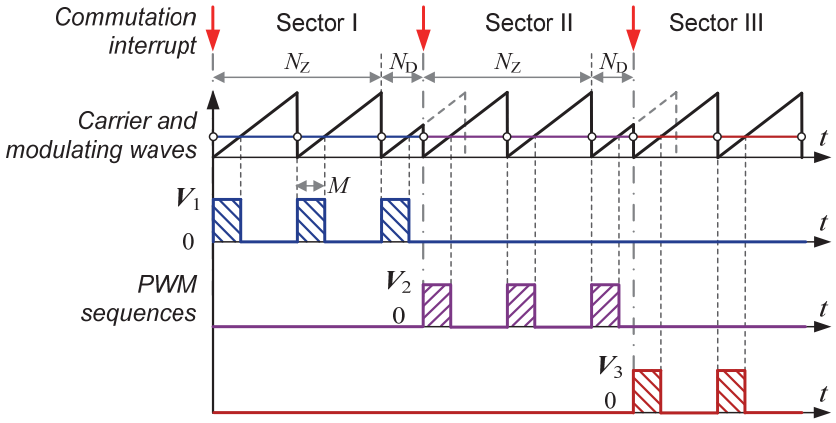

(a) Case 1.

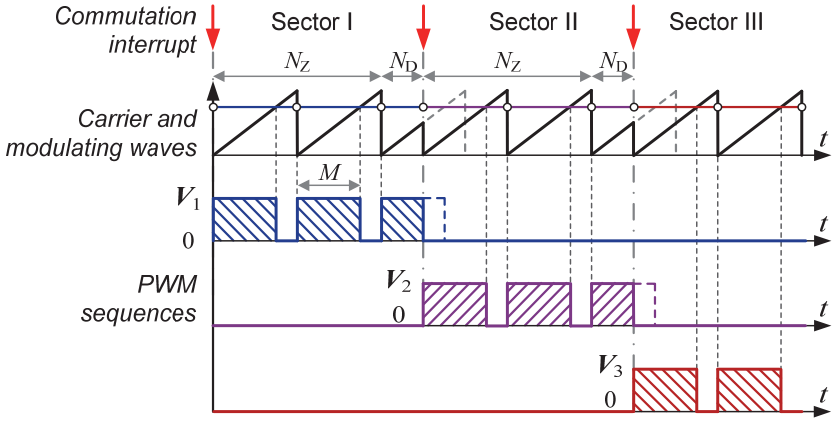

(b) Case 2.

Fig. 6.4. Schematic of PWM generation scheme based on CSC pattern.

6.3 Spectral Characteristics of NSC and RSC Patterns

Under normal conditions, the six-step voltage space vector contains $1+6k$ order harmonics, e.g. -5th, 7th, -11th, 13th, etc. However, under the circumstance of low

switching ratio, some sideband harmonics will be produced by the RSC and NSC patterns. These sideband harmonics will not only generate extra copper and iron losses, but also lead to torque ripples, vibrations and acoustic noise. Therefore, in order to reveal the spectral characteristics of RSC and NSC patterns, an analytical study is carried out as follows.

6.3.1 Extended Geometric Wall Model and Double Fourier Series

The PWM generation mechanism can be described by the geometric wall model in [HOL03] [BLA93]. However, this widely used model is initially limited in real number field, which can only be used to analyse one-dimensional scalar signals, e.g. the PWM sequence of a phase leg. In order to analyse two-dimensional PWM sequences generated by three-phase inverter, this model is extended to complex number field in this chapter.

In the first place, in this developed model, the unit cell is defined in Fig. 6.5. Here, x represents the carrier phase $\omega_c t$, y represents the fundamental phase $\omega_e t$, ω_c and ω_e are the angular frequencies of carrier and fundamental waves, respectively. The "walls" are denoted by the boundaries of different areas, representing the applied modulation waveform. For instance, Fig. 6.5 (a) shows the unit cell of sine-sawtooth modulation [HOL03]. The heights of these walls (areas) are real numbers (1 and 0), corresponding to the two possible switching states of a phase leg. In the developed model for the six step modulation, as shown in Fig. 6.5 (b), a unit cell consists of seven square areas. The height of the areas are not real numbers as the conventional model, but complex numbers $\boldsymbol{V}_1 \ldots \boldsymbol{V}_6$ and 0, corresponding to seven possible switching states generated by the inverter. Then, as shown in Fig. 6.6, the unit cell replicates over the x, y plane. Besides, $x = \omega_c t$ and $y = \omega_e t + \varphi_0$ define a straight line in the x, y plane, i.e. $y = \omega_e x / \omega_c + \varphi_0$. Here, φ_0 denotes the initial offset of y. The intersections of this line with the vertical boundary of areas correspond to the switching instants; the intersections of this line with the horizontal boundary of areas correspond to the commutation instants.

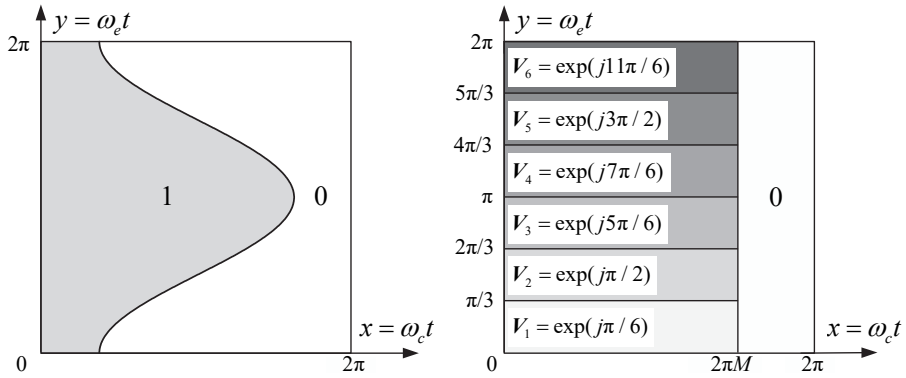

(a) Sine-sawtooth modulation [HOL03]. (b) Six-step modulation.

Fig. 6.5. Unit cell of geometric wall model.

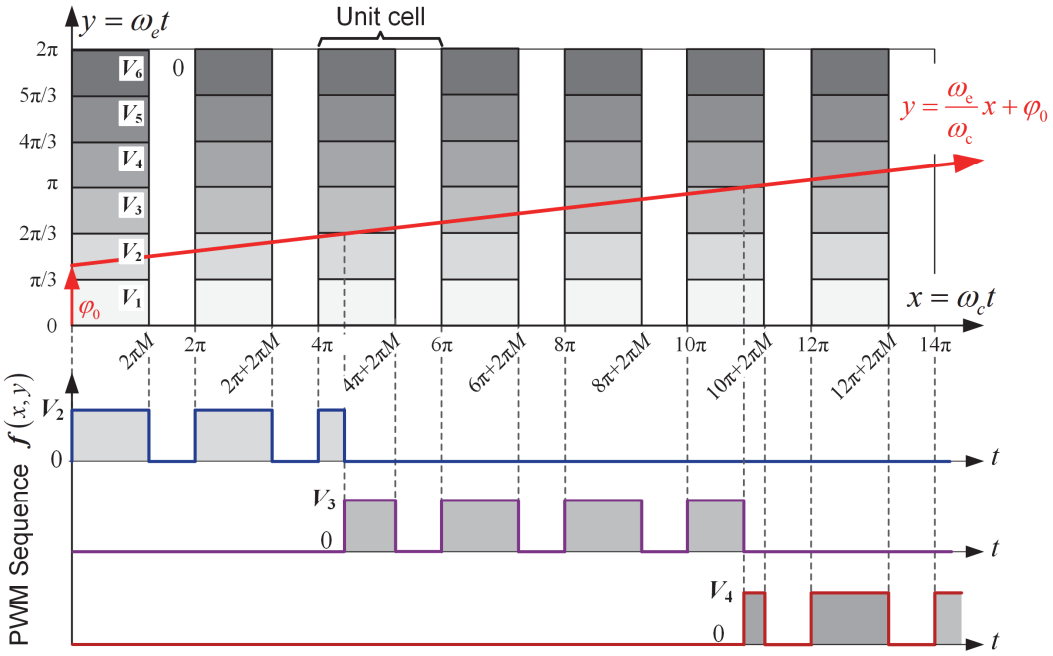

Fig. 6.6. Geometric wall model of the PWM generation for NSC.

Let $\boldsymbol{f}(x,y)$ denote the PWM sequence. As shown in Fig. 6.6, assuming that M denotes the PWM duty ratio, the function $\boldsymbol{f}(x,y)$ changes from 0 to $\boldsymbol{v}(y)$ when

$$x = 2\pi r \qquad r = 0,1,2,...,\infty \tag{6.2}$$

and $\boldsymbol{f}(x,y)$ changes from $\boldsymbol{v}(y)$ to 0 when

$$x = 2\pi r + 2\pi M \qquad r = 0,1,2,...,\infty\,. \tag{6.3}$$

Here, r represents the r^{th} carrier interval, and $\boldsymbol{v}(y)$ is a function of fundamental phase y as defined in (6.1).

The PWM sequence $\boldsymbol{f}(x,y)$ depends on two time variables, i.e. the carrier phase x and the fundamental phase y. According to the Fourier analysis theory, the double variable controlled function $\boldsymbol{f}(x,y)$ can be expressed in terms of its harmonic components as

$$\begin{aligned}\boldsymbol{f}(x,y) &= \sum_{m=-\infty}^{\infty}\sum_{n=-\infty}^{\infty} C_{mn} e^{j(mx+ny)} \\ &= \sum_{m=-\infty}^{\infty}\sum_{n=-\infty}^{\infty} C_{mn} e^{j[m\omega_c t + n(\omega_c t+\varphi_0)]}\end{aligned} \tag{6.4}$$

where m and n are integer-indices. The coefficient C_{mn} can be calculated by

$$C_{mn} = \frac{1}{4\pi^2}\int_0^{2\pi}\int_0^{2\pi} \boldsymbol{f}(x,y)\cdot e^{-j(mx+ny)}dxdy\,. \tag{6.5}$$

The equation used here is the complex exponential form of double Fourier series. It is worth noting that it delivers the double-sided spectrum of two-dimensional vector signals, which can differentiate positive and negative sequence harmonics. This will help make a deep analysis of spectral characteristics. By using the model, the analytical harmonic solution of NSC pattern is derived firstly. Then, on this basis, a modified model can be applied for the spectral analysis of RSC pattern.

6.3.2 Spectral Analysis of NSC Pattern

Equations (6.2) and (6.3) indicate that the integration regions defined in (6.5) for which $\boldsymbol{f}(x,y)$ are nonzero. Then, for the NSC pattern, the Fourier coefficients C_{mn} can be calculated as

$$C_{mn} = \frac{1}{4\pi^2}\int_0^{2\pi}\int_0^{2\pi M} \boldsymbol{v}(y)\cdot e^{-j(mx+ny)}dxdy\,. \tag{6.6}$$

Note that the integration regions do not contain variables, and hence, can be calculated separately as

$$\begin{aligned}C_{mn} &= \frac{1}{4\pi^2}\int_0^{2\pi M} e^{-jmx}dx \cdot \int_0^{2\pi} \boldsymbol{v}(y)\, e^{-jny}dy \\ &= \frac{1}{4\pi^2} I_x \cdot I_y\end{aligned} \tag{6.7}$$

where the two integration terms I_x and I_y are

$$I_x = \int_0^{2\pi M} e^{-jmx} dx = \begin{cases} 2\pi M & \text{for } m = 0 \\ \dfrac{e^{-jm2\pi M} - 1}{-jm} & \text{for } m \neq 0 \end{cases} \tag{6.8}$$

and according to (1), I_y can be broken into six segments as

$$\begin{aligned} I_y &= \int_0^{2\pi} \boldsymbol{v}(y)\, e^{-jny} dy = \int_0^{\frac{\pi}{3}} e^{j\frac{\pi}{6}} \cdot e^{-jny} dy + \int_{\frac{\pi}{3}}^{\frac{2\pi}{3}} e^{j\frac{\pi}{2}} \cdot e^{-jny} dy + \ldots \\ &= \frac{1}{-jn} e^{j\frac{\pi}{6}} \left(e^{-jn\frac{\pi}{3}} - 1 \right) \cdot \sum_{s=0}^{5} \alpha^s \end{aligned} \tag{6.9}$$

where $\alpha = e^{j\frac{\pi}{3}(1-n)}$ and its Σ sum term can be calculated as

$$\sum_{s=0}^{5} \alpha^s = \begin{cases} 6 & n = 1 + 6h \ (h \in \mathbb{Z}) \\ 0 & \text{elsewhere} \end{cases} \tag{6.10}$$

Then, by substituting (6.10) into (6.9), the integration term is simplified as

$$I_y = \begin{cases} \dfrac{6}{n} & n = 1 + 6h \ (h \in \mathbb{Z}) \\ 0 & \text{elsewhere} \end{cases} \tag{6.11}$$

Finally, the Fourier coefficients can be obtained as

$$C_{mn} = \begin{cases} \dfrac{3}{\pi} \cdot \dfrac{M}{n} & \begin{pmatrix} m = 0, \\ n = 1 + 6h \ (h \in \mathbb{Z}) \end{pmatrix} \\ \dfrac{3j}{2\pi^2} \cdot \dfrac{e^{-j2\pi mM} - 1}{mn} & \begin{pmatrix} m \neq 0, \\ n = 1 + 6h \ (h \in \mathbb{Z}) \end{pmatrix} \\ 0 & n \neq 1 + 6h \ (h \in \mathbb{Z}) \end{cases}. \tag{6.12}$$

Only when $n = 1 + 6h$, the coefficient C_{mn} has nonzero values. By substituting (6.12) into (6.4) and discarding the zero terms, the harmonic solution of the NSC can be obtained as

$$\begin{aligned} \boldsymbol{f}(x, y) &= \sum_{m=-\infty}^{\infty} \sum_{n=-\infty}^{\infty} C_{mn} e^{j(mx+ny)} \\ &= \sum_{h=-\infty}^{\infty} C_h e^{j(1+6h)(\omega_e t + \varphi_0)} + \sum_{\substack{m=-\infty \\ m \neq 0}}^{\infty} \sum_{h=-\infty}^{\infty} C_{mh} e^{j\left[m\omega_c t + (1+6h)(\omega_e t + \varphi_0)\right]} \end{aligned} \tag{6.13}$$

where

$$C_h = \frac{3}{\pi}\cdot\frac{M}{1+6h},\ C_{mh} = \frac{3j}{2\pi^2}\cdot\frac{e^{-j2\pi mM}-1}{m(1+6h)} \tag{6.14}$$

Note that $\boldsymbol{f}(x,y)$ consists of two parts. The first part defines the fundamental component and the baseband harmonics, such as: -5th, 7th, -11th, 13th, etc. The other part defines the sideband harmonic components.

6.3.3 Spectral Analysis of RSC Pattern

Fig. 6.7 illustrates the wall model of RSC pattern. Considering the retarding updating behaviour, the reference waveform should hold a constant value frozen at the beginning point of each carrier value. Thus, the intersection trajectory y (dashed line) is amended as a staircase variable y' (solid line) and can be expressed as

$$y' = y - \frac{\omega_e}{\omega_c}(x - 2\pi r) \tag{6.15}$$

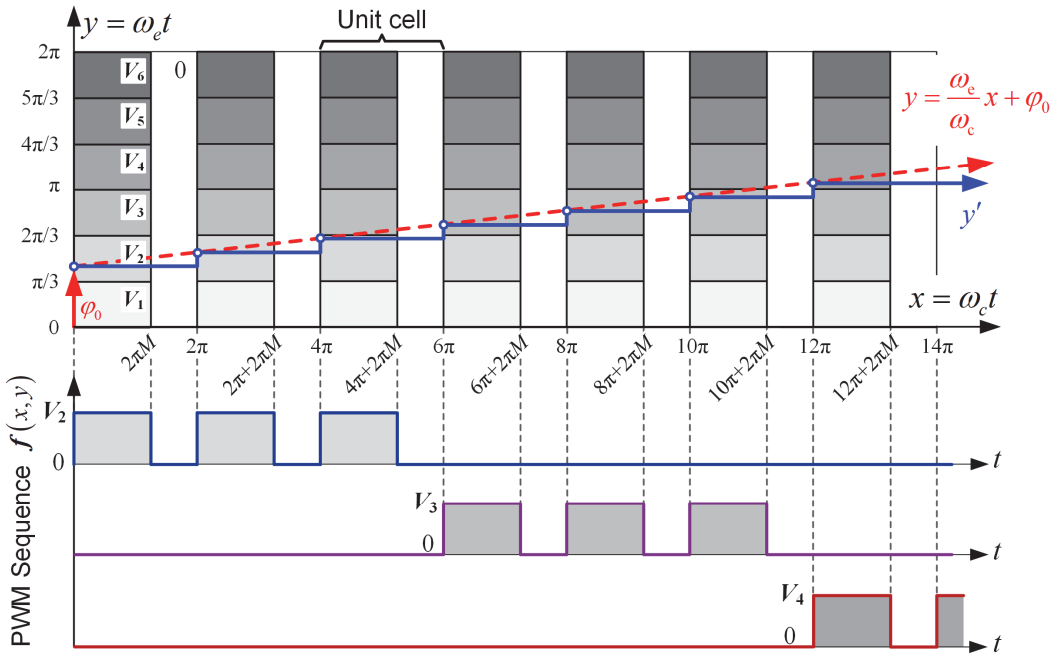

Fig. 6.7. Geometric wall model of the PWM generation for RSC.

where r represents the r^{th} carrier interval. Then, for RSC pattern, the Fourier coefficients C_{mn} can be calculated as

$$C_{mn}=\frac{1}{4\pi^2}\int_0^{2\pi}\int_0^{2\pi M}\boldsymbol{v}\left(y-\frac{\omega_{\mathrm{e}}}{\omega_{\mathrm{c}}}\left(x-2\pi r\right)\right)\cdot e^{-j(mx+ny)}dxdy\,. \tag{6.16}$$

Equation (6.16) can be simplified by changing the integration variable y to $y'=y-\omega_{\mathrm{e}}x/\omega_{\mathrm{c}}$. Here, the $2\pi r$ rollover term associated with x in (6.15) can be discarded since it has no effect on the integration, and it yields

$$C_{mn}=\frac{1}{4\pi^2}\int_0^{2\pi}\int_0^{2\pi M}\boldsymbol{v}\left(y'\right)\cdot e^{-j\left(\left[m+n\frac{\omega_e}{\omega_c}\right]x+ny'\right)}dxdy'\,. \tag{6.17}$$

With the same method, the integration can be calculated separately as

$$\begin{aligned}C_{mn}&=\frac{1}{4\pi^2}\int_0^{2\pi M}e^{-j\left[m+n\frac{\omega_e}{\omega_c}\right]x}dx\cdot\int_0^{2\pi}\boldsymbol{v}\left(y'\right)e^{-jny'}dy'\\&=\frac{1}{4\pi^2}I_x\cdot I_y\end{aligned} \tag{6.18}$$

where

$$I_x=\int_0^{2\pi M}e^{-j\left[m+n\frac{\omega_e}{\omega_c}\right]x}dx=\frac{e^{-j\left(m+n\frac{\omega_e}{\omega_c}\right)2\pi M}-1}{-j\left(m+n\frac{\omega_e}{\omega_c}\right)} \tag{6.19}$$

The calculation of I_y is the same as (6.9)-(6.11) and can be expressed as

$$I_y=\int_0^{2\pi}\boldsymbol{v}\left(y'\right)e^{-jny'}dy'=\begin{cases}\dfrac{6}{n} & n=1+6h\ (h\in\mathbb{Z})\\ 0 & \text{elsewhere}\end{cases}. \tag{6.20}$$

Then, the Fourier coefficients can be calculated as

$$C_{mn}=\begin{cases}\dfrac{3j}{2\pi^2 n}\cdot\dfrac{e^{-j\left(m+n\frac{\omega_e}{\omega_c}\right)2\pi M}-1}{m+n\frac{\omega_e}{\omega_c}} & n=1+6h\ (h\in\mathbb{Z})\\ 0 & \text{elsewhere}\end{cases}. \tag{6.21}$$

Likewise, only when $n=1+6h$, the coefficient C_{mn} has nonzero value. Discarding the zero terms, the harmonic solution for RSC pattern is obtained as

$$\boldsymbol{f}\left(x,y\right)=\sum_{m=-\infty}^{\infty}\sum_{n=-\infty}^{\infty}C_{mn}e^{j\left(mx+ny\right)}=\sum_{m=-\infty}^{\infty}\sum_{h=-\infty}^{\infty}C_{mh}e^{j\left[m\omega_c t+\left(1+6h\right)\left(\omega_e t+\varphi_0\right)\right]} \tag{6.22}$$

where

$$C_{mh}=\frac{3j}{2\pi^2}\cdot\frac{1}{1+6h}\cdot\frac{e^{-j\left(m+\left(1+6h\right)\frac{\omega_e}{\omega_c}\right)2\pi M}-1}{m+\left(1+6h\right)\frac{\omega_e}{\omega_c}} \tag{6.23}$$

6.3.4 Harmonic Distribution

As shown in (6.13) and (6.22), the NSC and RSC will produce sideband harmonic components of the frequency group $\omega_h=m\omega_c+\left(1+6h\right)\omega_e$. However, this frequency term ω_h is implicit, which simultaneously requires two integer-indices *m* and *h* to determine the frequency ω_h. For simplification, the spectral distribution can be analysed as follows. Generally, the number of pulses per sector *N* is a rational number and can be written as

$$N=\frac{\omega_c}{6\omega_e}=\frac{p}{q} \tag{6.24}$$

where *p* and *q* are co-prime numbers and p/q denotes the irreducible fraction. Then, define the element frequency $\Delta\omega$ as

$$\Delta\omega=\frac{\omega_c}{p}=\frac{6\omega_e}{q}. \tag{6.25}$$

By substituting (6.25) into the frequency term ω_h, it can be simplified as

$$\begin{aligned}\omega_h&=m\omega_c+(1+6h)\omega_e\\&=\omega_e+(mp+hq)\Delta\omega\\&=\omega_e+k\Delta\omega\end{aligned} \tag{6.26}$$

where $k=mp+hq$. According to Bézout's identity in number theory, since *p* and *q* are co-prime numbers, *k* could be any integers, i.e. $k\in\mathbb{Z}$. Besides, for the integer *k*, the set of Bézout coefficients is

$$\left\{m,h\right\}=\left\{km_0+lq,\ kh_0-lp\,\middle|\,k,l\in\mathbb{Z}\right\} \tag{6.27}$$

where (m_0, h_0) is one pair of Bézout coefficients and can be computed by extended Euclidean algorithm. Once a solution (m_0, h_0) is determined, all the general solution can be calculated by (6.27). Then, by substituting (6.26) and (6.27) into (6.13), the harmonic solution for NSC pattern could be simplified as

$$\boldsymbol{f}(x,y)=\sum_{h=-\infty}^{\infty}C_h^{\mathrm{NSC}}e^{j(1+6h)\omega_e t}+\sum_{k=-\infty}^{\infty}C_k^{\mathrm{NSC}}e^{j(\omega_e+k\Delta\omega)t}. \tag{6.28}$$

$$\begin{cases} C_h^{\mathrm{NSC}}=\dfrac{3M}{\pi}\cdot\dfrac{e^{j(1+6h)\varphi_0}}{1+6h} \\ C_k^{\mathrm{NSC}}=\dfrac{3j}{2\pi^2}\cdot\left(\displaystyle\sum_{\substack{l=-\infty \\ km_0+lq\neq 0}}^{\infty}\dfrac{e^{j\left[1+6(kh_0-lp)\right]\varphi_0}}{1+6(kh_0-lp)}\cdot\dfrac{e^{-j2\pi(km_0+lq)M}-1}{km_0+lq}\right) \end{cases} \tag{6.29}$$

Likewise, the harmonic solution (6.22) for RSC can be expressed as

$$\boldsymbol{f}(x,y)=\sum_{k=-\infty}^{\infty}C_k^{\mathrm{RSC}}e^{j(\omega_e+k\Delta\omega)t}. \tag{6.30}$$

where

$$C_k^{\mathrm{RSC}}=\frac{3j}{2\pi^2}\cdot\frac{e^{-j\left[\frac{\omega_e+k\Delta\omega}{\omega_c}\right]2\pi M}-1}{\left(\frac{\omega_e+k\Delta\omega}{\omega_c}\right)}\cdot\left(\sum_{l=-\infty}^{\infty}\frac{e^{j\left[1+6(kh_0-lp)\right]\varphi_0}}{1+6(kh_0-lp)}\right) \tag{6.31}$$

The analytical harmonic solutions (6.28) and (6.30) provide insightful revelation on the harmonic distribution of PWM sequence. Rather than the formula $\omega_h=m\omega_c+(1+6h)\omega_e$, the new harmonic frequency term can be determined by $\omega_h=\omega_e+k\Delta\omega$, requiring just one integer-index k. Fig. 6.8 (a) illustrates a typical harmonic spectrum of the RSC or NSC pattern. The integer k goes from -∞ to ∞. Every integer k corresponds to a frequency component in spectrum. The central frequency locates at the fundamental frequency ω_e. Various baseband and sideband harmonic components are evenly distributed around ω_e. The distance between two adjacent frequencies in spectrum is the element frequency $\Delta\omega$. In particular, when k equals to some specific values, they correspond to some important harmonic components, which can be summarized as follows.

1) When $k=0$, then $\omega_h=\omega_e$ is the fundamental component;

2) When $k=q,2q,3q...$ then $\omega_h=(1+6h)\omega_e$ is the baseband harmonic, e.g. -5th, 7th, -11th, 13th, etc.;

3) For other cases, ω_h will be sideband harmonics. Some of them are perhaps non-integer multiples of the fundamental frequency, i.e. the interharmonics. Even some frequencies are lower than the fundamental frequency, which are defined as subharmonics.

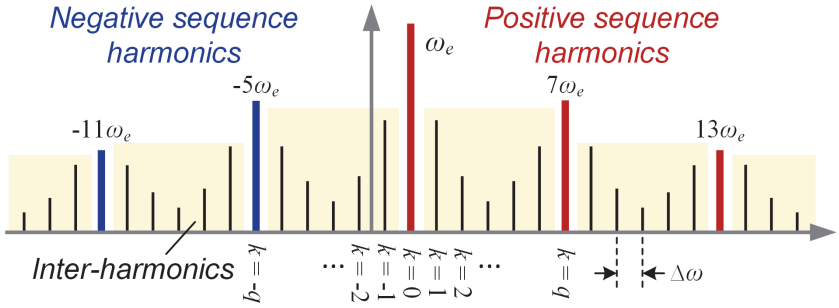

(a) RSC or NSC.

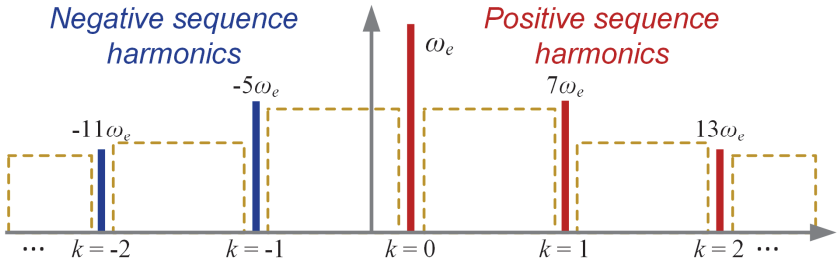

(b) CSC.

Fig. 6.8. Illustration of typical harmonic spectra.

For normal speed motor drives, it is generally supposed the sideband harmonic components only exist around the carrier and multiple carrier frequencies. However, for high-speed BLDC drives, sideband harmonics will be induced in low frequency range, no matter regular- or natural-sampled based PWM techniques are employed. These undesired sideband harmonic components will not only increase iron and copper losses, but also generate torque ripples, vibration and acoustic noise, which will deteriorate the drive performance.

6.4 Spectral Characteristics of CSC Pattern

In this section, the spectral characteristics of the CSC pattern are analysed. Since the CSC pattern is symmetrical in space, the PWM sequence can be expressed with single Fourier series as

$$\boldsymbol{f}\left(x,y\right)=\sum_{k=-\infty}^{\infty}C_n\cdot e^{jny}=\sum_{k=-\infty}^{\infty}C_n\cdot e^{jn\omega_e t} \tag{6.32}$$

The CSC can switch on and off at any instant within a carrier period when the commutation signal happens. Therefore, the actual commutation interval could be fractional times of carrier periods. As shown in Fig. 6.4, the number N can be separated into the integer part N_Z and the decimal part N_D:

$$N = N_Z + N_D\,. \tag{6.33}$$

For both of the cases in Figs. 6.4 (a) and (b), the first N_Z number of PWM pulses in each sector are definitely complete. The difference between the two cases is whether the last PWM pulse is complete or not, which is dependent on the duty ratio M and the decimal part N_D. Hence, the spectral analysis is carried out in terms of these two cases.

A. Case 1: $M \le N_D$

When the duty ratio M is less than N_D, as shown in Fig. 6.4 (a), the last PWM pulse is complete and thus there are N_Z+1 PWM pulses in each sector. For the CSC pattern, the voltage vectors are symmetrical in space. Thus, the Fourier coefficient of sector I is calculated firstly. Then, it can be deduced to overall six sectors.

In sector I, the Fourier coefficient C_n^{S1} can be calculated as

$$\begin{aligned} C_n^{S1} &= \frac{1}{2\pi}\sum_{\lambda=0}^{N_Z}\int_{2\pi\frac{\omega_e}{\omega_c}\lambda}^{2\pi\frac{\omega_e}{\omega_c}(\lambda+M)}\boldsymbol{V}_1\cdot e^{-jny}dy \\ &= \frac{\boldsymbol{V}_1}{-j2\pi n}\left(e^{-jn\frac{\omega_e}{\omega_c}2\pi M}-1\right)\cdot\sum_{\lambda=0}^{N_Z}e^{-jn\frac{\omega_e}{\omega_c}2\pi\lambda} \\ &= \frac{\boldsymbol{V}_1}{-j2\pi n}\left(E_n^M-1\right)\cdot\sum_{\lambda=0}^{N_Z}E_n^{\lambda} \end{aligned} \tag{6.34}$$

where E_n is defined as

$$E_n = e^{-jn\frac{\omega_c}{\omega_c}2\pi}. \tag{6.35}$$

The Σ sum term in the last line of (6.34) is a geometric sequence and can be calculated as

$$\sum_{\lambda=0}^{N_Z} E_n^{\lambda} = \frac{E_n^{N_Z+1}-1}{E_n-1} \tag{6.36}$$

The Fourier coefficient C_n^{S1} for sector I can be expressed as

$$C_n^{S1} = \frac{\boldsymbol{V}_1}{-j2\pi n}\frac{\left(E_n^{N_Z+1}-1\right)\left(E_n^{M}-1\right)}{E_n-1} \tag{6.37}$$

Then, the voltage space vector is the sum of six vectors corresponding to six sectors. Hence, the Fourier coefficient can be calculated as

$$\begin{aligned} C_n &= \frac{1}{2\pi}\sum_{s=1}^{6}\sum_{\lambda=0}^{N_Z}\int_{2\pi\frac{\omega_c}{\omega_c}\lambda+\frac{\pi}{3}(s-1)}^{2\pi\frac{\omega_c}{\omega_c}(\lambda+M)+\frac{\pi}{3}s}\boldsymbol{V}_s\cdot e^{-jny}dy \\ &= \frac{e^{j\frac{\pi}{6}}}{-j2\pi n}\frac{\left(E_n^{N_Z+1}-1\right)\left(E_n^{M}-1\right)}{E_n-1}\cdot\sum_{s=0}^{5}\alpha^s \end{aligned} \tag{6.38}$$

The derivation of $\sum_{s=0}^{5}\alpha^s$ has been calculated in (6.10). Finally, for case 1 of CSC pattern, the Fourier coefficient can be calculated as

$$C_n = \begin{cases} \dfrac{3\left(\sqrt{3}+j\right)}{-j2\pi n}\dfrac{\left(E_n^{N_Z+1}-1\right)\left(E_n^{M}-1\right)}{E_n-1} & n = 1+6k \\ 0 & \text{elsewhere} \end{cases} \tag{6.39}$$

B. Case 2: $M > N_D$

The derivation for CSC pattern case 2 is similar to that of case 1. When the duty ratio M is greater than N_D, as shown in Fig. 6.4 (b), the first N_Z PWM pulses in each sector are complete and the last one is incomplete. In this case, the Fourier coefficient can be obtained by subtracting the chop-off periods from sector I as

$$
\begin{aligned}
C_n^{S1} &= \frac{1}{2\pi}\left(\int_0^{\frac{\pi}{3}} \boldsymbol{V}_1 \cdot e^{-jny}dy - \sum_{\lambda=0}^{N_Z-1}\int_{2\pi\frac{\omega_e}{\omega_c}(\lambda+M)}^{2\pi\frac{\omega_e}{\omega_c}(\lambda+1)} \boldsymbol{V}_1 \cdot e^{-jny}dy\right) \\
&= \frac{1}{2\pi}\left(\int_0^{\frac{\pi}{3}} \boldsymbol{V}_1 \cdot e^{-jny}dy + \frac{\boldsymbol{V}_1}{jn}\frac{\left(E_n^{N_Z}-1\right)\left(E_n-E_n^{M}\right)}{E_n-1}\right)
\end{aligned}. \tag{6.40}
$$

Then, for case 2 of CSC pattern, the Fourier coefficient of voltage space vector for six sectors can be calculated as

$$
\begin{aligned}
C_n &= \frac{1}{2\pi}\sum_{s=1}^{6}\left(\int_{\frac{\pi}{3}(s-1)}^{\frac{\pi}{3}s} \boldsymbol{V}_s \cdot e^{-jny}dy - \sum_{\lambda=0}^{N_Z}\int_{2\pi\frac{\omega_e}{\omega_c}(\lambda+M)+\frac{\pi}{3}(s-1)}^{2\pi\frac{\omega_e}{\omega_c}(\lambda+1)+\frac{\pi}{3}s} \boldsymbol{V}_s \cdot e^{-jny}dy\right) \\
&= \begin{cases} \dfrac{1}{j2\pi n}\left[6j+3\left(\sqrt{3}+j\right)\dfrac{\left(E_n^{N_Z}-1\right)\left(E_n-E_n^{M}\right)}{E_n-1}\right] & n=1+6k \\ 0 & \text{elsewhere} \end{cases}
\end{aligned}. \tag{6.41}
$$

Finally, by discarding the zero terms, the PWM sequences for both of the cases in CSC pattern can be expressed in terms of harmonic components as

$$
\boldsymbol{f}(x,y) = \sum_{k=-\infty}^{\infty} C_k^{\mathrm{CSC}} \cdot e^{j(1+6k)\omega_e t} \tag{6.42}
$$

where C_k^{CSC} is the non-zero coefficient in (6.39) or (6.41), depending on the case. Fig. 8 (b) illustrates a typical spectrum of the CSC pattern. It should be noted that the Fourier coefficients of CSC pattern only contain 1+6*k* order harmonics. Therefore, in theory, the CSC pattern will not produce any additional sideband harmonic components, which provides a potential solution for the sideband harmonic cancellation.

6.5 Torque Ripples Caused by Harmonic Currents

6.5.1 Sideband Harmonic Currents of RSC and NSC Patterns

In order to analyse the torque ripples, the current vector has to be known. Strictly, however, the current vector cannot be derived directly from the PWM sequence (6.28) and (6.30) since the inverter with six-step operation contains nonlinear processes, e.g. commutation and freewheeling. Fortunately, one thing is certain, i.e. the current contains the harmonic components of the same frequencies as the PWM sequences do.

Thus, for the RSC and NSC patterns, the current vector $\boldsymbol{i}_S(t)$ in stator reference frame can be expressed as

$$\boldsymbol{i}_S(t) = \sum_{k=-\infty}^{\infty} I_k \cdot e^{j(\omega_e t + k\Delta\omega t + \theta_k)} \quad (I_k \in \mathbb{R}) \tag{6.43}$$

where I_k and θ_k are the magnitude and initial phase of the k^{th} harmonic. Then, by converting it into the rotor reference frame, the current vector $\boldsymbol{i}_R(t)$ can be calculated as

$$\boldsymbol{i}_R(t) = e^{-j\omega_e t}\boldsymbol{i}_S(t) = \sum_{k=-\infty}^{\infty} I_k \cdot e^{j(k\Delta\omega t + \theta_k)} \tag{6.44}$$

Its real part and imaginary part can be expressed as

$$\boldsymbol{i}_R(t) = \mathrm{Re}(\boldsymbol{i}_R(t)) + j \cdot \mathrm{Im}(\boldsymbol{i}_R(t)) \tag{6.45}$$

where

$$\mathrm{Re}(\boldsymbol{i}_R(t)) = I_0\cos(\theta_0) + \sum_{k=1}^{\infty}\left[I_k\cos(k\Delta\omega t + \theta_k) + I_{-k}\cos(-k\Delta\omega t + \theta_{-k})\right] \tag{6.46}$$

$$\mathrm{Im}(\boldsymbol{i}_R(t)) = I_0\sin(\theta_0) + \sum_{k=1}^{\infty}\left[I_k\sin(k\Delta\omega t + \theta_k) + I_{-k}\sin(-k\Delta\omega t + \theta_{-k})\right] \tag{6.47}$$

Note that the in rotor reference frame, the current contains AC components, whose frequencies are $\Delta\omega$ and its integer multiples. The imaginary part $\mathrm{Im}(\boldsymbol{i}_R(t))$ of the current is perpendicular to the rotor flux vector and thereby will produce average torque and torque ripples. The real part $\mathrm{Re}(\boldsymbol{i}_R(t))$ is aligned with the rotor flux vector. For a symmetrical machine without saliency, $\mathrm{Re}(\boldsymbol{i}_R(t))$ will not produce torque, but will generate additional copper and iron losses.

6.5.2 Torque Ripple Analysis of RSC and NSC Patterns

According to previous literature [BIA04], for high speed PM motors, the torque varies almost linearly with the current. This is due to the low value of the iron flux density, far from the saturation. Then, the torque T_e can be expressed as

$$T_e = p_n \psi_f \cdot \mathrm{Im}(\boldsymbol{i_R}(t)) \tag{6.48}$$

where p_n is the number of pole pairs, where ψ_f is the rotor flux constant. By substituting (6.47) into (6.48), the torque T_e can be expressed as

$$T_e = T_0 + \sum_{k=1}^{\infty} T_k(t) \tag{6.49}$$

where T_0 and $T_k(t)$ denotes the average torque and torque ripple, respectively, and can be expressed as

$$\begin{aligned} T_0 &= p_n \psi_f I_0 \sin(\theta_0) \\ T_k(t) &= p_n \psi_f \left(I_k \sin(k\Delta\omega t + \theta_k) + I_{-k} \sin(-k\Delta\omega t + \theta_{-k}) \right) \end{aligned} \tag{6.50}$$

It illustrates only the fundamental frequency current produces average torque. The sideband harmonic currents will produce periodic torque ripples with frequencies $k\Delta\omega$. The k^{th} harmonic torque ripple $T_k(t)$ is produced by a pair of sideband harmonic currents with frequencies $\omega_e + k\Delta\omega$ and $\omega_e - k\Delta\omega$. Thus, theoretically, the sideband harmonic currents of RSC and NSC patterns will produce abundant torque ripples at the frequency $\Delta\omega$ and its integer multiples. Besides, when $\Delta\omega$ is small, it will produce low-frequency torque ripples, even lower than the fundamental frequency. As a result, the drive performance will be deteriorated.

6.5.3 Torque Ripple Analysis of CSC Pattern

Likewise, the torque ripple of CSC pattern can be analysed as follows. According to (6.42), in stator reference frame, the current vector of CSC pattern can be expressed as

$$\boldsymbol{i_S}(t) = \sum_{k=-\infty}^{\infty} I_k \cdot e^{j(\omega_e t + 6k\omega_e t + \theta_k)} \quad (I_k \in \mathbb{R}) \tag{6.51}$$

Then, with the same analysis method above, the average torque and torque ripple can be calculated as

$$\begin{aligned} T_0 &= p_n \psi_f I_0 \sin(\theta_0) \\ T_k(t) &= p_n \psi_f \left(I_k \sin(6k\omega_e t + \theta_k) + I_{-k} \sin(-6k\omega_e t + \theta_{-k}) \right) \end{aligned} \tag{6.52}$$

Note that the frequencies of the torque ripple are $6k\omega_e$, which are produced by a pair of baseband harmonic currents with frequencies $(1+6k)\omega_e$ and $(1-6k)\omega_e$. Thus, different from RSC or NSC patterns, the CSC pattern will produce torque ripple only at 6*k* multiples of the fundamental frequency ω_e. The torque ripple frequency is at least six times of the fundamental frequency. For high-speed motor drive, the torque ripple frequencies are high enough thereby the influence can be negligible.

6.6 Simulation and Experimental Validations

The proposed compensation algorithm is verified on the high-speed BLDC motor experimental platform as shown in Appendix 1. The high-speed BLDC Motor-I in Appendix is used here. The DC-link voltage is 25V. The PWM switching frequency is 20 kHz. The commutation signal is generated by zero-crossing detection based sensorless algorithm. The test motor is a commercial high-speed motor for vacuum cleaners. Fan blades are mechanically integrated with the motor shaft to produce the load torque. The torque sensor or dynamometer cannot be installed to measure the torque or efficiency. In addition, the load type is aerodynamic load, which is very small (less than 50e-3 Nm). Even the mechanical friction will cause inaccurate load torque measurement. Due to above objective reasons, the torque ripples caused by harmonic currents cannot be measured and thereby are investigated through simulation in Matlab/Simulink software.

In order to illustrate the adverse influence of the sideband harmonics, a comprehensive validation is carried out across the three commutation patterns, including simulation (Fig. 6.9), theoretical prediction (Fig. 6.10) and experiment (Fig. 6.11). The motor speed is selected at 64 000 r/min (1067 Hz), equivalent to 3.125 PWM waves in each sector (N=3.125, p/q=25/8, $\Delta\omega=0.75\omega_o$=800Hz×2π).

Fig. 6.9 compares the phase currents (and spectra), PWM sequences, torque (and spectra) using three different commutation patterns in simulation. In the first place, for the RSC pattern in Fig. 6.9 (a), the phase currents oscillate periodically. It is shown in the PWM sequence $\boldsymbol{f}(x,y)$ (in the second row) that the durations of each sector are not

evenly distributed. In the current spectrum, the fundamental frequency locates in the middle, and all the harmonics are distributed evenly on both sides with the distance $\Delta\omega=0.75\omega_o$. Apart from the baseband $1+6k$ order harmonics, abundant sideband harmonic currents are produced. Besides, the torque waveform and the one processed by low pass filter are provided. As the theory predicts, the sideband harmonic currents produce abundant torque ripples at the frequency $\Delta\omega$ and its integer multiples. On the other hand, for the NSC pattern in Fig. 6.9 (b), the phenomenon is similar, i.e. the currents and torque oscillate periodically. It is shown in the PWM sequence $\boldsymbol{f}(x,y)$ that although the durations of each sector are identical, the PWM sequences are not symmetrical. From the current spectrum, the magnitudes of sideband harmonic components are reduced to some extent compared with the RSC pattern. However, the torque ripples increase significantly. Finally, when the CSC pattern is used in Fig. 6.9 (c), the durations of each sector are evenly distributed and the PWM sequences are symmetrical. The current envelope becomes flat without oscillations. From the current spectrum, all the sideband harmonic components are cancelled. As theoretically predicted, it only introduces baseband harmonic currents at frequencies $(1+6k)\omega_e$. The torque is stable and steady without low frequency ripples.

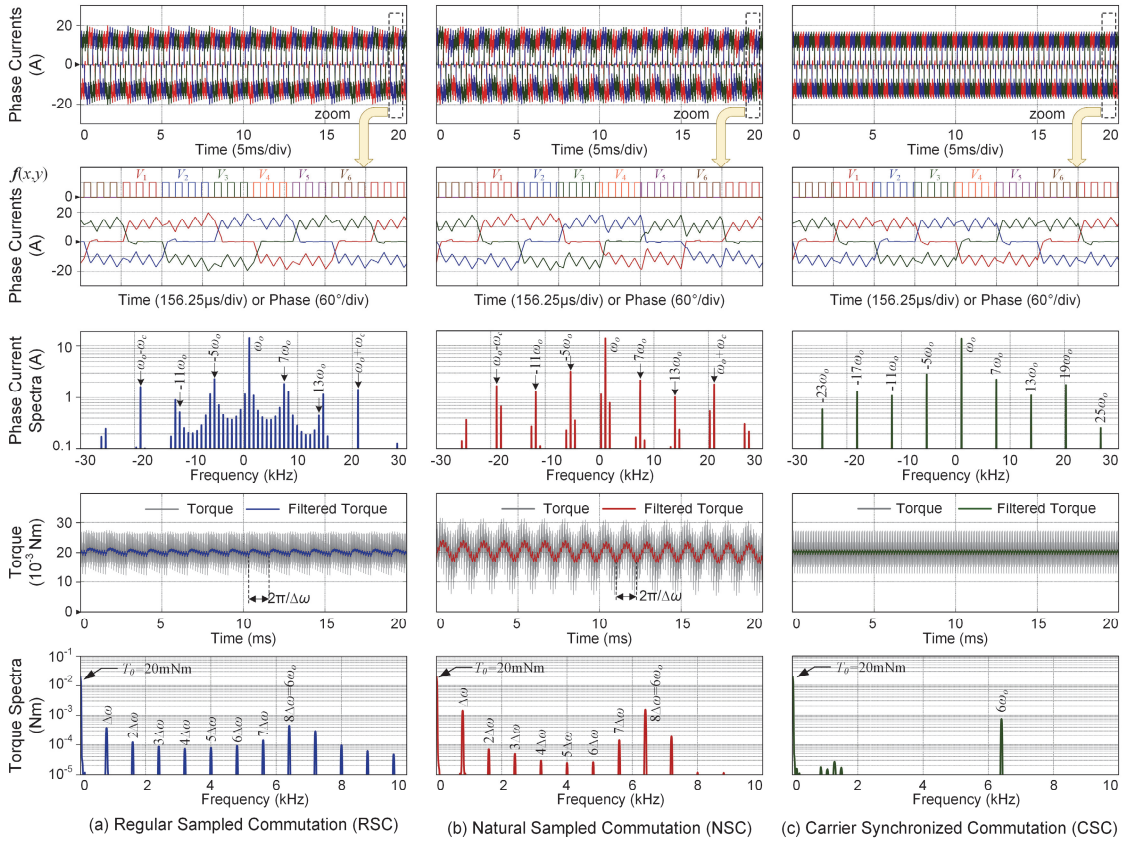

Fig. 6.9. Simulated phase currents (and spectra), PWM sequences, torque (and spectra) at 64000 r/min (1067 Hz).

Fig. 6.10 compares analytical and numerical spectra of PWM sequences $\boldsymbol{f}(x,y)$ for three different patterns. As mentioned earlier, since the six-step operation contains nonlinear processes such as commutation and freewheeling, the analytical harmonic solution of current vectors is hard to obtain. For this reason, analytical and numerical spectra of PWM sequences $\boldsymbol{f}(x,y)$ are provided. It clearly demonstrates the agreement between the analytical and numerical spectra for PWM sequences. In addition, it can be observed that the spectra of PWM sequences and currents are similar to each other. The currents contain harmonic components of the same frequencies as the PWM sequences do.

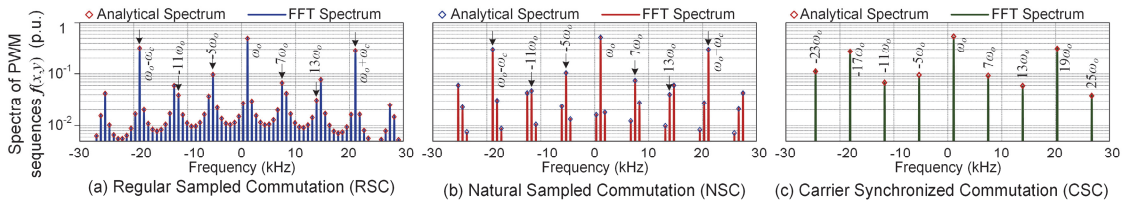

Fig. 6.10. Analytical and numerical spectra of PWM sequences $\boldsymbol{f}(x,y)$ at 64 000 r/min (1067 Hz).

The experimental results, including measured currents and the current spectra using three commutation patterns are compared in Fig. 6.11. The experimental results confirm the simulated and theoretical ones. Therefore, in the high-speed region when the switching ratio is limited, the CSC pattern presents better control performance without generating undesired sideband harmonic currents or low frequency torque ripples.

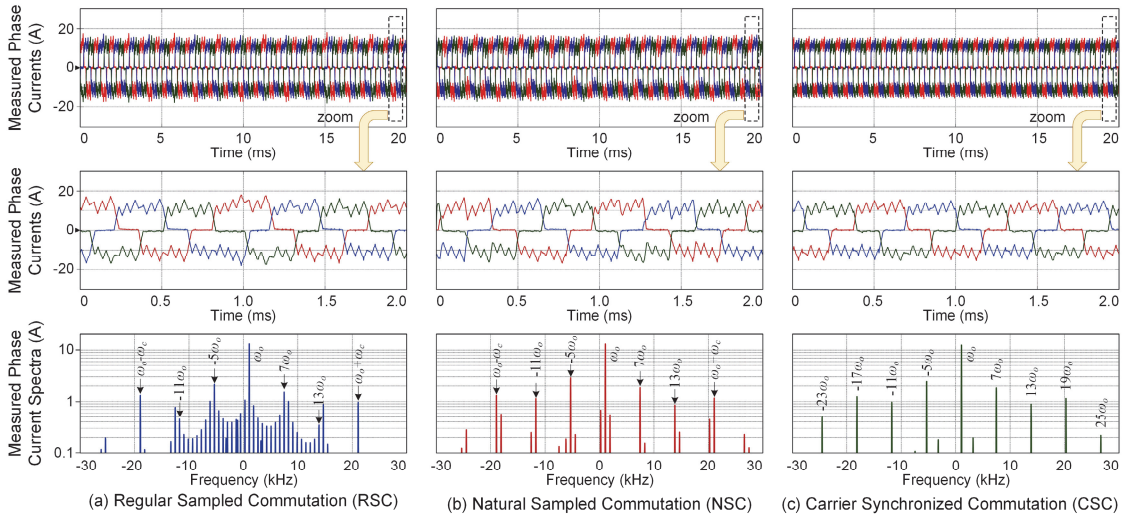

Fig. 6.11. Experimental phase currents and phase current spectra at 64 000 r/min (1067 Hz).

The above results verify the spectral analysis together with the sideband harmonic cancellation capability of CSC at a single speed 64 000 r/min. In order to make a verification in a wide speed range, a frequency sweeping analysis is carried out via experiment and theoretical prediction. In the first place, Fig. 6.12 compares the measured spectrograms of phase currents using different commutation patterns. The motor accelerates gradually from 477 Hz (N=7) to 1.1 kHz (N=3). The currents are recorded and the short time Fourier transform is employed to analyse the spectral characteristics. To help understand, the spectra at the moment 60 000 r/min (1 kHz) are exemplified above the spectrograms. The x-axis represents the spectral frequency ranging from -10 kHz to 10 kHz. The y-axis represents the fundamental frequency (motor speed). These spectrograms reveal the harmonic frequency trajectories versus the motor speed. As shown in Figs. 6.12 (a) and (b), for RSC and NSC patterns, in addition to the 1+6k order harmonic trajectories, abundant sideband harmonic trajectories with significant magnitudes can be observed clearly. It should be noted that

as long as N is not an integer, these sideband harmonic components will exist, especially in high-speed region. This phenomenon is confirmed by the predicted spectrograms of PWM sequences in Figs. 6.13 (a) and (b). On the other hand, for the results of CSC pattern in Fig. 6.12 (c) and Fig. 6.13 (c), all the sideband harmonic trajectories are remarkably reduced, the remaining dominant trajectories are the 1+6k order harmonics, which is a signature of the six-step control. Both experimental and theoretical results demonstrate that the CSC pattern has superior sideband harmonic cancellation capability compared with RSC and NSC patterns. Within a wide speed range, the performance is considerably improved by the CSC pattern.

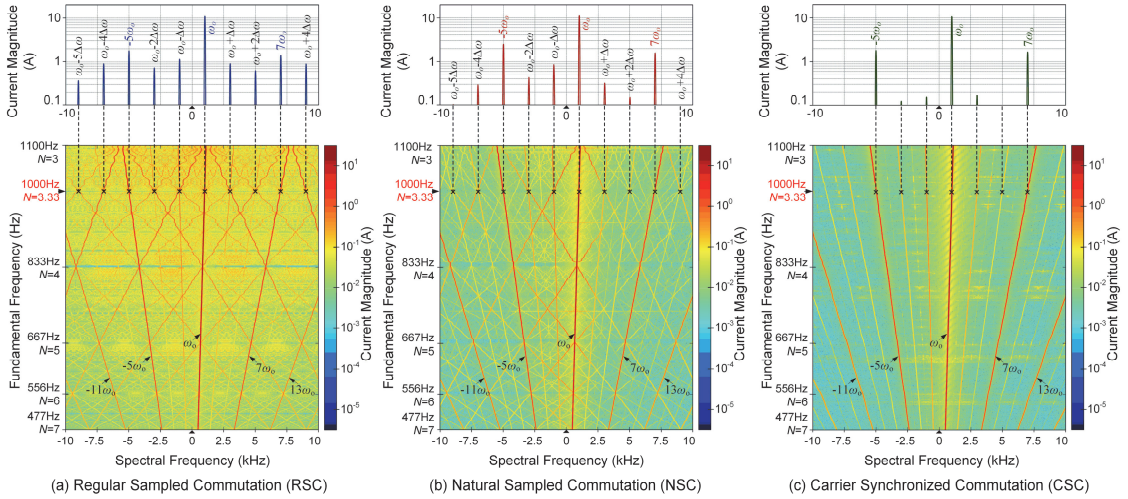

Fig. 6.12. Measured spectrograms of currents with fundamental frequency ranging from 477 Hz to 1.1 kHz.

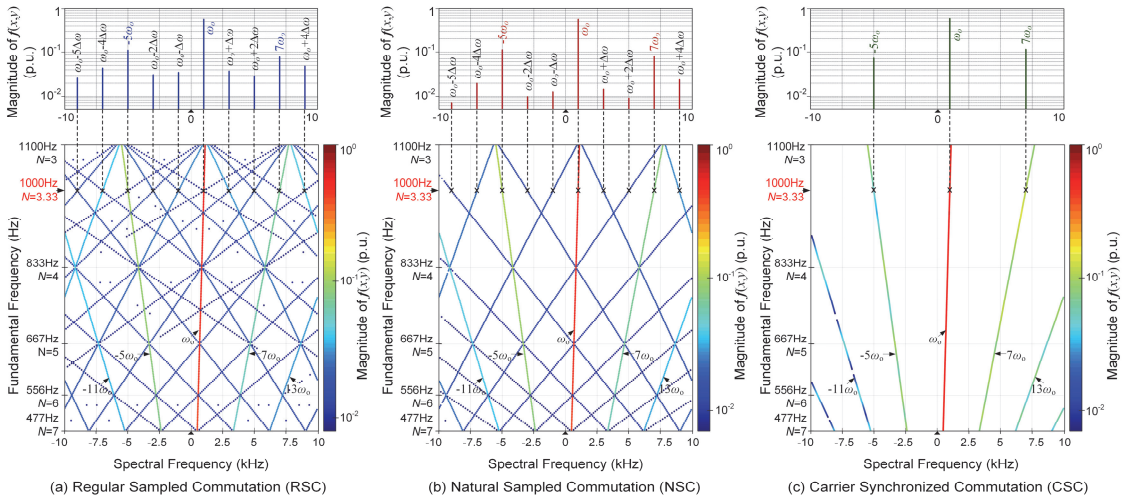

Fig. 6.13. Predicted spectrograms of PWM sequences with fundamental frequency ranging from 477 Hz to 1.1 kHz.

Fig. 6.14 compares the experimental results of dynamic speed change using three commutation patterns. The motor speed reference increases from 30 000 r/min (500 Hz, N≈6.67) to 78 000 r/min (1300 Hz, N≈2.56) within only four seconds and then decreases back to 30 000 r/min. The acceleration slope is set as high as 12 000 r/min/s (200 Hz/s). As it can be seen, only the proposed CSC pattern is able to complete this test; and the conventional RSC and NSC patterns fail in the test. In the first place, for the RSC pattern, as analysed in section 6.2, it will cause commutation delay that can reach a PWM period. As shown in the zoomed window of Fig. 6.14 (a), in high-speed region, the resultant commutation delay makes the currents increase sharply. Eventually it triggers the over-current protection and the drive fails at around 1110 Hz. Then, for the NSC pattern in Fig. 6.14 (b), although it can reach 1300 Hz, the currents fluctuate drastically at this speed and load torque. Eventually, it also fails soon after reaching 1300 Hz. As a contrast, the proposed CSC pattern is still effective in high-speed and high-torque region. As shown in the zoomed window of Fig. 6.14 (c), the three currents are balanced and symmetrical without fluctuations at 1300 Hz. Besides, the acceleration and deceleration processes are stable. Therefore, it demonstrates the proposed CSC pattern can achieve high performance and robustness for both steady and transient states.

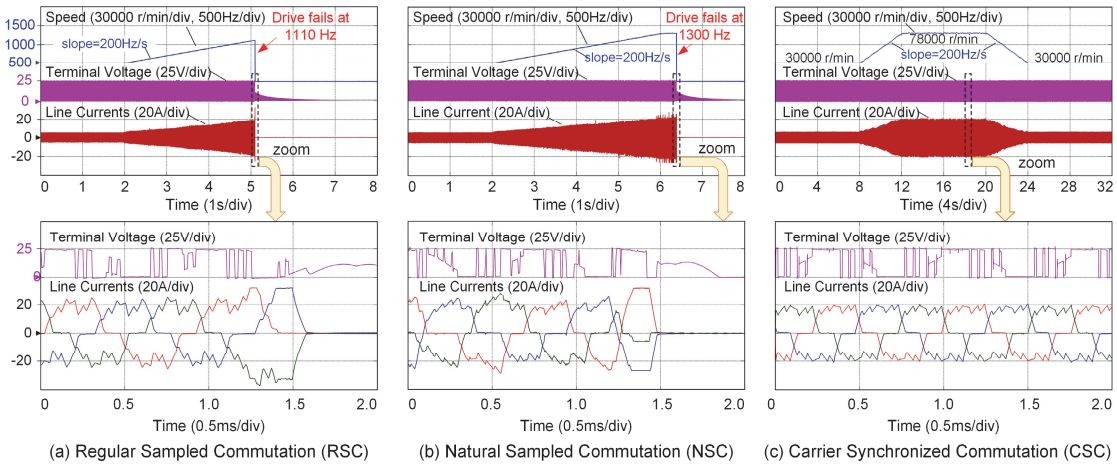

Fig. 6.14. Experimental comparison for acceleration and deceleration processes

6.7 Summary

This chapter has investigated the sideband harmonics generated in six-step operation in high-speed BLDC drives. When the switching ratio is insufficient, conventional RSC and NSC patterns will cause abundant sideband harmonics. In order to minimize these undesired sideband harmonics, the CSC pattern is proposed. A comparative analysis of the principles and spectral characteristics among RSC, NSC and CSC patterns is carried out. The extended geometric wall model that can be used for the Fourier decomposition of complex vectors is introduced to reveal the spectral characteristics of RSC and NSC pattern. It demonstrates RSC and NSC patterns will generate abundant sideband harmonics currents at frequencies $\omega_h = \omega_e + k\Delta\omega$, and will further cause torque ripple at frequencies $\omega_h = k\Delta\omega$. The proposed CSC pattern can considerably reduce these adverse influences and presents high performance and robustness at high-speed region.

CHAPTER 7

Discrete-time Current Controller and EMF Observer based on Generic Delay Model for High-speed BLAC Drive

7.1 Introduction

Generally, for BLAC operation, the sampling ratio f_s / f_e of the inverter is set relatively high to ensure the smooth current control (f_s and f_e denote the sampling frequency and the fundamental frequency, respectively). However, in some applications, drives have to operate with insufficient sampling ratio, which causes difficulties to the motor control. On one hand, difficulties emerge in some high-speed applications, e.g. high-speed drills and flywheel energy storage, whose maximum fundamental frequency could exceed 1 kHz [ZWY08]. However, the sampling (switching) frequency is limited within several tens of thousands hertz considering the switching loss and the micro-controller capacity. On the other hand, in high-power applications, e.g. rail traction systems, the sampling (switching) frequency is strictly limited to less than 1 kHz considering the switching loss [HOL09]. For these applications where the sampling ratio is insufficient, the drive performance will degrade due to non-negligible digital control delay and inaccurate machine modelling. As a result, it faces great challenges for such low sampling ratio applications.

The first challenge is the design of current controllers with low sampling ratio. It is commonly known that the cross-coupling exists between *d-q* axes and will increase with the fundamental frequency. The cross-coupling will cause slow current tracking response and undesired interaction between *d-q* components [ZHO17]. Besides, as the sampling ratio decreases, it will lead to a stronger cross-coupling due to the enlarged digital control delay. Some efforts have been made to deal with the delay. In continuous-time domain, the delay is usually approximated as a first-order low-pass filter and compensated through adjusting the phase and magnitude of the output voltage [BAE03]. This approach works well when the sampling ratio is sufficient. However,

with reduced sampling ratio, the tracking bandwidth will be affected. To improve the control performance, some current controllers are directly designed in discrete-time domain. In this way, the digital control delay can be modelled and counteracted more accurately. In [YEP14][ZHO17], the delay was modelled with Padé approximant in discrete-time domain, and corresponding current controllers were developed. An exact discrete-time model without approximations was presented in [KIM10], which pointed out that the digital control delay is composed of the sampling delay and the voltage latch (see section 7.2 for details). With the model in [KIM10], some improvements have been made with the current controller, such as dead beat response [BUS20], current loop auto-tuning [ERT20], and extension for salient machines [ALT16]. On the other hand, to counteract the delay, one-step current prediction can be incorporated with the current controller [YIM09] [SON19a] [SON19b] [ZHA17a].

Most of the above literature considered the sampling delay as a single period. In fact, however, the sampling delay could be non-integer periods in some modulating and sampling configurations. For instance, the case of one plus a fraction period delay was discussed in [FIS14]. But the voltage latch was not considered. In addition, the current controller considering half period sampling delay was designed in [HOF16] [BUS19]. However, it will be demonstrated in this chapter that their current controllers do not achieve maximum decoupling capability. Therefore, although the current controller design with single period sampling delay has been well established, for the cases of fractional period sampling delay, it still needs further investigations.

Another challenge is the rotor position estimation scheme with low sampling ratio. In typical BLAC operation, a mechanical sensor is equipped on the shaft to obtain the rotor position and speed signals. However, the sensor not only increases the system cost and size, but also reduces the reliability. Especially for high-speed drives, the installation of position sensor will enlarge the rotor axial length, leading to rotor vibration [EDE02][GER14]. Hence, sensorless schemes have attracted much attention in last decades. For medium- and high-speed BLAC operation, the rotor position estimation relies on the EMF observation technique, which can be implemented in stationary frame [BAO18][WAN13a] or estimated synchronous frame [LEE18c]

[KIM15]. Note that most EMF observers are designed in continuous-time domain and then discretized with Euler or Tustin approximation. Similar to the issue of current controller, the continuous-time EMF estimation will reduce the position estimation accuracy and even affect the system stability when the sampling ratio is insufficient. Not many documents can be found for specialized discrete-time observers. In [DIN20], discrete-time models were established in stationary frame and sliding mode observers were designed. In synchronous frame, discrete-time observers have been designed for nonsalient machines [YAN17b] and salient machines [ZHA17b][AWA16]. However, the above schemes considered the sampling delay as a single period. The discrete-time rotor position estimation considering fractional period sampling delay has been rarely studied.

In the low sampling ratio condition, both the designs of current controller and EMF observer need the exact discrete-time model that takes the digital control delay into consideration. Up to now, the exact models for two specific cases, i.e. single period sampling delay [KIM10] and half period sampling delay [BUS19], have been derived. For more generic cases, the exact models for arbitrary fractional period sampling delay are not available in literature.

To fill this gap, a comprehensive study on the digital control delay is carried out in this chapter. Firstly, a generic delay model that allows arbitrary fractional period sampling delay is proposed in section 7.2. The digital control delay including the sampling delay and the voltage latch is considered. Then, with this model, the new current controller and EMF observer can be directly designed in discrete-time domain. In section 7.3, it demonstrates that the new enhanced current controller can minimize the cross-coupling and the current tracking bandwidth is independent on the sampling ratio. In section 7.4, it illustrates how improper delay modelling will cause inaccurate rotor position estimation, which can be avoided with the new EMF observer. Section 7.5 concludes this chapter.

7.2 Generic Delay Model in Discrete-time Domain

7.2.1 Review of Current Sampling in Regular-sampled PWM

In digital control system, the digital control delay is an inevitable issue due to the calculation time and the updating mechanism of regular-sampled PWM. It was presented in [KIM10] that the digital control delay is composed of the sampling delay and the voltage latch. Fig. 7.1 shows the sequence of current sampling and voltage updating considering the digital control delay. The sampling delay is the interval between the instants from current sampling to modulation index update. The voltage latch refers to the interval during which the voltage is activated. Some documents regard the digital control delay as a whole instead of separated parts [BAE03].

The most common case is shown in Fig. 7.1 (a). After the k^{th} current sampling is proceeded at the beginning of a PWM period, it requires a short calculation time period before the k^{th} modulation index is updated. In this case, the sampling delay T_d equals to a sampling period T_s, i.e. $T_d = T_s$. Besides, the asymmetric PWM with double current sampling utilized in [ZHA17b] can be also classified into this case.

Another case is when the current is sampled in the middle of the PWM period as shown in Fig. 7.1 (b). This method is widely used to obtain the approximate average current value in a switching period [ALT15][HOF16]. For this case, the sampling delay is half a period, i.e. $T_d = \frac{1}{2} T_s$.

Besides, the sampling delay could be arbitrary fractional period. For instance, for the inverter with single DC-link current sensor, the phase currents are reconstructed with the DC-link current [HAJ10][GUY11][IMJ18]. Since in the zero voltage vector, the phase currents have no relationship with the DC-link current, the current sampling must be implemented between the top and bottom points of the carrier wave. In this condition, the sampling delay could be arbitrary fractional period and even time-variant.

It indicates that in practice, not only integer periods, but also fractional period sampling delay could happen. However, in most existing discrete-time models, the sampling delay was assumed equal to a single period. For this reason, an exact discrete-time model that allows the sampling delay to be fractional period will be derived in this section.

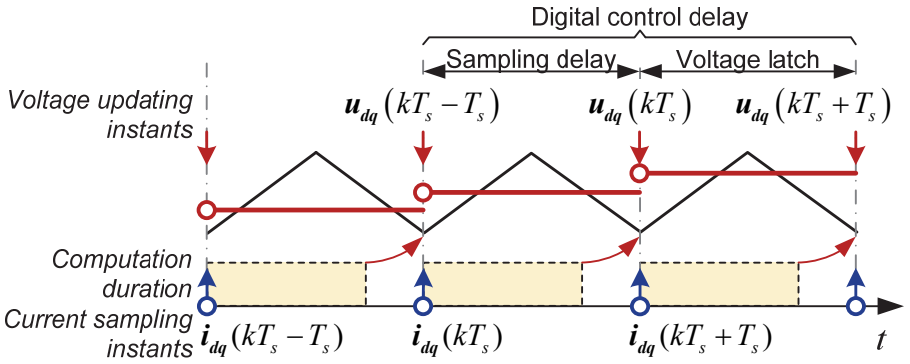

(a) Sampling in the beginning of PWM period $T_d = T_s$.

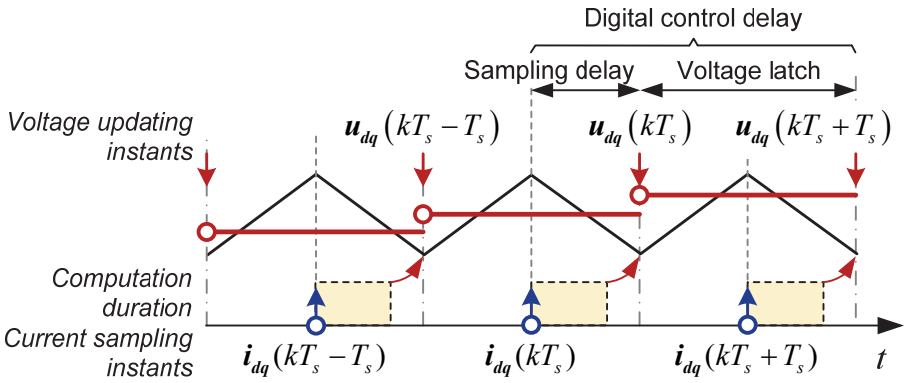

(b) Sampling in the middle of PWM period $T_d = \frac{1}{2}T_s$.

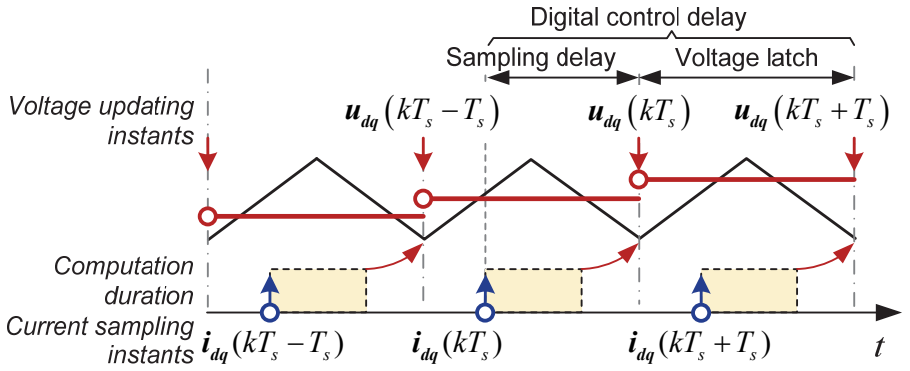

(c) Sampling in the arbitrary position of PWM period.

Fig. 7.1. Discrete-time sequence of current sampling and voltage updating.

7.2.2 Continuous-time Model

In the continuous-time system, the machine in α-β stationary frame can be modelled as

$$\frac{d}{dt}\boldsymbol{i}_{\alpha\beta}(t) = -\frac{R}{L}\boldsymbol{i}_{\alpha\beta}(t) + \frac{1}{L}\boldsymbol{u}_{\alpha\beta}(t) - \frac{1}{L}\boldsymbol{e}_{\alpha\beta}(t) \tag{7.1}$$

where R and L are the phase resistance and inductance, $\boldsymbol{i}_{\alpha\beta}(t)$, $\boldsymbol{u}_{\alpha\beta}(t)$ and $\boldsymbol{e}_{\alpha\beta}(t)$ are the current, voltage and back EMF vectors, respectively. Here, the bold letters denote the complex vectors, i.e. $\boldsymbol{f}_{dq} = f_d + j \cdot f_q$. By transforming (7.1) into d-q synchronous frame with $\boldsymbol{f}_{dq} = e^{-j\theta_e}\boldsymbol{f}_{\alpha\beta}$, it yields

$$\frac{d}{dt}\boldsymbol{i}_{dq}(t) = -(\frac{R}{L} + j\omega_e)\boldsymbol{i}_{dq}(t) + \frac{1}{L}\boldsymbol{u}_{dq}(t) - \frac{1}{L}\boldsymbol{e}_{dq}(t) \tag{7.2}$$

where ω_e is angular speed of the rotor. The additional term $j\omega_e$ is a complex quantity, which implies cross-coupling exists between d-q axes.

7.2.3 Discrete-time Model Considering Voltage Latch

In order to derive the discrete-time model of (7.2), the current differential equation (7.2) has to be solved. For simplicity, the model without sampling delay is considered here. Considering the interval between the sampling instants from kT_s to $(k+1)T_s$, the current response can be calculated as

$$\begin{aligned}\boldsymbol{i}_{dq}(kT_s + T_s) = {} & e^{-(\frac{R}{L}+j\omega_e)T_s}\boldsymbol{i}_{dq}(kT_s) \\ & + \frac{1}{L}\int_{kT_s}^{(k+1)T_s} e^{-(\frac{R}{L}+j\omega_e)[(k+1)T_s-\tau]}\boldsymbol{u}_{dq}(\tau)d\tau \\ & - \frac{1}{L}\int_{kT_s}^{(k+1)T_s} e^{-(\frac{R}{L}+j\omega_e)[(k+1)T_s-\tau]}\boldsymbol{e}_{dq}(\tau)d\tau\end{aligned} \tag{7.3}$$

To calculate the integral, the voltage $\boldsymbol{u}_{dq}(t)$ and back EMF $\boldsymbol{e}_{dq}(t)$ are required. Firstly, according to [KIM10], the back EMF is latched in the synchronous frame. Thus, it can be expressed as

$$\boldsymbol{e}_{dq}(t) = \boldsymbol{e}_{dq}(kT_s) \tag{7.4}$$

Secondly, the voltage is latched in the stationary frame, thus its derivation is a little complicated. Assume that the control system does not have delay, i.e. the output voltage is updated immediately after the current sampling, from the present sampling instant kT_s to the next instant $(k+1)T_s$, the output voltage $\boldsymbol{u}_{\alpha\beta}(t)$ generated by the inverter is held as a constant value in the α-β stationary frame as

$$\boldsymbol{u}_{\alpha\beta}(t) = e^{j\theta_e(kT_s)}\boldsymbol{u}_{dq}(kT_s) \tag{7.5}$$

where $\theta_e(kT_s)$ is the rotor position at the sampling instant kT_s. Considering the motor speed changes much slower than the electrical values, the machine speed is assumed to be a constant during the sampling instants from kT_s to $(k+1)T_s$, and it yields

$$\theta_e(t) = \theta_e(kT) + \omega_e \cdot (t - kT). \tag{7.6}$$

With (7.5) and (7.6), the voltage in the synchronous frame can be expressed as

$$\boldsymbol{u}_{dq}(t) = e^{-j\theta_e(t)} \cdot \boldsymbol{u}_{\alpha\beta}(t) = e^{-j\omega_e \cdot (t - kT_s)} \cdot \boldsymbol{u}_{dq}(kT_s). \tag{7.7}$$

In synchronous frame, the output voltage is not constant but time variant during the sampling instants. The voltage vector rotates reversely with the motor speed. Substitute (7.4) and (7.7) into (7.3), the current response can be calculated as

$$\boldsymbol{i}_{dq}(kT_s + T_s) = \boldsymbol{\Phi} \cdot \boldsymbol{i}_{dq}\left(kT_s\right) + \boldsymbol{\Gamma}_0 \cdot \boldsymbol{u}_{dq}(kT_s) + \boldsymbol{\Gamma}_e \cdot \boldsymbol{e}_{dq}(kT_s) \tag{7.8}$$

where

$$\begin{aligned}
\boldsymbol{\Phi} &= e^{-(\frac{R}{L} + j\omega_e)T_s} \\
\boldsymbol{\Gamma}_0 &= \frac{1}{R} e^{-j\omega_e T_s}\left(1 - e^{-\frac{R}{L}T_s}\right) \\
\boldsymbol{\Gamma}_e &= \frac{1}{R + j\omega_e L}\left(e^{-(\frac{R}{L} + j\omega_e)T_s} - 1\right)
\end{aligned} \tag{7.9}$$

Note that all the three coefficients $\boldsymbol{\Phi}$, $\boldsymbol{\Gamma}_0$ and $\boldsymbol{\Gamma}_e$ are complex quantities. Thus, compared with the continuous-time model (7.2), the *d*-*q* cross-coupling is also related to voltage and EMF in discrete-time domain.

7.2.4 Discrete-time Model Considering Sampling Delay

Most existing discrete-time model assumes sampling delay to be a single period. Different from those, in this study, a generic delay model is established. Fig. 7.2 shows the current and voltage considering delay. For generic expression, assume the delay from the k^{th} current sampling instant to the k^{th} voltage updating instant is $T_{d\text{-}total}$. Here, the sampling delay can be fractional multiple of, or even greater than a period T_s. Then, separate the sampling delay into an integer λ of periods plus a fraction as

$$T_{d-total} = \lambda \cdot T_s + T_d \tag{7.10}$$

where $\lambda \in \mathbb{Z}$, $0 \le T_d < T_s$. For simplicity, the case $T_{d-total} = T_s$ that should be denoted as $\lambda = 1, \cdot T_d = 0$ is denoted as $T_d = T_s$ in the follows of this chapter. Then, as shown in Fig. 7.2, during the sampling instants from kT_s to $(k+1)T_s$, two segments of voltage vectors contribute to the current response as

$$\boldsymbol{u}_{dq}(t) = \begin{cases} e^{\omega_e \cdot [t-(k-\lambda-1)T_s]} \cdot \boldsymbol{u}_{dq}\left((k-\lambda-1)T_s\right) & t \in (kT_s, kT_s + T_d) \\ e^{\omega_e \cdot [t-(k-\lambda)T_s]} \cdot \boldsymbol{u}_{dq}\left((k-\lambda)T_s\right) & t \in (kT_s + T_d, kT_s + T_s) \end{cases}. \tag{7.11}$$

Then, the integral of voltage in (7.3) is broken into two parts as

$$\begin{aligned} &\frac{1}{L}\int_{kT_s}^{kT_s+T_s} e^{-(\frac{R}{L}+j\omega_e)[(k+1)T_s-\tau]} \boldsymbol{u}_{dq}(\tau)d\tau \\ &= \underbrace{\frac{1}{L}\int_{kT_s+T_d}^{kT_s+T_s} e^{-(\frac{R}{L}+j\omega_e)[(k+1)T_s-\tau]} e^{-j\omega_e\cdot(\tau-kT_s)} d\tau}_{\boldsymbol{\Gamma_1}} \cdot \boldsymbol{u}_{dq}\left((k-\lambda)T_s\right) \\ &+ \underbrace{\frac{1}{L}\int_{kT_s}^{kT_s+T_d} e^{-(\frac{R}{L}+j\omega_e)[(k+1)T_s-\tau]} e^{-j\omega_e\cdot[\tau-(k-1)T_s]} d\tau}_{\boldsymbol{\Gamma_2}} \cdot \boldsymbol{u}_{dq}\left((k-\lambda-1)T_s\right) \end{aligned} \tag{7.12}$$

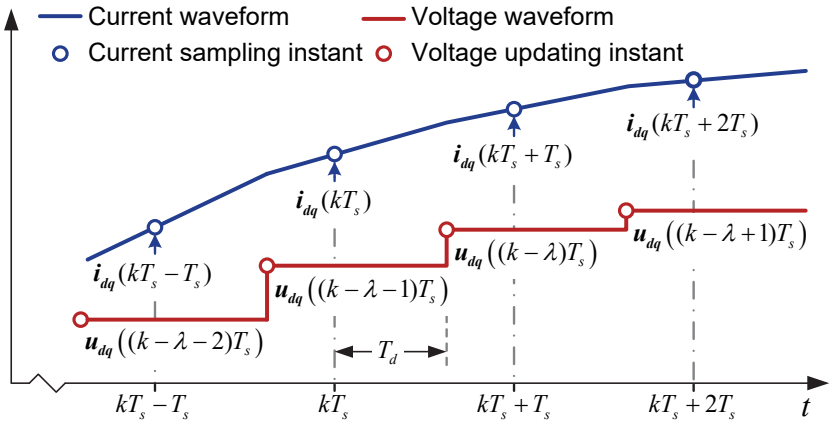

Fig. 7.2. Schematic of current and voltage with non-integer period sampling delay.

By substituting (7.12) into (7.3), the complete expression of the current response can be expressed as

$$\begin{aligned}\boldsymbol{i}_{dq}(kT_s+T_s)=&\boldsymbol{\Phi}\boldsymbol{i}_{dq}\left(kT_s\right)\\&+\boldsymbol{\Gamma}_1(T_{d-total})\boldsymbol{u}_{dq}\left((k-\lambda)T_s\right)+\boldsymbol{\Gamma}_2(T_{d-total})\boldsymbol{u}_{dq}\left((k-\lambda-1)T_s\right)\\&+\boldsymbol{\Gamma}_e\boldsymbol{e}_{dq}(kT_s)\end{aligned}\tag{7.13}$$

where $\boldsymbol{\Gamma}_1(T_{d-total})$ and $\boldsymbol{\Gamma}_2(T_{d-total})$ are functions of the sampling delay $T_{d-total}$ and can be expressed as

$$\begin{cases}\boldsymbol{\Gamma}_1(T_{d-total})=\dfrac{1}{R}e^{-j(1+\lambda)\omega_e T_s}\left(1-e^{-\frac{R}{L}(T_s-T_d)}\right)\\ \boldsymbol{\Gamma}_2(T_{d-total})=\dfrac{1}{R}e^{-(2+\lambda)j\omega_e T_s}\left(e^{-\frac{R}{L}(T_s-T_d)}-e^{-\frac{R}{L}T_s}\right)\end{cases}\tag{7.14}$$

In most machine control system, the total time delay is within a sampling period. Thus, the situation of $\lambda=0$ is considered in this study. Then, the proposed generic continuous time-delay model can be expressed as

$$\begin{aligned}\boldsymbol{i}_{dq}(kT_s+T_s)=&\boldsymbol{\Phi}\boldsymbol{i}_{dq}\left(kT_s\right)\\&+\boldsymbol{\Gamma}_1(T_d)\boldsymbol{u}_{dq}(kT_s)+\boldsymbol{\Gamma}_2(T_d)\boldsymbol{u}_{dq}(kT_s-T_s)\\&+\boldsymbol{\Gamma}_e\boldsymbol{e}_{dq}(kT_s)\end{aligned}\tag{7.15}$$

To simplify the expression, by omitting the sampling period T_s, the generic model (7.15) can be rewritten in discrete-time domain as

$$\boldsymbol{i}_{dq}[k+1]=\boldsymbol{\Phi}\boldsymbol{i}_{dq}[k]+\boldsymbol{\Gamma}_1(T_d)\boldsymbol{u}_{dq}[k]+\boldsymbol{\Gamma}_2(T_d)\boldsymbol{u}_{dq}[k-1]+\boldsymbol{\Gamma}_e\boldsymbol{e}_{dq}[k]\tag{7.16}$$

where the coefficients are

$$\begin{cases} \boldsymbol{\Gamma}_1(T_d) = \dfrac{1}{R} e^{-j\omega_e T_s} \left(1 - e^{-\frac{R}{L}(T_s - T_d)} \right) \\ \boldsymbol{\Gamma}_2(T_d) = \dfrac{1}{R} e^{-2j\omega_e T_s} \left(e^{-\frac{R}{L}(T_s - T_d)} - e^{-\frac{R}{L}T_s} \right) \end{cases} \tag{7.17}$$

Note that the generic model allows the sampling delay to be a fractional period. It indicates that when the voltage is updated between two adjacent current sampling instants, two segments of voltage vectors $\boldsymbol{u}_{dq}(kT_s)$ and $\boldsymbol{u}_{dq}(kT_s - T_s)$ contribute to the current response (for $\boldsymbol{\Gamma}_1 \neq 0, \boldsymbol{\Gamma}_2 \neq 0$). Then, by transforming (7.16) into complex discrete-time frequency domain, the plant transfer function from voltage $\boldsymbol{U}_{dq}(z)$ to the current $\boldsymbol{I}_{dq}(z)$ in *z*-domain can be expressed as

$$G_P(z) = \frac{\boldsymbol{I}_{dq}(z)}{\boldsymbol{U}_{dq}(z)} = \frac{\boldsymbol{\Gamma}_1(T_d)z + \boldsymbol{\Gamma}_2(T_d)}{z(z - \boldsymbol{\Phi})} = \frac{\boldsymbol{\Gamma}_1(T_d)\left(z + \dfrac{\boldsymbol{\Gamma}_2(T_d)}{\boldsymbol{\Gamma}_1(T_d)} \right)}{z(z - \boldsymbol{\Phi})} \tag{7.18}$$

It indicates that $G_P(z)$ contains a zero at $z = -\boldsymbol{\Gamma}_2(T_d)/\boldsymbol{\Gamma}_1(T_d)$, and two poles at $z = 0$ and $z = \boldsymbol{\Phi}$. The zero and pole of complex quantities are the origins of the *d-q* cross-coupling.

7.2.5 Particular Cases: Single and Half Period Sampling Delay

Based on the generic model (7.16), two particular cases in Fig. 7.1, i.e. single and half period sampling delay, are exemplified as follows.

1) Single Period Sampling Delay $T_d = T_s$

For the most common case of single period sampling delay, substitute $T_d = T_s$ into (7.16) and then it reduces to

$$\boldsymbol{i}_{dq}[k+1] = \boldsymbol{\Phi}\boldsymbol{i}_{dq}[k] + \boldsymbol{\Gamma}_2(T_s)\boldsymbol{u}_{dq}[k-1] + \boldsymbol{\Gamma}_e\boldsymbol{e}_{dq}[k] \tag{7.19}$$

where

$$\begin{cases} \boldsymbol{\Gamma}_1(T_s) = 0 \\ \boldsymbol{\Gamma}_2(T_s) = \dfrac{1}{R} e^{-2j\omega_e T_s} \left(1 - e^{-\frac{R}{L} T_s} \right) \end{cases} \tag{7.20}$$

Note that the model (7.8) of zero-delay ($T_d = 0$) and the model (7.19) of single sampling period time-delay ($T_d = T_s$) are two particular cases for the generic model (7.16). It can deduce that for integer period sampling delay cases, either of the voltage coefficient $\boldsymbol{\Gamma}_1$ or $\boldsymbol{\Gamma}_2$ is zero. Then, only one segment voltage vector contributes to the current response, e.g. in the model (7.8) for $T_d = 0$, $\boldsymbol{\Gamma}_2 = 0$ and only the voltage vector $\boldsymbol{u}_{dq}(kT_s)$ exists; in the model (7.19) for $T_d = T_s$, $\boldsymbol{\Gamma}_1 = 0$ and only the voltage vector $\boldsymbol{u}_{dq}(kT_s - T_s)$ exists.

The transfer function from voltage $\boldsymbol{U}_{dq}(z)$ to the current $\boldsymbol{I}_{dq}(z)$ in z-domain becomes

$$G_P^{T_d = T_s}(z) = \frac{\boldsymbol{I}_{dq}(z)}{\boldsymbol{U}_{dq}(z)} = \frac{\boldsymbol{\Gamma}_2(T_s)}{z(z - \boldsymbol{\Phi})} \tag{7.21}$$

This transfer function (7.21) matches the ones in [LOZ10] [BUS19] [YEP14].

2) *Half Period Sampling Delay* $T_d = 0.5T_s$

On the other hand, in the case of half period sampling delay $T_d = 0.5T_s$, the model (7.15) can be expressed as

$$\boldsymbol{i}_{dq}[k+1] = \boldsymbol{\Phi}\boldsymbol{i}_{dq}[k] + \boldsymbol{\Gamma}_1(\tfrac{1}{2}T_s)\boldsymbol{u}_{dq}[k] + \boldsymbol{\Gamma}_2(\tfrac{1}{2}T_s)\boldsymbol{u}_{dq}[k-1] + \boldsymbol{\Gamma}_e\boldsymbol{e}_{dq}[k] \tag{7.22}$$

where

$$\begin{cases} \boldsymbol{\Gamma}_1(\tfrac{1}{2}T_s) = \dfrac{1}{R} e^{-j\omega_e T_s} \left(1 - e^{-\frac{R}{L}\frac{T_s}{2}} \right) \\ \boldsymbol{\Gamma}_2(\tfrac{1}{2}T_s) = \dfrac{1}{R} e^{-2j\omega_e T_s} \left(e^{-\frac{R}{L}\frac{T_s}{2}} - e^{-\frac{R}{L}T_s} \right) \end{cases} \tag{7.23}$$

Note that when the time-delay is a fractional sampling period, it derives $\mathbf{\Gamma_1} \neq 0, \mathbf{\Gamma_2} \neq 0$, which means two segments of voltage vectors $\boldsymbol{u}_{\boldsymbol{dq}}(kT_s)$ and $\boldsymbol{u}_{\boldsymbol{dq}}(kT_s - T_s)$ contribute to the current response.

Likewise, the plant transfer function can be expressed as

$$G_P^{T_d=0.5T_s}(z) = \frac{\boldsymbol{I}_{\boldsymbol{dq}}(z)}{\boldsymbol{U}_{\boldsymbol{dq}}(z)} = \frac{\mathbf{\Gamma_1}(\frac{1}{2}T_s)\left(z + \frac{\mathbf{\Gamma_2}(\frac{1}{2}T_s)}{\mathbf{\Gamma_1}(\frac{1}{2}T_s)}\right)}{z(z-\mathbf{\Phi})} \tag{7.24}$$

This transfer function (7.24) matches the one in [BUS19].

7.3 Discrete-time Current Controller with Enhanced Decoupling Capability

7.3.1 Review of Existing Decoupling Controllers

In [KIM10][HOF16][BUS19], various discrete-time decoupled current controllers are proposed. The details for each controller are different but the controller structure is similar, which can be summarized as

$$G_{Con}(z) = \frac{\gamma}{\mathbf{K}} \cdot \frac{z-\mathbf{\Phi}}{z-1} \tag{7.25}$$

where γ and $\mathbf{K}$ are the gains of the controller, $\gamma \in \mathbb{R}$, $\mathbf{K} \in \mathbb{C}$. Fig. 7.3 shows the current control loop containing the current controller and the plant. The current controller (7.25) is designed based on classic pole-zero cancellation method. The controller zero $z = \mathbf{\Phi}$ is placed to cancel the pole of the plant at the same position. In this way, the cross-coupling caused by the complex value $\mathbf{\Phi}$ can be removed. In addition, the complex gain $\mathbf{K}$ is used to balance the cross-coupling caused by complex coefficients in the nominator of (7.21) and (7.24). The real gain γ is related to the tracking bandwidth. Two particular cases have been investigated in existing literature as follows.

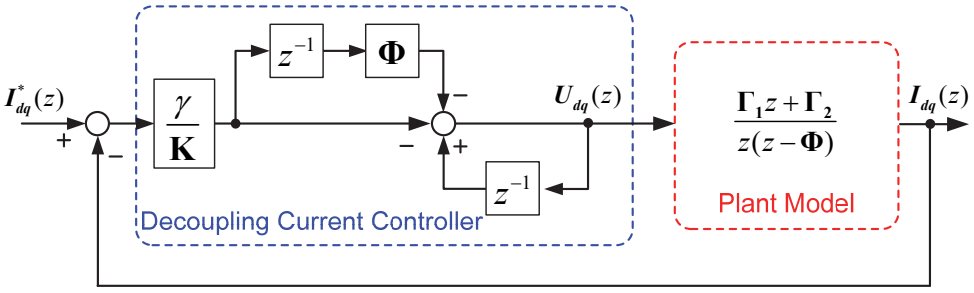

Fig. 7.3. Block diagram of current loop with decoupled current controller.

1) Single Period Sampling Delay $T_d = T_s$

In [KIM10][HOF16][BUS19], for the case of single period sampling delay, the complex gain $\mathbf{K}$ is set as $\mathbf{K} = \mathbf{\Gamma}_2(T_s)$, and the controller is

$$G_{Con}^{T_d=T_s}(z) = \frac{\gamma}{\mathbf{\Gamma}_2(T_s)} \cdot \frac{z-\mathbf{\Phi}}{z-1} \tag{7.26}$$

Then, combining with the model (7.21), the closed-loop transfer function can be calculated as

$$H_{Con}^{T_d=T_s}(z) = \frac{\boldsymbol{I}_{dq}(z)}{\boldsymbol{I}^*_{dq}(z)} = \frac{G_{Con}^{T_d=T_s}(z)G_P(z)}{1+G_{Con}^{T_d=T_s}(z)G_P(z)} = \frac{\gamma}{z^2-z+\gamma'}. \tag{7.27}$$

2) *Half Period Sampling Delay* $T_d = 0.5T_s$

For the case of half period sampling delay, i.e. $T_d = 0.5T_s$, according to the concept in [HOF16] [BUS19], $\mathbf{K}$ is set as $\mathbf{K} = \mathbf{\Gamma}_1(\frac{1}{2}T_s)$, and then the controller is

$$G_{Con}^{T_d=\frac{1}{2}T_s} = \frac{\gamma'}{\mathbf{\Gamma}_1(\frac{1}{2}T_s)} \cdot \frac{z-\mathbf{\Phi}}{z-1} \tag{7.28}$$

Here, the gain γ' is different from the one in (7.26). Then, the closed-loop transfer function can be expressed as

$$H_{Con}^{T_d=\frac{1}{2}T_s}(z) = \frac{\boldsymbol{I}_{dq}(z)}{\boldsymbol{I}^*_{dq}(z)} = \frac{G_{Con}^{T_d=\frac{1}{2}T_s}(z)G_P(z)}{1+G_{Con}^{T_d=\frac{1}{2}T_s}(z)G_P(z)} = \frac{\gamma'(z+\mathbf{A})}{z^2+(\gamma'-1)z+\gamma'\mathbf{A}}. \tag{7.29}$$

where $\mathbf{A} = \dfrac{\mathbf{\Gamma}_2(\frac{1}{2}T_s)}{\mathbf{\Gamma}_1(\frac{1}{2}T_s)}$.

The transfer function (7.27) for single period sampling delay has only real coefficients, which means the *d-q* axes can be completely decoupled when $T_d = T_s$. However, for the case $T_d = 0.5T_s$, the coefficients in transfer function (7.29) are complex values. It means the *d-q* axis cross-coupling still exists and needs further investigation.

In fact, not only the case $T_d = 0.5T_s$, as long as T_d is a fractional period, the zero of the plant transfer (7.18), i.e. $z = -\mathbf{\Gamma_2}(T_d)/\mathbf{\Gamma_1}(T_d)$, will exist and lead to cross-coupling. An intuitive solution based on the pole-zero cancellation is to set a pole with the same location in the current controller. Unfortunately, it will lead to instability and the reason is as follows. Fig. 7.4 shows the pole-zero map of the plant transfer function (7.18). It indicates that the zero is at the origin of z-plane when $T_d = 0$, and moves gradually outside the unit circle when T_d approaches to T_s. If a pole $z = -\mathbf{\Gamma_2}(T_d)/\mathbf{\Gamma_1}(T_d)$ is set in $G_C(z)$, it could lead to instability if the zero is not perfectly cancelled outside the unit circle. Thus, in theory, when T_d is a fractional period, the cross-coupling caused by the zero $z = -\mathbf{\Gamma_2}(T_d)/\mathbf{\Gamma_1}(T_d)$ cannot be eliminated completely.

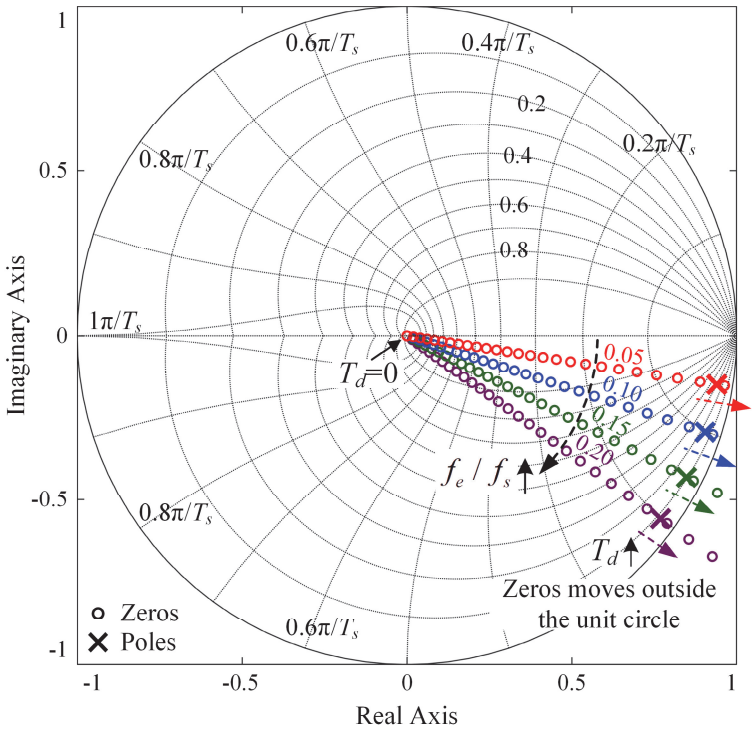

Fig. 7.4. Pole zero map of the plant transfer function taking delay T_d and fundamental frequency f_e as parameters.

7.3.2 Enhanced Decoupling Controller Based on Proposed Model

As the above analysis, for the fractional period sampling delay case, the cross-coupling caused by the zero $z=-\mathbf{\Gamma_2}(T_d)/\mathbf{\Gamma_1}(T_d)$ cannot be eliminated. Thus, the optimized result is to minimize the cross-coupling with the current controller. This can be realized through properly selecting the gain $\mathbf{K}$. Different from the scheme of (7.28) in [HOF16][BUS19], in this study, $\mathbf{K}$ is set as $\mathbf{K}=\mathbf{\Gamma_1}(T_d)+\mathbf{\Gamma_2}(T_d)$ and then, the enhanced current controller for generic time-delay model is

$$G_{En}(z)=\frac{\gamma}{\mathbf{\Gamma_1}(T_d)+\mathbf{\Gamma_2}(T_d)}\cdot\frac{z-\mathbf{\Phi}}{z-1}. \tag{7.30}$$

The closed-loop transfer function can be calculated as

$$H_{En}(z)=\frac{\boldsymbol{I}_{\boldsymbol{dq}}(z)}{\boldsymbol{I}^{*}_{\boldsymbol{dq}}(z)}=\frac{G_{En}(z)G_P(z)}{1+G_{En}(z)G_P(z)}=\frac{\gamma\mathbf{B}z+\gamma\mathbf{C}}{z^2+(\gamma\mathbf{B}-1)z+\gamma\mathbf{C}} \tag{7.31}$$

where $\mathbf{B}=\dfrac{\mathbf{\Gamma_1}(T_d)}{\mathbf{\Gamma_1}(T_d)+\mathbf{\Gamma_2}(T_d)}$ and $\mathbf{C}=\dfrac{\mathbf{\Gamma_2}(T_d)}{\mathbf{\Gamma_1}(T_d)+\mathbf{\Gamma_2}(T_d)}$. Note that the enhanced controller (7.30) is directly designed from the generic model (7.18), which means this enhanced controller is valid for arbitrary fractional period sampling delay.

7.3.3 Evaluation of Tracking and Decoupling Capabilities

In order to compare the enhanced and conventional current controllers, a method to evaluate the tracking and decoupling capabilities is introduced as follows. For a closed loop transfer function with complex coefficients, it can be broken into real and imaginary parts as

$$H(z)=\frac{\boldsymbol{I}_{\boldsymbol{dq}}(z)}{\boldsymbol{I}^{*}_{\boldsymbol{dq}}(z)}=\frac{P_N(z)+j\cdot Q_N(z)}{P_D(z)+j\cdot Q_D(z)}=P(z)+j\cdot Q(z) \tag{7.32}$$

where $P_N(z)$ and $Q_N(z)$ are the real and imaginary parts of the numerator; $P_D(z)$ and $Q_D(z)$ are the real and imaginary parts of the denominator; $P(z)$ and $Q(z)$ are the real and imaginary parts of the closed-loop transfer function and can be calculated as

$$\begin{cases} P(z) = \dfrac{P_N(z)P_D(z) + Q_N(z)Q_D(z)}{P_D{}^2(z) + Q_D{}^2(z)} \\ Q(z) = \dfrac{P_N(z)Q_D(z) + Q_N(z)P_D(z)}{P_D{}^2(z) + Q_D{}^2(z)} \end{cases} \tag{7.33}$$

Then, the complex transfer function (7.32) can be converted into scalar form as

$$\begin{bmatrix} I_d(z) \\ I_q(z) \end{bmatrix} = \begin{bmatrix} P(z) & -Q(z) \\ Q(z) & P(z) \end{bmatrix} \begin{bmatrix} I_d^*(z) \\ I_q^*(z) \end{bmatrix} \tag{7.34}$$

The transfer matrix in (7.34) reveals the relation between the reference and the response in *d-q* axes. It demonstrates that the current response of an axis is the summation of the reference in its own axis multiplying $P(z)$ and the reference in the other axis multiplying $Q(z)$ (or $-Q(z)$). Apparently, the diagonal term $P(z)$ determines the tracking capability; and the anti-diagonal term $Q(z)$ determines the decoupling capability. Based on this principle, the comparative analysis between the conventional decoupling controller and the proposed enhanced decoupling controller is carried out as follows.

1) Single Period Sampling Delay

In the case of $T_d = T_s$, the enhanced controller (7.30) is reduced to the conventional controller (7.26), which means the enhanced controller is equivalent to the one in [KIM10][HOF16][BUS19], i.e. $G_{En}^{T_d=T_s}(z) = G_{Con}^{T_d=T_s}(z)$. Then, the closed loop transfer function can be express as

$$H_{En}^{T_d=T_s}(z) = H_{Con}^{T_d=T_s}(z) = \frac{\gamma}{z^2 - z + \gamma} = P(z) + j \cdot Q(z) \tag{7.35}$$

where

$$\begin{cases} P(z) = \dfrac{\gamma}{z^2 - z + \gamma} \\ Q(z) = 0 \end{cases} \tag{7.36}$$

In this case, the imaginary part $Q(z)$ is zero, which means the *d-q* axis cross coupling is eliminated. Besides, the real part $P(z)$ has just one coefficient γ, which means the tracking performance is just dependent on γ and will not vary with the fundamental

frequency. Fig. 7.5 shows the bode diagram of $P(z)$ which indicates that the tracking bandwidth (-3dB) increases with γ .

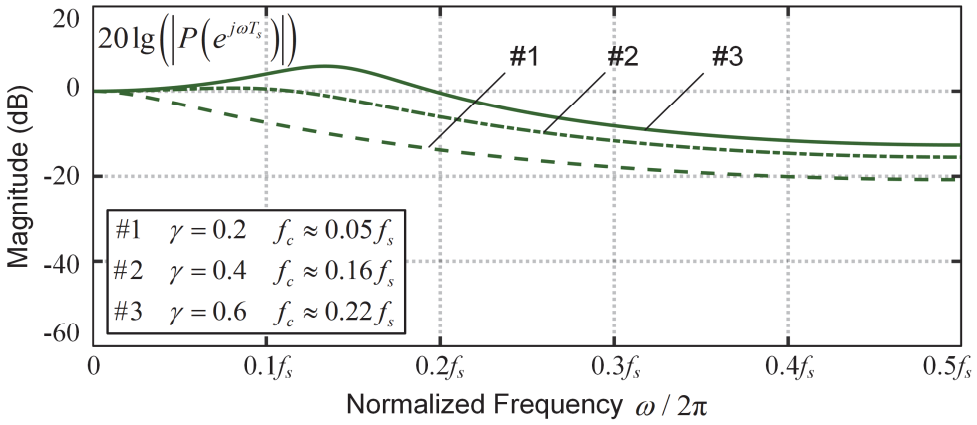

Fig. 7.5. Bode plot of $P(z)$ with $T_d = T_s$ and $f_e = 0.05 f_s$.

2) Fractional Period Sampling Delay

To demonstrate the performance of enhanced controller in the case of fractional period sampling delay, the conventional controller (7.29) that is for $T_d = 0.5T_s$ is selected for comparison. Its closed loop transfer function (7.30) can be expressed as

$$\begin{aligned} H_{Con}^{T_d=\frac{1}{2}T_s}(z) &= \frac{\gamma'\left(z+\mathbf{A}\right)}{z^2+\left(\gamma'-1\right)z+\gamma'\mathbf{A}} \\ &= \frac{\overbrace{\gamma'\left(z+\mathrm{Re}(\mathbf{A})\right)}^{P_N(z)}+j\cdot\overbrace{\gamma'\,\mathrm{Im}(\mathbf{A})}^{Q_N(z)}}{\underbrace{z^2+\left(\gamma'-1\right)z+\gamma'\,\mathrm{Re}(\mathbf{A})}_{P_D(z)}+j\cdot\underbrace{\gamma'\,\mathrm{Im}(\mathbf{A})}_{Q_D(z)}} \end{aligned} \tag{7.37}$$

On the other hand, for the enhanced controller (7.30), its closed loop transfer function (7.31) can be expressed as

$$\begin{aligned} H_{En}^{T_d=\frac{1}{2}T_s}(z) &= \frac{\gamma\mathbf{B}z+\gamma\mathbf{C}}{z^2+\left(\gamma\mathbf{B}-1\right)z+\gamma\mathbf{C}} \\ &= \frac{\overbrace{\gamma\left(\mathrm{Re}(\mathbf{B})z+\mathrm{Re}(\mathbf{C})\right)}^{P_N(z)}+j\cdot\overbrace{\gamma\left(\mathrm{Im}(\mathbf{B})z+\mathrm{Im}(\mathbf{C})\right)}^{Q_N(z)}}{\underbrace{z^2+\left(\gamma\,\mathrm{Re}(\mathbf{B})-1\right)z+\gamma\,\mathrm{Re}(\mathbf{C})}_{P_D(z)}+j\cdot\underbrace{\gamma\left(\mathrm{Im}(\mathbf{B})z+\mathrm{Im}(\mathbf{C})\right)}_{Q_D(z)}} \end{aligned} \tag{7.38}$$

With the terms $P_N(z)$, $Q_N(z)$, $P_D(z)$ and $Q_D(z)$, the real and imaginary parts, i.e. $P(z)$ and $Q(z)$, can be calculated with (7.32). Then, the tracking and decoupling

performance of the conventional and enhanced controllers can be compared. To ensure the frequency responses of conventional and enhanced controllers approximately equal to each other, the gain γ is set twice of γ'. Fig. 7.6 shows the Bode diagrams of $P(z)$ and $Q(z)$ at fixed fundamental frequency $f_e = 0.05 f_s$ with various γ (γ'). It shows that for both the controllers, as the gain γ (γ') increases, the -3dB tracking bandwidth f_b of $P(z)$ rises, and meanwhile the magnitude of $Q(z)$ rises. This implies the cross-coupling becomes severe as the bandwidth frequency f_b increases. Besides, it is shown in Fig. 7.6 (b) that across the whole frequency range (0 to $0.5f_s$), the $Q(z)$ magnitude of the enhanced controller is smaller than that of the conventional controller. It demonstrates the enhanced controller can reduce the cross-coupling without affecting f_b.

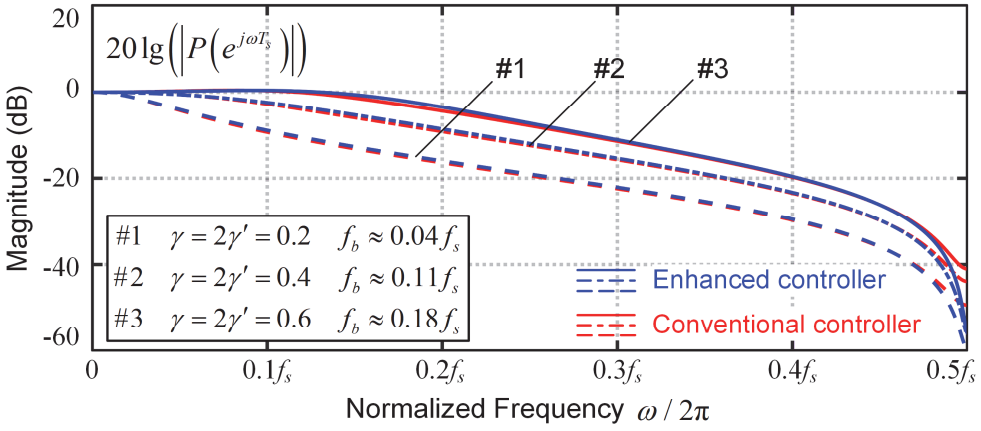

(a) Bode plot of $P(z)$.

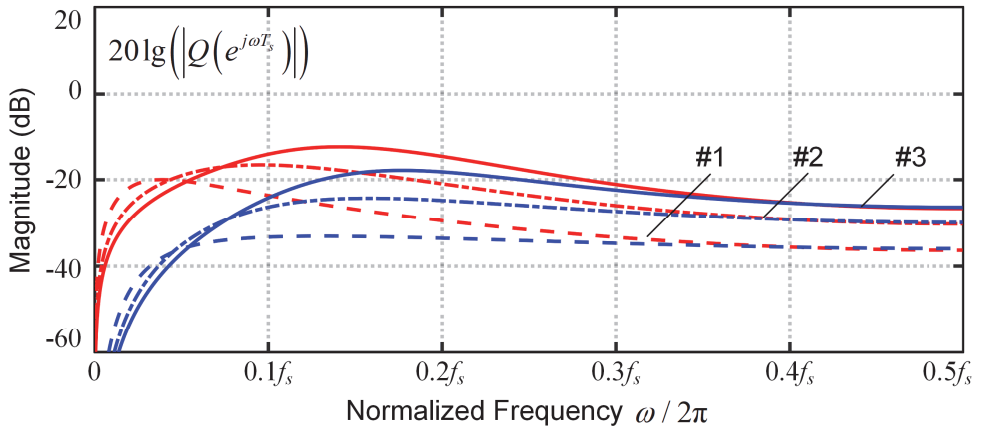

(b) Bode plot of $Q(z)$.

Fig. 7.6. Bode plot with $T_d = 0.5T_s$ and $f_e = 0.05 f_s$.

To compare the performance at high fundamental frequency (low sampling ratio), Fig. 7.7 shows the Bode plot with fixed $\gamma = 2\gamma' = 0.4$ and various fundamental

frequencies f_e / f_s (sampling ratios f_s / f_e). It shows that as the fundamental frequency f_e increases, the tracking bandwidth of conventional controller gradually decreases by 16% from $f_b = 0.11 f_s$ at $f_e = 0.01 f_s$ to $f_b = 0.092 f_s$ at $f_e = 0.1 f_s$. It means the tracking bandwidth is sensitive to low sampling ratio f_s / f_e. On the contrary, the tracking bandwidth of enhanced controller is almost independent on f_s / f_e. Besides, as shown in Fig. 7.7 (b), for any fundamental frequencies, the $Q(z)$ magnitude of the enhanced controller is smaller than that of the conventional controller.

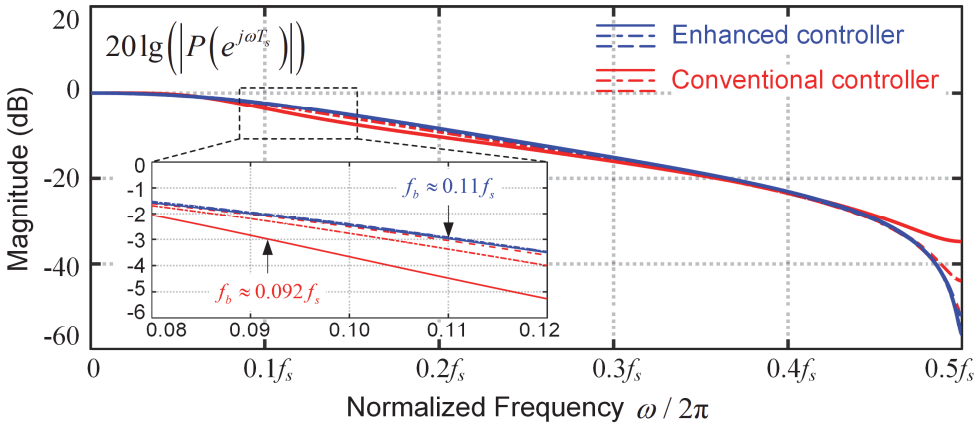

(a) Bode plot of $P(z)$.

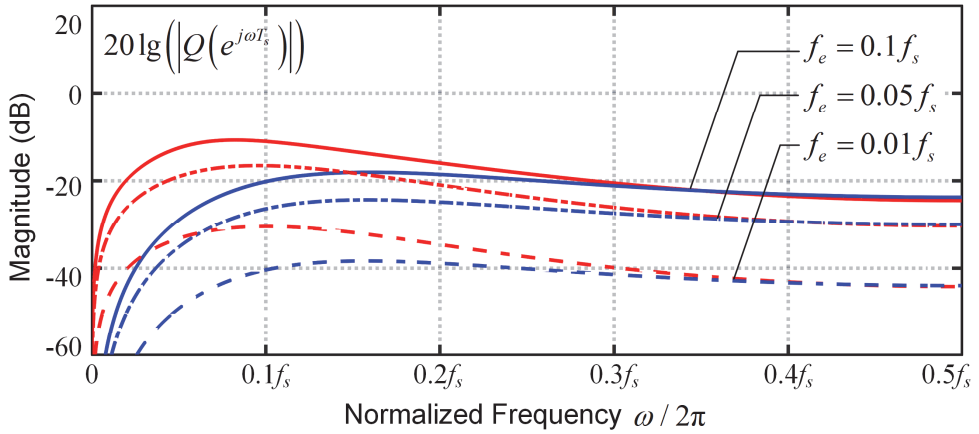

(b) Bode plot of $Q(z)$.

Fig. 7.7. Bode plot with $T_d = 0.5 T_s$ and $\gamma = 2\gamma' = 0.4$.

The comparison of the enhanced and conventional current controllers can be summarized as follows.

1) For the single period sampling delay case, the enhanced and conventional controllers are equivalent. Bode plot in Fig. 7.5 demonstrates that both of them can completely eliminate the *d-q* cross-coupling and the tracking bandwidth is independent on the sampling ratio.

2) For the half period sampling delay case, the enhanced controller has better performance than the conventional controller does. Bode plots in Figs. 7.6 and 7.7 demonstrate that the enhanced controller has stronger decoupling capability, and the tracking bandwidth is independent on the sampling ratio.

Therefore, for both integer and fractional period sampling delay cases, the enhanced controller can always achieve optimized tracking and decoupling performance.

7.3.4 Simulation Results

To validate the proposed enhanced current controller, the simulation analysis is carried out in this part. The parameters of Motor-I in Appendix is utilized. The switching and sampling frequencies are both 15kHz.

Figs. 7.8 and 7.9 compare the simulation results using three different current controllers as listed in Table 7.1. For simplification, controller A denotes the classic complex vector PI decoupling current controller designed in continuous-time domain with back-Euler discretization; controller B denotes the conventional discrete-time decoupling current controller; controller C denotes the proposed enhanced decoupling current controller. It should be noted that for conventional current controllers (controller B), only two specified cases have been studied, i.e. $T_d = 0.5T_s$ in [HOF16][BUS19] and $T_d = T_s$ in [KIM10]. In order to make a comparison for other two cases of fractional period sampling delay, i.e. $T_d = 0.25T_s$ and $T_d = 0.75T_s$, current controllers are modified according to the concept in [HOF16][BUS19]. The gain is set $\gamma = 0.35$ for controller C; controllers A and B are tuned to similar tracking bandwidth.

Table 7.1. Structures and Coefficients of Three Current Controllers.

No.	Structure	Coefficients		Origins
A	$G_{PI}(z)=\mathbf{k_p}+\frac{\mathbf{k_i}z}{z-1}$	$\mathbf{k_p}=\omega_n L, \mathbf{k_i}=\omega_n(R+j\omega_e L), \omega_n=800\times 2\pi$		Classic PI
B	$G_{Con}(z)=\frac{\gamma'}{\mathbf{K}}\cdot\frac{z-\mathbf{\Phi}}{z-1}$	$T_d=0.25T_s$	$\mathbf{K}=\mathbf{\Gamma_1}(0.25T_s), \gamma'=0.35\times 0.75$	Modified [HOF16]
		$T_d=0.5T_s$	$\mathbf{K}=\mathbf{\Gamma_1}(0.5T_s), \gamma'=0.35\times 0.5$	[HOF16]
		$T_d=0.75T_s$	$\mathbf{K}=\mathbf{\Gamma_1}(0.75T_s), \gamma'=0.35\times 0.25$	Modified [HOF16]
		$T_d=T_s$	$\mathbf{K}=\mathbf{\Gamma_2}(T_s), \gamma'=0.35$	[KIM10]
C	$G_{En}(z)=\frac{\gamma}{\mathbf{K}}\cdot\frac{z-\mathbf{\Phi}}{z-1}$	$\mathbf{K}=\mathbf{\Gamma_1}(T_d)+\mathbf{\Gamma_2}(T_d), \gamma=0.35$		This chapter

Fig. 7.8 shows the simulation results of *d*-axis current reference step change for the speed of 750Hz ($f_e=0.05f_s$) with various sampling delays. When a step change of reference is imposed to *d*-axis, the current response in *q*-axis reflects the decoupling capacity. The comparison is summarized as follows.

1) Controller A exhibits the worst decoupling capability. The *q*-axis current response due to cross-coupling is obvious and increases with the sampling delay.
2) Controller B shows the medium decoupling capacity. In the fractional period sampling delay cases $T_d=0.25T_s, 0.5T_s, 0.75T_s$ or T_s, the error in *q*-axis current response increases with the sampling delay with the controller designed in [HOF16]. In the integer period sampling delay case $T_d=T_s$, as the theory predicts, the *d*-*q* axes are completely decoupled with the controller in [KIM10].
3) Controller C presents the best decoupling capacity. In the fractional period sampling delay cases, the *q*-axis current response due to cross-coupling is minimum and does not vary with the sampling delay. In the integer period sampling delay case, controllers B and C are equivalent and the *d*-*q* axes are completely decoupled.

Fig. 7.9 shows the simulation results for the speed of 1500Hz ($f_e=0.1f_s$) with various sampling delays. When the samplings in each fundamental period become less as the motor speed increases, the *d*-*q* axis cross-coupling becomes severe. The performance of controllers A and B becomes worse compared to the result of 750Hz, except controller B with $T_d=T_s$ in Fig. 7.9 (d) in which the *d*-*q* axes are completely decoupled. Conversely, with the proposed controller C, the *d*-axis current follows the command rapidly within only six samples; the *q*-axis current shows a tiny ripple in the

cases of fractional period sampling delay and shows completely decoupled response in the integer period sampling delay case in Fig. 7.9 (d). All the simulation results agree well with the theoretical prediction. Therefore, it demonstrates the proposed controller C always achieves minimized cross-coupling, for both integer and fractional period sampling delay situations.

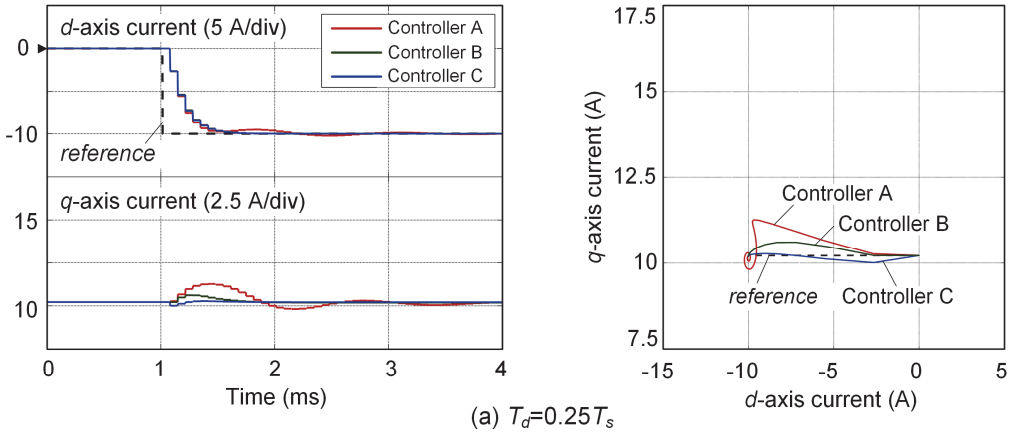

(a) T_d=0.25T_s

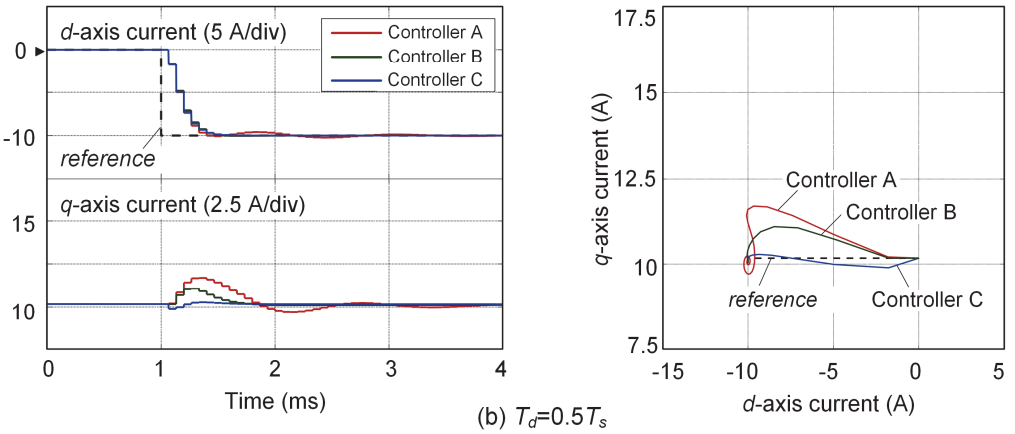

(b) T_d=0.5T_s

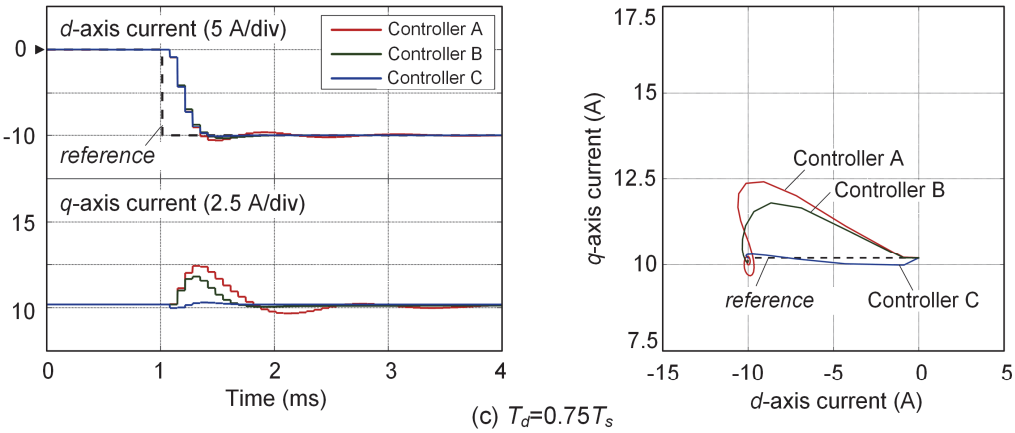

(c) T_d=0.75T_s

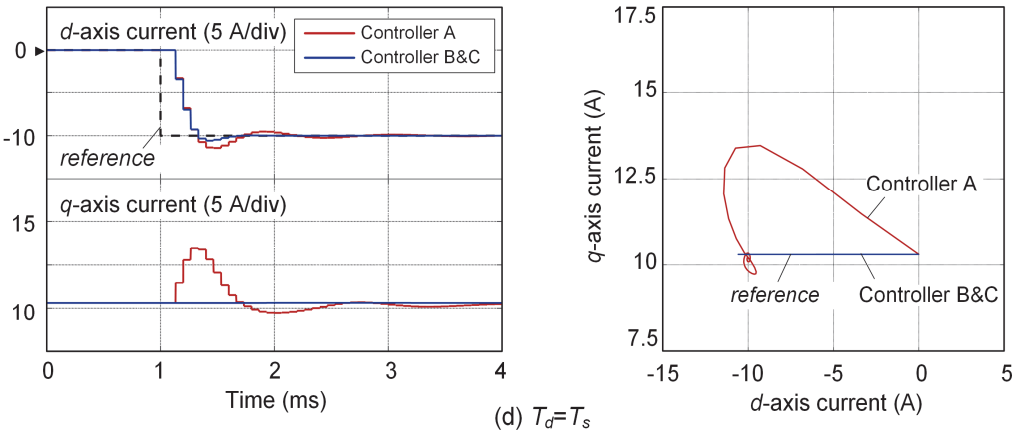

(d) T_d=T_s

Fig. 7.8. Simulation results of *d*-axis current reference step change for the speed of 750Hz ($f_e = 0.05 f_s$).

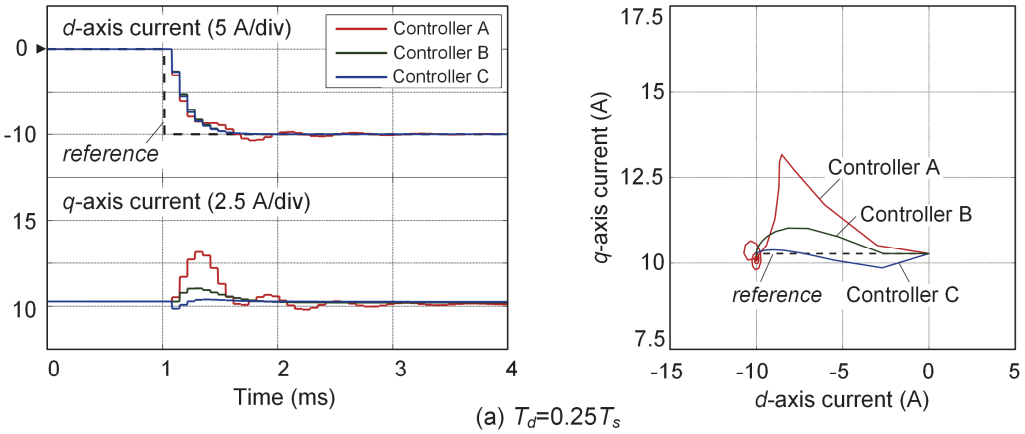

(a) T_d=0.25T_s

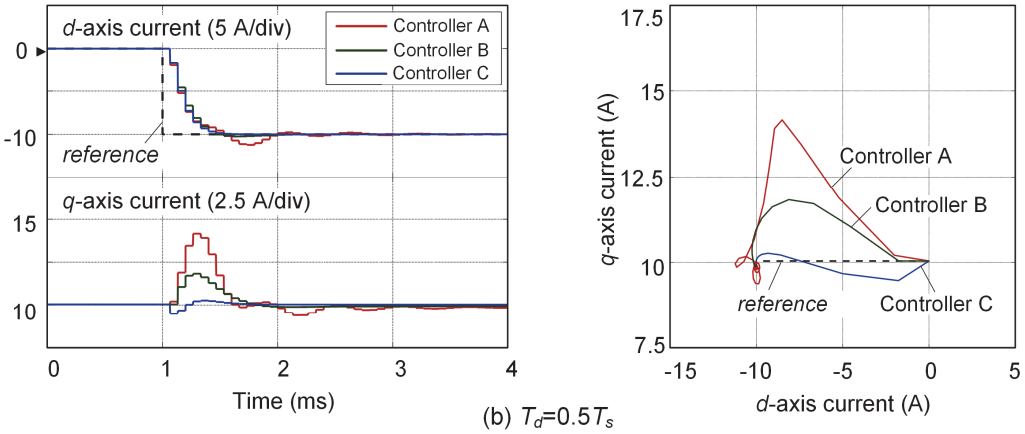

(b) T_d=0.5T_s

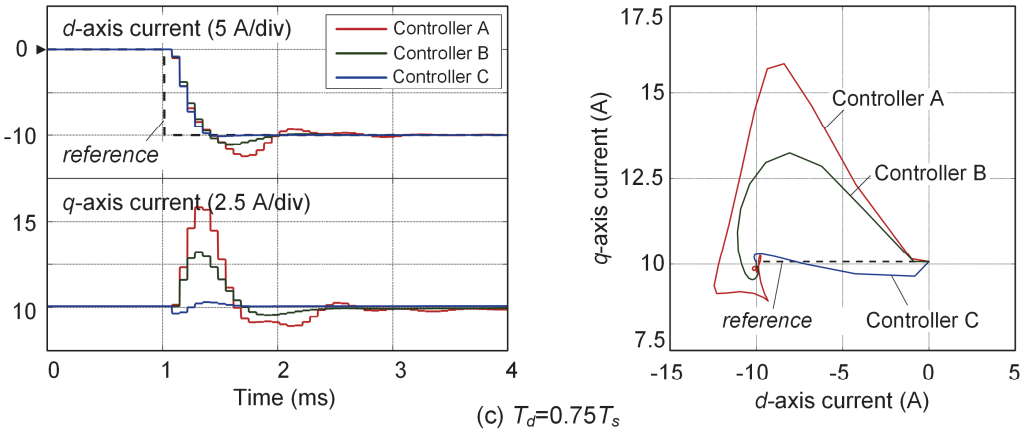

(c) T_d=0.75T_s

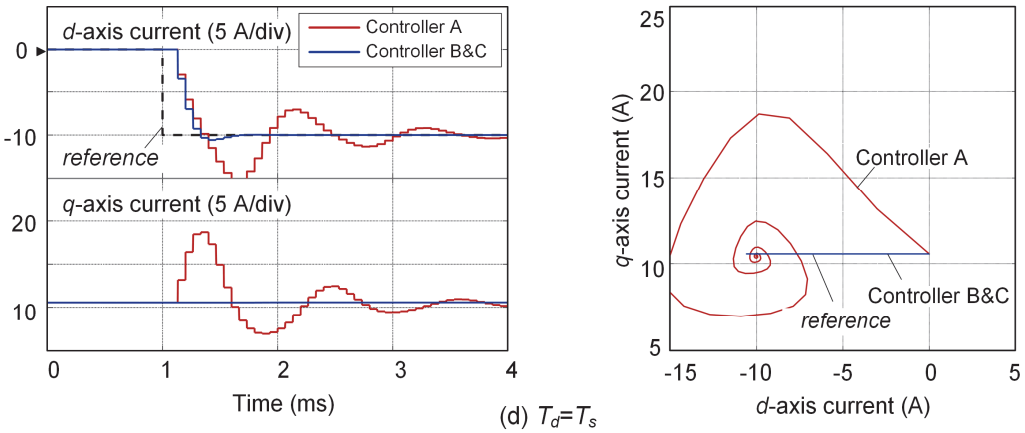

(d) T_d=T_s

Fig. 7.9. Simulation results of d-axis current reference step change for the speed of 1500Hz ($f_e = 0.1 f_s$).

7.4 Discrete-time State Observer for Rotor Position Estimation

7.4.1 EMF Observer based on Proposed Model

In a position sensorless drive system, the actual *d*-*q* frame cannot be utilized before the rotor position is detected. Thus, an estimated *d*-*q* frame (*γ*-*δ* frame) is established as Fig. 7.10. Here, $\tilde{\theta}$ is the position error between the actual position θ and the estimated position $\hat{\theta}$, i.e. $\tilde{\theta}=\theta-\hat{\theta}$. Transforming (7.16) from *d*-*q* frame to *γ*-*δ* frame with $f_{\gamma\delta}=e^{j\tilde{\theta}_e}f_{dq}$, it yields

$$\boldsymbol{i}_{\gamma\delta}[k+1]=\boldsymbol{\Phi}\boldsymbol{i}_{\gamma\delta}[k]+\boldsymbol{\Gamma}_1(T_d)\boldsymbol{u}_{\gamma\delta}[k]+\boldsymbol{\Gamma}_2(T_d)\boldsymbol{u}_{\gamma\delta}[k-1]+\boldsymbol{\Gamma}_e\boldsymbol{e}_{\gamma\delta}[k] \tag{7.39}$$

Every complex vector in (7.39) is shown in Fig. 7.10. The EMF signal can be expressed as

$$\begin{aligned}\boldsymbol{e}_{\gamma\delta}[k]&=e^{j\tilde{\theta}_e[k]}\boldsymbol{e}_{dq}[k]\\&=e^{j\tilde{\theta}_e[k]}j\psi_f\omega_e[k]\\&=\left(-\sin\left(\tilde{\theta}_e[k]\right)+j\cdot\cos\left(\tilde{\theta}_e[k]\right)\right)\psi_f\omega_e[k]\end{aligned} \tag{7.40}$$

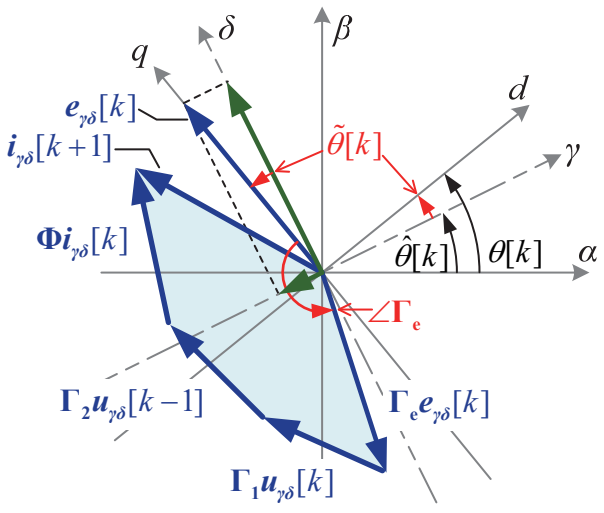

Fig. 7.10. Complex vectors in *α*-*β*, *d*-*q* and *γ*-*δ* frames.

where ψ_f is the rotor flux linkage. Since the machine speed changes much slower than the electrical values, thus during the sampling instants from kT_s to $(k+1)T_s$, the EMF vector keeps constant as

$$\boldsymbol{e}_{\gamma\delta}[k+1]=\boldsymbol{e}_{\gamma\delta}[k] \tag{7.41}$$

Based on the model equations (7.39) and (7.41) in γ-δ frame, a state observer can be established as

$$\begin{aligned}\hat{\boldsymbol{i}}_{\gamma\delta}[k+1]=&\boldsymbol{\Phi}\hat{\boldsymbol{i}}_{\gamma\delta}[k]+\overbrace{\boldsymbol{\Gamma}_1(T_d)\boldsymbol{u}_{\gamma\delta}[k]+\boldsymbol{\Gamma}_2(T_d)\boldsymbol{u}_{\gamma\delta}[k-1]}^{\text{Two segment voltages}}+\boldsymbol{\Gamma}_e\hat{\boldsymbol{e}}_{\gamma\delta}[k]\\&+\mathbf{G}_1\left(\boldsymbol{i}_{\gamma\delta}[k]-\hat{\boldsymbol{i}}_{\gamma\delta}[k]\right)\\\hat{\boldsymbol{e}}_{\gamma\delta}[k+1]=&\hat{\boldsymbol{e}}_{\gamma\delta}[k]+\mathbf{G}_2\left(\boldsymbol{i}_{\gamma\delta}[k]-\hat{\boldsymbol{i}}_{\gamma\delta}[k]\right)\end{aligned} \tag{7.42}$$

where the variables with hat ^ express estimated values, $\mathbf{G}_1$ and $\mathbf{G}_2$ are the feedback gains. Note that the state observer is directly designed from the proposed discrete-time model (7.15). Thus, it is valid for arbitrary fractional period sampling delay and it requires two segment voltages, i.e. $\boldsymbol{u}_{\gamma\delta}[k]$ and $\boldsymbol{u}_{\gamma\delta}[k-1]$, which is different from the existing discrete-time EMF estimation schemes [ZHA17b] [YAN17b].

The mechanism of the position estimation can be briefly illustrated as follows. When the estimated current $\hat{\boldsymbol{i}}_{\gamma\delta}$ converges to the actual current $\boldsymbol{i}_{\gamma\delta}$, the estimated EMF $\hat{\boldsymbol{e}}_{\gamma\delta}$ will converge to the actual EMF $\boldsymbol{e}_{\gamma\delta}$, which can be utilized for position estimation. According to (7.40), the position error $\tilde{\theta}$ can be extracted with

$$\sin\left(\tilde{\theta}_e[k]\right)=-\frac{\hat{\boldsymbol{e}}_\gamma[k]}{\sqrt{\hat{\boldsymbol{e}}_\gamma{}^2[k]+\hat{\boldsymbol{e}}_\delta{}^2[k]}}\approx\tilde{\theta}_e[k] \tag{7.43}$$

Then, by controlling the extracted position error $\tilde{\theta}_e$ to zero with the phase lock loop (PLL), the phase angle of $\hat{\boldsymbol{e}}_{\gamma\delta}$ will converge to $\pi/2$ and the rotor position can be estimated [WAN13b].

7.4.2 Influence of Improper Delay Modelling on Rotor Position Estimation

In most existing documents regarding the discrete-time EMF observer based sensorless drives, the sampling delay is assumed to be single period [ZHA17b] [YAN17b]. If such observers are employed for the plant with fractional period sampling delay, it will lead to additional position error. In this part, the influence of improper delay modelling on the position estimation will be analysed.

First, by transforming the discrete time model (7.39) into complex frequency-domain, it derives

$$\left(z-\boldsymbol{\Phi}\right)\boldsymbol{I}_{\gamma\delta}(z)=\left(\boldsymbol{\Gamma}_1(T_d)+\boldsymbol{\Gamma}_2(T_d)z^{-1}\right)\boldsymbol{U}_{\gamma\delta}(z)+\boldsymbol{\Gamma}_{\mathrm{e}}\boldsymbol{E}_{\gamma\delta}(z) \tag{7.44}$$

Likewise, the state observer (21) can be expressed as

$$\begin{aligned}\left(z-\boldsymbol{\Phi}\right)\hat{\boldsymbol{I}}_{\gamma\delta}(z)&=\left(\boldsymbol{\Gamma}_1(T_d')+\boldsymbol{\Gamma}_2(T_d')z^{-1}\right)\boldsymbol{U}_{\gamma\delta}(z)+\boldsymbol{\Gamma}_{\mathrm{e}}\hat{\boldsymbol{E}}_{\gamma\delta}(z)\\&\quad+\mathbf{G}_1\left(\boldsymbol{I}_{\gamma\delta}(z)-\hat{\boldsymbol{I}}_{\gamma\delta}(z)\right)\\\left(z-1\right)\hat{\boldsymbol{E}}_{\gamma\delta}(z)&=\mathbf{G}_2\left(\boldsymbol{I}_{\gamma\delta}(z)-\hat{\boldsymbol{I}}_{\gamma\delta}(z)\right)\end{aligned} \tag{7.45}$$

Here, T_d' is the delay utilized in the state observer. Fig. 7.11 illustrates the discrete-time position sensorless control system. Assume that the plant is with fractional sampling period time-delay ($\boldsymbol{\Gamma}_1(T_d)\neq 0, \boldsymbol{\Gamma}_2(T_d)\neq 0$) and the observer is designed with integer period sampling delay. Specifically, two cases are analysed here, 1) zero sampling delay $T_d'=0$ and then $\boldsymbol{\Gamma}_1(T_d')\neq 0, \boldsymbol{\Gamma}_2(T_d')=0$; 2) single period sampling delay $T_d'=T_s$ and then $\boldsymbol{\Gamma}_1(T_d')=0, \boldsymbol{\Gamma}_2(T_d')\neq 0$. By substituting (7.45) into (7.44), the estimated EMF can be expressed as

$$\hat{\boldsymbol{E}}_{\gamma\delta}(z)=\frac{\boldsymbol{\Gamma}_{\mathrm{e}}\mathbf{G}_2}{\boldsymbol{F}(z)}\boldsymbol{E}_{\gamma\delta}(z)+\frac{\left(\Delta\boldsymbol{\Gamma}_1+\Delta\boldsymbol{\Gamma}_2 z^{-1}\right)}{\boldsymbol{F}(z)}\boldsymbol{U}_{\gamma\delta}(z) \tag{7.46}$$

where $\Delta\boldsymbol{\Gamma}_1=\boldsymbol{\Gamma}_1(T_d)-\boldsymbol{\Gamma}_1(T_d')$ $\Delta\boldsymbol{\Gamma}_2=\boldsymbol{\Gamma}_2(T_d)-\boldsymbol{\Gamma}_2(T_d')$, and $\boldsymbol{F}(z)$ is the characteristic polynomial and can be expressed as

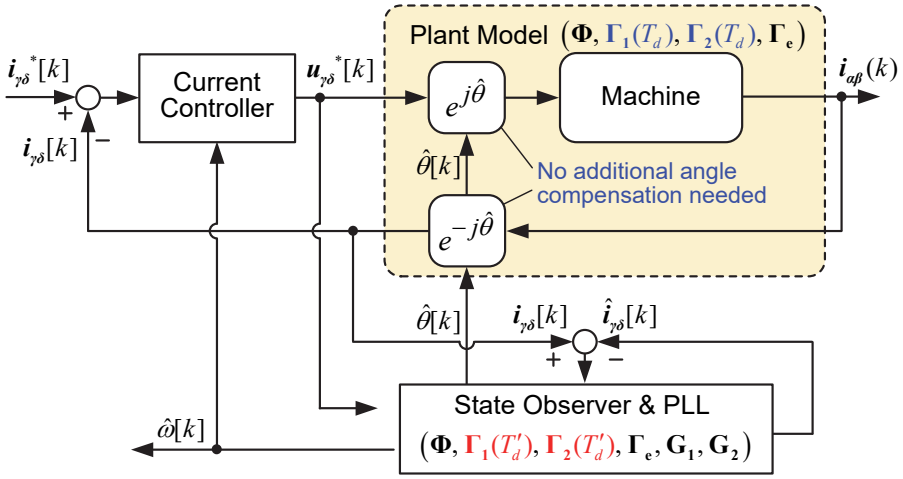

Fig. 7.11. Block diagram of discrete-time position sensorless control system.

$$\boldsymbol{F}(z) = z^2 + \left(1 - \boldsymbol{\Phi} + \mathbf{G}_1\right) z + \left(\boldsymbol{\Phi} - \mathbf{G}_2 + \boldsymbol{\Gamma}_e \mathbf{G}_2\right). \tag{7.47}$$

It is shown in (7.46) that the estimated EMF $\hat{\boldsymbol{E}}_{\gamma\delta}(z)$ is the summation of the actual EMF $\boldsymbol{E}_{\gamma\delta}(z)$ multiplying a low-pass filter and the actual voltage $\boldsymbol{U}_{\gamma\delta}(z)$ multiplying another low-pass filter. Note that in steady state $\boldsymbol{E}_{\gamma\delta}(z)$ and $\boldsymbol{U}_{\gamma\delta}(z)$ are mainly DC components. Thus, the time response of $\boldsymbol{U}_{\gamma\delta}(z)$ cannot descent to zero. In steady state, (7.46) can be transformed back into discrete-time domain as

$$\hat{\boldsymbol{e}}_{\gamma\delta}[k] = \boldsymbol{e}_{\gamma\delta}[k] + \underbrace{\left(\Delta\boldsymbol{\Gamma}_1 + \Delta\boldsymbol{\Gamma}_2\right)\boldsymbol{u}_{\gamma\delta}[k]}_{\Delta\boldsymbol{u}[k]} \tag{7.48}$$

where $\Delta\boldsymbol{u}[k]$ denotes voltage error vector caused by inaccurate coefficients $\boldsymbol{\Gamma}_1(T_d')$ and $\boldsymbol{\Gamma}_2(T_d')$ in the observer.

Figs. 7.12 (a) and (b) illustrate the influence of the voltage error $\Delta\boldsymbol{u}[k]$ on position estimation. The shaded areas represent the vector loop of actual voltage, current and EMF. For a plant with fractional period sampling delay, if the EMF observer is designed based on $T_d' = 0$ (Fig. 7.10 (a)) or $T_d' = T_s$ (Fig. 7.10 (b)), a voltage error $\Delta\boldsymbol{u}[k]$ will be introduced. Although the estimated current $\hat{\boldsymbol{i}}_{\gamma\delta}$ can converge to the actual current $\boldsymbol{i}_{\gamma\delta}$, the estimated EMF $\hat{\boldsymbol{e}}_{\gamma\delta}$ will converge to a fault vector, whose magnitude and phase angle are not consistent with the ones of the actual EMF $\boldsymbol{e}_{\gamma\delta}$. In this situation, if the PLL still controls the phase angle of estimated EMF $\hat{\boldsymbol{e}}_{\gamma\delta}$ to π/2, a false rotor position will be identified. The sign of the position error is related to the voltage error $\Delta\boldsymbol{u}[k]$. Negative and positive position error cases are exemplified in Figs. 7.10 (a) and (b), respectively. Therefore, if a voltage that is inconsistent with the actual machine voltage is fed into the state observer, it will lead to position estimation error. In addition, since $\Delta\boldsymbol{\Gamma}_1$ and $\Delta\boldsymbol{\Gamma}_2$ are functions of ω, the position estimation error will increase with the motor speed.

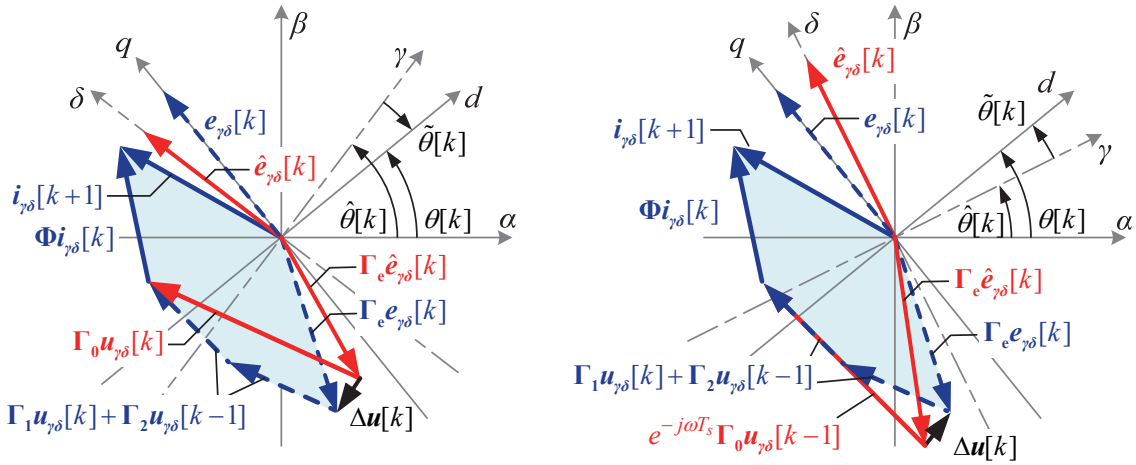

(a) Negative position error case. (b) Positive position error case.

Fig. 7.12. Complex vectors for voltage error.

7.4.3 Particular Case: Single Period Sampling Delay

Especially, for the plant with single period sampling delay $T_d = T_s$, it yields $\mathbf{\Gamma}_1(T_d) = 0$. Then, the EMF observer reduces to

$$\begin{aligned}\hat{\boldsymbol{i}}_{\gamma\delta}[k+1] &= \mathbf{\Phi}\hat{\boldsymbol{i}}_{\gamma\delta}[k] + \mathbf{\Gamma}_2(T_s)\boldsymbol{u}_{\gamma\delta}[k-1] + \mathbf{\Gamma}_e\hat{\boldsymbol{e}}_{\gamma\delta}[k] + \mathbf{G}_1\left(\boldsymbol{i}_{\gamma\delta}[k] - \hat{\boldsymbol{i}}_{\gamma\delta}[k]\right) \\ \hat{\boldsymbol{e}}_{\gamma\delta}[k+1] &= \hat{\boldsymbol{e}}_{\gamma\delta}[k] + \mathbf{G}_2\left(\boldsymbol{i}_{\gamma\delta}[k] - \hat{\boldsymbol{i}}_{\gamma\delta}[k]\right)\end{aligned} \tag{7.49}$$

Recently, literature [ZHA17b] and [YAN17b] presented the discrete-time position estimation algorithm for the plant with single period sampling delay ($T_d = T_s$). However, the coefficients utilized in their observers do not match the model of single period sampling delay ($T_d = T_s$) but the model (7.9) of zero sampling delay ($T_d = 0$) of this chapter. Thus, in fact, the observers in those papers are designed based on zero sampling delay model. In order to counteract the sampling delay, an additional angle compensation $j\omega_e T_s$ is introduced in the inverse park transformation. Although this method is valid for $T_d = T_s$, it is not suitable for plants with fractional period sampling delay.

On the contrary, in this study, both the proposed current controller and the EMF observer are directly originated from the generic delay model. Thus, as shown in Fig. 7.11, the additional angle compensation is not required, because the influence of sampling delay can be regarded as counteracted inherently inside the current controller

and the EMF observer, respectively. In addition, the importance is that the current controller and the EMF observer are suitable for both integer and fractional period sampling delay situations.

7.4.4 Simulation Results

The influence of improper delay modelling on the rotor position estimation is validated through simulation. The plant sampling delays are set $T_d = 0.25T_s$, $0.5T_s$, and $0.75T_s$ in Figs. 7.13, 7.14 and 7.15, respectively. In each figure, the observers with undervalued delay $T_d' = 0$, accurate delay $T_d' = T_d$ and overvalued delay $T_d' = T_s$ are compared. The left column is for fundamental frequency 750Hz ($f_e = 0.05 f_s$), and the right one is for 1500Hz ($f_e = 0.1 f_s$).

When the undervalued delay $T_d' = 0$ is utilized in the observer as in Figs. 7.13 (a), 7.14 (a) and 7.15 (a), the estimated EMF magnitude is less than the actual value and a negative position error is caused. Oppositely, when the overvalued delay $T_d' = T_s$ is utilized as in Figs. 7.13 (c), 7.14 (c) and 7.15 (c), the estimated EMF magnitude is greater than the actual value and a positive position error is caused. It can be concluded that estimation errors (including EMF error and position error) increase with the motor speed and the difference $\left|T_d - T_d'\right|$. The results exactly agree with the theoretical analysis in (7.46) and Fig. 7.12.

Conversely, when the observer is implemented with accurate delay $T_d' = T_d$ as in Figs. 7.13 (b), 7.14 (b) and 7.15 (b), the estimated EMF converge to the actual values and the position estimation error is eliminated. It demonstrates the new observer can accurately estimate the rotor position for the case of fractional period sampling delay.

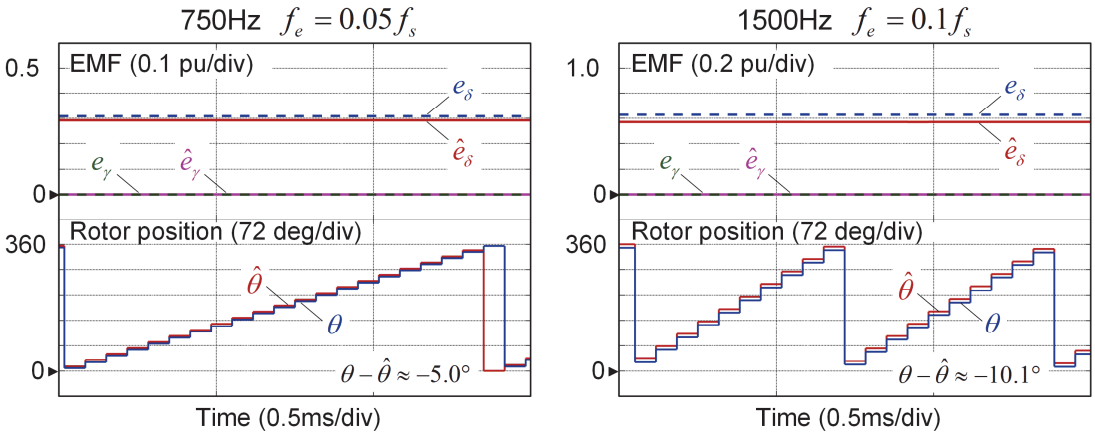

(a) $T_d = 0.25T_s, T_d' = 0$.

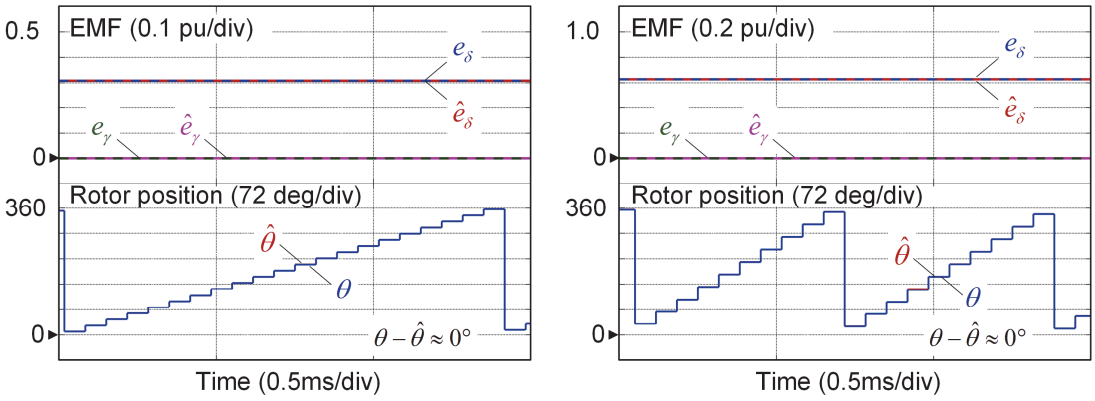

(b) $T_d = T_d' = 0.25T_s$.

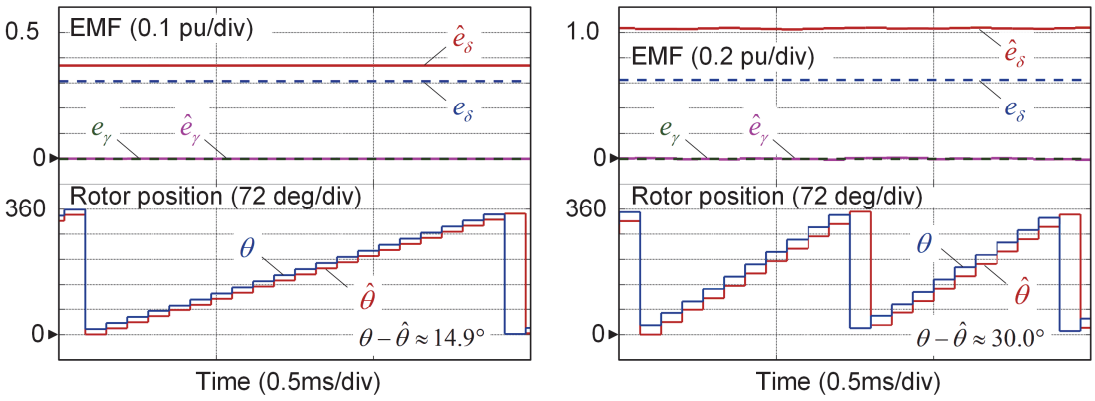

(c) $T_d = 0.25T_s, T_d' = T_s$.

Fig. 7.13. Simulation results of sensorless operation with sampling delay $T_d = 0.25T_s$, fundamental frequency 750Hz ($f_e = 0.05 f_s$ left column) and 1500Hz ($f_e = 0.1 f_s$ right column).

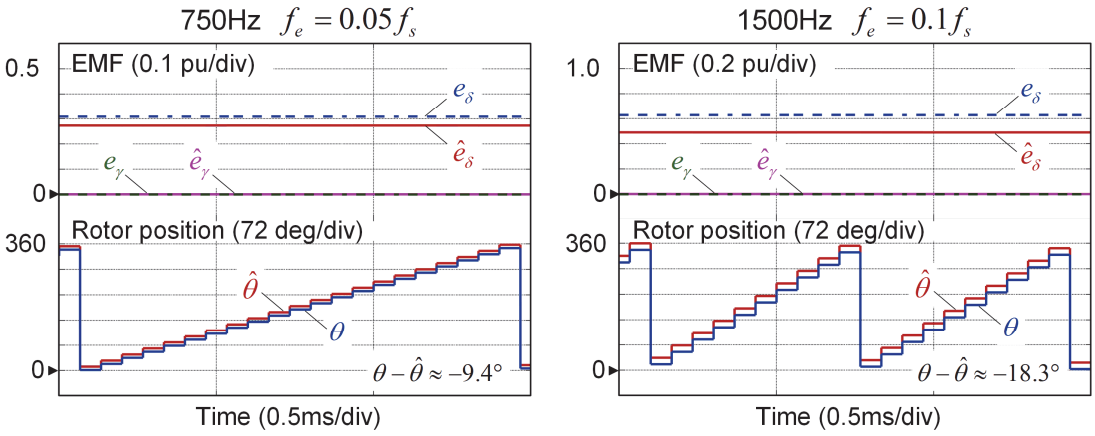

(a) $T_d = 0.5T_s, T_d' = 0$.

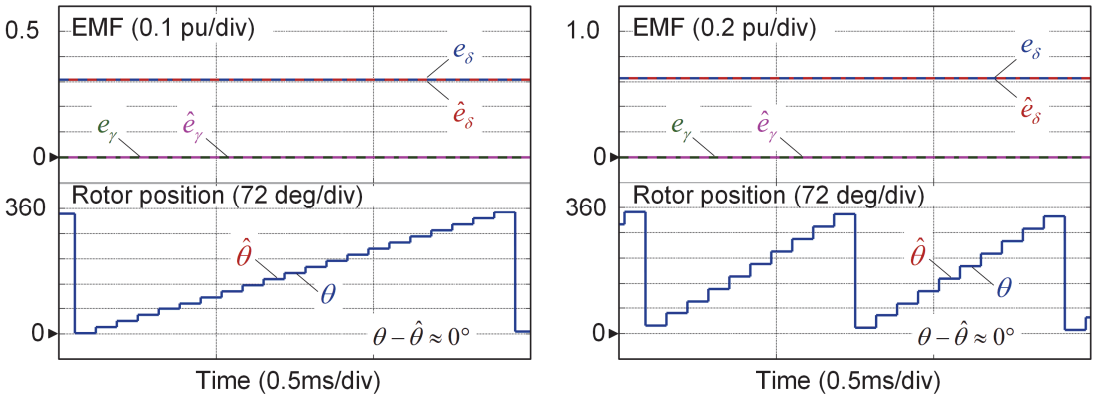

(b) $T_d = T_d' = 0.5T_s$.

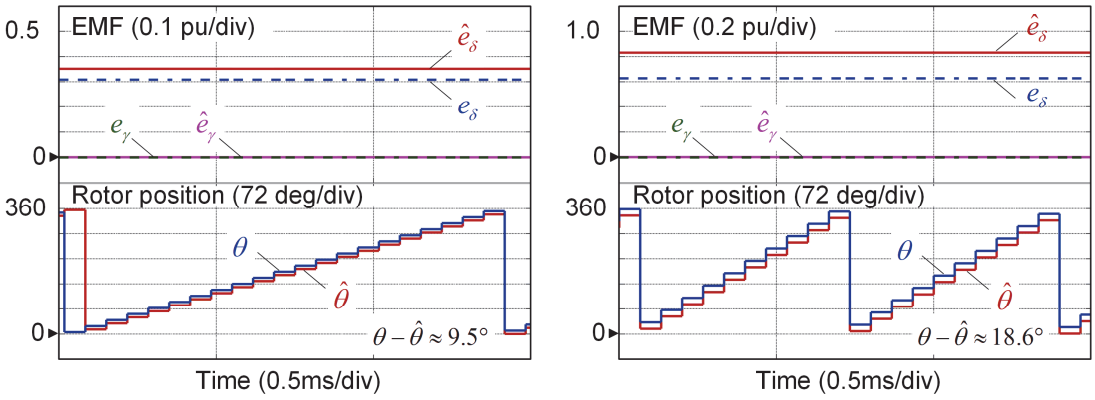

(c) $T_d = 0.5T_s, T_d' = T_s$.

Fig. 7.14. Simulation results of sensorless operation with sampling delay $T_d = 0.5T_s$, fundamental frequency 750Hz ($f_e = 0.05 f_s$ left column) and 1500Hz ($f_e = 0.1 f_s$ right column).

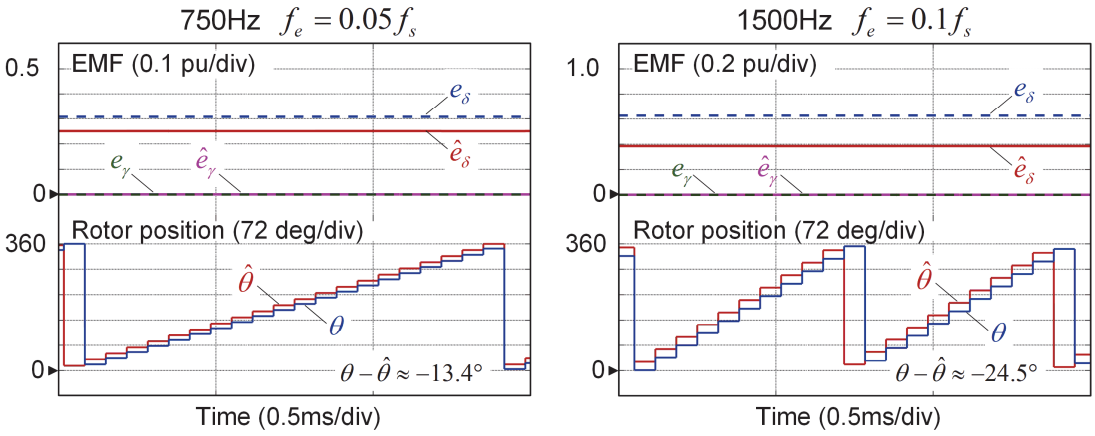

(a) $T_d = 0.75T_s, T_d' = 0$.

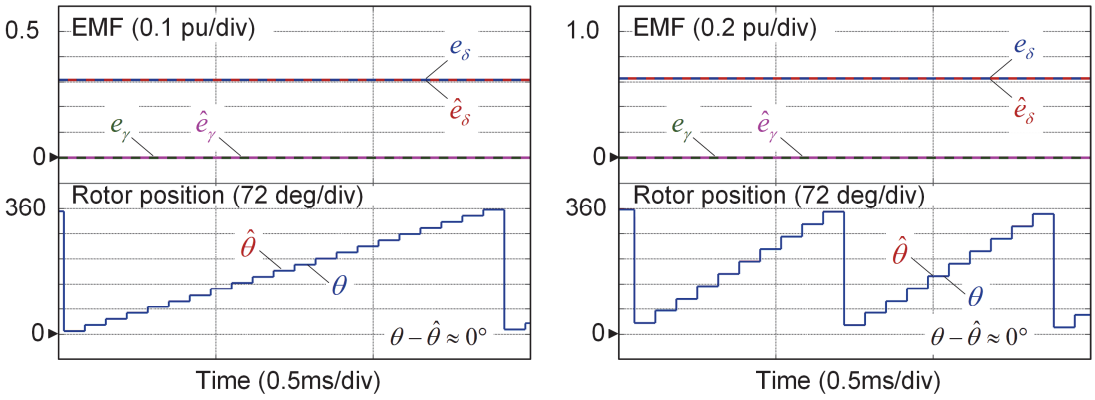

(b) $T_d = T_d' = 0.75T_s$.

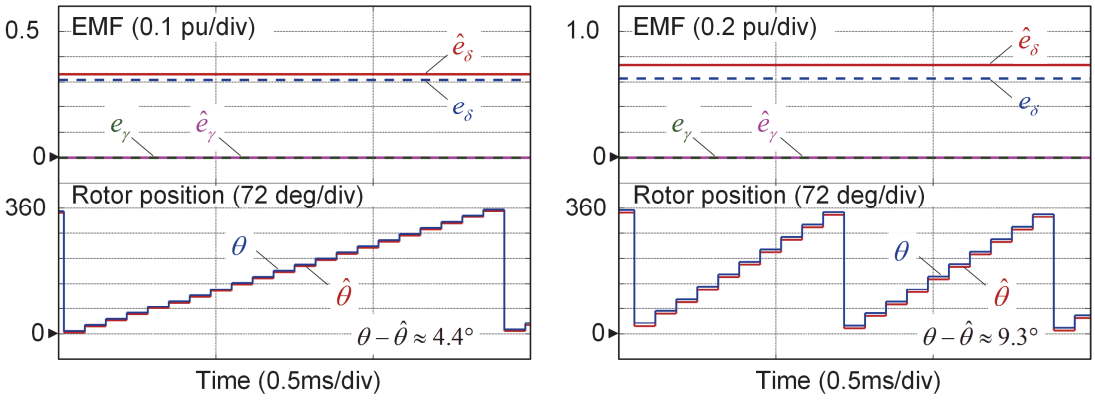

(c) $T_d = 0.75T_s, T_d' = T_s$.

Fig. 7.15. Simulation results of sensorless operation with sampling delay $T_d = 0.75T_s$, fundamental frequency 750Hz ($f_e = 0.05 f_s$ left column) and 1500Hz ($f_e = 0.1 f_s$ right column).

7.5 Summary

This chapter has investigated the discrete-time current controller and the EMF observer for sensorless high-speed BLAC drives considering low sampling ratio. In the first place, a generic discrete-time machine model considering fractional period sampling delay is established. Different from existing methods, the proposed model does not restrict the sampling delay to be a single period but allows arbitrary fractional period sampling delay. Then, based on this model, new current controller and rotor position observer are directly designed in discrete-time domain. The new current can achieve enhanced current tracking and decoupling capabilities. With the new EMF observer, the position estimation error caused by improper delay modelling can be avoided. This chapter reveals a deep insight into effects of digital control delay on designs of current controller and EMF observer. The theoretical analysis and the proposed algorithm are verified via simulation.

CHAPTER 8

General Conclusions and Discussions

This thesis has focused on sensorless brushless DC (BLDC) and brushless AC (BLAC) drives, particularly for high-speed applications. Some practical issues of sensorless methods, including the zero-crossing detection (ZCD) in BLDC drives and the back EMF observer in BLAC drives, have been discussed. Corresponding solutions have been presented and experimentally validated.

8.1 Sensorless High-speed Brushless DC Control

Considering the sensorless control is essential for high-speed motor drives, the 120° conduction six-step BLDC operation is the primary choice, because its sensorless operation is relatively easy-to-implement. When two of the three phases are conducted, the third phase is floating whose back EMF can be measured directly. Through detecting the zero-crossing point (ZCP) of the back EMF, the commutation point can be identified. After the commutation, it continues to search the back EMF ZCP and determines the next commutation point. By repeating such processes including ZCD and commutation, the sensorless BLDC operation can be realized. Although this method is simple and effective, some practical issues are still not solved perfectly in existing literature. Accordingly, some practical issues related to these two processes, i.e. ZCD (Chapters 2, 3 and 4) and commutation (Chapters 5 and 6), have been discussed in this thesis as shown in Fig. 8.1.

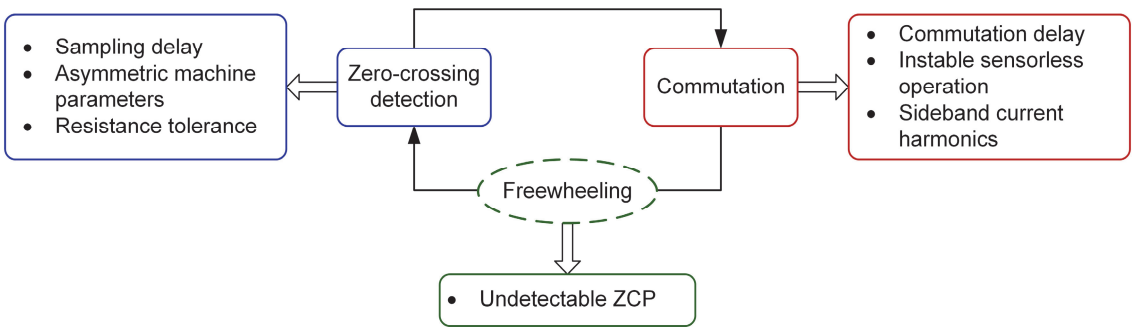

Fig. 8.1. Practical issues with sensorless BLDC drives.

Some non-ideal factors that influence the ZCD accuracy have been studied, including sampling-delay, asymmetric machine parameters and resistance tolerance of back EMF measurement circuits. These three factors will cause inaccurate detection of the zero-crossings and will further lead to commutation errors.

1) The envelope extraction based ZCD method suffers from the sampling delay issue. In the high-speed range, the sampling ratio is insufficient, which means that the interval between two consecutive samplings is unneglectable and will adversely influence the ZCD accuracy.
2) Asymmetric machine parameters (phase resistance and self-inductance) will lead to horizontal deviation of the back EMF envelope, which will further lead to unbalanced ZCPs in the virtual third harmonic method (Chapter 2) and the terminal voltage method (Chapter 3).
3) Inaccurate back EMF sampling caused by the resistance tolerance of measurement circuit will cause vertical deviation of the back EMF envelope, which will also cause unbalanced ZCPs of the terminal voltage (Chapter 3).

Inaccurate ZCD will lead to commutation errors and deteriorate the control performance. Thus, the corresponding solutions have been presented in this thesis. In the first place, the oversampling technique is employed to reduce the sampling delay in Chapter 2. Unlike the conventional method that detects the ZCP only once in each PWM period, the oversampling technique allows multiple ZCD in each PWM period. Besides, to fully utilize the available sampling duration, the number of samplings in each PWM period is dynamically adjusted according to the PWM duty ratio. In this way, the sampling delay of ZCD can be reduced significantly.

Influenced by the second and third non-ideal factors, the ZCP will deviate from ideal positions and the ZCP interval will become unbalanced. To suppress these two non-ideal factors, the mechanism has been studied and the corresponding commutation correction algorithm has been developed. For the virtual third harmonic method in Chapter 2, a simple commutation correction method based on direct calculation is proposed to suppress the errors caused by the second factor. For the terminal voltage

method in Chapter 3, the second and third factors coexist simultaneously. A commutation correction method based on feedback is proposed to suppress these two factors. The above solutions can guarantee that the ZCPs can be detected accurately.

It should be noted that the ZCP may be undetectable due to long freewheeling angle, which is a critical burden of the ZCD based sensorless method operating towards high-speed. When the freewheeling angle is larger than 30 electrical degrees, the ZCP will disappear and the sensorless drive will fail. In Chapter 4, the freewheeling angle issue of BLDC drives has been studied, which reveals how the freewheeling angle is affected by various factors. In particular, two conclusions are worth mentioning.

1) The PWM switching patterns have significant influences on the freewheeling angle, but were neglected in most existing literature. By analysing the freewheeling path of different PWM switching patterns, it is found the ON-PWM pattern can minimize the freewheeling angle.

2) Although the accurate freewheeling angle is hard to predict, its upper bound can be calculated with simple numerical iterative method, which provides a theoretical way to predict the maximum torque and speed area for sensorless control.

When the ZCP is detected after overcoming various difficulties, accurate commutation points can be identified. However, considering the unneglectable PWM switching delay in the high-speed range, the inverter could still perform the commutation with phase delay. This issue has been studied in Chapters 5 and 6, in which two conventional commutation patterns, i.e. regular-sampled commutation (RSC) and natural-sampled commutation (NSC), together with the novel carrier-synchronized commutation (CSC) are analysed comprehensively. Additionally, to reveal the spectral characteristics of conventional RSC and CSC patterns, an extended geometric wall model is introduced, which can be used for the Fourier decomposition of complex vectors. Important features of the three commutation patterns are summarized in Table 8.1. Good features are denoted by shaded background.

Table 8.1. Summary of Three Commutation Patterns

	RSC	NSC	CSC (Proposed)
Commutation delay	Y	N	N
Unstable sensorless control	Y	N	N
Sideband harmonics	Y	Y	N
Low-frequency torque ripples	Y	Y	N
Implementation complexity	Low	High	Medium

1) The conventional RSC pattern will introduce the PWM switching delay to commutation delay. Besides, this commutation delay will be accumulated and finally result in instability of ZCD based sensorless methods.

2) Both the conventional RSC and NSC patterns will lead to abundant sideband current harmonics when the switching ratio is insufficient. These sideband current harmonics will further result in low frequency torque ripples.

3) With the proposed CSC pattern, the commutation delay and the unstable sensorless control can be avoided and the sideband current harmonics can be eliminated, which can considerably improve the control performance.

As above mentioned, the ZCD based sensorless method includes two processes, i.e. ZCD and commutation. Issues of ZCD have been discussed in Chapters 2, 3 and 4; issues of commutation have been discussed in Chapters 5 and 6. According to these issues, the corresponding solutions have been proposed, which facilitate the drive operating towards high-speed, with particular considerations of insufficient sampling and switching ratios in the high-speed range.

8.2 Sensorless High-speed Brushless AC Control

For the sensorless high-speed BLAC control, the main challenge is the design of current controller and rotor position observer. Since the machine dynamic response with insufficient sampling (switching) ratio is quite different compared to the classical

continuous-time machine model, it is desired to design the current controller and rotor position observer directly in the discrete-time domain.

To this end, the generic discrete-time machine model is proposed in Chapter 7. Different from existing methods, the proposed model does not restrict the sampling delay to be a single period but allows arbitrary fractional period sampling delay. Based on this model, discrete-time current controller and rotor position observer are investigated. In particular, following conclusions are worth mentioning.

1) In the single period sampling delay case, the proposed current controller and the conventional current controller are equivalent and can achieve completely *d-q* axis decoupling control.

2) In the fractional period sampling delay case, the *d-q* cross-coupling cannot be completely removed in theory, since it introduces an additional zero in the transfer function. The proposed controller presents enhanced current tracking and decoupling performance compared to the conventional current controller.

3) Most existing EMF observers only considered integer period sampling delay and the ones for fractional period sampling delay were rarely investigated. As the theory predicts, these EMF observers for integer period sampling delay will cause position errors for plants with fractional period sampling delay. The proposed EMF observer is designed based on the generic model and can avoid the errors caused by improper delay modelling.

This study reveals a deep insight into effects of digital control delay on the BLAC control system. It demonstrates that the exact discrete-time machine model can improve the design of the current controller and the EMF observer.

8.3 Future Work

As regards the future work, two aspects are suggested to investigate for sensorless BLDC and BLAC drives, respectively.

1) In the study of asymmetric machine parameters in sensorless BLDC drives, only the phase resistance and self-inductance are considered in this thesis. In fact, the mutual inductance and the back EMF magnitude could be also asymmetric, which may result in commutation errors. Thus, it needs further investigation to suppress the commutation errors.

2) Further investigation is also desired for the sensorless BLAC control. Although the discrete-time current controller and rotor position observer present good performance in the condition of low sampling ratio, it relies on the accurate machine modelling. Some uncertainties such as machine parameter mismatches could impose adverse impacts on the sensorless control performance. Hence, improved sensorless control method needs to be developed to avoid this issue.

REFERENCES

[ACH20] R. K. Achary, S. Durgaprasanth, C. Nagamani and G. S. Ilango, "A simple voltage modulator scheme for torque ripple minimization in a permanent magnet brushless DC motor," *IEEE Trans. Power Electron*., vol. 35, no. 3, pp. 2809-2818, Mar. 2020.

[AHF10] A. Ahfock and D. Gambetta, "Sensorless commutation of printed circuit brushless direct current motors," *IET Electr. Power Appl.*, vol. 4, no. 6, pp. 397-406, Jul. 2010.

[ALM17] A. H. Almarhoon, Z. Q. Zhu, and P. Xu, "Improved rotor position estimation accuracy by rotating carrier signal injection utilizing zero-sequence carrier voltage for dual three-phase PMSM," *IEEE Trans. Ind. Electron.*, vol. 64, no. 6, pp. 4454–4462, Jun. 2017.

[ALT16] A. Altomare, A. Guagnano, F. Cupertino and D. Naso, "Discrete-time control of high-speed salient machines," *IEEE Trans. Ind. Appl.*, vol. 52, no. 1, pp. 293-301, Jan.-Feb. 2016.

[AWA16] H. A. A. Awan, T. Tuovinen, S. E. Saarakkala and M. Hinkkanen, "Discrete-time observer design for sensorless synchronous motor drives," *IEEE Trans. Ind. Appl.*, vol. 52, no. 5, pp. 3968-3979, Sep.-Oct. 2016.

[BAE03] B. Bae and S. Sul, "A compensation method for time delay of full-digital synchronous frame current regulator of PWM AC drives," *IEEE Trans. Ind. Appl.*, vol. 39, no. 3, pp. 802-810, May-Jun. 2003.

[BAO18] D. Bao, X. Pan, Y. Wang, X. Wang and K. Li, "Adaptive synchronous-frequency tracking-mode observer for the sensorless control of a surface PMSM," *IEEE Trans. Ind. Appl.*, vol. 54, no. 6, pp. 6460-6471, Nov.-Dec. 2018.

[BAS18] M. Baszynski and S. Pirog, 'Unipolar modulation for a BLDC motor with simultaneously switching of two transistors with closed loop control for four-quadrant operation,' *IEEE Trans. Ind. Informat.*, vol. 14, no. 1, pp. 146-155, Jan. 2018.

[BER14] T. Bernardes, V. F. Montagner, H. A. Gründling and H. Pinheiro, "Discrete-time sliding mode observer for sensorless vector control of permanent magnet synchronous machine," *IEEE Trans. Ind. Electron*., vol. 61, no. 4, pp. 1679-1691, Apr. 2014.

[BIA04] N. Bianchi, S. Bolognani and F. Luise, "Potentials and limits of high-speed PM motors," *IEEE Trans. Ind. Appl*., vol. 40, no. 6, pp. 1570-1578, Nov.-Dec. 2004.

[BIA06] N. Bianchi, S. Bolognani and F. Luise, "High speed drive using a slotless PM motor," *IEEE Trans. Power Electron*., vol. 21, no. 4, pp.

1083-1090, Jul. 2006.

[BLA93] H.S. Black, *Modulation Theory*, New York: Van Nostrand, 1993.

[BOL03] S. Bolognani, L. Tubiana and M. Zigliotto, “Extended Kalman filter tuning in sensorless PMSM drives,” *IEEE Trans. Ind. Appl.*, vol. 39, no. 6, pp. 1741-1747, Nov.-Dec. 2003.

[BOL08] I. Boldea, M. C. Paicu, and G.-D. Andreescu, “Active flux concept for motion-sensorless unified AC drives,” *IEEE Trans. Power Electron.*, vol. 23, no. 5, pp. 2612–2618, Sep. 2008.

[BOL09] I. Boldea, M. C. Paicu, G.-D. Andreescu, and F. Blaabjerg, ““Active flux” DTFC-SVM sensorless control of IPMSM,” *IEEE Trans. Energy Convers.*, vol. 24, no. 2, pp. 314–322, Jun. 2009.

[BUS19] C. A. Busada, S. G. Jorge and J. A. Solsona, “Comments on “digital current control in a rotating reference frame—part I: system modeling and the discrete time-domain current controller with improved decoupling capabilities”,” *IEEE Trans. Power Electron.*, vol. 34, no. 3, pp. 2980-2984, Mar. 2019.

[BUS20] C. A. Busada, S. G. Jorge and J. A. Solsona, “A synchronous reference frame PI current controller with dead beat response,” *IEEE Trans. Ind. Electron.*, vol. 35, no. 3, pp. 3097-3105, Mar. 2020.

[CHA15] K. T. Chau, “Permanent magnet brushless motor drives,” *in Electric Vehicle Machines and Drives: Design, Analysis and Application*, *IEEE*, 2015, pp.69-107.

[CHE03] Z. Chen, M. Tomita, S. Doki and S. Okuma, “An extended electromotive force model for sensorless control of interior permanent-magnet synchronous motors,” *IEEE Trans. Ind. Electron*., vol. 50, no. 2, pp. 288-295, Apr. 2003

[CHE07] C. H. Chen and M. Y. Cheng, “A new cost effective sensorless commutation method for brushless dc motors without phase shift circuit and neutral voltage,” *IEEE Trans. Power Electron.*, vol. 22, no. 2, pp. 644-653, Mar. 2007.

[CHE16] W. Chen, H. Sun, X. Gu and C. Xia, ‘Synchronized space-vector PWM for three-level VSI with lower harmonic distortion and switching frequency,’ *IEEE Trans. Power Electron*., vol. 31, no. 9, pp. 6428-6441, Sep. 2016.

[CHE17a] S. Chen, G. Liu and S. Zheng, “Sensorless control of BLDCM drive for a high-speed maglev blower using low-pass filter,” *IEEE Trans. Power Electron.*, vol. 32, no. 11, pp. 8845-8856, Nov. 2017.

[CHE17b] S. Chen, G. Liu and L. Zhu, “Sensorless control strategy of a 315 kw high-speed BLDC motor based on a speed-independent flux linkage function,” *IEEE Trans. Ind. Electron.*, vol. 64, no. 11, pp. 8607-8617,

Nov. 2017.

[CHE17c] W. Chen, Y. Liu, X. Li, T. Shi and C. Xia, “A novel method of reducing commutation torque ripple for brushless DC motor based on Cuk converter,” *IEEE Trans. Power Electron*., vol. 32, no. 7, pp. 5497-5508, Jul. 2017.

[CHE18] S. Chen, X. Zhou, G. Bai, K. Wang, and L. Zhu, “Adaptive commutation error compensation strategy based on a flux linkage function for sensorless brushless DC motor drives in a wide speed range,” *IEEE Trans. Power Electron.*, vol. 33, no. 5, pp. 3752-3764, May 2018.

[CHE19] W. Chen, Z. Liu, Y. Cao, X. Li, T. Shi and C. Xia, “A position sensorless control strategy for BLDCM based on flux-linkage function,” *IEEE Trans. Ind. Electron*., vol. 66, no. 4, pp. 2570-2579, Apr. 2019.

[CHO19] J. Choi, K. Nam, A. A. Bobtsov and R. Ortega, “Sensorless control of IPMSM based on regression model,” *IEEE Trans. Power Electron.*, vol. 34, no. 9, pp. 9191-9201, Sep. 2019,

[CHU14] T. W. Chun, Q. V. Tran, H. H. Lee and H. G. Kim, “Sensorless control of BLDC motor drive for an automotive fuel pump using a hysteresis comparator,” *IEEE Trans. Power Electron.*, vol. 29, no. 3, pp. 1382-1391, Mar. 2014.

[CUI15a] C. Cui, G. Liu, K. Wang and X. Song, “Sensorless drive for high-speed brushless DC motor based on the virtual neutral voltage,” *IEEE Trans. Power Electron*., vol. 30, no. 6, pp. 3275-3285, Jun. 2015.

[CUI15b] C. Cui, G. Liu and K. Wang, ‘A novel drive method for high-speed brushless DC motor operating in a wide range,’ *IEEE Trans. Power Electron.*, vol. 30, no. 9, pp. 4998-5008, Sep. 2015.

[DAM17] A. Damiano, A. Floris, G. Fois, I. Marongiu, M. Porru and A. Serpi, “Design of a high-speed ferrite-based brushless DC machine for electric vehicles,” *IEEE Trans. Ind. Appl*., vol. 53, no. 5, pp. 4279-4287, Sep.-Oct. 2017.

[DAR15] A. Darba, F. De Belie and J. A. Melkebeek, “A back-emf threshold self-sensing method to detect the commutation instants in BLDC drives,” *IEEE Trans. Ind. Electron*., vol. 62, no. 10, pp. 6064-6075, Oct. 2015.

[DEN19] W. Deng and S. Zuo, “Comparative study of sideband electromagnetic force in internal and external rotor PMSMs with SVPWM technique,” *IEEE Trans. Ind. Electron*., vol. 66, no. 2, pp. 956-966, Feb. 2019.

[DIN20] L. Ding, Y. Li and N. Zargari, “Discrete-time SMO sensorless control of current source converter-fed PMSM drives with low switching frequency,” *IEEE Trans. Ind. Electron*. doi: 10.1109/

TIE.2020.2972433

[EDE02] J. D. Ede, Z. Q. Zhu and D. Howe, “Rotor resonances of high-speed permanent-magnet brushless machines,” *IEEE Trans. Ind. Appl.*, vol. 38, no. 6, pp. 1542-1548, Nov.-Dec. 2002.

[ERT20] F. Erturk and B. Akin, “Spatial inductance estimation for current loop auto-tuning in IPMSM self-commissioning,” *IEEE Trans. Ind. Electron.*, vol. 67, no. 5, pp. 3911-3920, May 2020.

[FAN14] J. Fang, W. Li and H. Li, “Self-compensation of the commutation angle based on DC-link current for high-speed brushless dc motors with low inductance,” *IEEE Trans. Power Electron.*, vol. 29, no. 1, pp. 428-439, Jan. 2014.

[FIS14] J. R. Fischer, S. A. González, M. A. Herrán, M. G. Judewicz and D. O. Carrica, “Calculation-delay tolerant predictive current controller for three-phase inverters,” *IEEE Trans. Ind. Informat.*, vol. 10, no. 1, pp. 233-242, Feb. 2014.

[FUY18] Y. Fu, M. Takemoto, S. Ogasawra, and K. Orikawa, “Investigation of efficiency enhancement of an ultra-high-speed bearingless motor at 100,000 r/min by high switching frequency using SiC-MOSFET,” *in Proc. IEEE Energy Convers. Congr. Expo. (ECCE)*, Portland, OR, USA, Sep. 2018, pp. 2306–2313.

[GAB13] F. Gabriel, F. De Belie, X. Neyt, and P. Lataire, “High-frequency issues using rotating voltage injections intended for position self-sensing,” *IEEE Trans. Ind. Electron*., vol. 60, no. 12, pp. 5447–5457, Dec. 2013.

[GER14] D. Gerada, A. Mebarki, N. L. Brown, C. Gerada, A. Cavagnino and A. Boglietti, “High-speed electrical machines: technologies, trends, and developments,” *IEEE Trans. Ind. Electron*., vol. 61, no. 6, pp. 2946-2959, Jun. 2014.

[GON11] L. M. Gong and Z. Q. Zhu, “A novel method for compensating inverter nonlinearity effects in carrier signal injection-based sensorless control from positive-sequence carrier current distortion,” *IEEE Trans. Ind. Appl.*, vol. 47, no. 3, pp. 1283–1292, May/Jun. 2011.

[GUC18] C. Gu, X. Wang, X. Shi and Z. Deng, “A PLL-based novel commutation correction strategy for a high-speed brushless DC motor sensorless drive system,” *IEEE Trans. Ind. Electron.*, vol. 65, no. 5, pp. 3752-3762, May 2018.

[GUY11] Y. Gu, F. Ni, D. Yang and H. Liu, "Switching-state phase shift method for three-phase-current reconstruction with a single DC-link current sensor," *IEEE Trans. Ind. Electron*., vol. 58, no. 11, pp. 5186-5194, Nov. 2011.

[HAI16] G. Haines and N. Ertugrul, “Wide speed range sensorless operation of

brushless permanent-magnet motor using flux linkage increment," *IEEE Trans. Ind. Electron*., vol. 63, no. 7, pp. 4052–4060, Jul. 2016.

[HAJ03] J.-I. Ha, K. Ide, T. Sawa, and S.-K. Sul, "Sensorless rotor position estimation of an interior permanent-magnet motor from initial states," *IEEE Trans. Ind. Appl.*, vol. 39, no. 3, pp. 761–767, May/Jun. 2003.

[HAJ10] J. Ha, "Current prediction in vector-controlled PWM inverters using single DC-link current sensor," *IEEE Trans. Ind. Electron*., vol. 57, no. 2, pp. 716-726, Feb. 2010.

[HAN08] Q. Han, N. Samoylenko and J. Jatskevich, "Average-value modeling of brushless DC motors with 120° voltage source inverter," *IEEE Trans. Energy Convers*., vol. 23, no. 2, pp. 423-432, Jun. 2008.

[HIN12] M. Hinkkanen, T. Tuovinen, L. Harnefors and J. Luomi, "A combined position and stator-resistance observer for salient PMSM drives: design and stability analysis," *IEEE Trans. Power Electron.*, vol. 27, no. 2, pp. 601-609, Feb. 2012.

[HOF16] N. Hoffmann, F. W. Fuchs, M. P. Kazmierkowski and D. Schröder, "Digital current control in a rotating reference frame - Part I: System modeling and the discrete time-domain current controller with improved decoupling capabilities," *IEEE Trans. Power Electron.*, vol. 31, no. 7, pp. 5290-5305, Jul. 2016,

[HOL03] D. G. Holmes and T. A. Lipo, *Pulse Width Modulation of Power Converters: Principles and Practice*. Piscataway, NJ: Wiley-IEEE Press, 2003.

[HOL09] J. Holtz and N. Oikonomou, "Fast dynamic control of medium voltage drives operating at very low switching frequency—an overview," *IEEE Trans. Ind. Electron.*, vol. 55, no. 3, pp. 1005-1013, Mar. 2008.

[IMJ18] J. Im and R. Kim, "Improved saliency-based position sensorless control of interior permanent-magnet synchronous machines with single DC-link current sensor using current prediction method," *IEEE Trans. Ind. Electron*., vol. 65, no. 7, pp. 5335-5343, July 2018.

[JAN03] J.-H. Jang, S.-K. Sul, J.-I. Ha, K. Ide, and M. Sawamura, "Sensorless drive of surface-mounted permanent-magnet motor by high-frequency signal injection based on magnetic saliency," *IEEE Trans. Ind. Appl.*, vol. 39, no. 4, pp. 1031–1039, Jul./Aug. 2003.

[JAR11] R. K. Jardan, P. Stumpf, P. Bartal, Z. Varga, and I. Nagy, 'A novel approach in studying the effects of subharmonics on ultrahigh-speed AC motor drives,' *IEEE Trans. Ind. Electron.*, vol. 58, no. 4, pp. 1274–1281, Apr. 2011.

[JIA05] Quan Jiang, Chao Bi and Ruoyu Huang, "A new phase-delay-free method to detect back EMF zero-crossing points for sensorless control of spindle motors," *IEEE Trans. Magn.*, vol. 41, no. 7, pp. 2287-2294,

July 2005.

[JIA18] G. Jiang, C. Xia, W. Chen, T. Shi, X. Li and Y. Cao, “Commutation torque ripple suppression strategy for brushless DC motors with a novel noninductive boost front end,” *IEEE Trans. Power Electron*., vol. 33, no. 5, pp. 4274-4284, May 2018.

[JIA19] Y. Jiang, W. Xu, C. Mu, J. Zhu and R. Dian, “an improved third-order generalized integral flux observer for sensorless drive of PMSMs,” *IEEE Trans. Ind. Electron.*, vol. 66, no. 12, pp. 9149-9160, Dec. 2019

[KEZ17] Z. Ke, J. Zhang and R. Raich, ‘Low-frequency current oscillation reduction for six-step operation of three-phase inverters,’ *IEEE Trans. Power Electron*., vol. 32, no. 4, pp. 2948-2956, Apr. 2017.

[KHL12] A. Khlaief, M. Bendjedia, M. Boussak, and M. Gossa, “A nonlinear observer for high-performance sensorless speed control of IPMSM drive,” *IEEE Trans. Power Electron.*, vol. 27, no. 6, pp. 3028–3040, Feb. 2012.

[KIM04] T.-H. Kim and M. Ehsani, “Sensorless control of the BLDC motors from near zero to high speed,” *IEEE Trans. Power Electron.*, vol. 19, no. 6, pp. 1635–1645, 2004.

[KIM06] D. Kim, K. Lee and B. Kwon, ‘Commutation Torque Ripple Reduction in a Position Sensorless Brushless DC Motor Drive,’ *IEEE Trans. Power Electron*., vol. 21, no. 6, pp. 1762-1768, Nov. 2006.

[KIM10] H. Kim, M. W. Degner, J. M. Guerrero, F. Briz and R. D. Lorenz, “Discrete-time current regulator design for AC machine drives,” *IEEE Trans. Ind. Appl.*, vol. 46, no. 4, pp. 1425-1435, Jul.-Aug. 2010.

[KIM11] H. Kim, J. Son and J. Lee, “A high-speed sliding-mode observer for the sensorless speed control of a PMSM,” *IEEE Trans. Ind. Electron*., vol. 58, no. 9, pp. 4069-4077, Sep. 2011.

[KIM12] S. Kim, J.-I. Ha, and S.-K. Sul, “PWM switching frequency signal injection sensorless method in IPMSM,” *IEEE Trans. Ind. Appl.*, vol. 48, no. 5, pp. 1576–1587, Sep./Oct. 2012.

[KIM15] J. Kim, I. Jeong, K. Nam, J. Yang and T. Hwang, “Sensorless control of PMSM in a high-speed region considering iron loss,” *IEEE Trans. Ind. Electron.*, vol. 62, no. 10, pp. 6151-6159, Oct. 2015.

[KIM16] S. I. Kim, J. H. Im, E. Y. Song, and R. Y. Kim, “A new rotor position estimation method of IPMSM using all-pass filter on high-frequency rotating voltage signal injection,” *IEEE Trans. Ind. Electron.*, vol. 63, no. 10, pp. 6499–6509, Oct. 2016.

[KOW15] D. Kowal, P. Sergeant, L. Dupré and H. Karmaker, “Comparison of frequency and time-domain iron and magnet loss modeling including PWM harmonics in a PMSG for a wind energy application,” *IEEE*

Trans. Energy Convers., vol. 30, no. 2, pp. 476-486, Jun. 2015.

[KRA10] D. Krähenbühl, C. Zwyssig, H. Weser and J. W. Kolar, "A miniature 500 000-r/min electrically driven turbocompressor," *IEEE Trans. Ind. Appl.*, vol. 46, no. 6, pp. 2459-2466, Nov.-Dec. 2010.

[KSH12] P. Kshirsagar et al., "Implementation and sensorless vector-control design and tuning strategy for SMPM machines in fan-type applications," *IEEE Trans. Ind. Appl.*, vol. 48, no. 6, pp. 2402-2413, Nov.-Dec. 2012.

[LAI08a] Y. Lai and Y. Lin, "Quicken the pulse," IEEE Industry Applications Magazine, vol. 14, no. 5, pp. 34-44, Sep.-Oct. 2008.

[LAI08b] Y. Lai and Y. Lin, "Novel back-EMF detection technique of brushless DC motor drives for wide range control without using current and position sensors," *IEEE Trans. Power Electron*, vol. 23, no. 2, pp. 934-940, Mar. 2008.

[LAI11] Y. S. Lai and Y. K. Lin, "A unified approach to zero-crossing point detection of back EMF for brushless DC motor drives without current and hall sensors," *IEEE Trans. Power Electron.*, vol. 26, no. 6, pp. 1704-1713, Jun. 2011.

[LEE16] A. C. Lee, S. Wang, and C. J. Fan, "A current index approach to compensate commutation phase error for sensorless brushless DC motors with nonideal back EMF," *IEEE Trans. Power Electron*., vol. 31, no. 6. pp. 4389–4399, 2016.

[LEE17] A. Lee, C. Fan and G. Chen, "Current integral method for fine commutation tuning of sensorless brushless DC motor" *IEEE Trans. Power Electron.*, vol. 32, no. 12, pp. 9249-9266, Dec. 2017.

[LEE18a] M. Lee and K. Kong, "Fourier-series-based phase delay compensation of brushless DC motor systems," *IEEE Trans. Power Electron.*, vol. 33, no. 1, pp. 525-534, Jan. 2018

[LEE18b] W. Lee, D. Han and B. Sarlioglu, 'Comparative performance analysis of reference voltage-controlled pulse width modulation for high-speed single-phase brushless dc motor drive,' *IEEE Trans. Power Electron.*, vol. 33, no. 5, pp. 4560-4568, May 2018.

[LEE18c] Y. Lee and S. Sul, "Model-based sensorless control of an IPMSM with enhanced robustness against load disturbances based on position and speed estimator using a speed error," *IEEE Trans. Ind. Appl.*, vol. 54, no. 2, pp. 1448-1459, Mar.-Apr. 2018.

[LEE19] K. Lee, F. Li and W. Yao, "Comparative performance evaluation of hall effect sensorless control options in permanent magnet brushless DC motor drives," *in Proc. IEEE Int. Electric Mach. Drives Conf.*, San Diego, CA, USA, 2019, pp. 1110-1117.

[LEE20] Y. Lee, J. Gil and W. Kim, “Velocity control for sideband harmonics compensation in permanent magnet synchronous motors with low switching frequency inverter,” *IEEE Trans. Ind. Electron*. doi: 10.1109/TIE.2020.2979569.

[LIA13] W. Liang, J. Wang and W. Fang, “Analytical modeling of sideband current harmonic components in induction machine drive with voltage source inverter by an SVM technique,” *IEEE Trans. Power Electron.*, vol. 28, no. 11, pp. 5372-5379, Nov. 2013.

[LIA16] W. Liang, W. Fei and P. C. Luk, “An improved sideband current harmonic model of interior PMSM drive by considering magnetic saturation and cross-coupling effects,” *IEEE Trans. Ind. Electron*., vol. 63, no. 7, pp. 4097-4104, Jul. 2016.

[LIA17] D. Liang, J. Li and R. Qu, “Sensorless control of permanent magnet synchronous machine based on second-order sliding-mode observer with online resistance estimation,” *IEEE Trans. Ind. Appl.*, vol. 53, no. 4, pp. 3672-3682, July-Aug. 2017.

[LIA18] W. Liang, P. C. Luk and W. Fei, “Investigation of magnetic field interharmonics and sideband vibration in the FSCW IPMSM drive with the SPWM technique,” *IEEE Trans. Power Electron*., vol. 33, no. 4, pp. 3315-3324, Apr. 2018.

[LIH17] H. Li, S. Zheng and H. Ren, “Self-correction of commutation point for high-speed sensorless BLDC motor with low inductance and nonideal back EMF,” *IEEE Trans. Power Electron.*, vol. 32, no. 1, pp. 642-651, Jan. 2017.

[LIN11] Y. Lin and Y. Lai, “Pulsewidth modulation technique for BLDCM drives to reduce commutation torque ripple without calculation of commutation time,” *IEEE Trans. Ind. Appl*., vol. 47, no. 4, pp. 1786-1793, Jul.-Aug. 2011.

[LIU14] J. M. Liu and Z. Q. Zhu, “Improved sensorless control of permanent-magnet synchronous machine based on third-harmonic back EMF,” *IEEE Trans. Ind. Appl.*, vol. 50, no. 3, pp. 1861-1870, May-Jun. 2014.

[LIU16] G. Liu, C. Cui, K. Wang, B. Han and S. Zheng, “Sensorless control for high-speed brushless DC motor based on the line-to-line back EMF,” *IEEE Trans. Power Electron.*, vol. 31, no. 7, pp. 4669-4683, Jul. 2016.

[LIU17] G. Liu, S. Chen, S. Zheng and X. Song, “Sensorless low-current start-up strategy of 100-kW BLDC motor with small inductance,” *IEEE Trans. Ind. Inform.*, vol. 13, no. 3, pp. 1131-1140, Jun. 2017.

[LIU18] Y. Liu, J. Ou, M. Schiefer, P. Breining, F. Grilli and M. Doppelbauer, “Application of an amorphous core to an ultra-high-speed sleeve-free interior permanent-magnet rotor,” *IEEE Trans. Ind. Electron.*, vol. 65, no. 11, pp. 8498-8509, Nov. 2018.

[LIU19a] K. Liu, Z. Zhou and W. Hua, “A novel region-refinement pulse width modulation method for torque ripple reduction of brushless DC motors,” *IEEE Access*, vol. 7, pp. 5333-5342, 2019.

[LIU19b] J. Liu, W. Zhang, F. Xiao, C. Lian and S. Gao, ‘Six-step mode control of IPMSM for railway vehicle traction eliminating the DC offset in input current,’ *IEEE Trans. Power Electron*., vol. 34, no. 9, pp. 8981-8993, Sep. 2019.

[LIW16] W. Li, J. Fang, H. Li and J. Tang, “Position sensorless control without phase shifter for high-speed BLDC motors with low inductance and nonideal back EMF,” *IEEE Trans. Power Electron.*, vol. 31, no. 2, pp. 1354-1366, Feb. 2016.

[LIX16] X. Li, C. Xia, Y. Cao, W. Chen and T. Shi, “Commutation torque ripple reduction strategy of Z-Source inverter fed brushless DC motor,” *IEEE Trans. Power Electron*., vol. 31, no. 11, pp. 7677-7690, Nov. 2016.

[MOR96] J. C. Moreira, “Indirect sensing for rotor flux position of permanent magnet AC motors operating over a wide speed range,” *IEEE Trans. Ind. Appl.*, vol. 32, no. 6, pp. 1394-1401, Nov/Dec 1996.

[ODA13] M. Odavic, V. Biagini, M. Sumner, P. Zanchetta and M. Degano, “Low carrier–fundamental frequency ratio PWM for multilevel active shunt power filters for aerospace applications,” *IEEE Trans. Ind. Appl*., vol. 49, no. 1, pp. 159-167, Jan.-Feb. 2013.

[OGA91] S. Ogasawara and H. Akagi, “An approach to position sensorless drive for brushless DC motors,” *IEEE Trans. Ind. Appl.*, vol. 27, no. 5, pp. 928-933, Sep.-Oct. 1991.

[ORT11] R. Ortega, L. Praly, A. Astolfi, J. Lee, and K. Nam, “Estimation of rotor position and speed of permanent magnet synchronous motors with guaranteed stability,” *IEEE Trans. Control Syst. Technol.*, vol. 19, no. 3, pp. 601–614, May 2011.

[PAR17] J. S. Park and K. Lee, “Online advanced angle adjustment method for sinusoidal BLDC motors with misaligned hall sensors,” *IEEE Trans. Power Electron.*, vol. 32, no. 11, pp. 8247-8253, Nov. 2017.

[PAR18] J. Park, S. Jung and J. Ha, ‘Variable time step control for six-step operation in surface-mounted permanent magnet machine drives,’ *IEEE Trans. Power Electron*., vol. 33, no. 2, pp. 1501-1513, Feb. 2018.

[PAR19] J. S. Park, K. Lee, S. G. Lee and W. Kim, “Unbalanced ZCP compensation method for position sensorless BLDC motor,” *IEEE Trans. Power Electron.,* vol. 34, no. 4, pp. 3020-3024, Apr. 2019.

[PAR20] J. Park and D. Lee, “Simple commutation torque ripple reduction using PWM with compensation voltage,” *IEEE Trans. Ind. Appl*., vol.

56, no. 3, pp. 2654-2662, May-Jun. 2020.

[PON12] S. Po-ngam and S. Sangwongwanich, “Stability and dynamic performance improvement of adaptive full-order observers for sensorless PMSM drive,” *IEEE Trans. Power Electron.*, vol. 27, no. 2, pp. 588-600, Feb. 2012.

[QIA13] Z. Qiao, T. Shi, Y. Wang, Y. Yan, C. Xia and X. He, “New sliding-mode observer for position sensorless control of permanent-magnet synchronous motor,” *IEEE Trans. Ind. Electron*., vol. 60, no. 2, pp. 710-719, Feb. 2013.

[QUA14] N. K. Quang, N. T. Hieu and Q. P. Ha, “FPGA-based sensorless PMSM speed control using reduced-order extended Kalman filters,” *IEEE Trans. Ind. Electron.*, vol. 61, no. 12, pp. 6574-6582, Dec. 2014.

[RAC08] D. Raca, P. Garcia, D. Reigosa, F. Briz, and R. Lorenz, “A comparative analysis of pulsating vs. Rotating vector carrier signal injection-based sensorless control,” *in Proc. 32nd Annu. IEEE Appl. Power Electron. Conf. Expo.*, 2008, pp. 879–885.

[RAT13] A. K. Rathore, J. Holtz and T. Boller, ‘Generalized optimal pulsewidth modulation of multilevel inverters for low-switching-frequency control of medium-voltage high-power industrial AC drives,’ *IEEE Trans. Ind. Electron.*, vol. 60, no. 10, pp. 4215-4224, Oct. 2013.

[REI10] D. D. Reigosa, P. Garcia, F. Briz, D. Raca and R. D. Lorenz, “Modeling and adaptive decoupling of high-frequency resistance and temperature effects in carrier-based sensorless control of PM synchronous machines,” *IEEE Trans. Ind. Appl.*, vol. 46, no. 1, pp. 139-149, Jan.-Feb. 2010.

[SAH16] S. K. Sahoo and T. Bhattacharya, ‘Rotor flux-oriented control of induction motor with synchronized sinusoidal PWM for traction application,’ *IEEE Trans. Power Electron*., vol. 31, no. 6, pp. 4429-4439, Jun. 2016.

[SAH18] S. K. Sahoo and T. Bhattacharya, “Phase-shifted carrier-based synchronized sinusoidal PWM techniques for a cascaded H-Bridge multilevel inverter,” *IEEE Trans. Power Electron.*, vol. 33, no. 1, pp. 513-524, Jan. 2018.

[SCE16] G. Scelba, G. De Donato, M. Pulvirenti, F. Giulii Capponi and G. Scarcella, “Hall-effect sensor fault detection, identification, and compensation in brushless dc drives,” *IEEE Trans. Ind. Appl.*, vol. 52, no. 2, pp. 1542-1554, Mar.-Apr. 2016.

[SCH14] L. Schwager, A. Tüysüz, C. Zwyssig and J. W. Kolar, ‘Modeling and comparison of machine and converter losses for PWM and PAM in high-speed drives,’ *IEEE Trans. Ind. Appl.,* vol. 50, no. 2, pp. 995-1006, Mar.-Apr. 2014.

[SHA06] J. Shao, “An improved microcontroller-based sensorless brushless DC (BLDC) motor drive for automotive applications,” *IEEE Trans. Ind. Appl.*, vol. 42, no. 5, pp. 1216-1221, Sep.-Oct. 2006.

[SHE04] J. X. Shen, Z. Q. Zhu and D. Howe, “Sensorless flux-weakening control of permanent-magnet brushless machines using third harmonic back EMF,” *IEEE Trans. Ind. Appl.*, vol. 40, no. 6, pp. 1629-1636, Nov.-Dec. 2004.

[SHE06] J. X. Shen and S. Iwasaki, “Sensorless control of ultrahigh-speed PM brushless motor using PLL and third harmonic back EMF,” *IEEE Trans. Ind. Electron.*, vol. 53, no. 2, pp. 421-428, Apr. 2006.

[SHI12] Y. Shi, K. Sun, L. Huang and Y. Li, “Online identification of permanent magnet flux based on extended Kalman filter for IPMSM drive with position sensorless control,” *IEEE Trans. Ind. Electron.*, vol. 59, no. 11, pp. 4169-4178, Nov. 2012.

[SHI17] T. Shi, Y. Cao, G. Jiang, X. Li and C. Xia, “A torque control strategy for torque ripple reduction of brushless DC motor with nonideal back electromotive force,” *IEEE Trans. Ind. Electron.*, vol. 64, no. 6, pp. 4423-4433, Jun. 2017.

[SHI18] T. Shi, L. Wu, Y. Yan and C. Xia, “Harmonic spectrum of output voltage for space vector-modulated matrix converter based on triple Fourier series,” *IEEE Trans. Power Electron.*, vol. 33, no. 12, pp. 10646-10653, Dec. 2018.

[SIL14] S. Silber, J. Sloupensky, P. Dirnberger, M. Moravec, W. Amrhein and M. Reisinger, “High-speed drive for textile rotor spinning applications,” *IEEE Trans. Ind. Electron.*, vol. 61, no. 6, pp. 2990-2997, Jun. 2014.

[SON18a] X. Song, B. Han, S. Zheng and J. Fang, “High-precision sensorless drive for high-speed BLDC motors based on the virtual third harmonic back-EMF,” *IEEE Trans. Power Electron.*, vol. 33, no. 2, pp. 1528-1540, Feb. 2018.

[SON18b] X. Song, B. Han, S. Zheng and S. Chen, “A novel sensorless rotor position detection method for high-speed surface PM motors in a wide speed range,” *IEEE Trans. Power Electron.*, vol. 33, no. 8, pp. 7083-7093, Aug. 2018.

[SON19a] Z. Song, F. Zhou and Z. Zhang, “Parallel-observer-based predictive current control of permanent magnet synchronous machines with reduced switching frequency,” *IEEE Trans. Ind. Inform.*, vol. 15, no. 12, pp. 6457-6467, Dec. 2019,

[SON19b] Z. Song and F. Zhou, “Observer-based predictive vector-resonant current control of permanent magnet synchronous machines,” *IEEE Trans. Power Electron.*, vol. 34, no. 6, pp. 5969-5980, Jun. 2019.

[STU12] P. Stumpf, R. K. Jardan, and I. Nagy, 'Subharmonics generated by space vector modulation in ultrahigh speed drives,' *IEEE Trans. Ind. Electron.*, vol. 59, no. 2, pp. 1029–1037, Feb. 2012.

[SUN18] S. Sundeep and B. Singh, "Robust position sensorless technique for a PMBLDC motor," *IEEE Trans. Power Electron.*, vol. 33, no. 8, pp. 6936-6945, Aug. 2018.

[TAN19] B. Tan, X. Wang, D. Zhao, K. Shen, J. Zhao and X. Ding, "A lag angle compensation strategy of phase current for high-speed BLDC motors," *IEEE Access*, vol. 7, pp. 9566-9574, 2019.

[TSO12] S. Tsotoulidis and A. Safacas, "A sensorless commutation technique of a brushless DC motor drive system using two terminal voltages in respect to a virtual neutral potential," *in Proc. 2012 XXth International Conference on Electrical Machines*, Marseille, 2012, pp. 830-836.

[TSO15] S. Tsotoulidis and A. N. Safacas, "Deployment of an adaptable sensorless commutation technique on BLDC motor drives exploiting zero sequence voltage," *IEEE Trans. Ind. Electron*., vol. 62, no. 2, pp. 877-886, Feb. 2015.

[TUO12] T. Tuovinen, M. Hinkkanen, L. Harnefors and J. Luomi, "Comparison of a reduced-order observer and a full-order observer for sensorless synchronous motor drives," *IEEE Trans. Ind. Appl.*, vol. 48, no. 6, pp. 1959-1967, Nov.-Dec. 2012.

[TUY17] A. Tüysüz, F. Meyer, M. Steichen, C. Zwyssig and J. W. Kolar, "Advanced cooling methods for high-speed electrical machines," *IEEE Trans. Ind. Appl.*, vol. 53, no. 3, pp. 2077-2087, May-Jun. 2017.

[VAL17] R. L. Valle, P. M. de Almeida, A. A. Ferreira and P. G. Barbosa, 'Unipolar PWM predictive current-mode control of a variable-speed low inductance BLDC motor drive,' *IET Electr. Power Appl.*, vol. 11, no. 5, pp. 688-696, 5 2017.

[WAN13a] G. Wang, R. Yang and D. Xu, "DSP-based control of sensorless IPMSM drives for wide-speed-range operation," *IEEE Trans. Ind. Electron.*, vol. 60, no. 2, pp. 720-727, Feb. 2013.

[WAN13b] G. Wang, Z. Li, G. Zhang, Y. Yu and D. Xu, "Quadrature PLL-based high-order sliding-mode observer for IPMSM sensorless control with online MTPA control strategy," *IEEE Trans. Energy Convers.*, vol. 28, no. 1, pp. 214-224, March 2013.

[WAN15] S. Wang and A. C. Lee, "A 12-step sensorless drive for brushless DC motors based on back-EMF differences," *IEEE Trans. Energy Convers.*, vol. 30, no. 2. pp. 646–654, 2015.

[WAN20] G. Wang, M. Valla and J. Solsona, "Position sensorless permanent magnet synchronous machine drives—a review," *IEEE Trans. Ind. Electron*., vol. 67, no. 7, pp. 5830-5842, July 2020.

[WUS19] S. Wu, W. Tong, W. Li, S. Yu and R. Tang, “Electromagnetic vibration analysis of high-speed permanent magnet synchronous machines with amorphous metal stator cores considering current harmonics,” *IEEE Trans. Ind. Electron*., DOI: 10.1109/TIE. 2019.2959501

[XIA14] C. Xia, Y. Xiao, W. Chen and T. Shi, “Torque ripple reduction in brushless DC drives based on reference current optimization using integral variable structure control,” *IEEE Trans. Ind. Electron,* vol. 61, no. 2, pp. 738-752, Feb. 2014.

[XUE17] S. Xue, J. Feng, S. Guo, Z. Chen, J. Peng, W. Q. Chu, P. L. Xu, Z. Q. Zhu, “Iron loss model for electrical machine fed by low switching frequency inverter,” *IEEE Trans. Magn.*, vol. 53, no. 11, pp. 1-4, Nov. 2017.

[XUP16a] P. L. Xu and Z. Q. Zhu, “Novel square-wave signal injection method using zero-sequence voltage for sensorless control of PMSM drives,” *IEEE Trans. Ind. Electron*., vol. 63, no. 12, pp. 7444–7454, Dec. 2016.

[XUP16b] P. L. Xu and Z. Q. Zhu, “Carrier signal injection-based sensorless control for permanent-magnet synchronous machine drives considering machine parameter asymmetry,” *IEEE Trans. Ind. Electron.*, vol. 63, no. 5, pp. 2813-2824, May 2016.

[XUW19] W. Xu, Y. Jiang, C. Mu and F. Blaabjerg, “Improved nonlinear flux observer-based second-order SOIFO for PMSM sensorless control,” *IEEE Trans. Power Electron.*, vol. 34, no. 1, pp. 565-579, Jan. 2019.

[XUY16] Y. Xu, Y. Wei, B. Wang and J. Zou, “A novel inverter topology for brushless DC motor drive to shorten commutation time,” *IEEE Trans. Ind. Electron*., vol. 63, no. 2, pp. 796-807, Feb. 2016.

[YAN17a] H. Yang, Y. Zhang, G. Yuan, P. D. Walker and N. Zhang, ‘Hybrid synchronized PWM schemes for closed-loop current control of high-power motor drives,’ *IEEE Trans. Ind. Electron*., vol. 64, no. 9, pp. 6920-6929, Sep. 2017.

[YAN17b] S. Yang and G. Chen, “High-speed position-sensorless drive of permanent-magnet machine using discrete-time EMF estimation,” *IEEE Trans. Ind. Electron.*, vol. 64, no. 6, pp. 4444-4453, June 2017.

[YAN19a] L. Yang, Z. Q. Zhu, H. Bin and Z. Zhang, “Virtual third harmonic back-EMF based sensorless drive for high speed BLDC motors considering machine parameter asymmetries,” *in Proc. IEEE Int. Electric Mach. Drives Conf.*, San Diego, CA, USA, 2019, pp. 406-411.

[YAN19b] L. Yang, Z. Q. Zhu, H. Bin and Z. Zhang, “Safety operation area of zero-crossing detection based sensorless high speed BLDC motor drives,” *in Proc. IEEE Int. Electric Mach. Drives Conf.,* San Diego, CA, USA, 2019, pp. 1628-1633.

[YAN20] H. Yang, R. Yang, W. Hu and Z. Huang, “FPGA-based sensorless speed control of PMSM using enhanced performance controller based on the reduced-order EKF*,” IEEE Trans. Emerg. Sel. Topics Power Electron.* doi: 10.1109/JESTPE.2019.2962697

[YEP14] A. G. Yepes, A. Vidal, J. Malvar, O. López and J. Doval-Gandoy, “Tuning method aimed at optimized settling time and overshoot for synchronous proportional-integral current control in electric machines,” *IEEE Trans. Power Electron.*, vol. 29, no. 6, pp. 3041-3054, Jun. 2014.

[YIM09] J. Yim, S. Sul, B. Bae, N. R. Patel and S. Hiti, “Modified current control schemes for high-performance permanent-magnet AC drives with low sampling to operating frequency ratio,” *IEEE Trans. Ind. Appl.*, vol. 45, no. 2, pp. 763-771, Mar.-Apr. 2009,

[YOO11] Y.-D. Yoon, S.-K. Sul, M. Shinya, and K. Ide, “High-bandwidth sensorless algorithm for AC machines based on square-wave-type voltage injection,” *IEEE Trans. Ind. Appl.*, vol. 47, no. 3, pp. 1361–1370, May/Jun. 2011.

[ZHA17a] X. Zhang, B. Hou and Y. Mei, “Deadbeat predictive current control of permanent-magnet synchronous motors with stator current and disturbance observer,” *IEEE Trans. Power Electron.*, vol. 32, no. 5, pp. 3818-3834, May 2017.

[ZHA17b] G. Zhang, G. Wang, D. Xu and Y. Yu, “Discrete-time low-frequency-ratio synchronous-frame full-order observer for position sensorless IPMSM drives,” *IEEE Trans. Emerg. Sel. Topics Power Electron.*, vol. 5, no. 2, pp. 870-879, Jun. 2017.

[ZHA19] W. Zhao, A. Yang, J. Ji, Q. Chen and J. Zhu, “Modified flux linkage observer for sensorless direct thrust force control of linear vernier permanent magnet motor,” *IEEE Trans. Power Electron.*, vol. 34, no. 8, pp. 7800-7811, Aug. 2019.

[ZHO17] X. Zhou, X. Chen, F. Zeng and J. Tang, “Fast commutation instant shift correction method for sensorless coreless BLDC motor based on terminal voltage information,” *IEEE Trans. Power Electron.*, vol. 32, no. 12, pp. 9460-9472, Dec. 2017.

[ZHO17] S. Zhou, J. Liu, L. Zhou and Y. Zhang, “DQ current control of voltage source converters with a decoupling method based on preprocessed reference current feed-forward,” *IEEE Trans. Power Electron.*, vol. 32, no. 11, pp. 8904-8921, Nov. 2017.

[ZHO19] X. Zhou, Y. Zhou, C. Peng, F. Zeng and X. Song, “Sensorless BLDC motor commutation point detection and phase deviation correction method,” *IEEE Trans. Power Electron.*, vol. 34, no. 6, pp. 5880-5892, Jun. 2019.

[ZHO19] X. Zhou, Y. Zhou, C. Peng, F. Zeng and X. Song, “Sensorless BLDC motor commutation point detection and phase deviation correction method,” *IEEE Trans. Power Electron*., vol. 34, no. 6, pp. 5880-5892, Jun. 2019.

[ZHU01] Z. Q. Zhu, J. D. Ede, and D. Howe, “Design criteria for brushless DC motors for high-speed sensorless operation,” *Int. J. Appl. Electromagn. Mech*., vol. 15, pp. 79–87, 2001/2002.

[ZHU07] Z. Q. Zhu and D. Howe, “Electrical machines and drives for electric, hybrid, and fuel cell vehicles,” *in Proc. of the IEEE*, vol. 95, no. 4, pp. 746-765, Apr. 2007.

[ZWY08] C. Zwyssig, S. D. Round and J. W. Kolar, “An ultrahigh-speed, low power electrical drive system,” *IEEE Trans. Ind. Electron.*, vol. 55, no. 2, pp. 577-585, Feb. 2008.

APPENDIX 1

Specification and Parameters of Test Rig and PM Brushless Motors

A1.1 Hardware Design of Test Rig

An experimental platform of high-speed BLDC drive has been built up. As shown in Fig. A1.1, the platform contains high-speed BLDC motors (Midea), high-speed motor drive, oscilloscope (Yokogawa DL850) and a DC power supply (EA-PS 9080-50). Details of the printed circuit boards (PCB) of the drive are shown in Fig. A1.2.

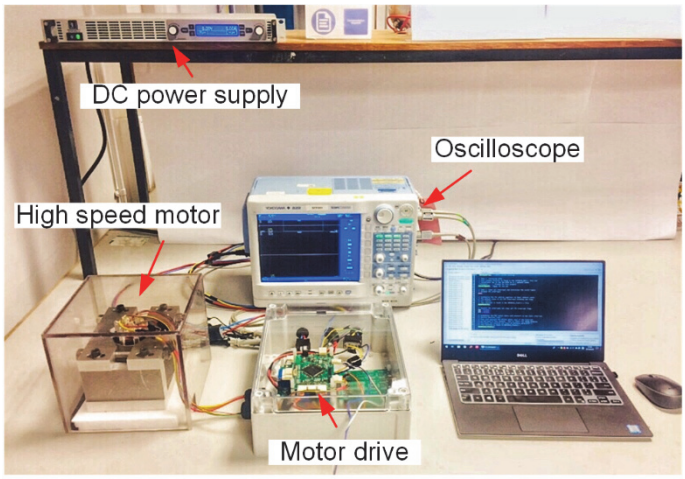

Fig. A1.1 High-speed BLDC drive platform.

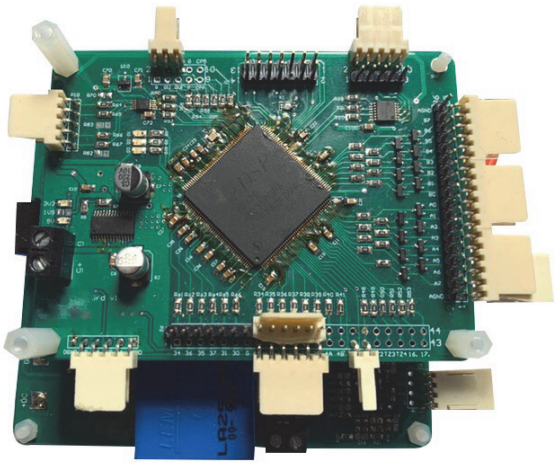

Fig. A1.2 Printed circuit boards of the drive.

The block diagram of hardware system is shown in Fig. A1.3. The whole system contains two parts, i.e. the digital control part and the inverter part, which are routed in two PCBs, respectively.

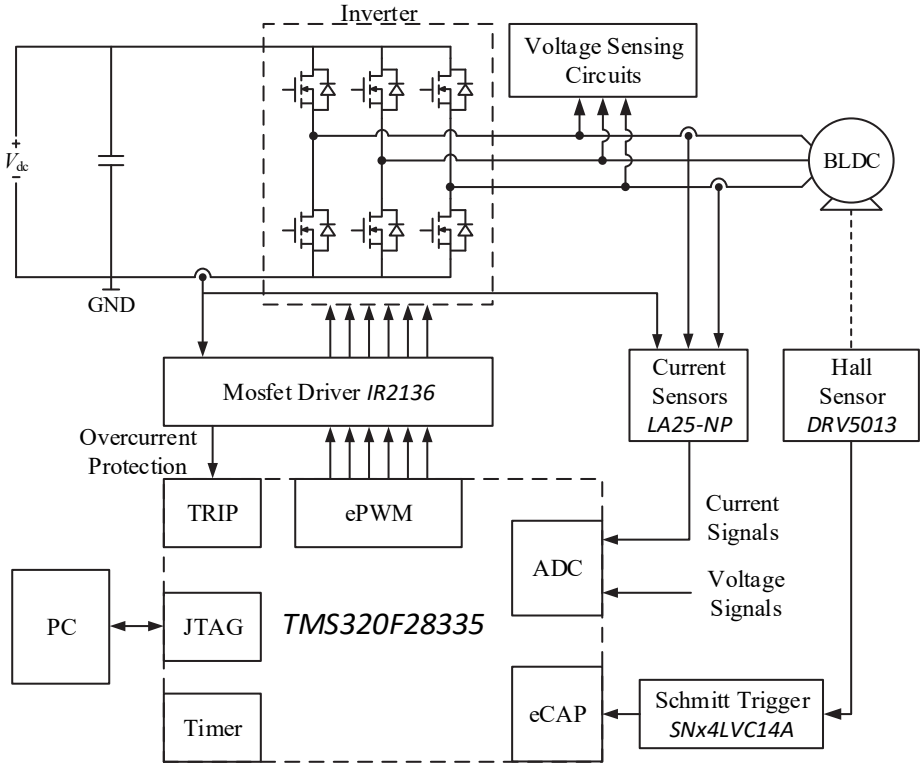

Fig. A1.3 Block diagram of overall hardware system.

1) Digital Control Board

The digital control part is based on high performance DSP chip TMS320F28335 with the frequency of 150 MHz. Some on-chip modules are applied, including eCAP, ADC, ePWM and CPU Timer, which are introduced as follows.

A. Hall-effect Sensors and eCAP Module

Three Hall-effect sensors (DRV5013) are installed on the stator of the motor to detect the rotor position. The output signal is reshaped with a Schmitt-trigger (SNx4LVC14A) and then connected with the eCAP module of DSP. The eCAP module can capture the rising and falling edges of digital signals, which are suitable for position detection with Hall-effect sensors.

B. Analog-to-Digital Converter (ADC)

The on-chip ADC is used to sample the current signals, including two phase currents and a DC-link current; and all the voltage signals for the sensorless BLDC drive. The ADC module is connected with the ePWM module to execute the PWM synchronization sampling technique.

C. ePWM Module with Overcurrent Protection

The ePWM module is to produce PWM signal and protect the drive from overcurrent. When the overcurrent occurs by any possible reasons, the DC-link current will soar up and trigger trip-zone submodule, which will shut down all the PWM signals for protection. Then, an algorithm interrupt will be triggered and further protection can be executed. Besides, the PWM synchronization sampling is a useful function for high-speed BLDC drive.

D. CPU Timer

For BLDC drive with six-step control, regardless sensor or sensorless techniques, only six discrete commutation signals are available. Thus, the CPU Timer is required for speed calculation and commutation instant detection.

The PCB routing of the digital control board is shown in Fig. A1.4.

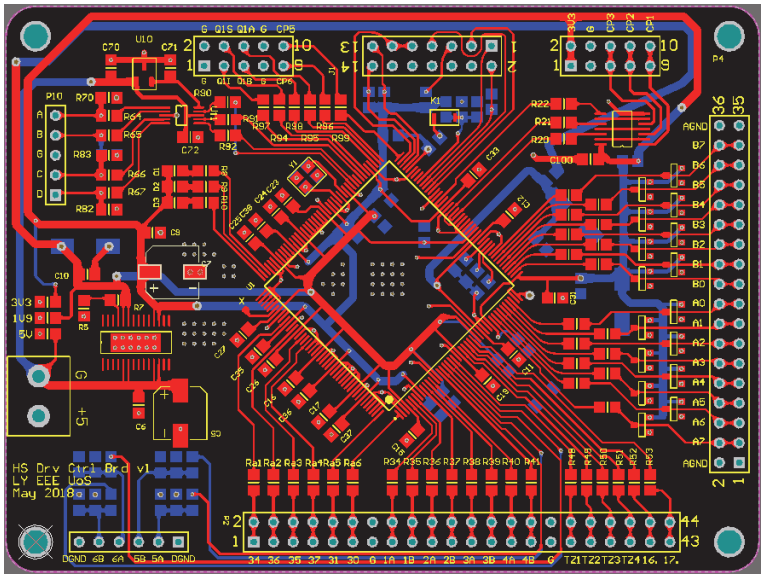

Fig. A1.4 PCB routing of the digital control board.

2) Inverter Board

As shown in Figs. A1.5 and A1.6, the three-phase bridge driver IR2136 is employed to drive the inverter based on MOSFET IRFS4410. This driver IR2136 contains three independent high and low side channels for three-phase applications. Thus, all the six PWM channels can be controlled independently, which is desirable for BLDC drive. Besides, this chip supports overcurrent protection and cross-conduction prevention. When an overcurrent event is detected, all the six channel will be shut down and an interrupt signal will be sent to DSP. The cross-conduction prevention function will protect two power devices in a leg from conducting simultaneously. These two functions will help reduce unnecessary troubles.

Fig. A1.7 shows the Hall current sensor LA25-NP and analog amplifier circuit. Three Hall current sensors are used for current acquisition, including a DC-link current for the BLDC drive and two phase currents the for BLAC drive. The primary to secondary current ratio is 1000:1. At the secondary side, a 100Ω resistor with 0.1% tolerance is used to convert current signal into voltage signal, and thus the current to voltage ratio is actually 10:1. Then, as shown in Fig. A1.7, a 1.5V DC offset is added by the operational amplifier in order to detect the negative current signal.

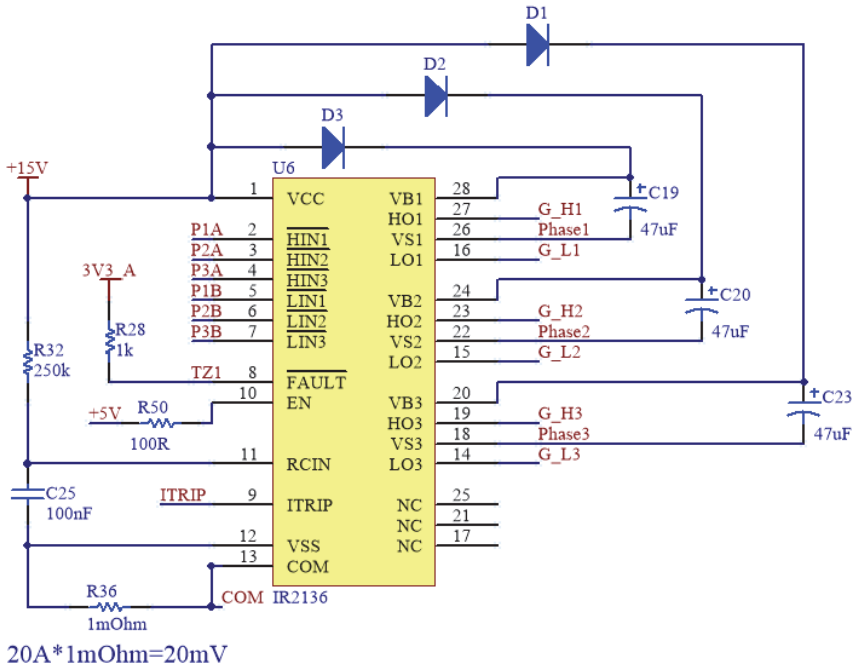

Fig. A1.5 Three-phase bridge driver based on IR2136.

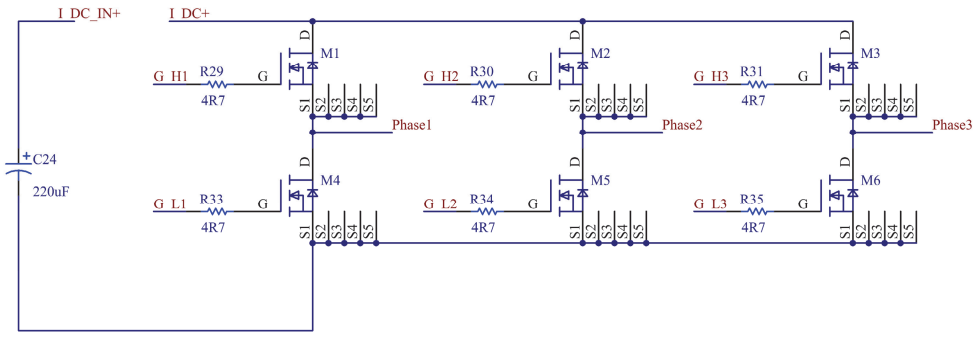

Fig. A1.6. Inverter based on MOSFET IRFS4410.

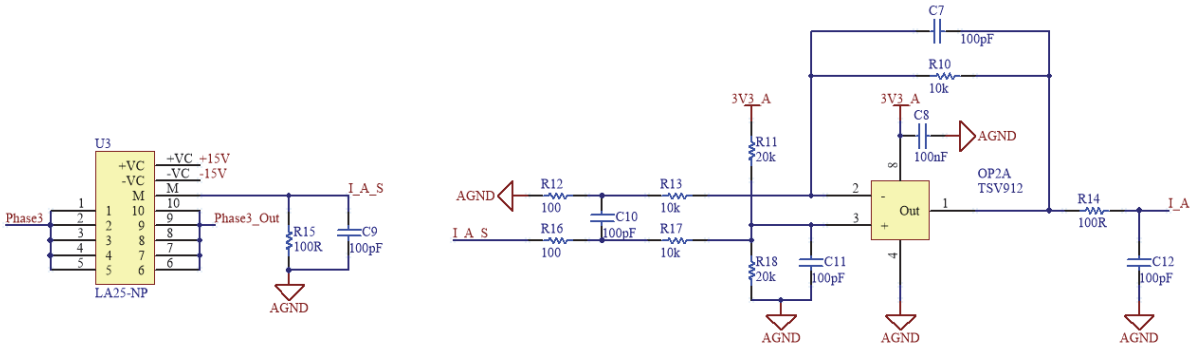

Fig. A1.7. Hall current sensor LA25-NP and analog amplifier circuit.

The PCB routing of the inverter board is shown in Fig. A1.7.

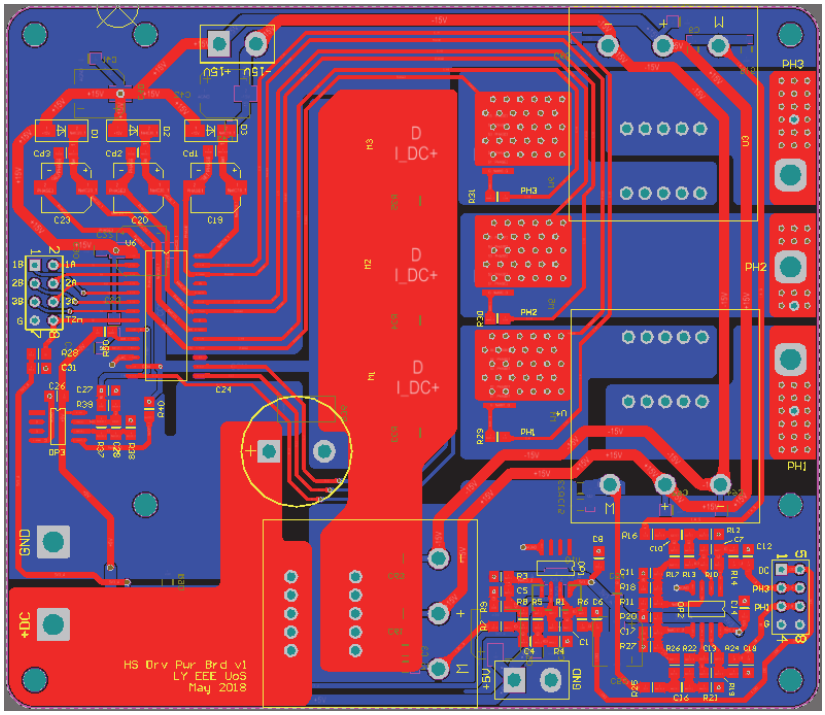

Fig. A1.8. PCB routing of the inverter board.

A1.2 High-speed PM Brushless Motors

1) Motor-I

The test Motor-I is shown in Fig. 1.9. Fan blades are mechanically integrated with the motor shaft to produce the load torque. The parameters are listed in Table A1.1. This motor is employed for the experimental validation in Chapters 2, 4, 5 and 6.

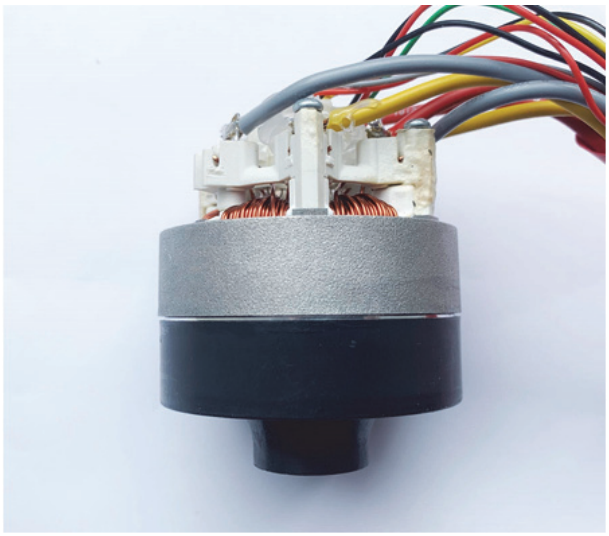

Fig. A1.9. High-speed PM brushless Motor-I.

Table A1.1 Parameters of Motor-I

Parameter	Value	
DC-link voltage	15 V	25V
Maximum speed	60 000 r/min	90 000 r/min
Maximum current	30 A	
Flux linkage	0.00098 V·s/rad	
Pole pairs	1	
Phase resistance	21 mΩ	
Phase self-inductance	22 μH	
Mutual inductance	3 μH	

2) Motor-II

The test Motor-II is as shown in Fig. 1.10. The same as Motor-I, fan blades are mechanically integrated with the motor shaft to produce the load torque. The parameters are listed in Table A1.2. It should be noted that the three-phase resistance and inductance parameters are asymmetric. This motor is utilized for the experimental validation in Chapter 3.

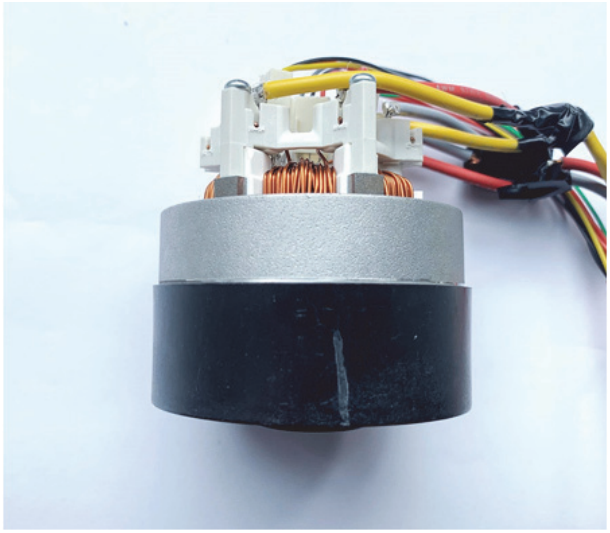

Fig. A1.10. High-speed PM brushless Motor-II.

Table A1.2 Parameters of Motor-II

Parameter	Value
DC-link voltage	15 V
Maximum speed	54 000 r/min
Maximum current	14 A
Flux linkage	0.00127 V·s/rad
Pole pairs	1
Phase Resistance (mΩ)	R_A=38.1 R_B=37.5 R_C=43.5
Phase self-inductance (μH)	L_A=27.5 L_B=27.2 L_C=28.6
Mutual inductance (μH)	4

APPENDIX 2

Specification and Parameters of Simulation Models

Simulation models have been built up in the Matlab/Simulink software. In Chapters 5 and 7, the models are used to validate the work. As shown in Fig. A.2.1, the whole models consists of three parts, the control algorithm, the inverter and the BLDC/BLAC motor, which are denoted as 1, 2 and 3, respectively.

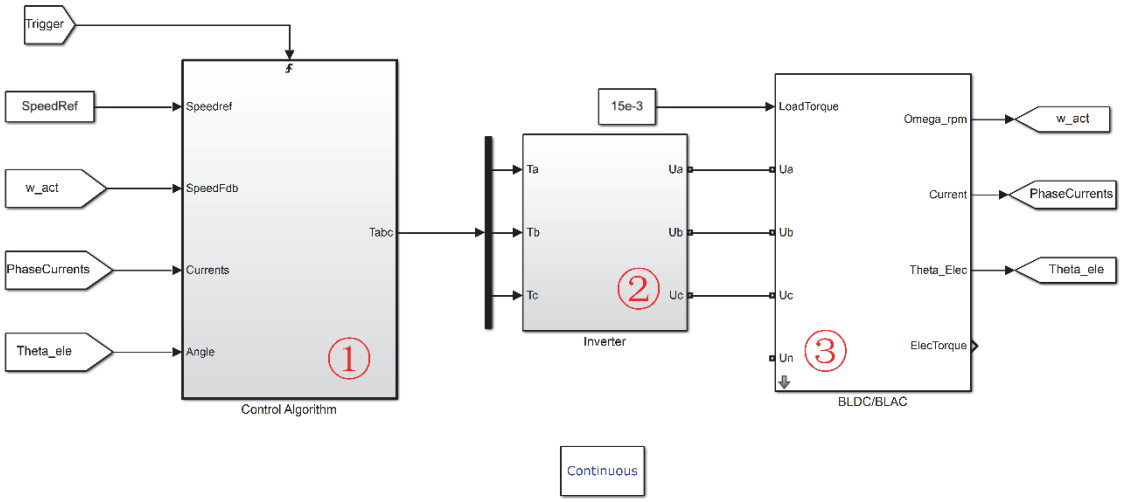

Fig. A2.1. Simulation models in Matlab/Simulink software.

The first block named control algorithm is programed by Matlab language. Four signals are fed into this block, speed reference, speed feedback, phase currents and electrical angle. The sampling frequency is set 20kHz in Chapters 5 and 15kHz in Chapter 7. Besides, a trigger signal that is generated in synchronized to the carrier signal is used to enable this block. In this way, the algorithm is always operated in synchronization with the PWM generation, which matches the practical experiment.

The second block is the inverter, which is composed of six MOSFETs. The PWM frequency is set the same as the sampling frequency, i.e. 20kHz in Chapters 5 and 15kHz in Chapter 7.

The third block is the BLDC/BLAC motor. The parameters are set the same as Motor-I (Table A1.1).

APPENDIX 3

Publications During PhD Study

Journal papers:

[1] L. Yang, Z.Q. Zhu, B. Shuang, and H. Bin, "Adaptive threshold correction strategy for sensorless high-speed brushless DC drives considering zero crossing point deviation," *IEEE Trans. Ind. Electron.,* vol. 67, no. 7, pp. 5246-5257, Jul. 2020.

[2] L. Yang, Z. Q. Zhu, H. Bin, Z. Zhang, and L. Gong, "Virtual third harmonic back-EMF based sensorless drive for high-speed BLDC motors considering machine parameter asymmetries," *IEEE Trans. Ind. Appl*.

[3] L. Yang, Z. Q. Zhu, H. Bin, Z. Zhang, and L. Gong, "Safety operation area of zero-crossing detection based sensorless high-speed BLDC motor drives," *IEEE Trans. Ind. Appl.*

[4] L. Yang, Z. Q. Zhu, Hong Bin, and Liming Gong, "Spectral analysis and sideband harmonic cancellation of six-step operation with low switching ratio for high-speed brushless DC drives," *IEEE Trans. Ind. Electron.*

Conference papers:

[5] L. Yang, Z. Q. Zhu, H. Bin, and Z. Zhang, "Virtual third harmonic back-EMF based sensorless drive for high-speed BLDC motors considering machine parameter asymmetries," *2019 IEEE International Electric Machines & Drives Conference (IEMDC)*, San Diego, CA, USA, 2019, pp. 406-411.

[6] L. Yang, Z. Q. Zhu, H. Bin, and Z. Zhang, "Safety operation area of zero-crossing detection based sensorless high-speed BLDC motor drives," *2019 IEEE International Electric Machines & Drives Conference (IEMDC)*, San Diego, CA, USA, 2019, pp. 1628-1633.